



## City Research Online

### City, University of London Institutional Repository

---

**Citation:** Sishtla, V. M. (2003). Analysis and testing of refrigerant lubricated bearings for centrifugal compressors. (Unpublished Doctoral thesis, City, University of London)

This is the accepted version of the paper.

This version of the publication may differ from the final published version.

---

**Permanent repository link:** <https://openaccess.city.ac.uk/id/eprint/30909/>

**Link to published version:**

**Copyright:** City Research Online aims to make research outputs of City, University of London available to a wider audience. Copyright and Moral Rights remain with the author(s) and/or copyright holders. URLs from City Research Online may be freely distributed and linked to.

**Reuse:** Copies of full items can be used for personal research or study, educational, or not-for-profit purposes without prior permission or charge. Provided that the authors, title and full bibliographic details are credited, a hyperlink and/or URL is given for the original metadata page and the content is not changed in any way.

**ANALYSIS AND TESTING OF REFRIGERANT  
LUBRICATED BEARINGS FOR CENTRIFUGAL  
COMPRESSORS**

by

**Vishnu Mohan Sishtla**

**A Thesis Submitted for the  
Degree of Doctor of Philosophy  
In Mechanical Engineering  
City University London**

**School of Engineering and Mathematical Sciences  
City University  
Northampton Square  
London EC1V 0HB**

**December 2003**

## Table of Contents

Title	1
Table of contents	2
Notation	11
Acknowledgements	13
Abstract	14
1. INTRODUCTION	15
1.1 The Limitation of oil as lubricant	15
1.2 Water-cooled chillers	16
1.3 Fluid Film Lubrication	19
1.4 Oil Free Compressor Design	21
1.5 Conclusion	23
1.6 References	24
2. AIMS OF THE THESIS	25
2.1 Outline of the thesis	25
3. LITERATURE SURVEY	27
3.1 Introduction	27
3.2 Stability of the flow between two concentric rotating cylinders	28
3.3 Analysis of Turbulent flow in Journal Bearings	32
3.4 Conclusion	37
3.5 References	38
4. HYDROSTATIC BEARING DESIGN AND ANALYSIS	40
4.1 Introduction	40
4.2 Compressor Design	41
4.3 Hydrostatic Bearing	43
4.4 Modeling of fluid flow in hydrostatic bearings	45
4.4.1 Bearing Stiffness and Damping	47
4.5 Bearing design	47
4.6 Results of Hydrostatic bearing design study	50
4.6.1 Effect of Pocket Orientation and Number Of Pockets	50
4.6.2 Effect Of Orifice Diameter	53
4.6.3 Effect of Radial Clearance	59
4.6.4 Effect Of Supply Pressure	62
4.6.5 Effect Of Pocket Depth	64
4.6.6 Effect Of Speed	64
4.6.7 Final Bearing Design	65
4.7 The Compressor Rotordynamics	68
4.7.1 Modeling of the rotating system	68
4.7.2 Undamped Critical Speed Analysis	70
4.7.3 Damped Critical Speeds and Rotor-Bearing Stability	77
4.7.4 Unbalance Response Analysis	81

4.7.5	Determination of magnitude and location of unbalance	82
4.7.6	Results of the unbalance response analysis	84
4.7.7	Discussion of the results	86
4.8	Conclusion	89
4.9	References	96
5.	HYDROSTATIC BEARING TESTING	97
5.1	Introduction	98
5.2	Test System	98
5.3	Instrumentation	100
5.4	Test Results	101
5.5	Discussion of test results	102
5.5.1	Accuracy of test results – Effect of electrical and mechanical runout (Glitch)	102
5.5.2	Comparison of measured and estimated unbalance response amplitudes	103
5.5.3	Rotor response as a function of Compressor Capacity	105
5.5.4	Rotor response due to aerodynamic instability	107
5.5.5	Verification of Rotor-Bearing stability	109
5.5.6	Effect of speed on Rotor-Bearing Stability	109
5.5.7	Effect of Supply Pressure on Sub Synchronous Amplitude	114
5.5.8	Rotor response due to unsteady supply pressure (Pump cavitation)	114
5.6	Conclusions	117
5.7	References	117
6.	REFRIGERANT LUBRICATED HYDRODYNAMIC BEARING	118
6.1	Introduction	118
6.2	Turbulent Reynolds equation for lubrication	121
6.3	Analysis of turbulence in the Bearing	123
6.3.1	Limitations of computer analysis code	124
6.4	Discussion of results	124
6.5	Conclusion	125
6.6	References	125
7.	COMPUTATIONAL FLUID DYNAMICS ANALYSIS OF FLOW IN HYDRODYNAMIC BEARINGS	129
7.1	Introduction	129
7.2	CFD Analysis	130
7.2.1	Boundary conditions	130
7.3	Turbulent Flow Modeling	132
7.3.1	Turbulence Models	133
7.3.2	Treatment of low near wall	135

7.4	Refrigerant Lubricated Hydrodynamic bearing – Geometry and Analysis model	136
7.5	Analytical Procedure	140
	7.5.1 Mesh Density optimization	141
	7.5.2 Turbulence model selection	142
7.6	Discussion of results	143
	7.6.1 Comparison with simple zero-equation finite difference code	149
7.7	Conclusion	152
8.	SUMMARY, CONCLUSIONS AND RECOMMENDATIONS FOR FURTHER WORK	154
8.1	Summary	154
8.2	Conclusions	154
8.3	Recommendations for further work	156

### APPENDICES

Appendix A: Results of Unbalance Response analysis	157
Appendix B: Shaft vibration measurement	189
Appendix C: Hydrostatic Bearing Compressor Test Procedure	192
Appendix D: Test results of Hydrostatic Bearing	204
Appendix E: Derivation Of Laminar Lubrication Equation - Reynolds Equation	234
Appendix F: Derivation Of Turbulent Reynolds equation for journal bearings	247
Appendix G: Computational Fluid Dynamics Analysis	255

### LIST OF FIGURES

Chapter 1		
Figure 1.1	Water-cooled chiller system	17
Figure 1.2	Cross section of a geared compressor	18
Figure 1.3	Lubrication System for geared compressor	19
Figure 1.4	Classification of fluid film lubrication	19
Figure 1.5	Bearing Loads for a Geared compressor	22
Figure 1.6	Direct Drive compressor	23
Chapter 4		
Figure 4.1	Direct Drive Compressor showing major components	41
Figure 4.2	Hydrostatic Bearing Geometry	44
Figure 4.3A	Effect of number of pockets on load	51
Figure 4.3B	Effect of number of pockets on flow rate	51
Figure 4.3C	Effect of number of pockets on stiffness	52

Figure 4.3D	Effect of number of pockets on damping	52
Figure 4.4A	Effect of orifice diameter on load	55
Figure 4.4B	Pocket pressure variation vs Orifice diameter	55
Figure 4.4C	Film thickness vs orifice diameter	56
	Flow rate vs Orifice diameter	56
Figure 4.4E	Stiffness vs Orifice diameter	57
Figure 4.4F	Damping vs Orifice diameter	57
Figure 4.4G	Load carrying capacity vs ratio of orifice diameter/radial clearance	58
Figure 4.4H	Load carrying capacity vs ratio of orifice diameter/radial clearance	58
Figure 4.5A	Minimum Film Thickness vs radial clearance for bearing load of 450N	59
Figure 4.5b	Power loss vs Radial Clearance for bearing load of 450N	60
Figure 4.5C	Flow Rate vs Radial clearance for a bearing load of 450N	60
Figure 4.5D	Stiffness vs Radial Clearance bearing load 450N	61
Figure 4.5E	Damping vs Radial Clearance bearing load = 450N	61
Figure 4.6A	Minimum film thickness vs Supply Pressure	62
Figure 4.6B	Flow Rate vs Supply Pressure	63
Figure 4.6C	Stiffness vs supply pressure	63
Figure 4.6D	Damping vs Supply Pressure	64
Figure 4.7A	Solid model of front or Impeller side hydrostatic bearing	65
Figure 4.7B	Hydrostatic bearing cross section – Front or Impeller side	66
Figure 4.7C	Hydrostatic Bearing cross section – Rear or motor Side	67
Figure 4.7D	Solid model of rear or motor side hydrostatic bearing	67
Figure 4.8	Rotor Model Showing Balancing planes	69
Figure 4.9	Rotor Static Deflection Plot	69
Figure 4.10	Stations for Rotor Dynamic Modelling	71
Figure 4.11A	Undamped Critical Speed Map	73
Figure 4.11B	Rotor Mode shape at bearing stiffness = 1766kN/m	74
Figure 4.11C	Rotor Mode shape at bearing stiffness = 17660kN/m	74
Figure 4.11D	Rotor mode shape at bearing stiffness = 43750kN/m	75
Figure 4.11E	Rotor mode shape at bearing stiffness = 87600kN/m	75
Figure 4.11F	Rotor mode shape at bearing stiffness = 176000kN/m	76
Figure 4.11G	Rotor mode shape at bearing stiffness = 87600kN/m	76

Figure 4.12A	Stability and rotor mode shape supply pressure = 2.1 MPa – Forward whirl	80
Figure 4.12B	Stability and rotor mode shape supply pressure = 2.1 MPa – Backward whirl	81
Figure 4.13A	Typical synchronous response vibration amplitude output	85
Figure 4.13B	Typical synchronous response bearing force output	86
Figure 4.13C	Amplification Factor based on major orbit	86
Figure 4.14	Critical speed vs supply pressure based on unbalance response analysis	90
Figure 4.15A	Amplification factor at first critical speed vs supply pressure	90
Figure 4.15B	Vibration Amplitude at bearings at First critical speed vs supply pressure	91
Figure 4.15C	Amplification factor at second critical speed vs supply pressure	91
Figure 4.15D	Vibration Amplitude at bearings at second critical speed vs supply pressure	92
Figure 4.16A	Comparison of response at Rear bearing with in-phase (dashed line) and out of (solid line) unbalance	92
Figure 4.16B	Comparison of response at middle of rotor with in-phase (dashed line) and out of (solid line) unbalance	93
Figure 4.16C	Comparison of response at Impeller end bearing with in-phase (dashed line) and out of (solid line) unbalance	93
Figure 4.16D	Comparison of response at Impeller end bearing with in-phase (dashed line) and out of (solid line) unbalance	94
Figure 4.17A	Force at Rear bearing. In-phase unbalance	94
Figure 4.17B	Force at Impeller bearing. In-phase unbalance	95
Figure 4.17C	Force at Rear bearing. Out of-phase unbalance	95
Figure 4.17D	Force at Impeller bearing. Out of-phase unbalance	96

## CHAPTER 5

Figure 5.1	Test Schematic of Hydrostatic bearing compressor	99
Figure 5.2	Measured rotor synchronous amplitude at bearings - supply pressure 2.1MPa	104

Figure 5.3	Measured rotor synchronous amplitude at bearings - supply pressure 2.1MPa	104
Figure 5.4	Shaft orbit near Impeller during steady state, 13200 rpm Scale, 25.4 microns/div	105
Figure 5.5A	Front bearing Horizontal vibration spectrum as a function of load Speed 12600 rpm supply pressure 2.1 MPa	106
Figure 5.5B	Front bearing Horizontal vibration spectrum as a function of load, Speed 12600 rpm, supply pressure 2.1 MPa	106
Figure 5.6	Rotating stall	107
Figure 5.7	Shaft orbit near Impeller orbit during Stall 13,200 rpm supply pressure = 2.1 MPa	108
Figure 5.8A	Spectrum Plot during stall, Y-direction at Impeller	108
Figure 5.8B	Spectrum Plot during stall, X-direction at Impeller	109
Figure 5.9A	Front Bearing X-direction. Start of Instability at 240 Hz, Supply pressure 2.1Mpa	111
Figure 5.9B	Front Bearing Y-direction. Start of Instability at 240 Hz, Supply pressure 2.1Mpa	111
Figure 5.10A	Subsynchronous Vibration – as a function of speed. Supply pressure 2.1Mpa	112
Figure 5.10B	Subsynchronous Vibration – as a function of speed. Supply pressure 2.1Mpa	112
Figure 5.11A	Subsynchronous Vibration – as a function of speed. Supply pressure 2.1Mpa	113
Figure 5.11B	Subsynchronous Vibration – as a function of speed. Supply pressure 2.1Mpa	113
Figure 5.12	Supply pressure During Pump Cavitation	115
Figure 5.13A	Vibration at Front bearing, X direction before supply pressure instability due to pump cavitation	116
Figure 5.13B	Vibration at Front bearing, X direction during supply pressure instability due to pump cavitation	116

## Chapter 6

Figure 6.1	Bearing Nomenclature	119
Figure 6.2	Hydrodynamic Bearing Lubrication System	120
Figure 6.3	Hydrodynamic Journal Bearing	123
Figure 6.4	Load vs Eccentricity ratio, Lubricant - HFC134a liquid	126
Figure 6.5	Load vs Minimum clearance, Lubricant - HFC134a	126
Figure 6.6	Load vs Eccentricity ratio, with Lubricant HFC134a – Turbulent flow and Oil-Laminar flow	127
Figure 6.7	Power loss Load vs Eccentricity ratio, HFC134a liquid lubricant, for turbulent and laminar flow	127
Figure 6.8	Stiffness vs Eccentricity ratio Lubricant - HFC134a liquid	128
Figure 6.9	Damping vs Eccentricity ratio Lubricant - HFC134a liquid	128

## Chapter 7

Figure 7.1	Bearing geometry with shaft	137
Figure 7.2A	Overall Mesh 128886 nodes	138
Figure 7.2B	Mesh in the inlet region	138
Figure 7.2C	Mesh in the clearance region	139
Figure 7.3	Locations of results sections	139
Figure 7.4	Pressure distribution for Reynolds stress model at section A-A with four different mesh sizes	142
Figure 7.5	Pressure distribution at section A-A with three different Turbulence models	143
Figure 7.6	Pressure distribution at Section A-A, Reynolds Stress model, 128886 nodes	144
Figure 7.7	Pressure and clearance distribution at Section A-A, Reynolds Stress model, 128886 nodes	145
Figure 7.8	Pressure and clearance distribution, section C-C, Reynolds stress model, 128886 nodes	145

Figure 7.9	Axial distribution of maximum pressure Reynolds stress model, 128886 nodes	146
Figure 7.10	Pressure distribution for Reynolds stress model, 128886 nodes	147
Figure 7.11	Grooved bearing with smooth transition	148
Figure 7.12	Pressure distribution in grooved bearing	148
Figure 7.13	Pressure drop in the transition region at section A-A	149
Figure 7.14	Comparison of pressure distribution with CFD and 2-D Zero equation finite difference code	150
Figure 7.15	Axial pressure distribution with CFD and 2-D Zero equation finite difference code	150
Figure 7.16	Comparison of pressure distribution with CFD and 2-D Zero equation finite difference code, grooved bearing	151
Figure 7.17	Comparison of amplitude of vibration between hydrostatic and hydrodynamic bearings	152

## List of Tables

### Chapter 4

Table 4.1	Hydrostatic Journal Bearing Characteristics	97
-----------	---	----

### Chapter 5

Table 5.1	Measured vs Calculated response values	103
Table 5.2:	Vibration Amplitude (peak to peak in microns) due to whirl instability as a function of supply pressure	114

### Chapter 6

Table 6.1	Lubricant Properties	121
-----------	----------------------	-----

### Chapter 7

Table 7.1	Details Of Computational Mesh	136
Table 7.2	Lubricant Viscosity at operating temperatures	140
Table 7.3	Summary of results with different mesh densities	141
Table 7.4	Comparison of CFD and simple finite difference code results	151

## NOTATION

Symbol	Description	Units
C	damping (with subscript), constant	kN. s .m <sup>-1</sup>
C <sub>d</sub>	coefficient of discharge	
C <sub>r</sub>	radial clearance	m
d	radial gap, diameter	m
$\bar{f}$	bearing force	N
f	frequency	Hz
F	bearing force	N
G	Turbulent correction factors	
h	local film thickness	m
K	stiffness	kN. m <sup>-1</sup>
k	kinetic energy	J
l	length	m
L	length	m
N	Speed	r/min
p	number of poles, pressure	Pa
P	pressure, power loss	Pa, kW
Q	flow rate , amplification factor	m <sup>3</sup> s <sup>-1</sup>
R	Radius	m
Re	Reynolds number	
t	Time	s
Ta	Taylor number	
u	Velocity	m s <sup>-1</sup>
U	shaft surface velocity	m s <sup>-1</sup>
u	Velocity	m s <sup>-1</sup>
v	Velocity	m s <sup>-1</sup>
V	volume , velocity	m <sup>3</sup> , m s <sup>-1</sup>
W	Rotor weight, velocity	N, m s <sup>-1</sup>
w	Velocity	m s <sup>-1</sup>
x, y, z	Cartesian coordinates. z axial direction, y direction in film thickness	
Y <sup>+</sup>	dimensionless distance	
?	Angular velocity	radians. s <sup>-1</sup>
?	kinematic viscosity	mm <sup>2</sup> . s <sup>-1</sup>
?	Density	kg . m <sup>-3</sup>
? <sub>w</sub>	ratio of finite length to infinite length bearing force	
?	compressibility factor	
?	dynamic viscosity	Pa . s
?	angular velocity	radians. s <sup>-1</sup>
?	attitude angle	degrees
?	turbulent dissipation energy	J
?	shear stress	Pa. m <sup>-2</sup>

## NOTATION (Continued)

<b>Subscript</b>	<b>Description</b>
1	Inner
2	Outer
cr	Critical
m	Mean
i	Inlet
r	Recess
s	Supply
o	Orifice
c	Capillary
x,y,z	Cartesian coordinates. z axial direction, y direction in film thickness
n	peak amplitude
eff	effective
t	turbulent

<b>Superscript</b>	<b>Description</b>
.	time rate of change
-	average, non-dimesnional
'	Fluctuating

## ACKNOWLEDGEMENTS

In preparing and submitting this thesis, I wish to take this opportunity to thank the many people who helped to make it all possible. Firstly, I would like to thank the past and present management team of my employers, Carrier Corporation, notably, Mr. William Rousseau and Mr. William Delaurier and Mr. Mead Rusert and Mr. John Jacobs, who allowed me to spend so much time on it. In addition, I would like to thank Dr. Joost Brasz, who took time from his busy schedule to be my industrial supervisor. Also, I would like to thank Prof A.R.D. Thorley of City University for his initial suggestion of the scheme and Mr. Richard Ertinger, Director Of Engineering, Carrier Corporation for its endorsement and his encouragement. I would like to thank all the designers and technicians at Carrier, who helped me during the oil-free compressor test programme. Prof. Ian Smith, of City University, made many helpful suggestions during the preparation of the thesis manuscript. Lastly, but by no means least, I would like to thank my wife Sailaja, and my children Haritha and Abhiram, who were a great source of inspiration and support throughout this effort.

## ABSTRACT

Centrifugal compressors with oil lubricated bearings are widely used to pressurise the refrigerant in large air-conditioning chiller systems. If the bearings, were lubricated with liquid refrigerant, the friction losses would be reduced and the oil system could be eliminated. This would increase the COP. Also, the absence of oil would increase the heat exchanger effectiveness and reduce manufacturing costs.

This thesis describes work carried out to develop a centrifugal compressor with refrigerant lubricated fluid film bearings of either:

- i) The externally pressurised hydrostatic type
- or
- ii) The simple hydrodynamic type, which do not need a high-pressure external pump.

The low refrigerant viscosity makes flow through both types of bearing turbulent.

The hydrostatic bearing was analysed using a computer program based on a 2-D Navier-Stokes turbulent model. Analysis showed that bearing load, dynamic properties and compressor vibrations are a strong function of supply pressure, radial clearance and orifice diameter. Vibration analysis carried out on the rotor-bearing system, predicted the onset of instability at supply pressures of less than 2.1 MPa.

An experimental programme was carried out on a centrifugal compressor to confirm this. Bearing instability was detected even at pressures as high as 2.1 MPa but with acceptable levels of vibration amplitude. At lower supply pressures, the vibration amplitudes were unacceptable.

A computer code was used to analyse hydrodynamic bearings, assuming two-dimensional flow and a simple zero-equation turbulence model. This showed that turbulence has a significant effect on the load carrying capacity and dynamic properties. A CFD code was used for a more detailed 3-D analysis to determine the effect of three different turbulence models on the pressure profile within the clearance. Nearly equal pressure profiles were predicted in all cases, but the peak pressures were 13% higher than the values obtained from the 2-D model. The predicted bearing size could thus be reduced.

# CHAPTER ONE

## INTRODUCTION

### 1.1 The limitation of oil as a lubricant

Oil lubricated bearings are widely used in industry to support shafts of rotating machinery. A thin film of oil within them separates the rotating shaft from the stationary bearing and thus reduces both frictional resistance and wear. The oil film also provides the desired stiffness and damping to the bearing system, to prevent harmful shaft vibrations and guarantee smooth operation of the machine.

In fluid processing machinery, where the presence of oil has an adverse effect on performance or contaminates the process fluid within it:

- 1) a buffer gas can be used to separate the oil from the process fluid
- 2) the process fluid itself can be used as the lubricant instead of oil

Typically, in air separation plants, oxygen compressors use an inert gas such as nitrogen to prevent the oil from entering the compressor and forming an explosive mixture with the oxygen<sup>1</sup>. In the nuclear industry, the sodium pumps used in fast breeder reactors use sodium (the process fluid itself) as the bearing lubricant to prevent contamination of oil and sodium<sup>2</sup>.

In conventional large air-conditioning systems, oil is used to lubricate the compressor bearings and gears. This comes in contact with the refrigerant and, since oil and refrigerant are miscible, the oil contaminates the refrigerant and vice versa.

The presence of oil in the refrigerant reduces the boiling heat transfer coefficient in the evaporator, while the presence of refrigerant in the oil reduces the viscosity of oil, which affects the bearing design. Hence, the introduction of a new refrigerant also involves a search for new oils.

A standard oil lubricating system comprises an oil sump, an oil pump, oil supply lines and an oil cooler. However, in a refrigeration system, an oil separator is also needed to remove entrained oil from the compressed refrigerant vapour, together with a reclaim system. This is needed to recover and transfer oil, dissolved in the liquid refrigerant, which separates out in the evaporator, and return it to the oil sump. Consequently, the elimination of oil from a refrigeration compressor would bring a number of benefits, such as increased system efficiency, elimination of the oil management system and acceleration of the process of introducing new refrigerants.

This thesis deals with the design and analysis of oil-free bearings for centrifugal compressors in water-cooled chillers. A brief description and operation of water-cooled chiller is therefore presented next.

## **1.2 Water-cooled chillers**

Figure 1.1 shows a water-cooled centrifugal chiller with its main components. The function of a water-cooled chiller is to supply cold water at around 6.5°C. In air conditioning applications, the chilled water leaving the cooler (evaporator) is used to cool and dehumidify the air circulating within a building. In process applications, the chilled water is used to cool an industrial process fluid. The return water from the building or process re-enters the chiller evaporator at 12° to 15 °C. There its temperature is reduced by heat transfer to the low temperature liquid refrigerant, which evaporates as it circulates round the water tubes, at a rate sufficient to maintain the desired chilled water exit temperature. The vaporized refrigerant leaving the evaporator is compressed to a high pressure by a centrifugal compressor. Water, entering the condenser vessel, from a cooling tower or river is used to condense the high-pressure refrigerant vapour.

The centrifugal compressor forms a critical component of the system and as such its reliability is of the utmost importance. A motor driven centrifugal compressor, for a 1.7 MW cooling capacity chiller, operates at 14500 rpm to achieve the optimum aerodynamic efficiency.

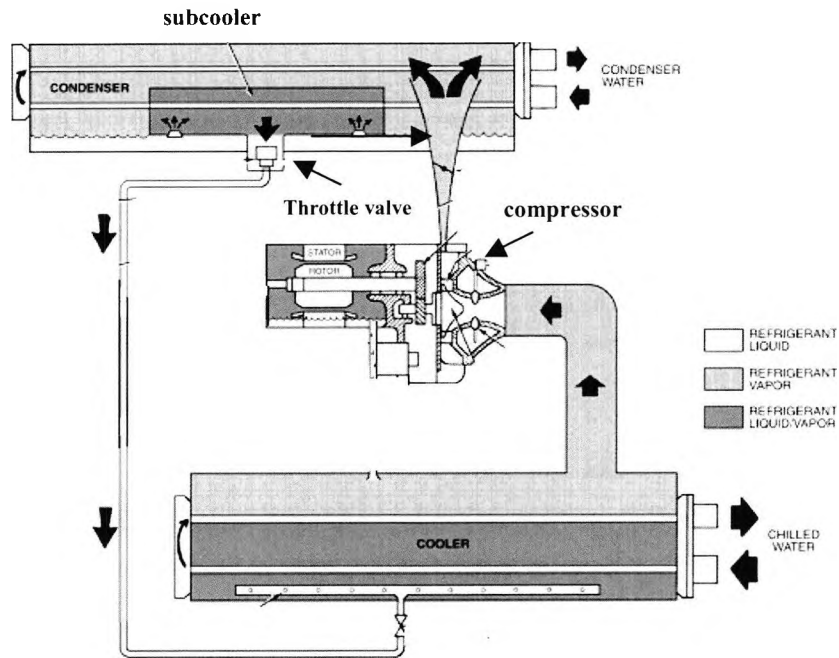


**Figure 1.1 Water-Cooled chiller system**

The motor input power is 300 kw and its corresponding speed, with a 60 hz power supply, is 3600 rpm. Figure 1.2 shows a cut-away view of the compressor with its main components. The required compressor speed of 14500 rpm is achieved through a speed increasing gear (items 4 and 11). The compressor has four bearings to compensate for the radial and axial loads, two on the high-speed shaft at 6 & 13 and two on the low speed shaft at 3. Besides taking care of the radial and axial thrust loads, the bearing design influences the rotor dynamics of the overall system. All the compressor components, including its motor (items 1 & 2) , are enclosed in the refrigerant atmosphere. This arrangement eliminates any leakage through shaft seals, which are used on a system where the motor is outside the refrigerant atmosphere. Also, since the motor is cooled by refrigerant taken from the condenser, which is more effective than air, its size can thus be reduced. The aerodynamic components consist of the inlet guide vanes (item 7), the impeller (item 9) and a pipe diffuser (item 10). The system capacity is regulated by moving the guide vanes from the open to the closed position. The fluid momentum at the impeller exit is reduced in the pipe diffuser, in order to attain the full discharge pressure. The refrigerant leaves the pipe diffuser, through a collector, to enter the condenser.

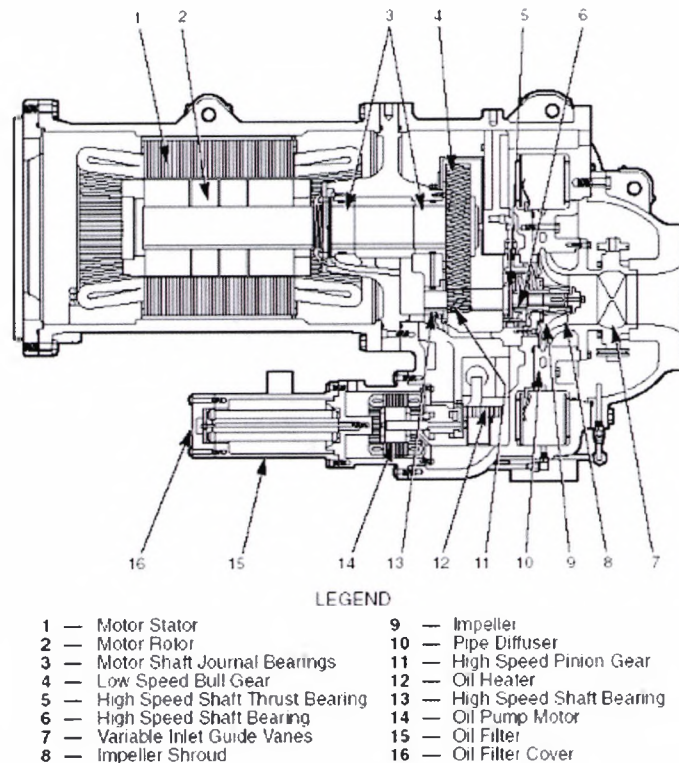


**Figure 1.2: Cross Section of a Geared Compressor**

Figure 1.3 shows the various components that make up the lubrication system, such as the oil pump, the oil cooler, the oil heater, the filter, the isolation valves, the piping and the auxiliary equipment. Oil from the sump is pumped to the bearings through the filter and the oil cooler. The discharge oil from the bearings is drained back into the sump. Any oil that leaks into the motor housing, during startup or shutdown, is carried by the refrigerant into the evaporator via the motor drain. The refrigerant/oil mixture from the evaporator enters the compressor via the inlet. The oil is separated in the suction housing cavity. The separated oil is returned to the sump through the reclaim line. An oil heater is provided to maintain the refrigerant solubility below 30% when the machine is shut down. The solubility of refrigerant in the oil during operation is between 8 to 10%.

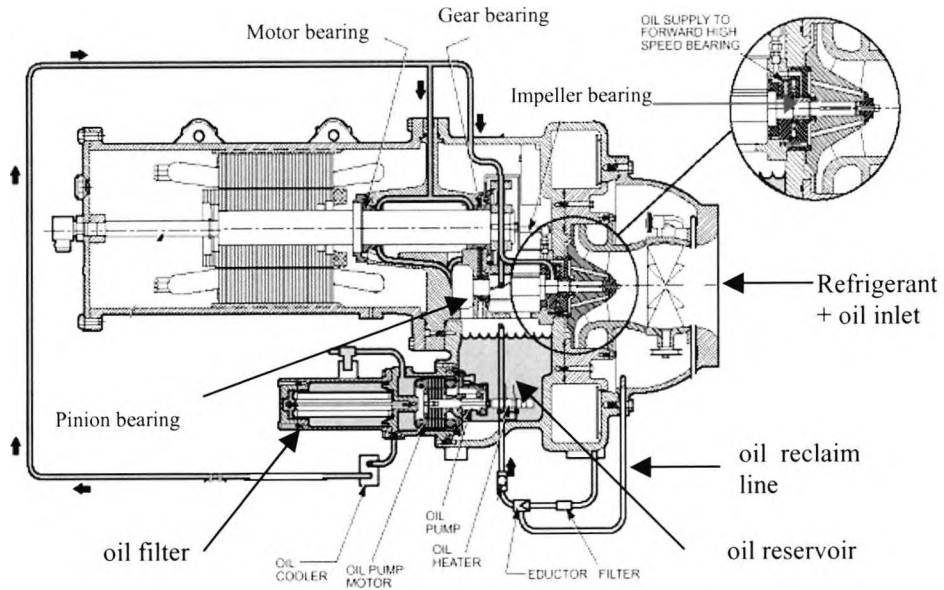


**Figure 1.3: Lubrication System for Geared Compressor**

### **1.3. Fluid Film Lubrication**

Fluid film lubrication can be classified on the basis of the film thickness as full film, partial film and boundary lubrication, as shown in Figure 1.4. The differences between these will be described for radial load carrying journal bearings.

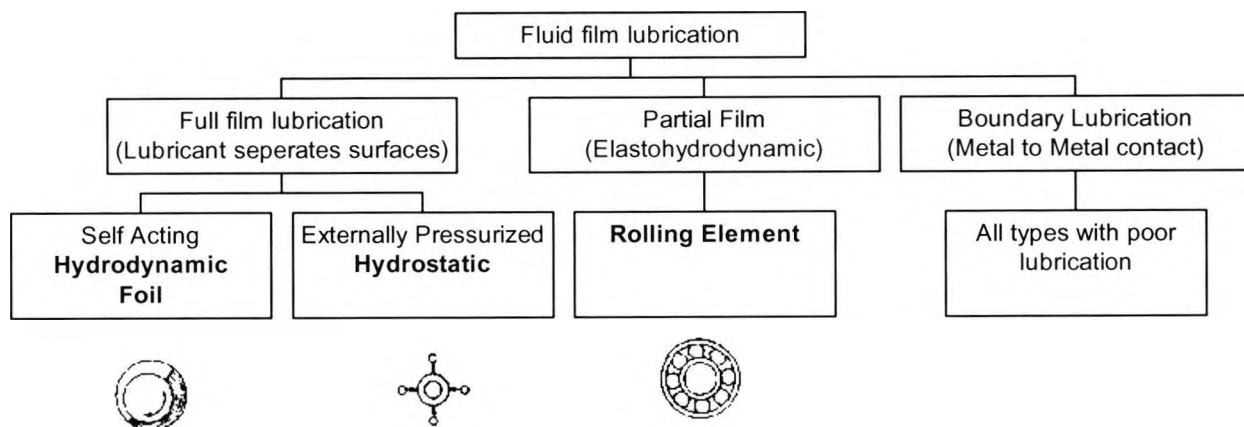


**Figure 1.4. Classification of fluid film lubrication**

Full-film lubrication implies that there is complete physical separation of the shaft and the bearing. The film thickness of the bearing is approximately one to two orders of

magnitude larger than the surface roughness of the mating bearing surfaces. Typical film thicknesses range from 25 to 80  $\mu\text{m}$  whereas surface roughness is normally of the order of 0.8  $\mu\text{m}$ . Bearings using full-film lubrication have conformal surfaces, i.e. the bearing encloses the shaft. Hydrodynamic and foil type bearings fall under this category. Their load carrying capacity is generated by virtue of the relative motion between the shaft and the bearing. Hence, they are described as self-acting. Typically, this type of bearing is used for high-speed applications.

The other bearing type using full film lubrication is the hydrostatic bearing. It requires external pressure to support the load. Typically this type of bearing is used for heavy load and low speed applications. It is also used with low viscosity lubricants at moderate loads and high speeds.

The physics of full film lubrication is completely described by the Navier-Stokes equation, whether based on the hydrodynamic or the hydrostatic bearing principle.

Partial film bearings have a film thickness comparable to the surface roughness of the shaft and the journal. Partial film bearings involve non-conformal surfaces. Rolling elements (also called anti-friction bearings) fall under this category. A rolling element bearing has an inner ring attached to the shaft, an outer ring attached to the housing and rollers or balls placed between the inner and outer rings. Bearing clearances within them are at least an order of magnitude lower than in full film bearings. The lubricant film is generated by relative motion between the inner ring and the rollers. The pressures generated in the lubricant film are extremely high and deform the surfaces. The extent of these deformations, which are of the same order of magnitude as the film thickness, determine the bearing life. The analysis of a partial film bearing requires the solution of both the Navier-Stokes and the elasticity equations, thus explaining the name "elastohydrodynamic" often used for this type of bearing.

Boundary lubrication involves contact between the shaft and the journal during operation. All full and partial film bearings operate in the boundary lubrication regime during startup and coastdown. Bearings that continuously operate in the boundary lubrication regime are usually made out of non-metallic materials and are used for low

speeds and light loads. The choice of either full or partial film bearings in high-speed compressor applications is dependent on the relative importance of such factors as long life or low power loss.

#### **1.4 Oil free compressor design**

A centrifugal compressor, driven by an induction motor operating at mains frequency, requires a speed increasing gearbox in which large forces are generated. The magnitude and direction of the resultant bearing loads due to the gear forces and the rotor weight is a function of the transmitted power. Typically, the radial bearing loads for a gear driven compressor operating in a 1.7 MW chiller, plotted as a function of compressor power, are shown in Figure 1.5. An alternative approach is to drive the compressor directly with a high-speed motor and thus eliminate the gearbox. The number of journal bearings required is then reduced from four to two, while the gearbox forces are eliminated. In the case of a direct drive compressor, illustrated in Figure 1.6, the radial bearing loads are constant and are only needed to support the motor rotor weight, which is equal to 1 kN. By reducing the bearing loads in this manner, a number of alternative bearing types become viable. Another advantage of low bearing loads is that the use of the refrigerant as a lubricant, in place of oil, becomes possible. Due to its low viscosity, this would result in reduced bearing losses. Also, the elimination of oil from the system would make the oil separation system redundant and improve heat transfer rates in the evaporator and condenser by getting rid of the film of oil, which forms on the heat transfer surfaces. It should be noted that thrust loads are a function of impeller design and as such can be reduced by including a balance piston in the system or using a shrouded impeller. However, due to its low viscosity, the flow of refrigerant liquid in a bearing is turbulent. The effect of flow instability and the transition from laminar to turbulent flow on bearing behaviour must therefore be considered. Despite these potential advantages, to date there is no record of the use of the process liquid as a lubricant in chiller systems.

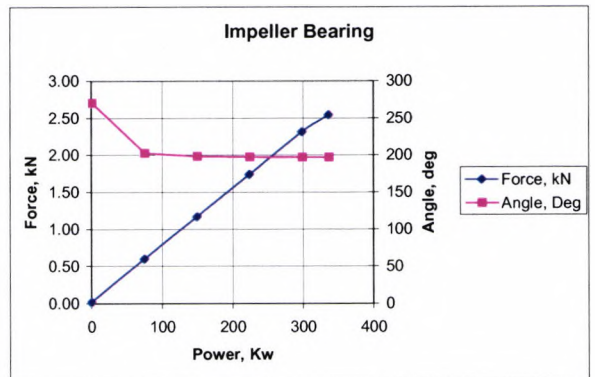
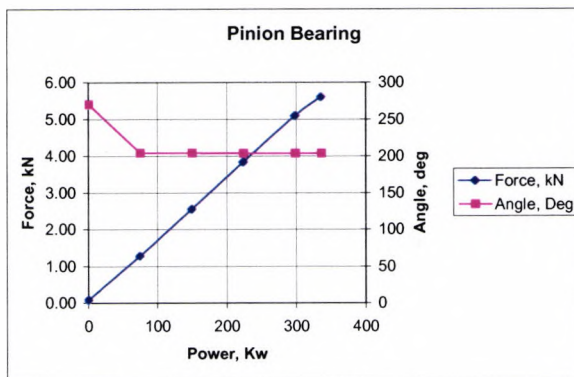
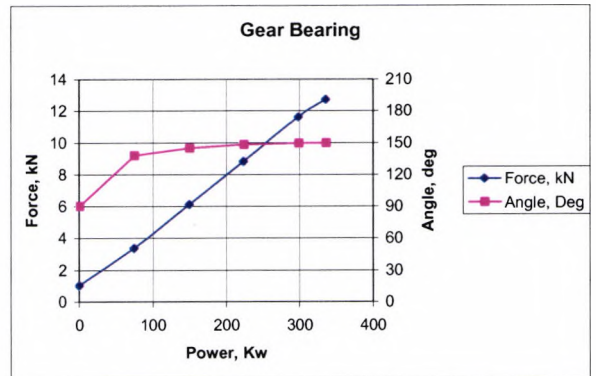
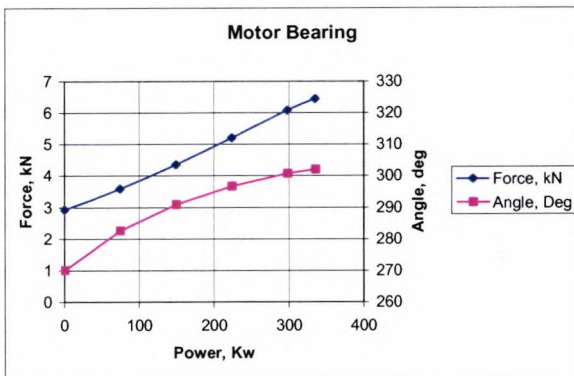


**Figure 1.5 : Bearing Loads for a Geared Compressor**

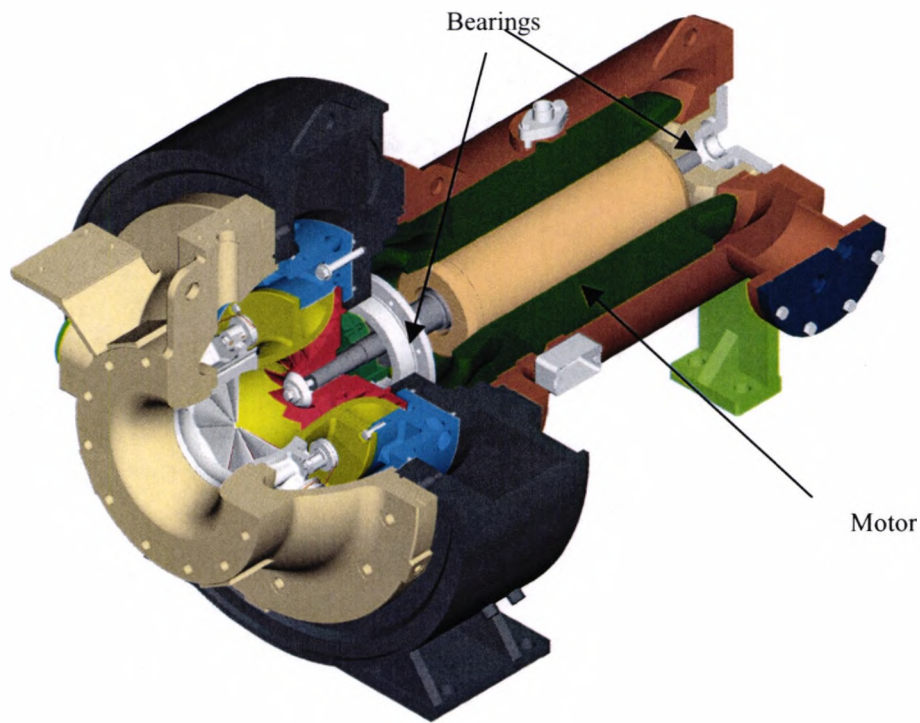


**Figure 1.6: Direct Drive Compressor**

**1.5 Conclusion:** The centrifugal compressor is an important component of a water-cooled chiller system. When it is gear driven, oil-lubricated bearings are required to support the large gear loads. Oil degrades the performance of the chiller and results in higher power consumption. An oil-free compressor driven by a high-speed motor requires smaller bearing loads and this opens up the possibility of using low viscosity refrigerant as the lubricant. An oil-free compressor improves the performance of the system by way of reducing the bearing power loss and improving the heat transfer rate in the heat exchangers.

## **1.6 References:**

1) "Centrifugal Compressors for Petrochemical Applications"  
American petroleum Industry Standard 617.

2) "Sodium Pump Development"

R. H. Fakkal,

Proceedings Of a Symposium on Progress in Sodium Cooled Fast Reactor Engineering,  
Monaco, IAEA, March 23-27, 1970

## **CHAPTER TWO**

### **AIMS OF THE THESIS**

In view of the potential advantages of liquid refrigerant as a bearing lubricant, as described in Chapter 1, the object of this investigation was to investigate its use in two types of fluid film bearings, namely, externally pressurized hydrostatic and self-acting hydrodynamic bearings.

In particular it was considered to be important to analyse both types, with and without consideration of turbulence effects, to determine the importance of turbulence in bearing design. Also, the effect of bearing turbulence on shaft rotordynamics and how this affected vibrations was thought to be worthy of study.

#### **2.1 Outline of the thesis**

In order to achieve the objectives described, an extensive study of the two types of bearings was carried out, which is described in the thesis is as follows:

Chapter 3: A literature survey on turbulent journal bearing analysis is presented. The survey shows that very little work was carried out in modeling of turbulent flow in the last two decades.

Chapter 4: The analysis and design of hydrostatic bearings is described. The effect of bearing geometry and supply pressure on the bearing load carrying capacity and dynamic properties is also presented. The chapter concludes with the vibration analysis of a compressor with hydrostatic bearings.

Chapter 5: This describes a test programme carried out on a compressor with hydrostatic bearings, which used refrigerant R134-as the lubricant. Details of the system and test results are given.

Chapter 6: Due to the complexity of the hydrostatic bearing system, another more simple type of bearing, namely the hydrodynamic bearing is analyzed. The beginning of the chapter gives an overview of turbulence and its application to flow in a bearing. The chapter discusses the effect of turbulence on bearing load carrying capacity and dynamic properties. The finite difference method of bearing analysis is used to simplify the turbulent equations by neglecting inertia terms and pressure variation in the radial direction. The turbulence model used is a zero equation eddy viscosity model.

Chapter 7: This presents an analysis of turbulent hydrodynamic bearings by the use of Computational Fluid Dynamics (CFD). A commercial software program based on the finite volume method was employed to solve the 3-D Navier–Stokes equation describing flow in the bearing clearance. The program uses wall functions to analyze flow near the shaft and bearing. This approach reduces both the mesh size requirements and the computational time.

Chapter 8: This presents a summary of the study and includes recommendations for future work.

## CHAPTER THREE

### LITERATURE SURVEY

#### 3.1 Introduction

The oil lubricated bearings, currently used in refrigeration centrifugal compressors, operate in the laminar flow regime. Replacing the oil by refrigerant, which is far less viscous, can possibly result in turbulent flow within them. It is therefore important to understand how changes in the flow regime in the bearing affect such characteristics as load carrying capacity, friction, damping and stiffness. Previous work on determining such effects has already been done by the power generation industries.

The development of steam turbines for power generation stimulated analytical and experimental work on fluid film bearings. Initially, turbomachinery speeds were low, due to material limitations, and bearings operated in the laminar regime. Advances in materials science enabled larger and higher-speed steam turbines to be built. It was then found that there were unaccountable increases in power losses above certain given speeds. Experimental work on bearing test rigs by researchers at GE and Westinghouse in the U.S and GEC and English Electric in England then showed that this could be due to bearing losses, which could no longer be predicted reliably by the assumption of laminar flow. Attention was then drawn towards the pioneering work of Lord Rayleigh<sup>1</sup> and Taylor<sup>2</sup> in the 1920's on the stability of flow between rotating cylinders. The stage was set for rigorous experimental and analytical work on the prediction of bearing characteristics in the turbulent regime.

This literature survey reviews the analytical and experimental work done on the stability of flow in concentric cylinders, eccentric cylinders and journal bearings. Most of this work on flow regimes in journal bearings was carried out between 1920 and 1980. During the 1980's and 1990's, as a result of significant growth in computing power, the field of computational fluid dynamics (CFD) gained popularity, especially in the area of turbomachinery aerodynamics. However, no publications have been found on the application of CFD methods to bearing flows.

### 3.2 Stability of the flow between two concentric rotating cylinders

Flow in a journal bearing has similarities to flow between two concentric rotating cylinders. Rayleigh<sup>1</sup> studied the stability of a fluid moving in concentric layers, assuming inviscid flow. He predicted that the flow in the gap is stable when the inner cylinder is stationary and the outer cylinder rotates. For the case where the inner cylinder rotates but the outer cylinder is fixed, Rayleigh's predictions indicate unstable flow at all speeds but experiments show a stable flow at low speed followed by a break down of the laminar flow into an organized vortex flow above a certain critical speed. At still higher speeds, the organized vortex flow pattern changes into a chaotic turbulent flow pattern.

In 1923, Taylor<sup>2</sup> predicted the onset of vortex flow fluid instability between two concentric cylinders analytically. He verified his predictions by experiments. Taylor predicted the critical speed at which instability sets in by assuming a symmetrical disturbance to the radial, tangential and axial flow components around the axis. Results are presented for the inner cylinder rotating and the outer cylinder fixed, the outer cylinder rotating and the inner cylinder fixed and both cylinders rotating in the same and in opposite directions. The case that is pertinent to journal bearings is the one with the outer cylinder fixed and the inner cylinder rotating. Taylor's analysis resulted in the following equation for the critical speed  $\Omega_{cr}$  :

$$\Omega_{cr} = \frac{\nu \pi^2 \sqrt{R_1 + R_2}}{\sqrt{2p} R_1 d^{3/2}} \quad (3.1)$$

where  $\nu$  = the kinematic viscosity

$R_1$  = the radius of the inner cylinder

$R_2$  = the radius of the outer cylinder

$d$  = the radial gap ( $R_2 - R_1$ )

and  $p = 0.057 \left( 1 - 0.652 \frac{d}{R_1} \right) + 0.00056 \left( 1 - 0.652 \frac{d}{R_1} \right)^{-1}$

For small clearances ( $d/R \ll 1$ ) Equation (3.1) can be simplified to the following critical speed equation widely used in the literature:

$$\Omega_{cr} = \frac{41.2\nu}{\left(R_m^{1/2} d^{3/2}\right)} \quad (3.2)$$

with  $R_m$  defined as the average of the inner and outer cylinder radii.

From equation (3.2), a non-dimensional term called the Taylor number is defined as:

$$Ta = \frac{\Omega \left(R_m^{1/2} d^{3/2}\right)}{\nu} \quad (3.3)$$

Taylor number represents the centrifugal effect divided by the viscous effect.

Equation (3.2) can be written in terms of Taylor number, as:

$Ta_{cr} = 41.2$ , where  $Ta_{cr}$  is the critical Taylor number.

Equation (3.3) can also be rewritten, as given below, showing the relationship between Taylor and Reynolds numbers:

$$Re = Ta \left(\frac{R_m}{d}\right)^{0.5} \quad (3.4)$$

Taylor carried out experiments to measure the critical speed, the number of vortices and their spacing. The experimental setup consisted of an outer cylinder of radius 4.035 cm and 90 cm long. Three different diameter inner cylinders, 3.00, 3.55 and 3.8 cm, were used in the experiment. A 10 cm long glass section was placed in the middle of the outer cylinder to record the speed of the onset of instability and to count the number of vortices. All experiments were carried out with water. A solution of eosin and alcohol with the same density as water was used as the dye to visualize the vortices. The dye was injected through six holes arranged in a circle at the gap mean radius. The inner cylinder was driven by an electric motor and the outer cylinder was driven through a continuously variable speed gear. The values of the observed and calculated critical speeds were found to differ by less than  $\pm 5\%$ . The critical speed is lowest for the case of the fixed outer cylinder and increases as clearance is decreased.

Equation (3.2) can be rearranged as follows

$$\frac{V_{cr}d}{\nu} = 41.2 \left(\frac{R_m}{d}\right)^{1/2} \quad (3.5)$$

$V_{cr}$  is the critical tangential of velocity ( $\Omega_{cr} \times R_m$ )

The left hand side of Equation (3.3) is a Reynolds number. The critical Reynolds number for the flow in concentric cylinders based on the cylinder tangential velocity and the cylinder gap is

$$Re_{cr} = 41.2 \left( \frac{R_m}{d} \right)^{1/2} = Ta_{cr} \left( \frac{R_m}{d} \right)^{1/2} \quad (3.6)$$

In 1957 Cole<sup>3</sup> reported on an experimental investigation of the critical speed in a rotating cylinder with an eccentric gap. This case represents a loaded journal bearing, wherein the shaft is eccentric to the stationary housing. To avoid overheating and vibrations at high speeds, low viscosity fluids such as paraffin, water and large clearance to radius ratios were used (0.05 to 0.3, compared with typical bearing clearance ratios of 0.001 - 0.002). The maximum operating speed of his test rig was 15,000 rpm. The critical speed was recorded for different eccentricities and axial flows. Fine aluminium powder was used as a dye to photograph the onset of instability. The measured mixture viscosity of the test fluid and aluminium powder mixture was found to be close to that of the test fluid. The important findings of his test results were that:

- 1) The axial flow of the fluid raises the critical speed only marginally.
- 2) The critical speed increases with an increase in eccentricity.
- 3) The value of the critical speed is higher than the Taylor critical speed based on mean clearance, but considerably lower than the Taylor critical speed based on minimum clearance.

In 1958 Kaye and Elgar<sup>4</sup> published the results of their experiments on the flow clearance between concentric rotating cylinders through which there was an axial flow of air. The study was aimed at improving methods of cooling electric motors. The diameter of the inner cylinder was 70 mm and the clearance between the inner and the outer cylinders was 12 mm. The study showed that the magnitude of the axial flow velocity affects the presence or absence of vortex flow formation during the transition from laminar to turbulent flow.

In 1959 DiPrima<sup>5</sup> analyzed the effect on stability of pumping liquid tangentially into the annular gap with the inner cylinder rotating. Pumping was modelled as a pressure gradient in the direction of or opposite to the direction of rotation. The critical speed was calculated as a function of the assumed circumferential pressure gradient. Results showed that pumping in the direction opposite to rotation increases the critical speed.

In 1960, DiPrima<sup>6</sup> analyzed the stability of viscous fluid between concentric rotating cylinders with a small axial flow. The equations of motion were solved assuming a parabolic axial velocity profile in the radial gap. The analysis revealed a slow increase in critical speed up to an axial Reynolds number ( $Re_{axial}$ ) of 20. For  $Re_{axial} > 20$ , the critical speed was found to increase more rapidly. These predictions were compared with experimental values and found to be in good agreement at smaller clearances for values of  $Re_{axial} < 40$ .

In 1963 DiPrima<sup>7</sup> extended the above analysis to the case of a journal bearing with eccentricity, which gives rise to a circumferential pressure gradient. The pressure in the circumferential direction was calculated assuming the flow to be laminar. Results indicated that the critical speed, based on the minimum film thickness, increases with eccentricity. Based on the maximum film thickness, the critical speed first decreases with an increase in eccentricity, up to an eccentricity ratio of 0.67, and increases for greater values. The eccentricity ratio is defined as the ratio of the eccentricity between the bearing and shaft centers to radial clearance. DiPrima suggests that Taylor type of instability sets in when the Taylor number approaches 41.2 before the Reynolds number based on clearance reaches 2000. This can be seen from the relationship between Reynolds number and Taylor number given by equation (3.6). Substituting a value of 2000 for  $Re_{cr}$  and 41.2 for  $Ta_{cr}$ , the equation (3.6) becomes:

$$\frac{R_m}{d} \approx 2357$$

For all values of  $\frac{R_m}{d}$  greater than 2357, the Reynolds number will be greater than 2000 for a Taylor number smaller than 41.2. Hence, transition from laminar to turbulent flow will not result in vortex formation.

In 1968 Ritchie<sup>8</sup> published an analysis for the flow in an eccentric cylinder using a method similar to Taylor's. Ritchie solved the Navier Stokes equation to calculate the circumferential pressure gradient. The results indicate critical speed values higher than those obtained by DiPrima. The calculations are based on maximum clearance.

### **3.3 Analysis Of Turbulent Flow in Journal bearings**

In 1950 Wilcock<sup>9</sup> reported anomalous results when measuring frictional torque during an investigation of the operating characteristics of large clearance sleeve bearings at high speeds. His paper describes experimental work on a journal bearing in which flow occurred in both the laminar and turbulent regions, with Reynolds numbers of 10 to 10,000. His experimental rig was capable of testing bearings with diameters of 100 - 200 mm and speeds up to 15000 rpm. The test bearing was fitted with thermocouples and pressure tappings to measure the oil film temperature and pressures. All tests were conducted with an oil inlet temperature of 40° C and the bearings were designed for a unit loading of 10 kg/cm<sup>2</sup>. The oil viscosity was calculated at the outlet temperature. A plot of non-dimensional torque versus Reynolds number, revealed abnormally high power losses above a certain speed. Wilcock also investigated the effect of oil inlet position on the onset of turbulence. The start of a convergent film is the leading edge and the trailing edge is located 180° away. When the oil feed was located only at the leading edge, frictional torque was considerably less than with two oil feeds, one at the leading and the other at the trailing edge. The lower frictional torque was attributed to the low amount of oil supply in the upper half of the bearing where the Reynolds number peaks due to the large clearance.

In 1953 Pai<sup>10</sup> analyzed turbulent flow between infinite parallel plates and applied the theory to two cases, namely Poiseuille and Couette flow. Time-averaged Reynolds equations for two-dimensional flow were developed. The mean values of turbulent velocity fluctuations were taken as a function of the transverse direction with finite distance. The equations of motion reduced from four equations and ten unknowns to two equations with four unknowns, namely pressure, mean velocity, turbulent stress and turbulent intensity. For Poiseuille flow, the solution for the velocity profile and turbulent stress is a power series function of transverse distance. Coefficients of power series terms were evaluated by fitting the experimental data of Laufer<sup>22</sup>. The Couette flow case, also resulted in a power series. However, the coefficients could not be evaluated due to lack of experimental data.

In 1956 Smith & Fuller<sup>11</sup> investigated turbulent flow in a journal bearing and used Pai's analysis to predict the pressure profile. The authors carried out measurements of the pressure profile in the convergent film and bearing power loss. The apparatus was designed with the object of attaining a turbulent flow at low rotational speed, while holding power losses to reasonable values. Water was used as the lubricant. Its low kinematic viscosity helped to attain turbulent flow at low speeds. In order to avoid problems of wear during start-up the load was applied after the shaft attained full speed. A two-part test bearing was placed at the middle of the shaft. The test shaft was supported at either end by ball bearings and driven through belted pulleys by a 1.5 HP motor. The bearing film pressure was measured at the median plane using five tappings. Provision was made to rotate the bearing, thereby enabling the pressure to be recorded in increments of 7.5 deg over an arc of 255°. The frictional torque was measured by hanging weights from the end of a lever arm.

The frictional torque became 1.5 to 3 times higher than for laminar flow as the speed increased just above the Taylor critical value. In the turbulent region, the friction factor was high at zero eccentricity and decreased with increasing eccentricity or load. This was attributed to the dominance of lower loss viscous shear in the smaller clearance area compared to higher loss Reynolds stresses over the larger area of the bearing. The flow remained turbulent in areas where the clearance was a maximum. A comparison of the pressure profiles between the

laminar and the turbulent case was presented. Although the shape of both profiles was similar, the load carrying capacity was higher for the turbulent case.

In his 1958 and 1960 publications, Tao<sup>12, 13</sup> described an analysis based on semi-empirical theories for the velocity distribution. The governing equation for turbulent lubrication was derived from Blasius' law of friction. The velocity in the lubricant film was the vector sum of its axial and circumferential components. For a short bearing, the pressure variation in the circumferential direction was small compared to that in the axial direction. The average axial velocity in the annulus was related to the pressure gradient according to Blasius' law of friction. The circumferential mean velocity was assumed to be half the shaft speed. Equations for load carrying capacity were derived and showed that for the same eccentricity, the load carrying capacity for a turbulent flow bearing is higher than that for a laminar flow bearing. The analysis was extended to long bearings where the circumferential pressure gradient was appreciable compared to the axial pressure gradient. For the velocity distribution in Couette flow, Tao used the results of Pai<sup>9</sup>.

Prandtl's mixing length theory was used by Constantinescu<sup>14</sup>, Chou et al.<sup>15</sup> and Arwas et al.<sup>16</sup> to calculate turbulent stresses. Time averaged Navier-Stokes equations were developed for turbulent flow and simplified by assuming the flow to be in thin layers. As a consequence, all mean velocity gradients and turbulent stresses in directions other than the film thickness were negligible and removed from the equations.

Unlike the case of laminar flow, the pressure across the thickness of the oil film was not zero for turbulent flow and depends upon the turbulent stress  $-\frac{\partial}{\partial y}(\rho \overline{v'^2})$ . However, since the velocity is influenced only by the pressure gradient in the axial and circumferential directions, this difference could be ignored. The mixing length was calculated from midsection to satisfy the boundary condition of zero turbulent stresses at the walls. The mixing length calculation was based on experimental results of fully developed turbulent flow in a two-dimensional channel. The flow in such a case is planar, i.e. velocity changes occur only in one dimension. However, in a bearing, the flow is non-planar, velocities vary across the film thickness and in the

circumferential direction due to the pressure gradient. Hence, the analysis can be improved by using correlations from non-planar flow. Although the equations were simplified by the thin layer assumption, a closed form solution for the velocity profile was still not possible and a numerical analysis had to be carried out to obtain a solution. The following summarises the of results from Arwas et al.<sup>16</sup>:

1) There is a large increase in load carrying capacity and stiffness when the flow changes from laminar to turbulent. The relation between turbulent and laminar bearing forces is shown as:

$$\frac{\bar{f}_{turb}}{\bar{f}_{laminar}} = 0.0415(Re)^{0.6} \quad (3.7)$$

2) There is also an increase in attitude angle, which is the angle between the load vector and the line of bearing and shaft centers.

3) A simple relation shown below was established for the ratio of friction coefficients under turbulent and laminar conditions.

$$\frac{Cf_{turb}}{Cf_{laminar}} = 0.039(Re)^{0.6} \quad (3.8)$$

In laminar bearing analysis, the fluid film forces for bearings of finite length are obtained from the corresponding values for infinite length by means of leakage factors, which are defined as:

$$\lambda_w = \frac{\bar{f}}{\bar{f}_{L/D=\infty}} \quad (3.9)$$

A relationship between leakage factors for turbulent and laminar flow was established as

$$\lambda_{w,turbulent} = 0.375\lambda_{w,laminar} \quad (3.10)$$

The shortcomings of the mixing length approach are as follows:

The flow near the wall has two regions: an inner or laminar sublayer and an outer layer. Constantinescu<sup>14</sup> assumed a parabolic velocity profile in the laminar sublayer and applied the mixing length theory to the outer layer. Matching of the velocity gradient at the edge of laminar sublayer causes a discontinuity in the shear stress since:

- 1) The laminar sublayer thickens doesn't confirm with the law of the wall
- 2) The mixing length formulation as used shows zero shear stress at maximum velocity gradient.

To overcome these problems Ng<sup>17</sup>, Ng and Pan<sup>18</sup> and Elrod and Ng<sup>19</sup> treated the turbulent flow problem in a journal bearing by using the "law of the wall" for velocity profiles in the turbulent layer.

In 1964 Ng<sup>17</sup> applied the "law of the wall" in which the shear velocity, defined as the square root of the ratio of shear stress to density, was calculated based on the wall shear stress. He also showed that by using Reichardt's<sup>23</sup> formula for the Eddy diffusivity with constants  $\delta_1^+ = 10.7$  and  $\kappa = 0.4$ , the velocity profile in the laminar sub-layer, the buffer and the turbulent layer matches with experimental data of the flow over a smooth surface measured by Ludweig and Tillman<sup>24</sup>. The analysis was carried out for an infinitely long bearing, thus neglecting the effect of a transverse pressure gradient. The load carrying capacity is smaller than calculated by Constantinescu.

Ng and Pan<sup>18</sup> presented a study in 1965 using the following four assumptions in formulating the equations of motion for turbulent flow:

- 1) Isotropy of eddy viscosity
- 2) The use of local shear in the law of the wall as opposed to wall shear. This idea was based on experimental data published by Townsend<sup>25</sup> on turbulent boundary layers in the presence of an adverse pressure gradient.
- 3) An unavoidable difficulty in adapting the "law of the wall" to the analysis of a channel flow is the presence of two walls. Thus the channel was divided into two parts, each of which was associated with one wall. The interaction between the two walls was neglected. The consequence would be some error in computing eddy viscosity especially at the mid point. Since the velocity gradient is small at mid channel, the error was small.
- 4) Linearization of the equations, i.e. higher order terms were neglected in deriving pressure-flow equations. Since, non-linearity is caused by turbulence, inaccuracy, due to linearization, may become serious only when Reynolds number is large. Also at large eccentricities the pressure gradient is large, hence, linearization results in error. Hence, this theory cannot be applied for large eccentricities.

In deriving the equations, inertia effects and variation of shear stress along surface coordinates were neglected. Load carrying capacities of full journal bearings, as given by Smith & Fuller<sup>11</sup>, are in good agreement up to eccentricity

ratios of 0.7. When compared with the results of the partial arc bearing tested by Orcutt<sup>20</sup>, the load carrying capacity predicted is lower than the experimental results.

Elrod et al.<sup>19</sup> refined the analysis by calculating the eddy diffusivity with Reichardt's formula in the inner region and Clauser's<sup>26</sup> formulation for the outer or core region. The equation contained two variables  $G_x$  and  $G_z$ , which were functions of the local Reynolds number and pressure gradient. In deriving the equations, no linearization was used. Charts were presented to calculate  $G_x$  and  $G_z$ . The analysis presented by Elrod et al. can be used both for hydrodynamic journal bearings and for hydrostatic bearings when the axial pressure gradients are much larger than the circumferential pressure gradients.

Reddecliff and Vohr<sup>21</sup> applied Elrod's analysis to design hydrostatic bearings with high eccentricity for use in high-pressure cryogenic rocket engine turbopumps. Results were presented for load capacity, stiffness and mass flow as a function of the recess geometry. The effect of turbulence on load carrying capacity and stiffness was found to be small due to the fact that the load carrying capacity is determined by supply pressure rather than hydrodynamic phenomena. However, the mass flow is reduced due to increased effective viscosity caused by turbulence.

In 1974, the ASME Tribology section dedicated its January Transaction issue to the subject of turbulence in journal bearings. Wilcock<sup>27</sup> gave an historical perspective on the subject of turbulence in bearings. He presented power loss, flow rate and eccentricity for three different 200 mm high speed bearing designs operating at 10 000 rpm with a load of 3000 kg. Of the three designs, the floating sleeve bearing, exhibited the lowest losses.

### **3.4 Conclusion**

The literature survey shows that much of the work on turbulent bearing modelling was carried out before the mid 1970's. The reason for this was that advances in the design of high-speed turbomachines for aerospace and power generation in the late 1960's pushed the operation of bearings into the turbulent flow regime. All analytical work is based on turbulence models for planar flows. The effect of inlet geometry could not be analyzed numerically due to computing restrictions. In the 1980's and 1990's turbulence research has advanced due to rapid

growth in computing power. Modelling of complex flows in compressors and turbines using computational fluid dynamics (CFD) has gained wide acceptance. However, the application of CFD to bearing flows is non-existent.

### 3.5 References

1. Lord Rayleigh, "On the Dynamics of Revolving Fluids", Royal Society Proceedings, A, 1916, pp. 148-154.
2. Taylor, G.I., *Stability Of a Viscous Liquid contained between Two Rotating Cylinders*, Philosophical Transactions of the Royal Society Of London, series A, vol.223, 1923, pp 289-343.
3. Cole, J.A., *Experiments on the flow in rotating annular clearances*, Paper 15, Conference on Lubrication and Wear, IMechE, London, 1957.
4. Diprima, R.C., *The stability of a viscous fluid between rotating cylinders with an axial flow*, Journal Of Fluid Mechanics, 1960, vol 9, pp 621-631.
5. Diprima, R.C., *The stability of viscous flow between rotating concentric cylinders with a pressure gradient acting around the cylinders*, Journal Of Fluid Mechanics, 1959, vol 6, pp 463 – 468.
6. Diprima, R.C., *A note on the stability of flow in loaded journal bearings*, ASLE Transactions 6, 1963, pp 249-253.
7. Ritchie, G.S., *On the stability of viscous flow between eccentric rotating cylinders*, Journal Of Fluid Mechanics, 1968, vol 32, part 1, pp 131 – 144.
8. Kaye, J., Elgar, E.C., Wilcox, D.F., *Modes of Adiabatic and Diabatic fluid flow in an annulus with an inner rotating cylinder*, Trans ASME, 1958, vol 80, 753 –765.
9. Wilcox, D.F., *Turbulence in high speed journal bearings*, Transactions of the ASME, 1950, vol 72, pp 825 – 834.
10. Pai, S.I., *On turbulent flow between parallel plates*, Journal Of Applied Mechanics, March 1953, vol 75, pp 109-114.
11. Smith, M.I., Fuller, D.D., *Journal bearing operation at superlaminar speeds*, Transactions of the ASME, April 1956, pp 469 – 474.
12. Tao, L.N., *A Theory Of Lubrication in short journal bearings with turbulent flow*, Trans ASME, 1958, vol 80, pp 1734 – 1740.
13. Tao, L.N., *A Theory Of Lubrication with turbulent flow and its application to slider bearings*, Journal Of Applied Mechanics, March 1960, pp 1-4.
14. Constantinescu, V.N., *On turbulent lubrication*, Proceedings of Institution Of Mechanical Engineers, vol 1973, no 38, 1959, pp 881 – 896.
15. Chou, Y.T., Saibel, E., *The effect of turbulence on slider bearing lubrication*, Trans ASME, Journal Of Applied Mechanics, March 1959, pp 122 – 126.
16. Arwas, E.B., Sternlicht, B., Wernick, R.J., *Analysis of plain cylindrical journal bearings in turbulent regime*, Trans ASME Journal Of Basic Engineering, June 1964, pp 387 – 395.
17. Ng, C.W., *Fluid dynamic foundation of turbulent lubrication theory*, ASLE Transactions, 7, 1964, pp 311 – 321.
18. Ng, C.W., Pan, C.H.T. *A linearized turbulent lubrication theory*, ASME Journal Of Basic Engineering, Sept 1965, pp 675 – 688.
19. Elrod, H.G., Ng, C.W., *A Theory Of Turbulent Fluid Films and its application to Bearings*, Trans ASME Journal Of Lubrication Technology, July 1967, pp 347 – 362.

20. F.K. Orcutt, Investigation of a Partial Arc Pad bearing in the superlaminar regime, *Journal of Basic Engineering*, Trans ASME, Series D, Vol 87, 1965, pp 147-152.
21. J. M. Reddecliff, J. H. Vohr, *Hydrostatic Bearings for cryogenic Rocket Engine Turbopumps*, Trans ASME Journal Of Lubrication Technology, July 1969, pp 557 – 575.
22. J. Laufer, *Some Recent measurements in a Two-Dimensional Turbulent Channel*, *Journal Of Aeronautical Sciences*, vol 17, pp 277-287.
23. Reichardt H. *Vollstandige darstellung der turbulenten Geschwindigkeitsverteilung in glatten Leitungen*, *Z. angew Math. Mech.* 31, 208 (1951)
24. Ludwig, H and Tillman, W., *Ingr-Arch*, 17, 288 (1949)
25. Townsend, A. A. *The Development of Turbulent Boundary Layers with Negligible Wall Stress*, *Journal Of Fluid Mechanics*, vol 6, 1960, pp 143-155.
26. Clauser, F. H. *The Turbulent Boundary Layer*, *Advances in Applied Mechanics*, vol 4, 1965, pp1-51
27. D. F. Wilcock, *Turbulent Lubrication - Its genesis and role in modern design*, Trans ASME Journal Of Lubrication Technology, vol 96, Jan 1974, pp 2 – 6.
28. San Andre's, L., and Velthuis, J., 1991, "Laminar Flow in a Recess of a Hydrostatic Bearing," STLE Paper No. 91TC3B3, STLE/ASME Tribology Conference, October 13-16, St. Louis, Missouri.
29. Braun, M. J., Dzodzo, M., and Lattime, S., 1996, "Some Qualitative and Quantitative Aspects of Flow in a Hydrostatic Journal Bearing Pocket," FEDVol. 239, Fluid Engineering Division Conference, 4, ASME 1996 pp. 109–114.
30. Braun, M. J., and Dzodzo, M., 1996, "A Three Dimensional Model for a Hydrostatic Bearing," 32nd AIAA/ASME/SAE/ASEE Joint Propulsion Conference July 1–3, 1996/Lake Buena Vista, FL.
31. Braun, M. J., and Dzodzo, M., 1996, "Three Dimensional Flow and Pressure Patterns in a Hydrostatic Journal Bearing Pocket," *ASME J. Tribol.*, 119, pp.711–719.
32. Braun, M. J., Choy, F. K., and Zhu, M., 1993, "The Effects of a Hydrostatic Pocket Aspect Ratio, and Its Supply Orifice Position and Attack Angle on Steady-State Flow Pattern, Pressure and Shear Characteristics," *ASME J. Tribol.*, 115(4), pp. 678–886.
33. Braun, M. J., Choy, F. K., and Zhu, N., 1995, "Flow Pattern and Dynamic Characteristics of a Lightly Loaded Hydrostatic Pocket of variable Aspect Ratio and Supply Jet Strength," *STLE Trans.*, 389(1), pp. 128–136.
34. Braun, M. J., and Dzodzo, M., 1995, "Effects of Hydrostatic Pocket Shape on the Flow Patterns and Pressure Distribution," *Int. J. Rotating Mach.*, 1(3-4), pp. 225–235.
35. Braun, M. J., and Dzodzo, M., 1995, "Effects of the Feedline and Hydrostatic Pocket Depth on the Flow Patterns and Pressure Distribution," *ASME J. Tribol.*, 117(2), pp. 224–233.
36. Helene, M., Arghir, M., and Frene, J., 2003, "Numerical Three-Dimensional Pressure Patterns in a Recess of a Turbulent and Compressible Hybrid Journal Bearing." *ASME J. Tribol.* **125**, p 301
37. Helene, M., Arghir, M., and Frene, J., 2003, "Numerical Study of the Pressure Pattern in a Two-Dimensional Hybrid Journal Bearing Recess. Laminar. and Turbulent Flow Results." *ASME J. Tribol.* **125**, pp 283-290.

## CHAPTER FOUR

### HYDROSTATIC BEARING DESIGN & ANALYSIS

#### 4.1 Introduction

Modern turbomachines produce or absorb large amounts of power in a relatively small package. The most impressive example is NASA's space shuttle main engine turbopump, which produces 50 MW, in two turbine stages, only the size of a frisbee. In the case of air-conditioning applications, a centrifugal compressor impeller absorbs 350 kW in a diameter of 0.25 m and a length of 0.10 m, whereas a positive displacement screw compressor for the same duty, requires a diameter of 0.30 m and a length of 0.30 m. The main characteristic of turbomachines, which enables such high energy densities and flow rates, is that they rotate at much higher shaft speeds than other types of machine of the same physical size. However, high speeds are associated with high inertia loads and hence potential vibration problems, such as rotor dynamic instability.

The engineering challenge presented by aerodynamic and hydrodynamic flows in the design of blading sometimes causes the rotor dynamic requirements of turbomachinery design to be overlooked. Too often it has happened that expensive turbomachines were built and then found to be incapable of producing their performance, or even of running at all, because of an ignorant assumption that to make the rotor run smoothly and reliably at the design speed is a trivial problem. In all rotor dynamic problems, bearing design forms an important part and is even more critical when using low viscosity fluids such as HFC134a.

This chapter deals with design and analysis of refrigerant-lubricated hydrostatic bearings for a gear-less centrifugal compressor powered by a high-speed inverter-driven electric motor. The choice of hydrostatic bearings is based on the availability of the refrigerant at high pressure. The bearing design part deals with the effect of geometry and refrigerant supply pressure on dynamic properties, namely stiffness and damping, and performance parameters such as flow rate, minimum film thickness and power loss. The analysis of the bearing design includes incorporation of the bearing system into the compressor and performing a rotor dynamic analysis to identify possible regions of instability. A compressor with process-fluid lubricated hydrostatic

bearings was designed, built and tested. This chapter covers the design of this bearing system.

#### **4.2 Compressor Design**

A centrifugal compressor with hydrostatic bearings was designed for a 1.7 MW water-cooled chiller. The compressor was driven by a high-speed motor with a variable frequency drive or inverter. The main features of the compressor are:

Speed: 14 500 rpm

Impeller:  $\phi$  0.2375 m, with 11 main and 11 splitter blades, Mass =3.2 kgs

Diffuser: 18 pipes

Motor: 300 kW, 2-pole induction, rotor Mass = 55 kgs

The major compressor components are shown in Figure 4.1. The compressor casing and motor housing were constructed from welded steel plates. The bearing housings were machined out of cylindrical steel bars. The aerodynamic components such as the inlet guide vanes, impeller and diffuser were from an existing design. Also, the suction housing was made from an existing grey iron casting.

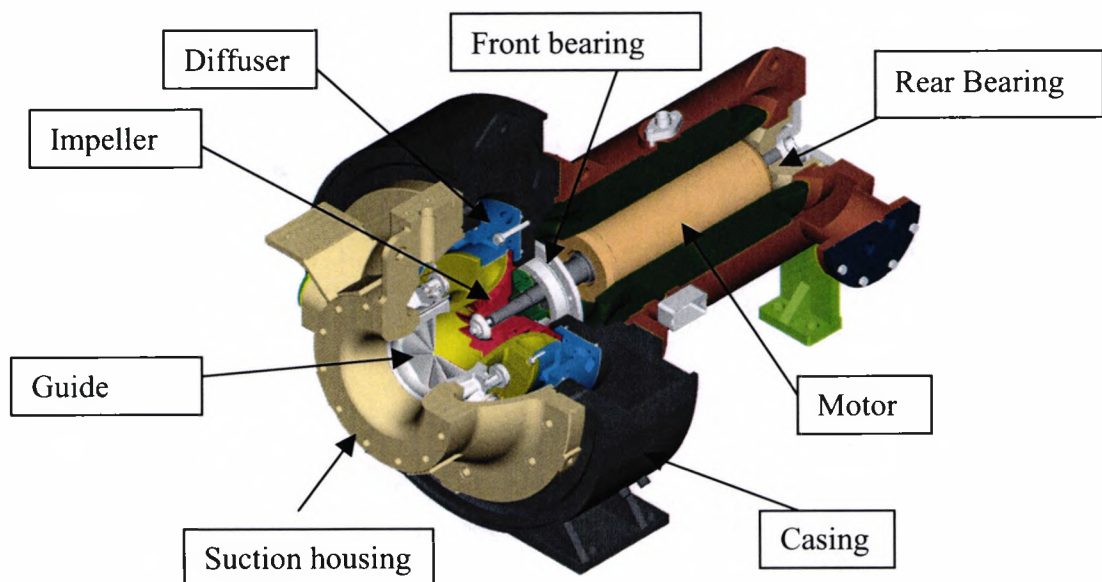


**Figure 4.1: Direct Drive Compressor showing major components**

The speed of an induction motor  $N$  (in rpm) is proportional to the power supply frequency and, neglecting slip, is given as

$$N = 120 \frac{f}{p} \quad (4.1)$$

Where  $f$  is the frequency of the power supply voltage (in Hz)

$p$  is the number of poles.

To achieve a motor speed of 14500 rpm, a power supply frequency of 242 Hz was required. Since the normal power supply frequency is 60 Hz, a variable frequency drive with an output frequency of 20 to 300 Hz was used to power the motor. The variable frequency drive consisted of two sections, a converter and an inverter. The converter section was comprised of a six diode bridge and converted input A-C voltage to DC voltage. A reactor on the line side minimized harmonics feeding back to the grid. The inverter consisted of power transistors such as IGBT's (Insulated Gate Bipolar Transistors) to convert the DC back to AC of the required frequency.

From a rotor dynamic standpoint the successful design of a turbomachine involves:

1. Avoiding critical speeds, if possible.
2. Minimizing dynamic response at resonance, if critical speeds must be traversed
3. Avoiding seal rubs, while keeping seal clearances as tight as possible.
4. Avoiding rotor dynamic instability.
5. Avoiding torsional vibration resonance.

Items 1 to 4 are controlled by rotor and bearing design. As such, the goal of the bearing design should be to furnish the required dynamic characteristics to avoid any vibration problems. The following steps were taken for the bearing design and rotor dynamic analysis:

1. The shaft dimensions were established based on the power transmission requirements and geometry of the main components such as the motor and the impeller. The shaft dimension so calculated represents the minimum bearing diameter. The bearing span was kept to a minimum to obtain a rigid shaft design.
2. Undamped critical speed analysis was carried out to establish the limits of stiffness for operating in the rigid rotor region. The rigid rotor region was identified on a critical speed versus stiffness map, as that where the critical speed is influenced by the bearing stiffness.
3. Unit loading criteria determined the principal bearing dimensions, such as the lengths and diameters.

4. A detailed bearing analysis was carried out to study the effect of the geometric parameters and lubricant supply pressure on the dynamic characteristics. Geometric parameters, which have little effect on dynamic characteristics, were determined by performance criteria such as low flow rate and power losses. The parameters, which strongly influence the dynamic characteristics, were established after carrying out the vibration analysis.
5. Rotor dynamic stability and response analysis was carried out for different bearing designs or supply pressures.

The final design was selected based on the following criteria:

- a) A separation margin of 20% between the operating and critical speeds.
- b) No rotor dynamic instability up to a maximum operating speed of 14500 rpm.
- c) The unbalanced response peak amplitudes should not be more than 25% of the bearing, seal and impeller clearances.

### **4.3 Hydrostatic Bearing**

A typical hydrostatic journal bearing is shown in Figure 4.2. Each pad contains a supply orifice, a land region and a pocket or recess. The land region has a shaft to bearing clearance ratio, typical of that in hydrodynamic bearings, of 0.001 based on the bearing diameter. The land region acts as a restrictor to the pockets. Fluid at high pressure is supplied separately through either a capillary or an orifice device to each pocket. High-pressure fluid is supplied either from within the system or by an external pump. The load carrying capacity and dynamic characteristics are developed through combined hydrostatic and hydrodynamic action.

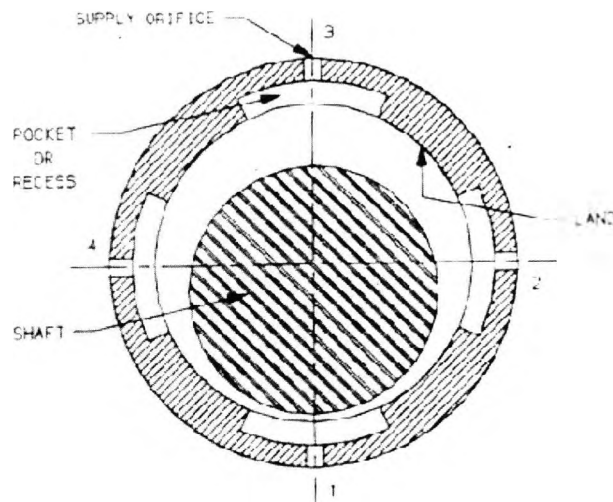


**Figure 4.2: Hydrostatic Bearing Geometry**

A hydrostatic bearing has two principal fluid reactions. Firstly, the lands generate a hydrodynamic effect. Secondly, the high-pressure fluid, supplied to the pockets, provides a hydrostatic effect. The pressure developed by the hydrostatic effect does not depend on the shaft rotation or other dynamic action of the bearing. While the hydrostatic forces are partially governed by the geometry of the bearing, the flow and pressure in the bearing will respond to the shaft movement.

As the shaft is displaced closer to a recess or pocket, the flow leaving that pocket is reduced. This increases the pressure in the pocket that in turn increases the force acting on the shaft. A reverse reaction occurs in the opposite pocket whose distance to the shaft has increased. The net force acts as the retardant to the shaft motion or position.

The hydrodynamic effect in the land generates load capacity from viscous pumping of the lubricant through a small clearance region. To generate pressure, the resistance to pumping must increase in the direction of fluid flow. This is accomplished by a displacement of the journal, such that the clearance distribution takes on the form of tapered wedge in the direction of rotation. Further, the displacement of the journal is not along a line that is coincident with the load vector. A load in one direction causes not only displacement in that direction but orthogonal displacements as well. Similarly,

a displacement of the journal in the bearing will cause a load opposing the displacement, and a load orthogonal to it. The orthogonal force causes orthogonal motion. Thus, there are strong cross-coupling influences introduced by the hydrodynamic mechanism. It is the cross-coupling characteristics of a journal bearing that promote self-excited instabilities in the form of bearing whirl. Low values of cross-coupling damping and stiffness are desirable.

Damping is the dynamic resistance to shaft displacement. The majority of the damping in a hydrostatic bearing is generated by the squeeze effect in the pocket. As the shaft takes on a velocity towards one pocket, the rate of fluid leaving that pocket is increased by the "squeezing" effect of the shaft. Since it is being forced through a restriction, the increased flow must be accompanied by an increase in the pocket pressure. A small amount of damping is generated in the land region due to the squeeze effect of the shaft.

Stiffness is the steady-state resistance to shaft displacement and is generated by a change in the resistance to flow leaving the pocket. As the shaft is positioned nearer to a bearing pocket, the film thickness surrounding the pocket is decreased. The decreased gap around the pocket acts as an additional resistance to flow leaving the pocket. The resulting reduction in flow causes the pressure to increase. The pressure in the pocket continues to increase as the shaft draws nearer to the pocket. At the point of contact or closure of the recess the supply pressure level is reached, at which time the flow leaving the pocket will be zero. The supply pressure is a design parameter in hydrostatic bearings. Given that the supply pressure can be very high, hydrostatic bearings can be designed with extreme stiffness levels.

#### **4.4 Modeling of Fluid Flow in Hydrostatic Bearings**

The performance characteristics of hydrostatic bearings are governed by momentum and continuity considerations at the film lands and flow continuity through the pockets. The former define the pressure and flow fields over the film region, whereas the latter provide values for the pressure in the recess. The load carrying capacity and the dynamic properties are obtained from the pressure distribution in the circumferential and axial direction within the bearing.

The continuity equation for one recess defines the relationship between the various effects which determine the recess pressure and hence the resultant force exerted by that recess. However, it is based on the assumption of incompressible flow and hence, in the event of the fluid cavitating, it does not apply, as a result of the change in density caused by the vapour formation. The continuity equation at each recess is obtained by equating the flow from the control device into the recess  $Q_i$ , to the flow from the recess across the axial flow lands and across the inter-recess lands. In addition, consideration must be given to the change of mass within the control volume of the recess due to the squeeze velocities and the fluid compressibility.

$$Q_i = Q_r + \frac{\partial V_r}{\partial t} + V_r \beta \frac{\partial P_r}{\partial t} \quad (4.2)$$

where  $Q_r$  = the flow from the recess into the lands,

$$\beta = \frac{1}{\rho} \frac{\partial \rho}{\partial P} = \text{the fluid compressibility factor}$$

$V_r$  = the recess volume including supply orifice

$P_r$  = the fluid pressure in the recess.

The inlet flow  $Q_i$  through the external restrictor depends on the nature of the control device, i.e for an orifice;

$$Q_i = C_d \frac{\pi d_o^2}{4} \left[ \frac{2(P_s - P_r)}{\rho} \right]^{1/2} \quad (4.3)$$

and for a capillary

$$Q_i = \frac{\pi d_c^4}{128 \mu l_c} (P_s - P_r) \quad (4.4)$$

where  $P_s$  = the supply pressure.

The recess flow,  $Q_r$ , into the lands was obtained by solving the Reynolds equation for lubrication which is obtained from the momentum and continuity equations, assuming that the film thickness is small compared to the axial and radial dimensions. The solution of the Reynolds equation with proper boundary conditions yields the pressure and flow fields in the lands. For turbulent flow, the eddy viscosity was calculated using Elrod and Ng's formulation. (Reference 19 of chapter 3)

Once the pressure field was established for the entire bearing, the load capacity and the forces on the shaft were obtained by integrating the pressure field over the circumference of the bearing.

**4.4.1 Bearing Stiffness and damping:** Unbalance in the rotor and aerodynamic forces cause compressor vibrations. Hence, during normal operation, the rotor in the bearing orbits about a steady state equilibrium position. When the size of the orbit is relatively small compared to the bearing radial clearance, the fluid film forces acting on the shaft can be replaced by equivalent stiffness and damping coefficients obtained from considering small changes in displacement and velocity. Introducing an x-y coordinate system the fluid film forces can be written as:

$$F_x = K_{xx} x + C_{xx} \dot{x} + K_{xy} y + C_{xy} \dot{y} \dots\dots\dots (4.5)$$

$$F_y = K_{yy} y + C_{yy} \dot{y} + K_{yx} x + C_{yx} \dot{x} \dots\dots\dots (4.6)$$

$K_{xx}$  is called the principal horizontal stiffness and corresponds to the force in the horizontal or x- direction produced by a small displacement in the horizontal direction. The term  $K_{yx}$  corresponds to the vertical force due to a small displacement in the horizontal direction. This couples the vertical and horizontal directions. Hence it is called the cross-coupled stiffness. The damping coefficients are defined similarly, except that small velocities replace small displacements. Low cross-coupled stiffness and damping values are necessary to avoid rotor instability.

**4.5 Bearing Design**

The modelling approach described in section 4.4 has been incorporated into the HYDROB<sup>2</sup> computer code, developed by the University of Virginia, and this program was used to calculate the bearing stiffness and damping characteristics. The radial (journal) load for each bearing, due to the weight of the compressor rotor was estimated to be 0.44 kN. The thrust bearing was designed to carry an axial load of 2.2 kN. The aim was to use high-pressure liquid refrigerant from the condenser as the bearing supply and to discharge this into this liquid into the evaporator. During normal operation, the condenser pressure may vary from 1.27 down to 0.54 MPa while typical condenser and evaporator pressures may be taken as 0.98 and 0.34

MPa respectively. Hence, the differential pressure across bearing could vary from 0.93 to 0.20 MPa. Also, during start-up, the differential pressure would be zero.

Based on shaft design and power loss considerations, the bearing diameter was fixed at 0.038m and its length at 0.038m. The analysis, with a pressure differential of 0.98 MPa, then showed that it was not possible to support a load of 440 N without a minimum liquid film thickness of 25  $\mu\text{m}$ , which is the minimum permissible. Hence, the analysis was repeated assuming higher bearing inlet pressures for which an external pump would be required.

The effects of varying each of the following main bearing design parameters were then considered:

- 1) Pocket orientation and number of pockets
- 2) Orifice diameter
- 3) Radial clearance
- 4) Supply pressure
- 5) Pocket Depth

In addition, the effect of speed variation was included in the study.

For each of the above variables, the following conditions were assumed:

1) Variable: Number Of pockets

Supply Pressure	1.7 MPa
Ambient pressure	0.35 MPa
Orifice Diameter	0.00125 m
Radial Clearance	51 $\mu\text{m}$
Load	440 N
Pocket Depth	203 $\mu\text{m}$
Speed	14 500 rpm

2) Variable: Orifice Diameter

Supply Pressure	2.0 MPa
Ambient pressure	0.35 MPa
Shaft eccentricity	0.5
Radial Clearance	51 $\mu\text{m}$
Speed	14 500 rpm
Number of Pockets	6

3) Variable: Radial Clearance

Supply Pressure	1.7 MPa
Ambient pressure	0.35 MPa
Minimum Film Thickness	25.4 $\mu\text{m}$
Orifice Diameter	0.00125 m
Speed	14 500 rpm
Number of Pockets	6

4) Variable: Supply Pressure

Radial Clearance	51 $\mu\text{m}$
Ambient pressure	0.35 MPa
Load	440 N
Orifice Diameter	0.00125 m
Speed	14 500 rpm
Number of Pockets	6

#### **4.6 Results of the Bearing Design Study**

**4.6.1 The Effect of Pocket Orientation and Number Of Pockets:** Two different arrangements were investigated, one with the load vector directed towards the middle of the pocket and the other with the load vector falling between the pockets. The results showed very little difference in the bearing characteristics of these two configurations. The analysis for determining the influence on the bearing of the number of pockets was then carried out assuming the load was on the pocket. The results of this, as presented in figures 4.3a - d, show that the bearing characteristics are only weakly dependent on the number of pockets. Low cross-coupled stiffness is essential for rotor dynamic stability. Hence using this as a major criterion, together with good load carrying capacity, a bearing with 6 pockets was selected.

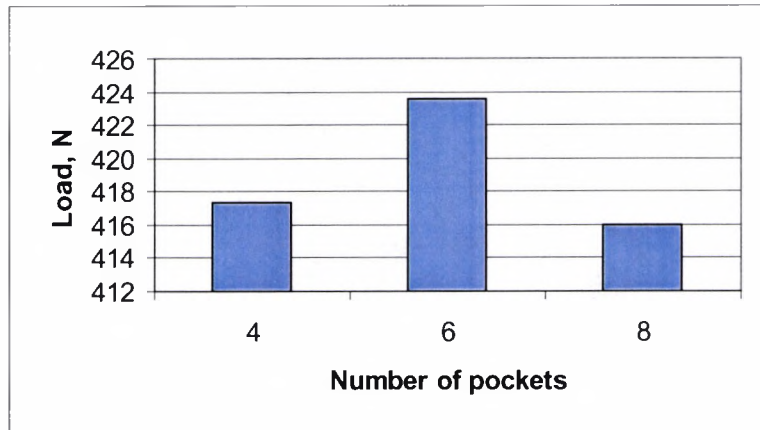


**Fig 4.3a: Effect of number of pockets on load**

(Supply pressure = 1.7 MPa, orifice diameter = 0.00125m, radial clearance = 51 $\mu$ m,  
Pocket depth=203 $\mu$ m, load = 440N, speed = 14500 rpm)

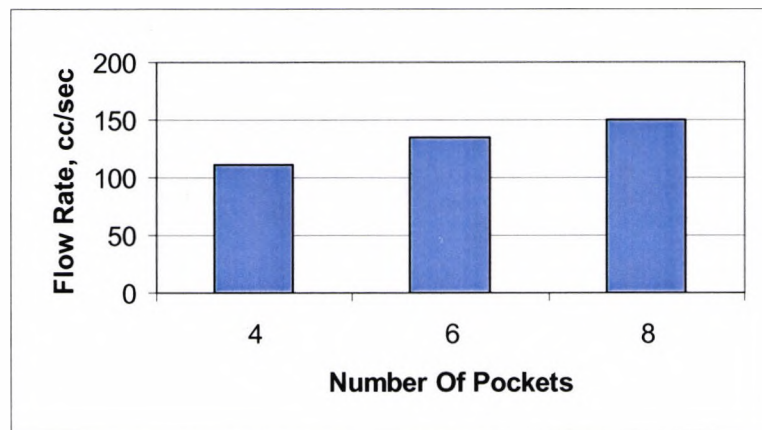


**Fig 4.3b: Effect of number of pockets on flow rate**

(Supply pressure = 1.7 MPa, orifice diameter = 0.00125m, radial clearance = 51 $\mu$ m,  
Pocket depth=203 $\mu$ m, load = 440N, speed = 14500 rpm)

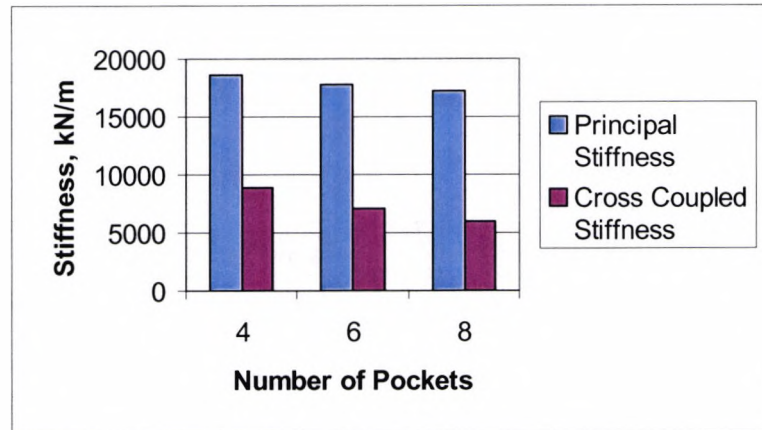


**Fig 4.3c: Effect of number of pockets on stiffness**

(Supply pressure = 1.7 MPa, orifice diameter = 0.00125m, radial clearance = 51 $\mu$ m,  
 Pocket depth=203 $\mu$ m, load = 440N, speed = 14500 rpm)

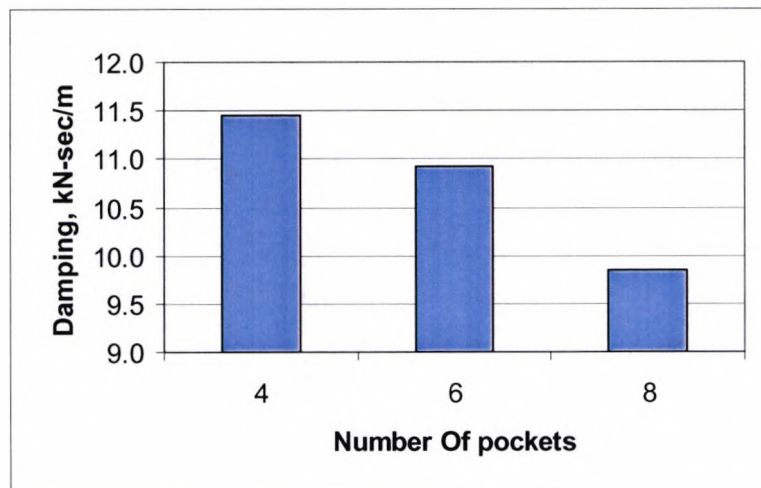


**Fig 4.3d: Effect of number of pockets on damping**

(Supply pressure = 1.7 MPa, orifice diameter = 0.00125m, radial clearance = 51 $\mu$ m,  
 Pocket depth=203 $\mu$ m, load = 440N, speed = 14500 rpm)

**4.6.2 The Effect Of Orifice Diameter:** The effects of variation of orifice diameter on bearing performance are shown in Figures 4.4a to 4.4f. As may be seen from Figure 4.4a, the load carrying capacity is strongly dependent on the orifice diameter, first increasing with diameter, up to a maximum and decreasing for further increases in orifice size. The reason for this, is as follows:

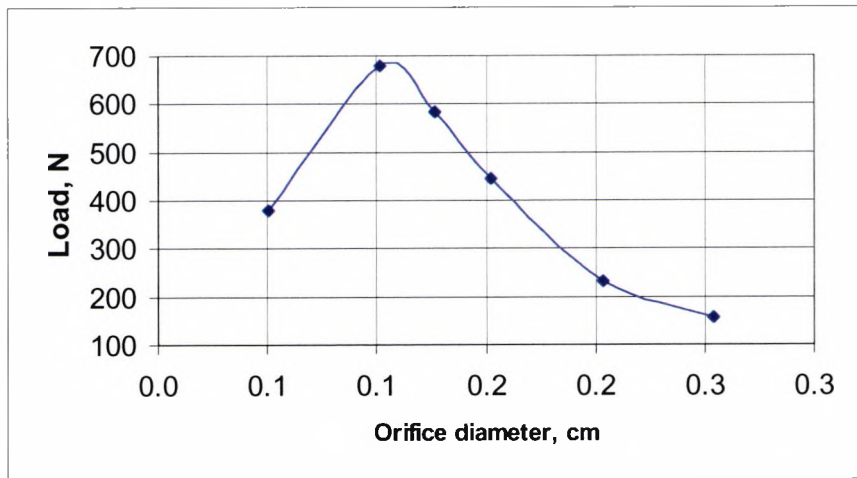
As discussed in Section 4.4, the pocket pressure is determined by the flow rate, which in turn is determined by the resistances in the orifice and the bearing clearance. This can be viewed as two orifices in series. For very small orifice diameters the flow is mainly controlled by the orifice diameter and experiences a large pressure drop for relatively small flow rates. Thus, a small orifice reduces the load carrying capability of the bearing because the pocket pressures, which are more or less equal, are thereby diminished. For larger orifice diameters, the mass flow is controlled by the bearing clearance and hence more variation in the flow rate through and pressure in each pocket becomes possible as the clearance around the bearing varies due to eccentricity of the shaft in the bearing. Despite, this pressure variation, the overall increase in the pressure of each pocket causes an increase in load carrying capability. For still larger orifice diameters, the pocket pressures become nearly equal to the supply pressure and variation between the pockets is minimal despite variations in clearance around the bearing. Since the resultant load is the vector sum of the force around the bearings, a minimal variation of pocket pressure results in a reduction in load carrying capacity. Pressure variations among the different pockets are shown in Figure 4.4b for orifice diameters shown in Figure 4.4a for a radial clearance of  $51\ \mu\text{m}$ . The difference between minimum and maximum pocket pressures is a measure of the load carrying capacity, the larger the difference higher the load carrying capacity. Figure 4.4b shows that the orifice diameter 0.01 cm has the largest difference, which also has the highest load capacity as shown in figure 4.4a.

The required bearing load of 440 N can be obtained for various orifice diameters by changing the radial clearance. The important design parameter to watch is the minimum film thickness. The variation of minimum film thickness as a function of orifice diameter is shown in Figure 4.4c. The film thickness increases with orifice diameter and decreases after reaching a peak value. The explanation is the same as

the one given above for the variation in load carrying capability with orifice diameter. This is the reason that the curves in Figures 4.4a and 4.4c have a similar shape. The flow rate obviously increases with an increase in orifice diameter and the extent of this is shown in Figure 4.4d.

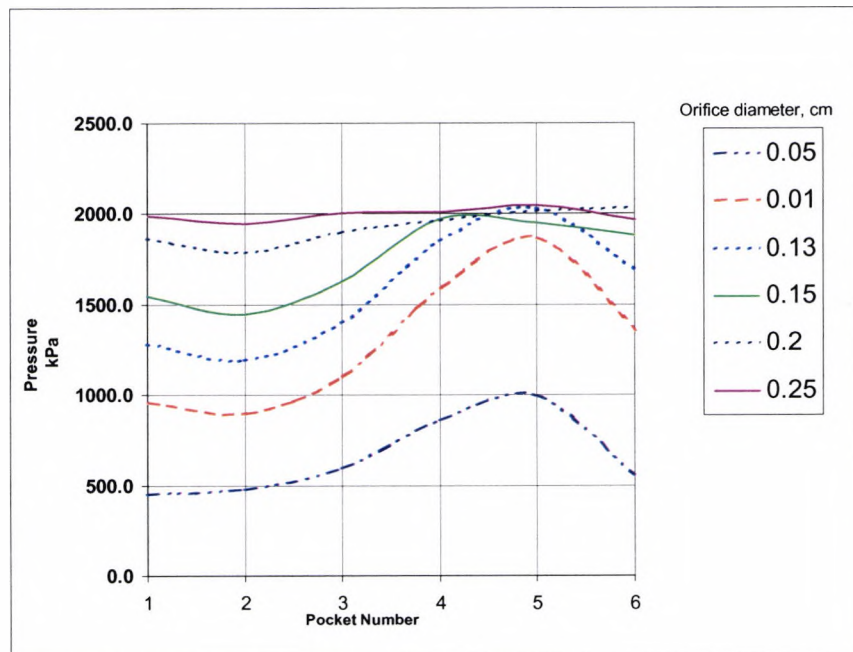
Figure 4.4e shows that principal damping reaches a minimum value between orifice diameters of 0.001 m to 0.0015 m and increases above an orifice diameter of 0.0015 m reaching a maximum at an orifice diameter of 0.0021 m. Further increase in the orifice diameter has no effect on damping. The principal stiffness reaches a maximum at an orifice diameter of 0.001 m as illustrated by Figure 4.4f. A steep drop in principal stiffness takes place when the orifice diameter increases from 0.001 to 0.002 m. This shows that the orifice diameter is a critical parameter and has to be closely controlled during the manufacturing process. The cross coupling stiffness becomes positive at an orifice diameter of 0.0017 m. Although this is desirable from a stability point of view, the minimum film thickness and stiffness are very low at this orifice diameter.

Figure 4.4 g shows the load carrying capacity for a 6 pocket design with 1.7 Mpa supply pressure. From figures 4.4a and 4.4g it can be concluded that the ratio of orifice diameter to radial clearance at which load carrying capacity is maximum is independent of supply pressure. The load carrying capacity, for a 4, 6 and 8 - pocket design with a radial clearance of 100  $\mu\text{m}$  at an eccentricity of 0.5, is presented in figure 4.4h as a function of non-dimensional orifice diameter/radial clearance ratio. It's worth noting that the maximum load carrying capacity occurs at a ratio of 22 for a 6-pocket design, independent of radial clearance. Figure 4.4h also shows that the ratio at which maximum load carrying capacity occurs decreases with increase in number of pockets.



**Fig 4.4a: Effect of orifice diameter on load**

(Supply pressure = 2.0 MPa, number of pockets = 6, pocket depth=203 $\mu$ m,  
Radial clearance = 51 $\mu$ m, load = 440N, speed = 14500 rpm)



**Fig 4.4b: Pocket pressure variation vs Orifice diameter**

(Supply pressure = 2.0 MPa, number of pockets = 6, pocket depth=203 $\mu$ m,  
Radial clearance = 51 $\mu$ m, load = 440N, speed = 14500 rpm)

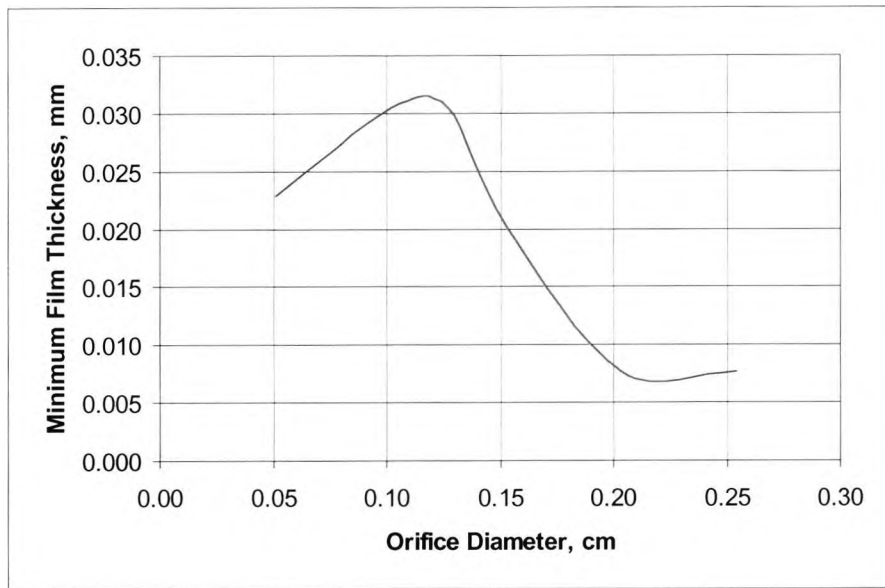


**Fig 4.4c: Film thickness vs orifice diameter**

(Supply pressure = 2.0 MPa, number of pockets = 6, pocket depth=203 $\mu$ m,  
Radial clearance = 51 $\mu$ m, load = 440N, speed = 14500 rpm)

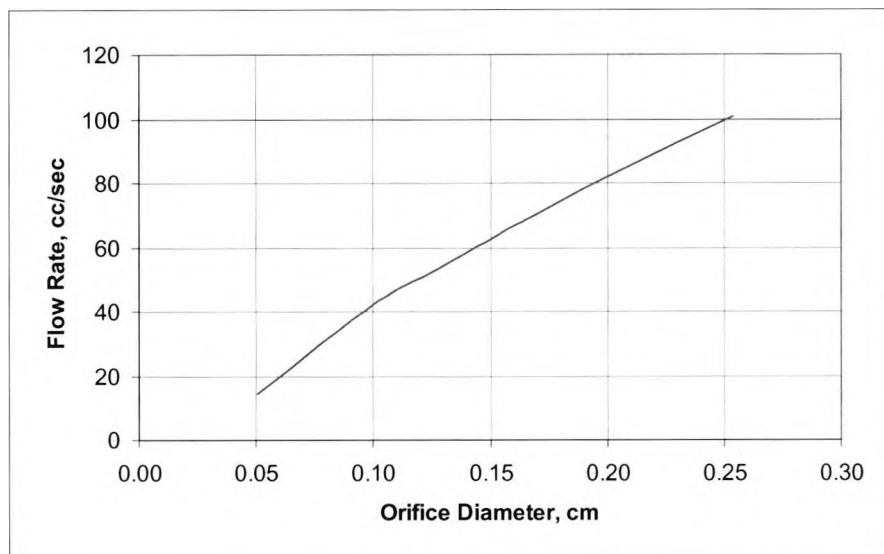


**Fig 4.4.d: Flow rate vs Orifice diameter**

(Supply pressure = 2.0 MPa, number of pockets = 6, pocket depth=203 $\mu$ m,  
Radial clearance = 51 $\mu$ m, load = 440N, speed = 14500 rpm)

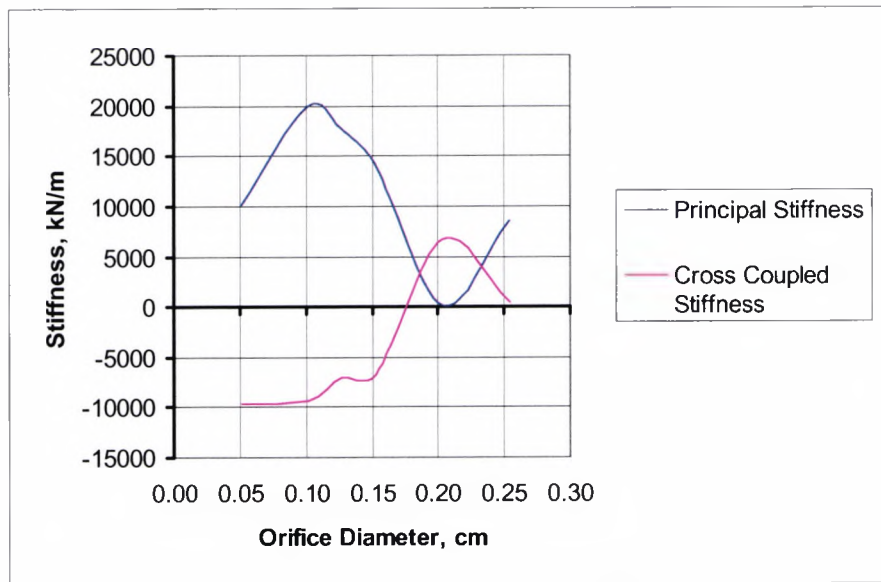


**Fig 4.4e: Stiffness vs Orifice diameter** (Supply pressure = 2.0 MPa, number of pockets = 6, pocket depth=203 $\mu$ m, Radial clearance = 51 $\mu$ m, load = 440N, speed = 14500 rpm)

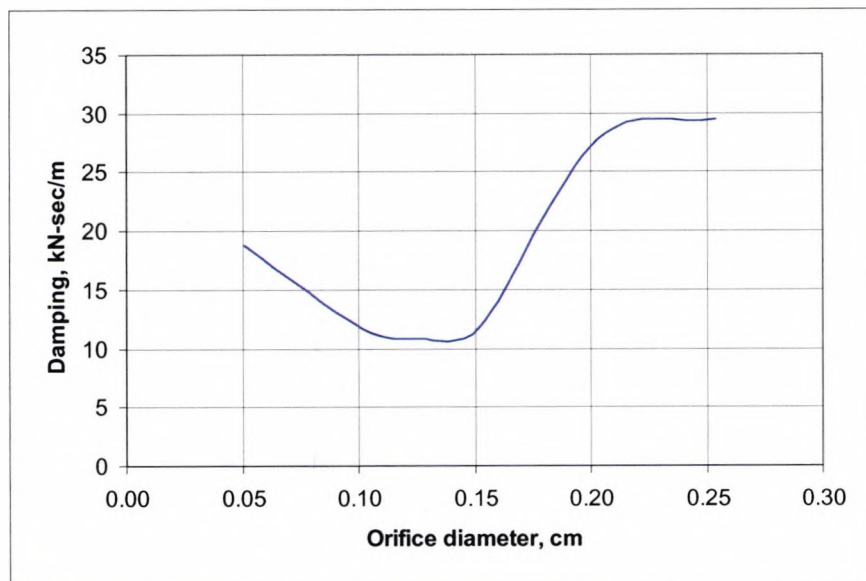


**Fig 4.4f: Damping vs Orifice diameter**  
 (Supply pressure = 2.0 MPa, number of pockets = 6, pocket depth=203 $\mu$ m,  
 Radial clearance = 51 $\mu$ m, load = 440N, speed = 14500 rpm)

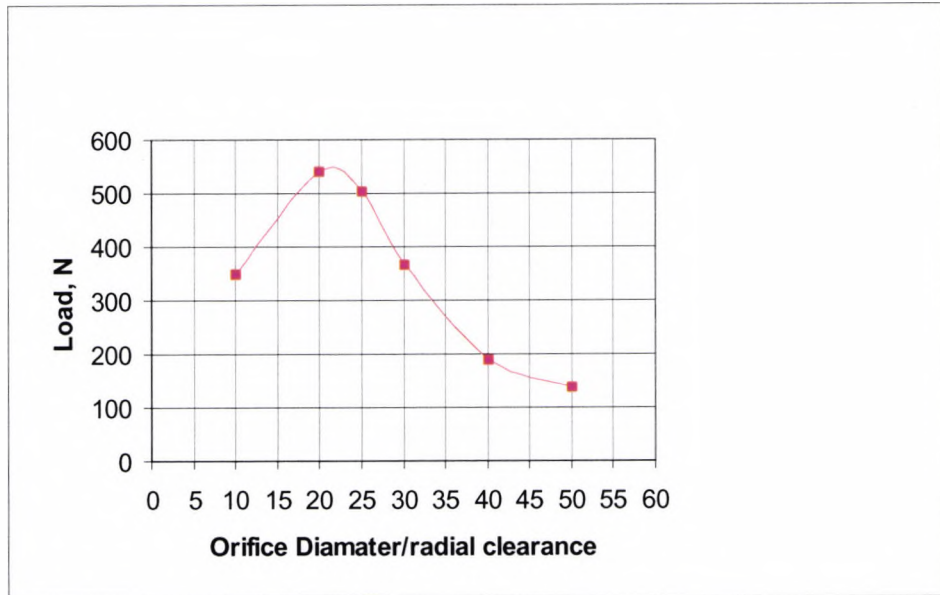


**Figure 4.4g: Load carrying capacity vs ratio of orifice diameter/radial clearance**

(Supply pressure = 1.7 MPa, number of pockets = 6, pocket depth=203 $\mu$ m,  
Radial clearance = 51 $\mu$ m, load = 440N, speed = 14500 rpm)

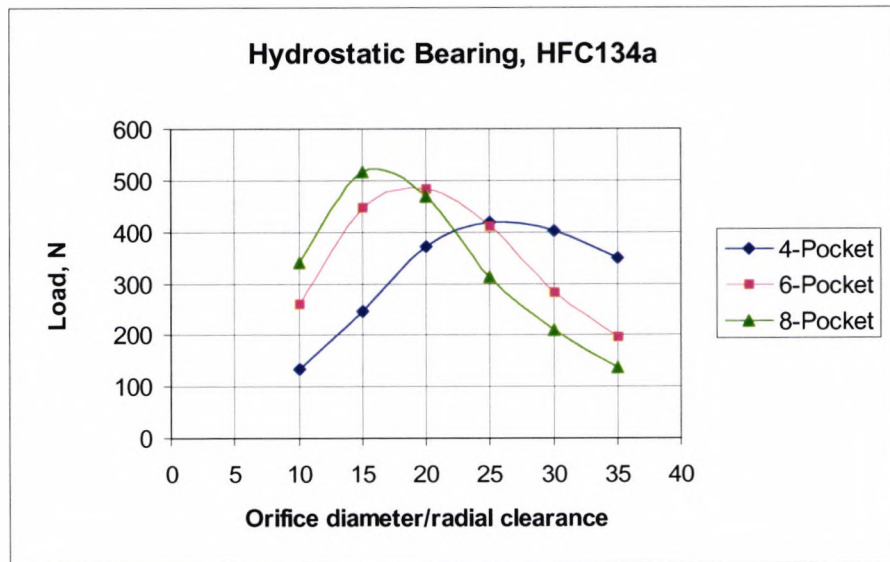


**Figure 4.4h: Load carrying capacity vs ratio of orifice diameter/radial clearance**

(Supply pressure = 1.7 MPa, number of pockets = 6, pocket depth=203 $\mu$ m,  
Radial clearance = 100 $\mu$ m, load = 440N, speed = 14500 rpm)

**4.6.3 The Effect of Radial Clearance:** The results of the effects of change of radial clearance on bearing performance are presented in Figures 4.5a to 4.5e. The power loss rapidly increases with clearance below a clearance of 50  $\mu\text{m}$ . The rate of increase of minimum film thickness and flow rate decreases above a radial clearance of 80  $\mu\text{m}$ . The principal and cross coupled stiffness decrease gradually as the radial clearance increases. Initially, principal damping decreases rapidly with an increase in radial clearance and above a clearance of 58 $\mu\text{m}$ , the damping remains constant with increase in radial clearance.

The effect of dynamic properties on the vibration characteristics is as follows:

- a) Principal stiffness establishes the critical speed value.
- b) Cross-coupled stiffness and damping establish the threshold speed of instability.

Principal damping dictates the amplitude at resonance.

A bearing with high principal stiffness and damping and low cross-coupled stiffness should be selected. Also, the power loss and flow rate should be kept as low as possible to increase the mechanical efficiency and decrease the pump size. From a manufacturing point of view, the range of radial clearance needs to be established. It may be concluded from the data that a range of 40 - 60  $\mu\text{m}$  is the best compromise.

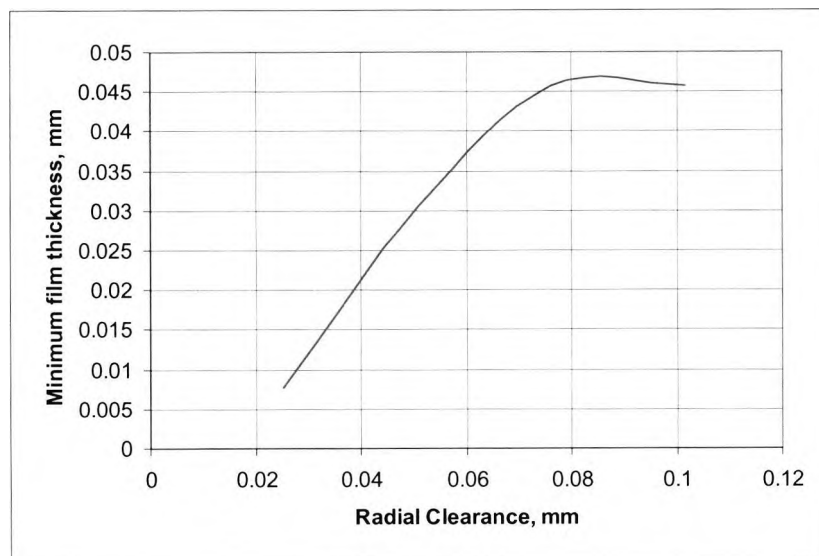


**Fig 4.5a: Minimum Film Thickness vs radial clearance for bearing load of 450N**

(Supply pressure = 1.7 MPa, number of pockets = 6, pocket depth=203 $\mu\text{m}$ ,  
orifice diameter = 0.00125m, Min. film thickness = 25.4  $\mu\text{m}$ , speed = 14500 rpm)

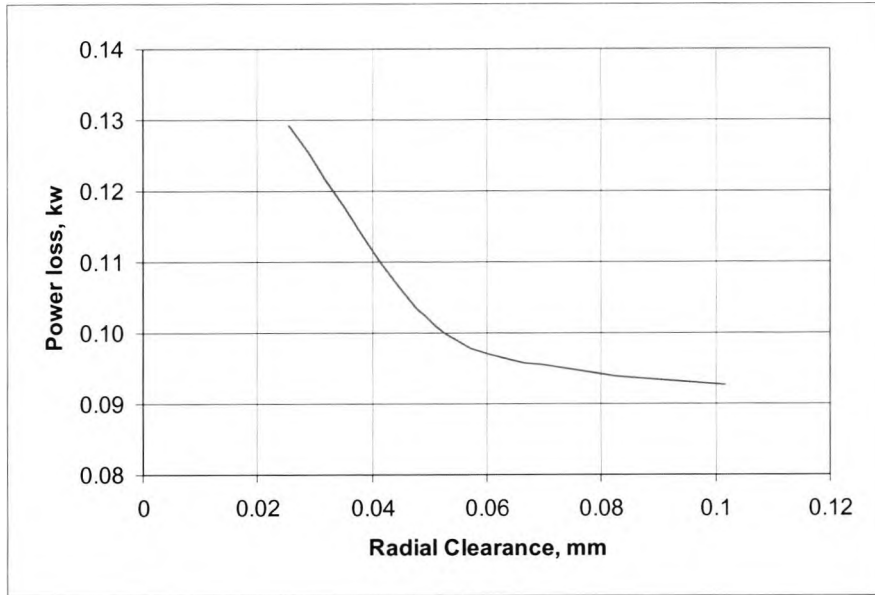


**Fig 4.5b: Power loss vs Radial Clearance for a bearing load of 450 N**

(Supply pressure = 1.7 MPa, number of pockets = 6, pocket depth=203 $\mu$ m,  
orifice diameter = 0.00125m, Min. film thickness = 25.4  $\mu$ m, speed = 14500 rpm)

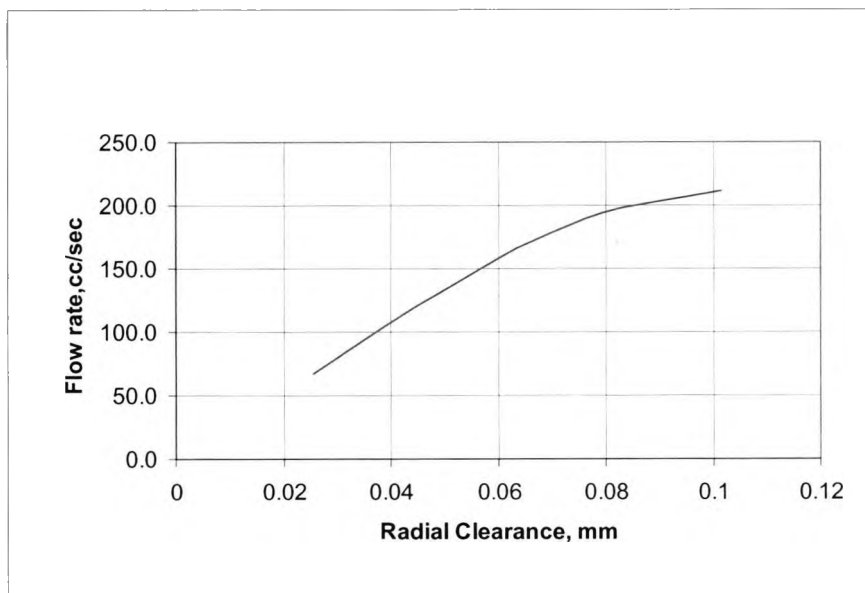


**Fig 4.5c: Flow Rate vs Radial clearance for a bearing load of 450 N**

(Supply pressure = 1.7 MPa, number of pockets = 6, pocket depth=203 $\mu$ m,  
orifice diameter = 0.00125m, Min. film thickness = 25.4  $\mu$ m, speed = 14500 rpm)

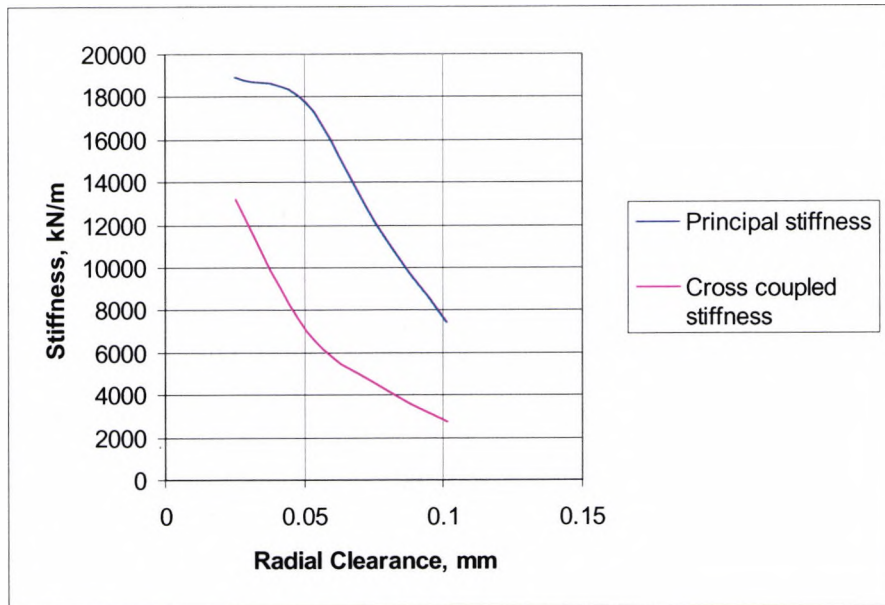


**Fig 4.5d: Stiffness vs Radial Clearance**

(Supply pressure = 1.7 MPa, number of pockets = 6, pocket depth=203 $\mu$ m, orifice diameter = 0.00125m, Min. film thickness = 25.4  $\mu$ m, speed = 14500 rpm)

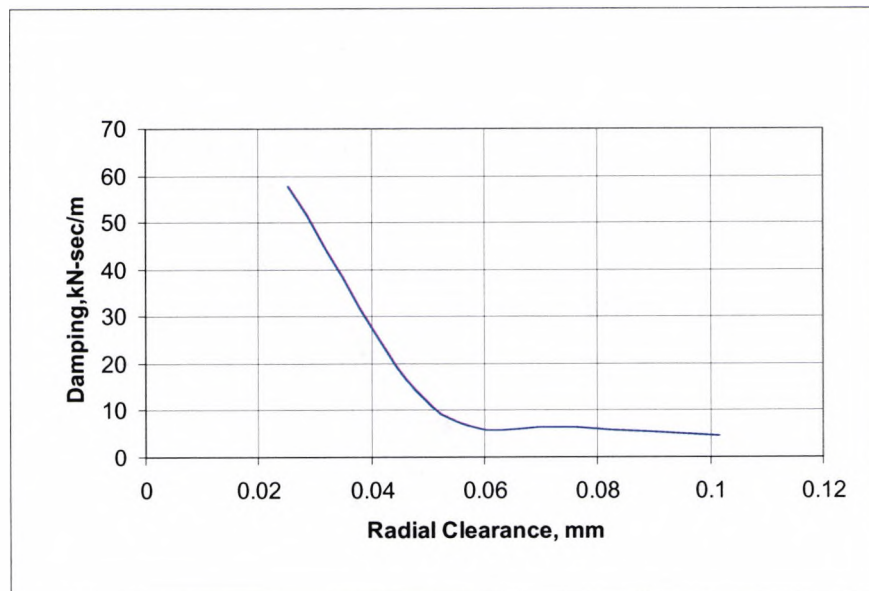


**Fig 4.5e: Damping vs Radial Clearance, bearing load = 450 N**

(Supply pressure = 1.7 MPa, number of pockets = 6, pocket depth=203 $\mu$ m, orifice diameter = 0.00125m, Min. film thickness = 25.4  $\mu$ m, speed = 14500 rpm)

**4.6.4 The Effect Of Supply Pressure:** Results of estimates of the effect of lubricant supply pressure on bearing performance are shown in figures 4.6a to 4.6d. Film thickness and flow rate increase with supply pressure. The principal stiffness increases with supply pressure. At supply pressures of up to 1.5 MPa, the cross-coupled stiffness decreases as the pressure increases. Beyond that value the trend is reversed and it increases slightly with further increases in pressure. The variation of principal damping with supply pressure is broadly similar in character to that of the cross-coupled stiffness with minimum values for each being attained at more or less identical supply pressures.

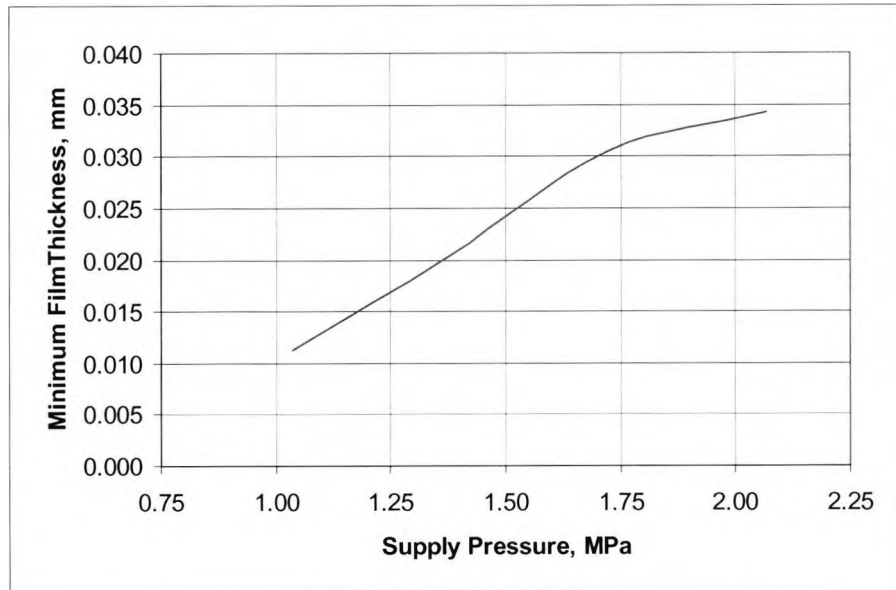


**Fig 4.6a: Minimum film thickness vs Supply Pressure**

(Number of pockets = 6, orifice diameter = 0.00125m, radial clearance = 51 $\mu$ m,  
Pocket depth=203 $\mu$ m, load = 440N, speed = 14500 rpm)

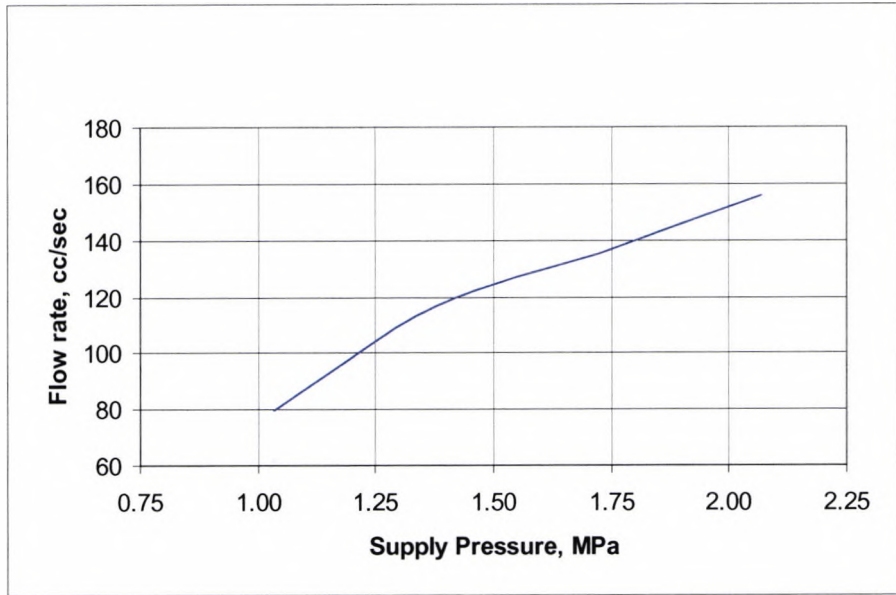


**Fig 4.6b: Flow Rate vs Supply Pressure**

(Number of pockets = 6, orifice diameter = 0.00125m, radial clearance = 51  $\mu$ m,  
Pocket depth=203 $\mu$ m, load = 440N, speed = 14500 rpm)

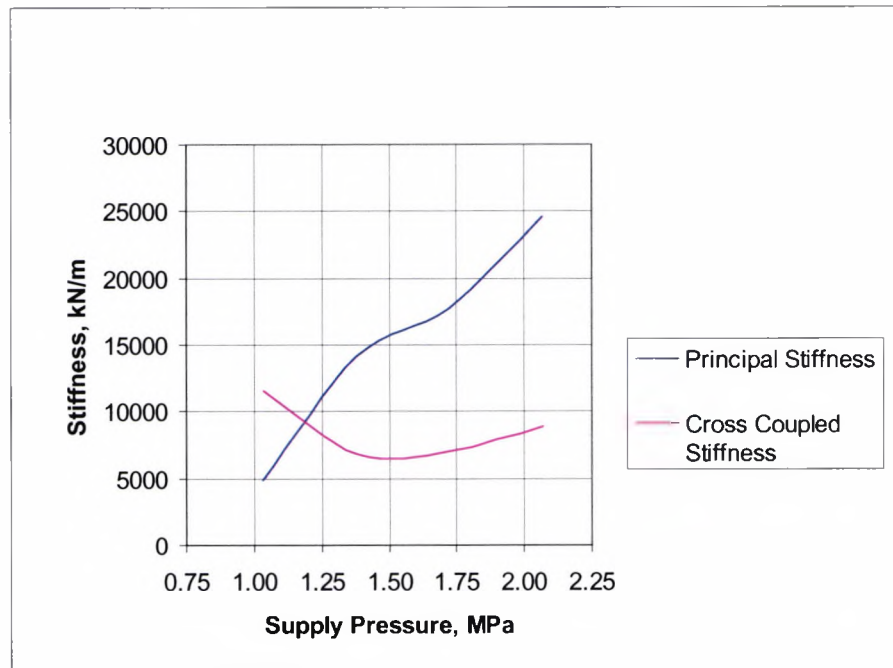


**Fig 4.6c: Stiffness vs Supply Pressure**

(Number of pockets = 6, orifice diameter = 0.00125m, radial clearance = 51  $\mu$ m,  
Pocket depth=203 $\mu$ m, load = 440N, speed = 14500 rpm)

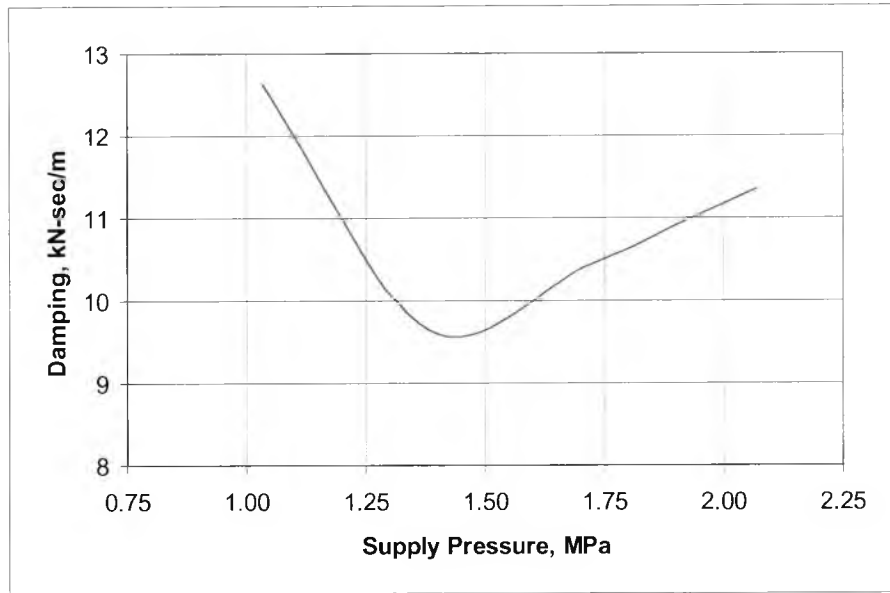


Fig 4.6d: Damping vs Supply Pressure

(Number of pockets = 6, orifice diameter = 0.00125m, radial clearance = 51 $\mu$ m,  
Pocket depth=203 $\mu$ m, load = 440N, speed = 14500 rpm)

**4.6.5 The Effect Of Pocket Depth:** The results of performance estimates assuming differing pocket depths are shown in the table below. The depth has little effect on either the principal or the cross coupled stiffness. Thus, the value of the pocket depth chosen was taken as 200  $\mu$ m for ease of manufacture.

Depth $\mu$ m	Min Film $\mu$ m	K <sub>xx</sub> kN/m	K <sub>yx</sub> kN/m	C <sub>max</sub> kN-sec/m	Flow rate L/sec
80	30	18433	-8075	10.6	0.0137
100	30	18390	-7406	10.7	0.0136
200	30	17384	-6905	10.7	0.0135
250	30	17384	-6878	10.7	0.0135
510	30	17382	-6844	10.7	0.0135
2540	30	17403	-6862	10.8	0.0135

**4.6.6 The Effect of Speed:** The hydrodynamic effect of the bearing is limited due to the small length of land. As such, its effect on the variation of load carrying capacity, stiffness and damping is very small.

**4.6.7 The Final bearing design:** Based on the above analysis, a bearing with 6 – pockets, radial clearance of 50  $\mu\text{m}$  and an orifice diameter of 0.125 cm was designed. Note that the ratio of orifice diameter to radial clearance is 25, which is slightly higher than the optimum ratio of 22. However, the larger orifice diameter is easier to drill and reduces risk of contaminants clogging the orifice. The final bearing design is shown in figures 4.7a through 4.7 d and its performance is shown in Table (4.1).



**Figure 4.7a: Solid model of front of hydrostatic bearing**

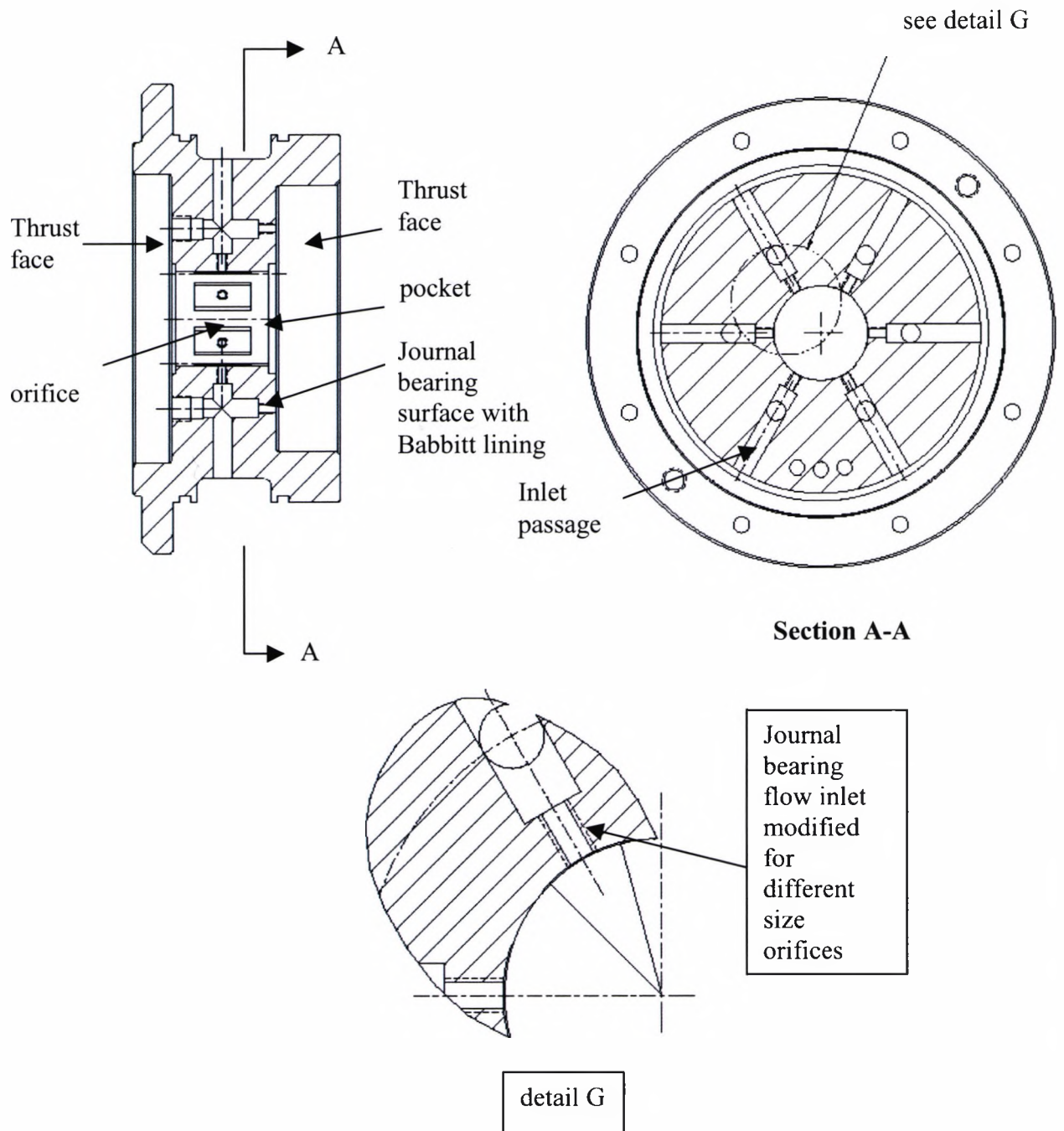
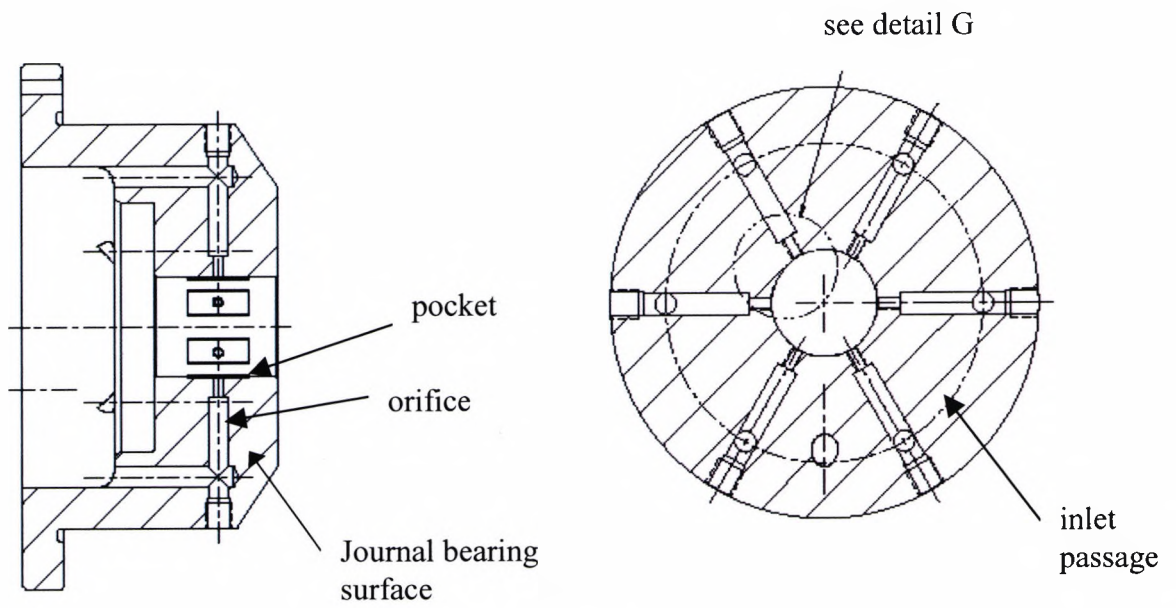
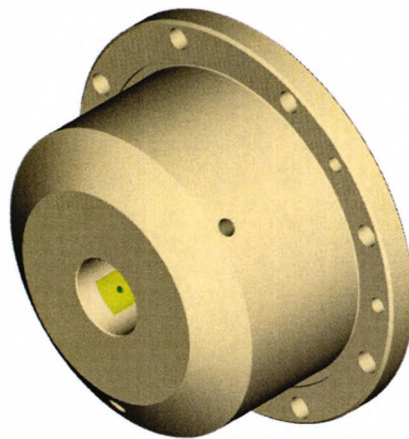


Figure 4.7b: Hydrostatic Bearing cross section– Front or Impeller side



Note: detail G same as in figure 4.7 b

**Figure 4. 7c: Hydrostatic Bearing cross section– rear or motor Side**



**Figure 4.7d: Solid model of hydrostatic bearing – rear side**

## **4.7 The Compressor Rotor Dynamics**

**4.7.1 Modelling of the Rotating System:** The rotor consists of a shaft and its attached masses, namely, the impeller and the motor. The physical model is transformed into mathematical equations by one of two types of modelling approaches, namely, the Lumped-Parameter or Transfer Matrix and the Finite Element method. Both approaches are described in standard vibration textbooks<sup>(1)</sup>, hence only their main features are presented here. In the Transfer Matrix approach, the rotor is broken down into subsystems with elastic and dynamical properties. The formulation is in terms of the *state vector*, which is a column matrix of the displacements and internal forces; a *point matrix*, which contains the dynamical properties of the subsystem; and the *field matrix*, which describes the elastic properties of the subsystem. In terms of these quantities, calculations are made to proceed from one end of the system to the other, the natural frequencies being established by satisfying the appropriate boundary conditions. A constant cross section of shaft is replaced by lumped masses connected by sections of zero mass.

The Finite Element method also divides the rotor into subsystems. However, the mass of the shaft is not lumped at the ends of the section. Instead it is distributed uniformly along the section. Both the Finite Element and the Transfer Matrix methods have been successfully used in industry for predicting rotor dynamic behaviour. The main advantage of the Finite Element method is that it requires fewer sections in the model, especially if long constant cross sections are included. In the case of an overhung rotor, the values of critical speed and unbalance response, estimated by both procedures, resulted in differences of less than 2%. For stability analysis or damped natural frequency analysis, the difference in natural frequency was of the order of 5%, with the finite element method yielding the higher values.

The vibration analysis was carried out by a finite element based computer program developed by University of Kentucky and widely used in industry. The rotor assembly is illustrated in Figure 4.8, while its static deflection derived from the

analysis is shown in Figure 4.9. The nominal rotor stiffness derived from the maximum deflection was found to be 96000 kN/m.

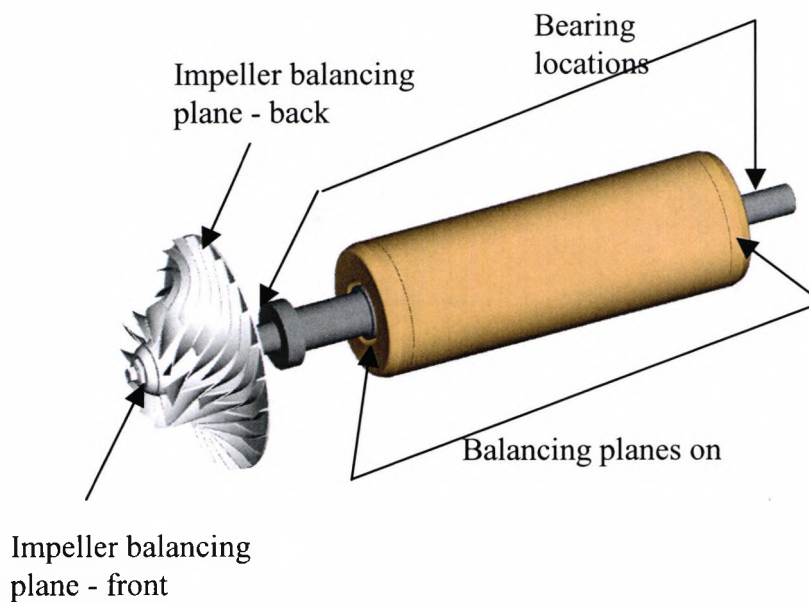


**Figure 4.8: Rotor Model Showing Balancing planes**

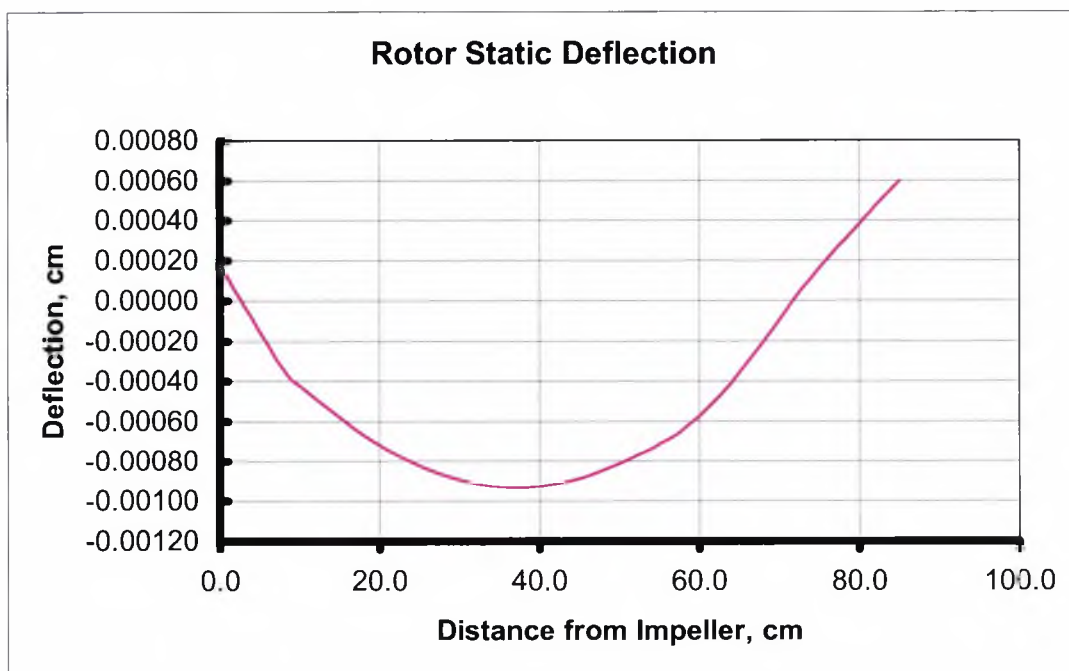


**Figure 4.9: Rotor Static Deflection Plot**

**4.7.2 Undamped Critical Speed Analysis:** A rotor-bearing system has a number of discrete natural frequencies of lateral vibration. Associated with each natural frequency is a mode shape, which can be thought of as a snapshot of the rotor deflection curve at the instant of maximum strain or displacement during vibration. Resonance occurs when the shaft speed coincides with one of the natural frequencies. The shaft speed that coincides with that natural frequency is called the "critical speed". Due to unbalance in the rotor, the rotor does not vibrate, but rather is bowed into the mode shape with the particular natural frequency and whirls about its bearing centre line. To a stationary external observer the rotor appears to vibrate, but this is simply the planar projection of the whirl orbit as seen from one side.

In mathematical terms, the natural frequencies are called eigenvalues and the mode shapes are called eigenvectors. Theoretically, a distributed mass-elastic system has an infinite number of eigenvalues and associated eigenvectors. In practice, only the lowest three or four critical speeds and associated whirl modes are excited in the operating range of a typical turbomachine. The mode shapes are determined by the distribution of mass and stiffness along the rotor, as well as by the bearing support stiffness'.

The first step in rotor dynamic analysis is to calculate critical speeds as functions of stiffness. Since damping is not taken into consideration, the critical speeds are called undamped critical speeds. The rotor is divided into sections of equal diameter. The compressor impeller is modeled as a mass located at its centre of gravity and polar and transverse moments of inertia. The motor rotor is divided into several disks of constant mass, polar and transverse moments of inertia. The disks are considered rigid and so is the attachment between the disc and the shaft. The latter assumption leads to the fact that the plane of the disk remains normal to the shaft during

vibration. Figure 4.10 shows the rotor dynamic model with the location of each section.

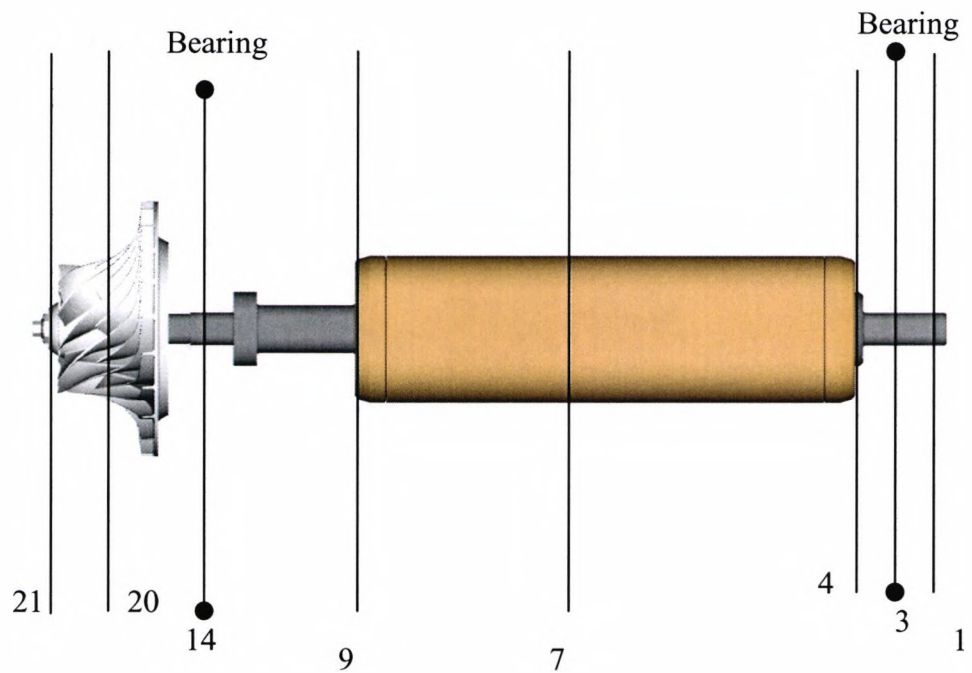


**Figure 4.10: Stations For Rotor dynamic Modelling**

The results of the undamped critical speed calculation are presented in Figure 4.11A. Also, shown on the plot are the bearing stiffness at supply pressures of 1.04, 1.4, 1.7 and 2.1 MPa. The stiffness values are obtained from the bearing analysis. The first and second critical speeds initially increase with support stiffness and then become insensitive to stiffness. The region where the support stiffness affects the critical speeds is termed the rigid rotor region, and the insensitive region is known as the flexible rotor region. Since the operating speed range of the compressor is 10 000 - 14500 rpm, the following can be concluded from Figure 4.11A:

- a) For a supply pressure of 1.04 MPa, the operating speed range is between the second and third critical speeds.
- b) For supply pressures of 1.4, 1.7 and 2.1 MPa, the minimum operating speed is above the first critical speed and the maximum operating speed is above the second critical speed. For a speed of 10 000 rpm, the operating speed coincides with the critical speed. This is not detrimental to the rotor as long as the bearings have enough damping to contain the amplitude of vibration.
- c) For a stiffness above 500 000 kN/m, the first critical speed stays constant at 10 000 rpm. Hence, the rotor will operate in the flexible rotor region if the bearing stiffness is above 500 000 kN/m. Operation in the flexible rotor region will limit the displacement as shown by the mode shape in Figure 4.11G. Hence, there will be less damping in the bearing due to reduced displacement. Damping is essential to reduce the amplitude of vibration when operating near or passing the critical speeds.

Rotor mode shapes at different values of bearing support stiffness' are shown in Figures 4.11B – 4.11G. The following conclusions can be drawn from them:

- a) Up to a stiffness of 87600 kN/m, the deflection at the bearings is large. These high deflections, increase the whirl velocity in the bearings thereby generating more damping. The deflection decreases with increase in support stiffness, thus resulting in lower damping.
- a) The deflection at the bearings at the third critical speed mode is always lower than at the first and second critical speeds. Due to this lower deflection, the damping in the bearings will be less. High vibrations will therefore result for operating speeds near or while crossing the third critical speed.

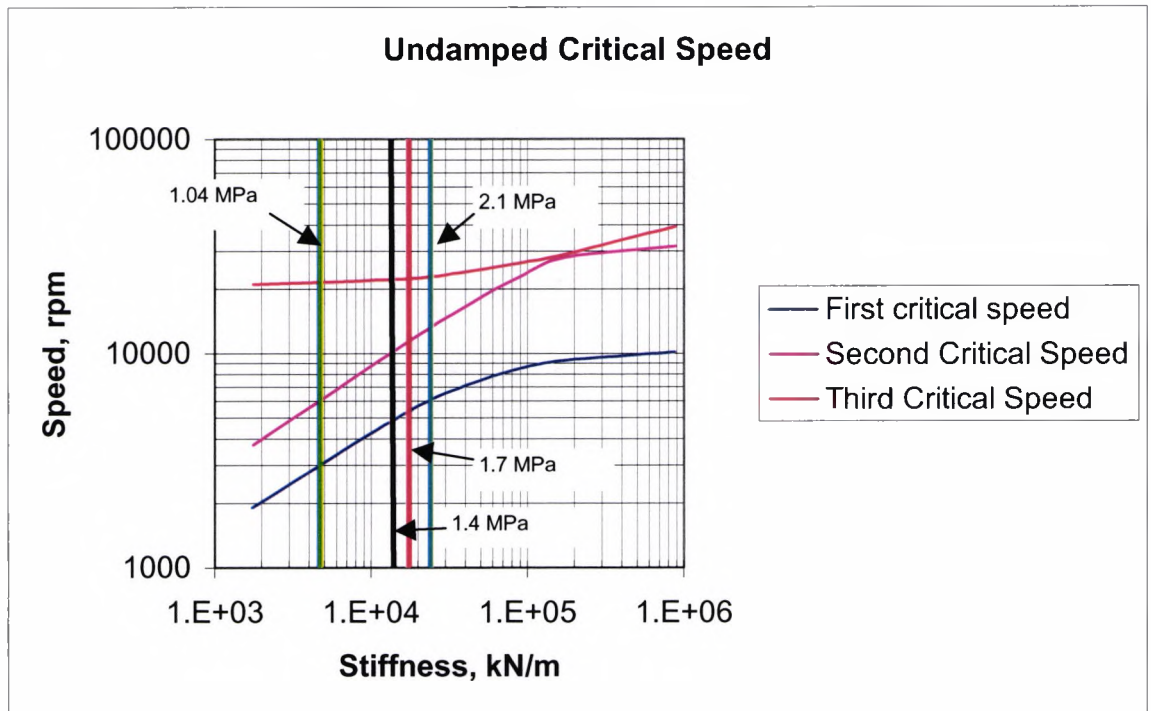


**Figure 4.11A: Undamped Critical Speed Map as a function of bearing stiffness.** Supply pressures and corresponding stiffness values shown in the table below are also shown on the figure

Supply Pressure, MPa	Principal Stiffness, kN/m
1.04	4 620
1.4	13 600
1.7	17 000
2.1	23 700

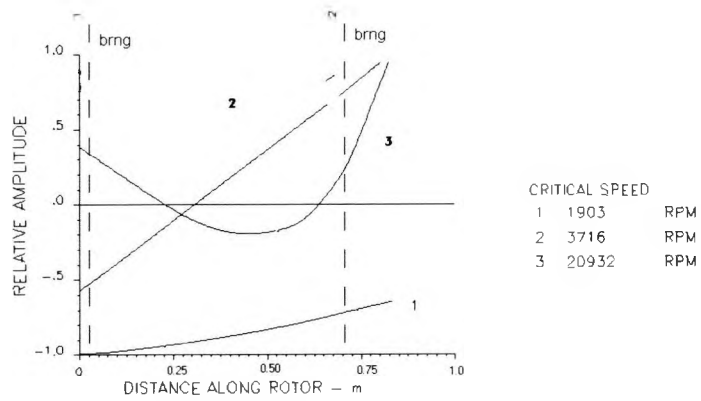


Figure 4. 11B: Rotor mode shape at bearing stiffness = 1766 kN/m

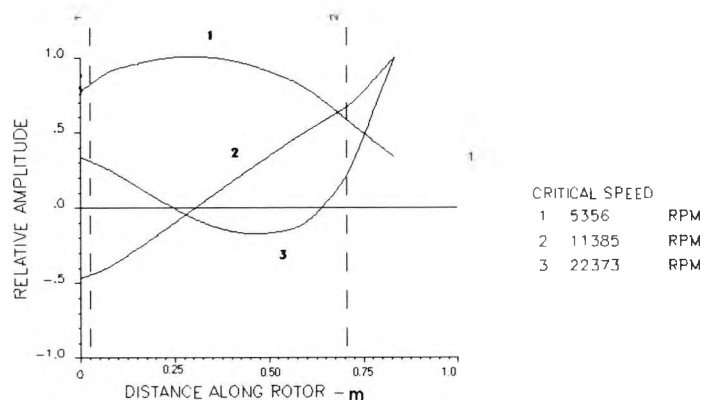


Figure 4. 11C: Rotor mode shape at bearing stiffness = 17660 kN/m

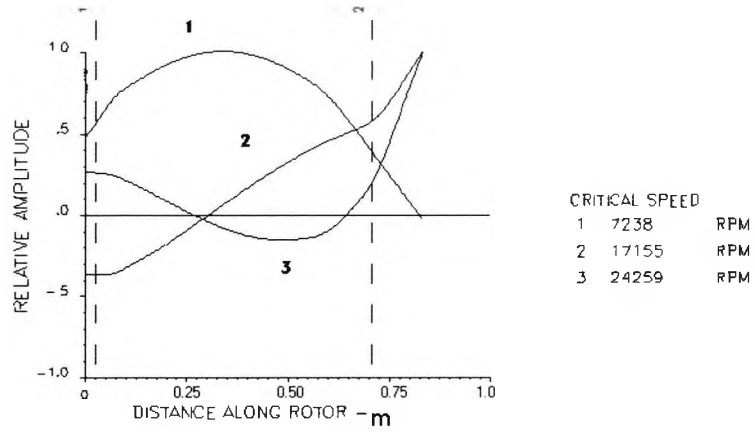


Figure 4. 11D: Rotor mode shape at bearing stiffness = 43750 kN/m

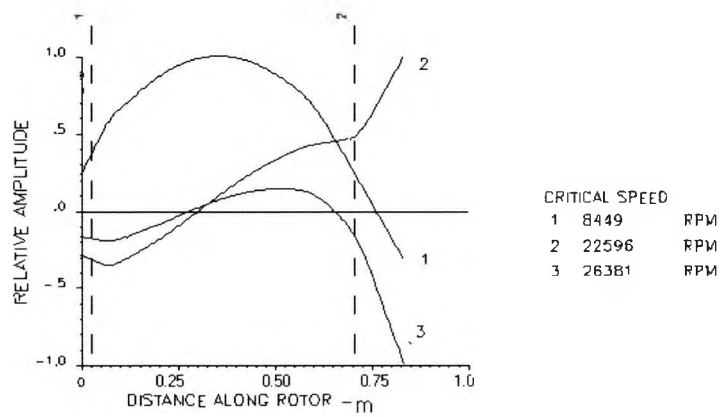


Figure 4.11E: Rotor mode shape at bearing stiffness = 87600 kN/m

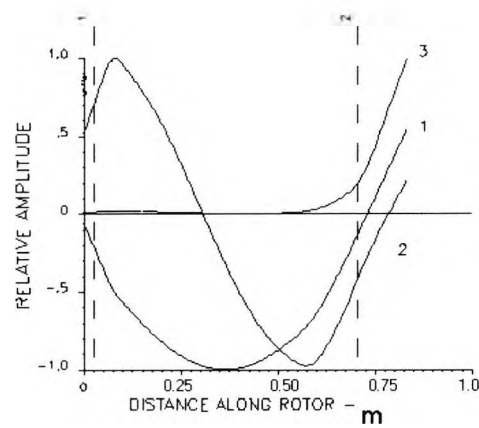


Figure 4.11F: Rotor mode shape at bearing stiffness = 176000 kN/m

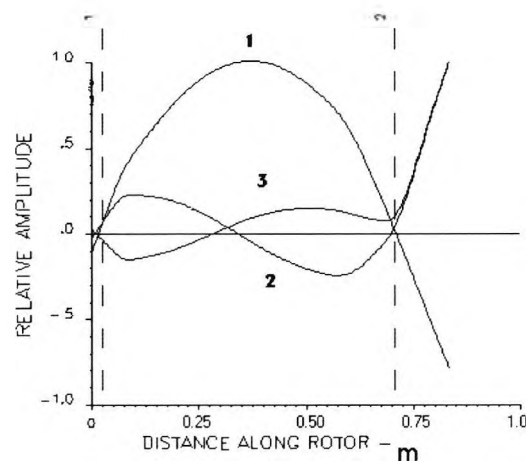


Figure 4. 11G: Rotor mode shape at bearing stiffness = 876000 kN/m

**4.7.3 Damped Critical Speeds and Rotor-Bearing Stability:** A fluid film bearing supporting a rotor may be likened to a spring-dashpot system in that the bearing reaction to small displacements may be expressed in terms of stiffness and damping. A mass supported by springs has a number of natural frequencies depending on the complexity of the spring system and the possible modes of motion of the mass. If any mode of motion is excited at the natural frequency by an external harmonic force, the response of the system will be a maximum. If the system possesses effective damping for this mode of excitation, then the response will be bounded and the system will not be unstable. If, on the other hand, the natural frequency of a mode of motion corresponds to a condition where the effective damping of the system is negative, then the motion of the system will increase without bounds without any external excitation, and the system is considered as being unstable, i.e. subject to self-excited vibration. If a natural frequency occurs at a condition of zero damping, then the system is said to be at the threshold of instability, where infinitesimally small exciting forces applied over a period of time will result in ever increasing amplitudes of response.

The undamped critical speeds of a rotor bearing system refer to resonant responses of the system to unbalanced forces of the system that, by their nature, are applied at a frequency synchronous with the rotational speed of the shaft. Since fluid film bearings have, in general, positive damping to synchronous speed oscillations, critical speeds are not instabilities but represent a condition of large resonant response to inherent unbalanced forces. Fluid film bearings, however, do have an effective damping to various modes of motion that tends to zero when the motion occurs at some fraction of the running speed, usually at half the running speed. Thus, as the running speed of a rotor increases beyond the first critical speed, the rotor will begin to approach the condition where the first resonant or natural frequency will coincide with the fractional frequency at which effective damping goes to zero. When this coincidence occurs, the rotor is said to have reached the whirl threshold speed. A further increase in rotor speed results in a very rapid growth of whirl amplitude and, in almost all cases, the whirl threshold speed represents the upper limit for safe operation of the rotor. It is the cross-coupled stiffness ( $K_{xy}$ ,  $K_{yx}$ ) of journal bearings that destabilises the system.

Lund<sup>(2)</sup> published a method of calculating damped critical speeds for the more general case of the translatory, conical and bending modes of a non-symmetric rotor. The procedure is incorporated in the computer program developed by the University of Kentucky. The input to the program is the geometry of the rotor and the four stiffness and four damping coefficients for each of the bearings. The program output consists of the damped natural frequency, the logarithmic decrement value and the mode shape and whirl or precession direction with respect to shaft speed. The logarithmic decrement value is defined as the natural logarithm of the ratio of any two successive amplitudes at time  $t$  and  $t + \delta t$ , where  $\delta t$  is one period. For stable operation, the amplitude should decrease with increase in time. Hence, a positive logarithmic decrement value shows that the system is stable.

Typical output of the analysis is shown in figures 4.12a and 4.12 b. Each figure shows the relative amplitude in X and Y directions at stations along the length of the rotor. Additional information such as the mode number, the logarithmic decrement value (LD), the critical speed and the direction of whirl forward (FWD) or backward (BKW) is printed at the top. Equal magnitude of relative amplitude at a particular station in X and Y direction shows a circular whirl orbit. Unequal magnitudes of the amplitudes result in an elliptical orbit. The bearing stiffness and damping control the magnitude of amplitude. Due to different bearing stiffness and damping properties in vertical and horizontal directions, each mode will be split into two, one corresponding to the minimum bearing stiffness and the other corresponding to maximum stiffness. The forward whirl is excited by unbalance in the system, whereas the backward whirl is excited by rotor stator rubs. The lowest whirl frequency together with the log decrement value for forward and backward precession for different supply pressures at 14500 rpm are tabulated below.

### Forward Whirl

<b>Supply Pressure MPa</b>	<b>Lowest Whirl Frequency Cpm</b>	<b>Log Dec</b>
1.04	4210	-1.160
1.4	4898	-0.302
1.7	5323	-0.180
2.1	5947	-0.149

### Backward Whirl

<b>Supply Pressure MPa</b>	<b>Lowest whirl Frequency Cpm</b>	<b>Log Dec</b>
1.04	5273	3.081
1.4	5262	2.07
1.7	5811	1.658
2.1	6176	1.334

Note that the backward whirl modes all have a positive logarithmic decrement value and hence are stable. However, the forward whirl modes have negative logarithmic decrement values and are unstable. The following conclusions can be drawn from the results:

- 1) The forward whirl frequency increases with the supply pressure.
- 2) The log decrement value for forward whirl increases with the supply pressure, i.e. the rotor stability increases with the supply pressure.
- 3) For backward whirl, both frequency and logarithmic decrement value decrease with increase in supply pressure.
- 4) Analysis carried out from 16 000 rpm down to a speed of 10 000 rpm did not show any change in whirl frequency or log decrement value. This is due to the dominance of the hydrostatic effect over the hydrodynamic effect in the bearing

5) Analysis shows that the rotor is unstable at all of the above supply pressures because of negative logarithmic decrement values for forward whirl modes that are excited by rotor unbalance. There are several cases cited in literature where a rotor, which theoretically should be unstable, has operated at speeds in excess of the instability threshold speed. The hypothesis has frequently been advanced that the non-linearity of the fluid film bearing forces may be the stabilizing factor in the sense that, even if the static equilibrium position of the rotor is unstable and results in whirling, the amplitude doesn't grow without bounds. Instead the rotor whirls in a stable finite orbit. Hence, experimental analysis of the compressor will show if the rotor can be operated between 10 000 and 14500 rpm.

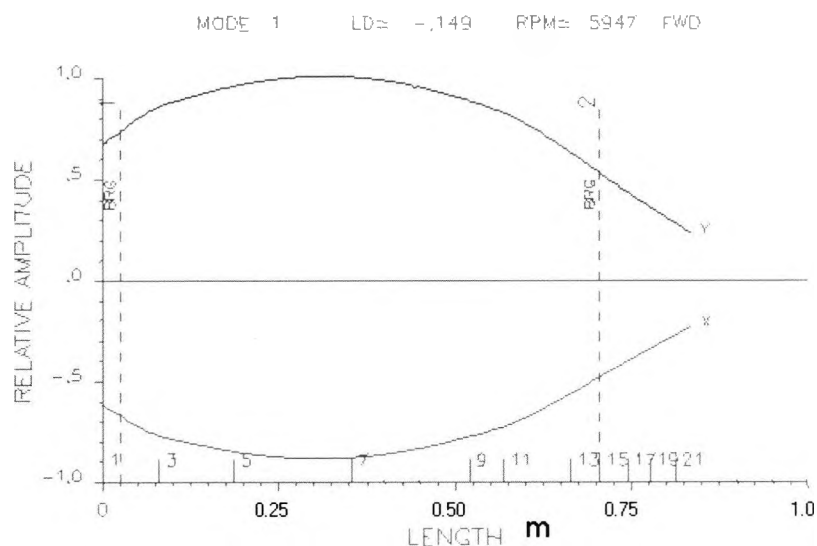


**Figure 4.12a: Stability and rotor mode shape with Supply pressure = 2.1 MPa – Forward whirl**

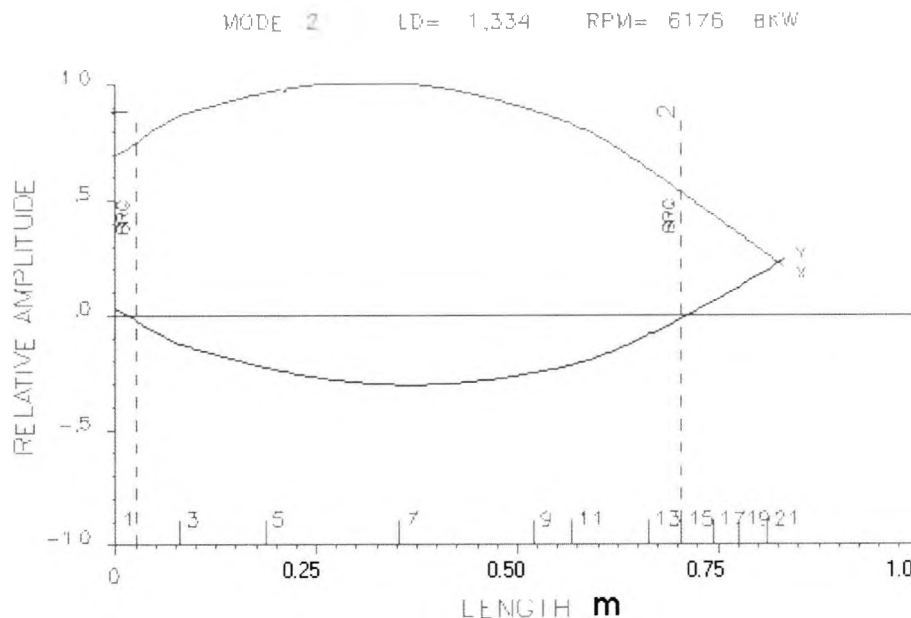


**Figure 4.12b: Stability and rotor mode shape with Supply pressure = 2.1 MPa - Backward whirl**

**4.7.4 Unbalance Response Analysis:** The most common source of vibration in turbomachinery is rotor imbalance. If the centre of mass of a rotating disc or shaft does not lie on the axis of rotation, it consequently orbits about the axis and generates a centrifugal force that must be reacted by the bearings and support structure. Since the force rotates at shaft speed, the vibrating frequency in the non-rotating structure is synchronous. When the unbalanced masses all lie in a single plane, as in the case of a thin rotor disk, the resultant imbalance is a single radial force. Such an unbalance can be detected by a static test, in which the disk is supported on an axle and the disk will roll to a position where the heavy point is directly below the axle. Since such unbalance can be detected without spinning the wheel, it is called static unbalance.

Another type of unbalance called dynamic unbalance appears when the unbalance is in more than one plane. A rotor carrying two discs having equal and opposite unbalance will be statically balanced. However, when spun about its axis, a couple is

created which rotates at synchronous speed. The source of unbalance is primarily due to machining tolerances which result in the geometric and mass centres not coinciding.

**4.7.5. Determination of unbalance magnitude and location :** Rotors operating at low shaft speeds and with a bearing stiffness less than the shaft stiffness are classified as rigid. Thus, undamped critical speed modes in such a case will be rigid rotor modes. On the other hand, rotors operating at high speeds on rigid supports exhibit significant rotor bending and such rotors are classified as flexible rotors.

From the undamped critical speed map, Figure 4.11A, it can be seen that between 10000 and 14500 rpm, the rotor operates in a region where the bearing stiffness controls the critical speed. Also, it can be seen from the undamped critical speed map and mode shapes that, for different lubricant supply pressures, at up to the second critical speed, the rotor behaves as if it is rigid. Hence, speeds up to this value can be considered as "low". From the principles of statics, it can be shown that two planes are sufficient for balancing a rigid rotor.

From the compressor assembly drawing, figure 4.1, it can be seen that, either the impeller or the motor rotor has to be assembled after the shaft is assembled in the front bearing. Since, the motor rotor is heavier than the impeller, it is easier to assemble the impeller after the motor rotor and bearings are in place. Although the rotor is balanced as a single unit together with the impeller and motor, compressor assembly requirements force the impeller to be disassembled after balancing. Care has to be taken therefore to mark the impeller with respect to shaft before disassembly so that it can be assembled at the same circumferential location. Another problem is that since the impeller is shrink fitted on the shaft, additional time is required for the balancing process in its assembly and removal. To reduce balancing time and improve productivity, the shaft is balanced with the motor rotor fitted while the impeller is balanced separately and assembled at a later stage. The balancing planes for the shaft and motor rotor assembly are situated at the ends of the motor rotor, as shown in Figure 4.8. The balancing planes for the impeller are at the rear and front ends. Unbalance in the system is reduced by either adding material into threaded

holes provided in the balancing planes or by removing material. Unbalance response calculations are carried out with the residual unbalance distributed at the impeller and ends of the motor rotor.

The allowable amount of residual unbalance in the rotor can be calculated from the unbalance response analysis based on the following criteria:

- 1) The amplitude of vibration at the bearings, seal, impeller and motor locations should be less than 25 % of the "running" clearance.
- 2) The force transmitted at the bearings should be less than the fatigue limit of the bearing lining material. For tin based lining material the limit is 1MPa.

The recommended values for the maximum amount of unbalance for different rotor configurations are listed in ISO and API standards<sup>(3,4,5)</sup>. The maximum residual unbalance for the compressor rotor (based on a weight of 89 kgs) is shown below.

Standard	Formula	Allowable unbalance (total)		Comments
		(oz-in)	(gm-mm)	
API – 617	$56405 * W / N^2$	0.056	41	W in lbs, N in rpm
ISO-1940, G 2.5	$2.5W / \omega$	0.22	159	W in gm, $\omega$ in rad/sec

Note: W is the rotor mass in the units indicated above.

N is the rotor speed,  $\omega$  is the rotor angular velocity.

The rotor unbalance, calculated in accordance with ISO standards, was used in the analysis. The impeller unbalance, calculated in accordance with ISO-1940 grade G6.3 as 16 gm-mm, was used in the analysis. The reason for using a lower grade level than that given in the table is that the impeller is cast and is therefore difficult to manufacture with a G2.5 unbalance level. For synchronous analysis, unbalance is placed at the impeller and the ends of the motor rotor, which are the balancing planes. Based on the rotor mode shape for operation above the second critical speed, as shown in Figures 4.11 B-C, the unbalance distribution that resulted in the highest amplitude was that with unbalance at the motor rotor near the rear bearing opposite

to that at the impeller and rotor close to the front bearing. The unbalance analysis was carried out with the following two distributions:

- 1) Unbalance in all three planes in the same direction (16 gm-mm at impeller, 79.5 gm-mm at the motor end planes)
- 2) Unbalance at the rear bearing plane opposite to that of the impeller and rotor plane near the front bearing. (16 gm-mm at the impeller, 79.5gm-mm at the motor end near the front bearing and 79.5 gm-mm at 180 deg out of phase at the rear bearing).

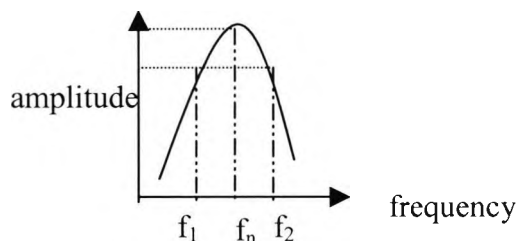
**4.7.6 Results of the Unbalance response analysis:** The rotor was divided into 21 stations starting from the shaft end opposite to the impeller. Stations 3 and 14 are near the bearing locations and stations 4 to 9 comprise the motor. Station 20 corresponds to the impeller.

The response analysis was carried out for supply pressures of 1.04, 1.4, 1.7 and 2.1 MPa. The analysis calculated the vibration amplitude and the force at the bearings, for a given unbalance, as a function of shaft speed. The plot of vibration amplitude and force as a function of speed exhibits some peaks. The sharpness of a peak is a function of the damping present in the system. The sharpness is quantified by the "Amplification Factor", which is defined as:

$$Q \equiv \frac{f_n}{(f_2 - f_1)},$$

where  $f_n$  is the peak amplitude frequency,  $f_1$  and  $f_2$  are the

frequencies corresponding to 0.707X (amplitude at  $f_n$ )



For a single degree of freedom system, it can be shown <sup>(6)</sup> that the amplification factor,  $Q$ , is inversely proportional to the damping. Peak frequencies with amplification factors less than 5 are considered to be well damped. The peaks are identified as critical speeds. In the majority of cases, the critical speeds, identified from the peaks of the unbalance response, are close to those calculated from the

undamped critical speed analysis. However, if the damping is high, peaks may not appear and it becomes possible to miss a critical speed.

Typical output of the unbalance response analysis program is shown in Figures 4.13A, B and C. The unbalance response plot, in Figure 4.13A, shows major and minor axis vibration amplitude as a function of speed at selected stations along the rotor. The unbalance response plot shows the speeds at which the peak amplitudes occur. Continuous operation at these speeds is normally avoided. In the top part of the unbalance response plot, shaft orbits with their direction of precession are shown at stations along the rotor. Figure 4.13 B shows the output of the bearing force magnitude together with the phase angle in the X and Y directions. Figure 4.13 C shows a table of a summary of the speeds at which the peak amplitudes occur and their corresponding amplification factors.

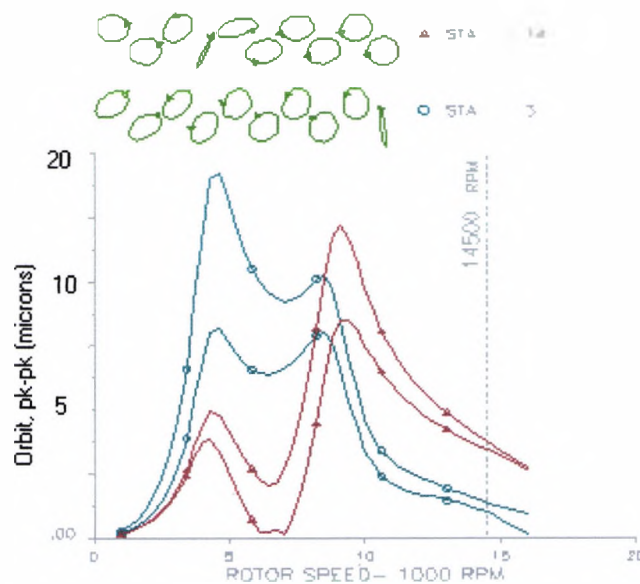


**Figure 4.13A: Typical synchronous response vibration amplitude output**  
**Supply pressure = 1.04 MPa**

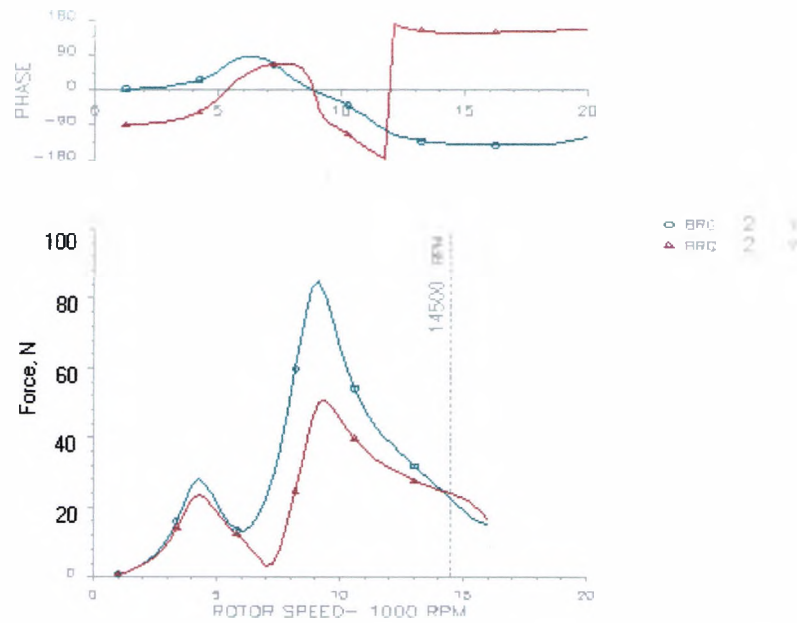


**Figure 4.13B: Typical synchronous response bearing force output**  
 Supply pressure = 1.04 MPa

STATION	PK NO	RPM	AMPLIF FACTOR
3	1	4600.00	2.04
3	2	8500.00	1.45
4	1	4600.00	2.05
4	2	8500.00	1.44
7	1	4600.00	2.25
7	2	9400.00	.00
9	1	4300.00	2.37
9	2	9400.00	2.90
14	1	4300.00	2.68
14	2	9100.00	4.33
20	1	4300.00	.43
20	2	8800.00	4.53

**Figure 4.13c: Amplification Factor based on major orbit**  
 (supply pressure =1.04 Mpa)

**4.7.7 Discussion of the results:** The graphical output from the program at the following supply pressures is shown in Appendix A:

- 1) Supply pressure 1.04 MPa
- 2) Supply pressure 1.4 MPa
- 3) Supply pressure 1.7 MPa

#### 4) Supply pressure 2.1 MPa

From the data shown in the appendix, the critical speed, amplification factor, vibration amplitude and bearing force are shown in Figures 4.14 through to 4.18. The first and second peaks in the response curves identify the first and second critical speeds. The results can be summarized as follows:

Critical Speed: Figure 4.14 shows that both the first and second critical speeds increase with supply pressure. This is to be expected as an increase in supply pressure increases the principal stiffness (see Figure 4.6C). Also, the variation of the critical speed with the position of unbalance is very small. This is due to the fact that the critical speed is a function of the rotor geometry and support stiffness and not the position or magnitude of unbalance.

Amplification factor: Figure 4.15A shows that the amplification factor at the first critical speed initially increases with the supply pressure, reaches a peak and decreases thereafter. The supply pressure at which the peak amplification factor occurs with the in-phase unbalance amplification factor agrees with the supply pressure at which the minimum damping occurs, as shown in Figure 4.6D. Since the amplification factor is inversely proportional to the damping, it is expected that a high amplification factor is associated with low damping. The amplification factor is high with the in-phase unbalance up to a supply pressure of 1.5 MPa. Above this supply pressure, the amplification factor with out of phase unbalance is higher.

Fig 4.15 A also shows that the peak amplification factor depends upon the orientation of the unbalance. The variation of the amplification factor with the phase of unbalance can be explained from the definition of damping force, which is a product of the damping coefficient, vibration amplitude and frequency. For a given magnitude of unbalance, the vibration amplitude at the bearing depends on the phase between the unbalance at different locations on the rotor. Fig 4.15B shows that the vibration amplitude near the bearings is higher for in-phase unbalance than for out of phase unbalance. Since the frequency at the critical speed is the same for both types of unbalance, the in-phase unbalance results in higher damping and hence lowers the amplification factor. In contrast, it should be pointed out that at a supply

pressure 1.4 MPa, the amplification factor for the in-phase unbalance is higher than in the out of phase unbalance case.

Figure 4.15C shows a small variation of amplification factor with supply pressure and phase of unbalance at the second critical speed,. The magnitude of vibration amplitude, Figure 4.15D at the second critical speed is higher for out of phase unbalance than for in-phase unbalance. Also, for out of phase unbalance, the magnitude decreases with increase in the supply pressure. However, for in-phase unbalance, the magnitude shows very little variation with supply pressure. The explanation for variation of amplification factor given for the first critical speed does not explain the trends for the second critical speed amplification factor.

The variation of vibration amplitude can be explained from the mode shape at the first and second critical speeds given by figures 4.11 B, C and D. The mode shape at the first critical speed is translatory and in-phase unbalance results in a force that is in the same direction along the shaft which, in turn, creates a larger amplitude. For the translatory mode, the out of phase unbalance results in a lower resultant force and hence a lower amplitude. At the second critical speed, the mode shape is conical with the node at the middle of the motor. An out of phase unbalance creates a larger resultant force and hence a larger amplitude of vibration.

Vibration Amplitude: Vibration amplitudes at important locations, such as the rear bearing, the middle of the motor, the front or impeller bearing and the impeller in the speed range 10 000 to 16 000 rpm are presented in figures 4.16 A through D.

The following are the main observations:

- 1) Except at the middle of the motor, the amplitudes are high with out of phase unbalance. The reason for this is that the rotor is operating above the second critical speed with a conical mode shape.
- 2) The variation in vibration amplitude as a function of supply pressure decreases with increase in speed. This is because the speed is moving away from the second critical speed.
- 3) For in-phase unbalance, the variation in vibration amplitude with supply pressure is small at all speeds between 10 000 and 16 000 rpm. The reason for

the low amplitudes is the mode shape is more close to the second critical speed and the in-phase unbalance does not affect this mode shape.

- 4) For out of phase unbalance, at supply pressures 1.04 and 1.4 MPa, the vibration amplitude decreases with speed at all four locations.
- 5) For out of phase unbalance, at supply pressures 1.7 and 2.1 MPa, the vibration amplitude increases with speed, reaches a maximum and then decreases with speed at all four locations.

Bearing force: The force at the bearings due to unbalance is shown in figures 4.17A-D. The main observation is that the force is higher with in-phase unbalance than with out of phase unbalance. The in-phase unbalance case shows a peak at the first critical speed and the out of unbalance shows a peak at the second critical speed.

Based on a criterion of a maximum amplification factor of 5, continuous operation at speeds between 4000 and 6000, and supply pressures below 2.1 MPa has to be avoided.

#### **4.8 Conclusions of the Dynamic Analysis:**

The main conclusions of the analysis are that the compressor design is marginally stable, the log decrement value is close to zero and the amplitudes are higher than 25% of the film thickness. Also, the bearing dynamic force is slightly higher than 10% of the bearing load. The amplification factor at the first critical speed is highest at a supply pressure corresponding to the lowest damping. The magnitude of the highest amplification factor is also a function of phase of unbalance, with the out of phase unbalance higher than the in-phase unbalance. The amplification factor at the second critical speed shows little variation with the supply pressure and the phase of unbalance. The analysis also shows that by manipulating unbalance distribution, it's possible to reduce vibration amplitude.

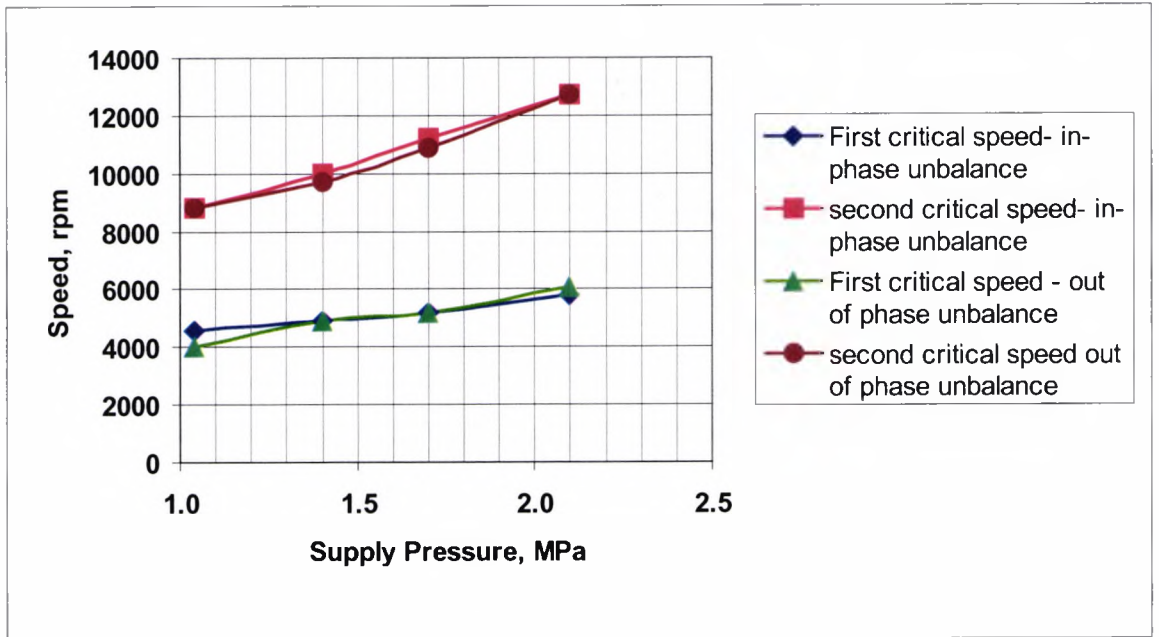


Figure 4.14: Critical Speed vs supply pressure based on unbalance response analysis

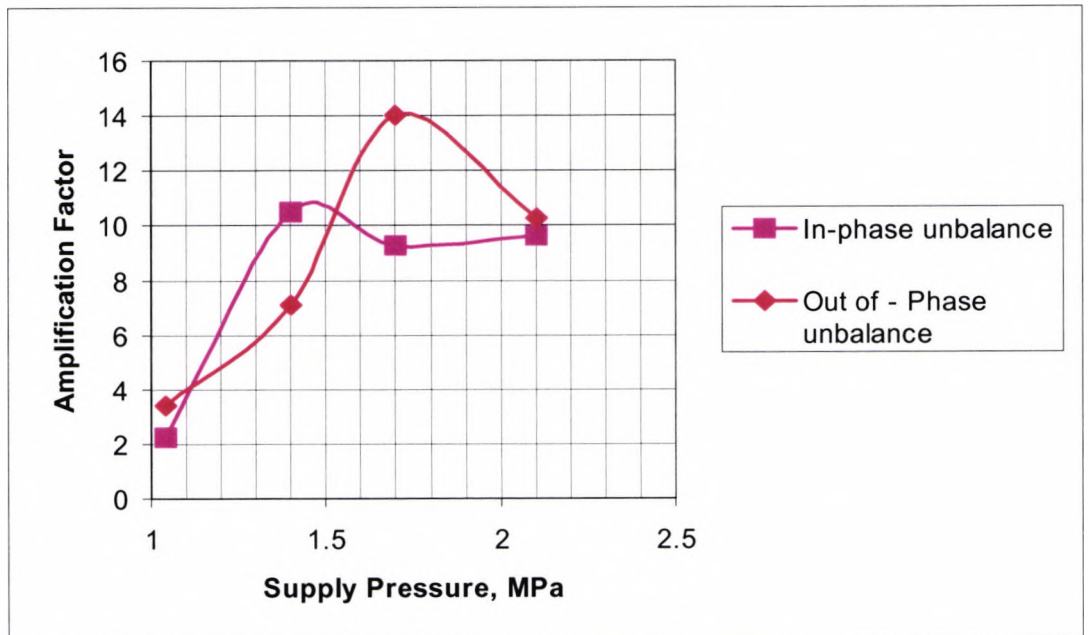


Figure 4.15A: Amplification factor at first critical speed vs supply pressure

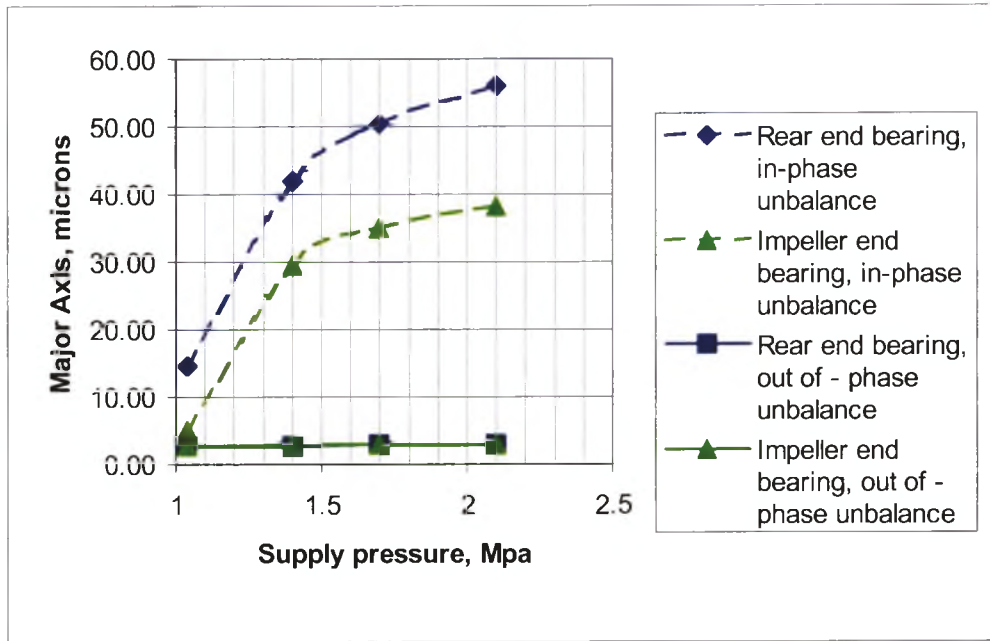


Figure 4.15B: Vibration Amplitude at bearings at First critical speed vs supply pressure.

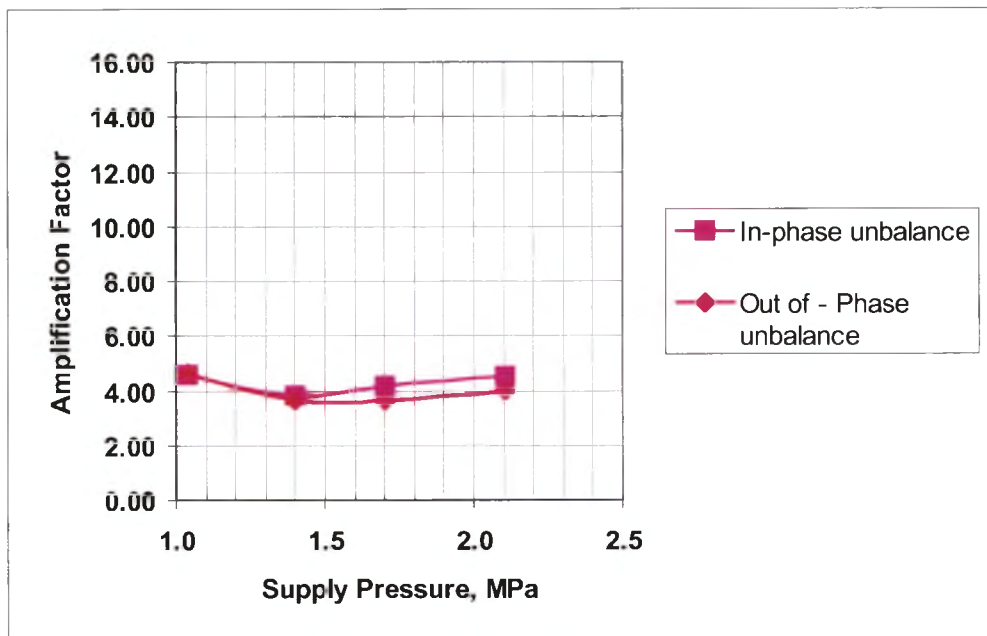


Figure 4.15C: Amplification factor at second critical speed vs supply pressure

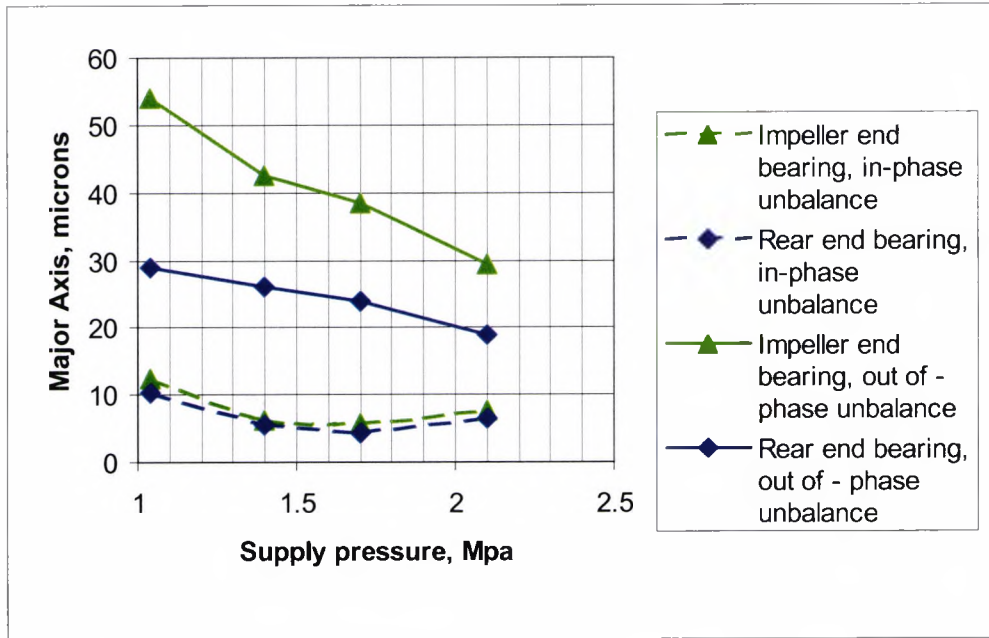


Figure 4.15D: Vibration amplitude at bearings at second critical speed vs supply pressure.

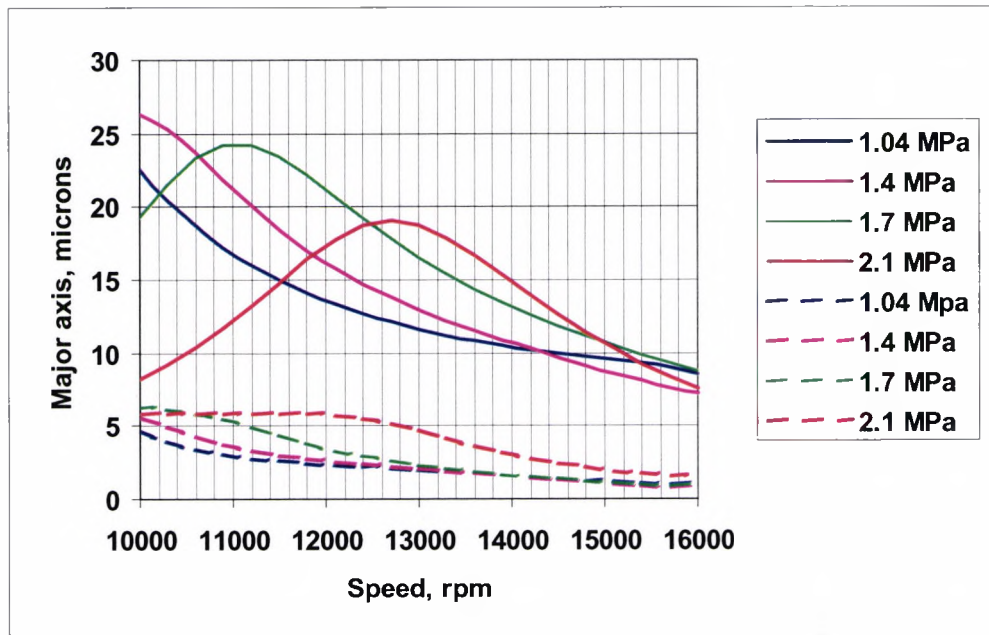


Figure 4.16A: Comparison of response at Rear bearing with in-phase (dashed line) and out of phase (solid line) unbalance

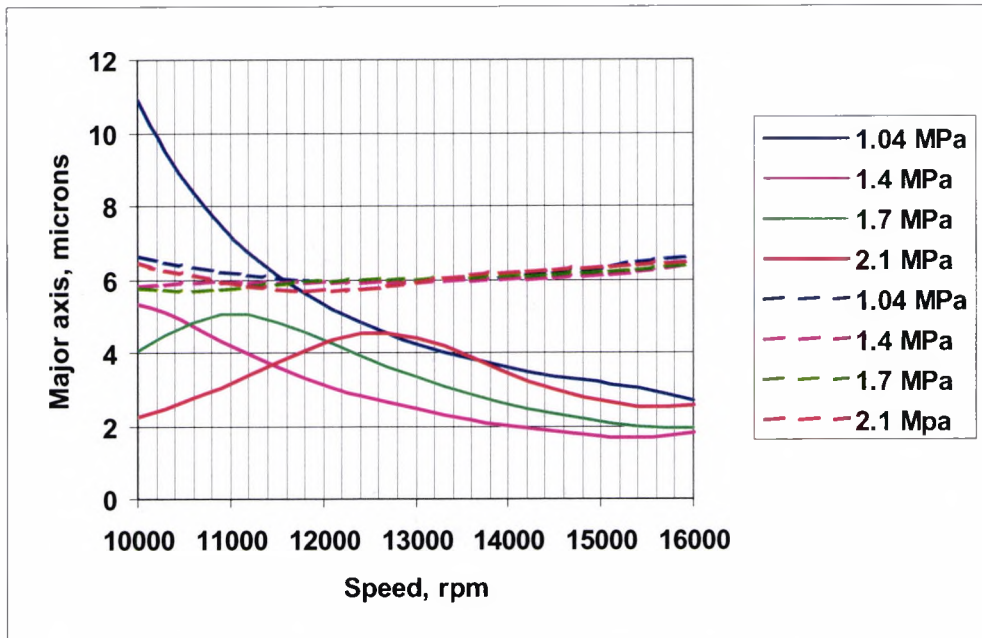


Figure 4.16B: Comparison of response at middle of motor rotor with in-phase (dashed line) and out of phase (solid line) unbalance

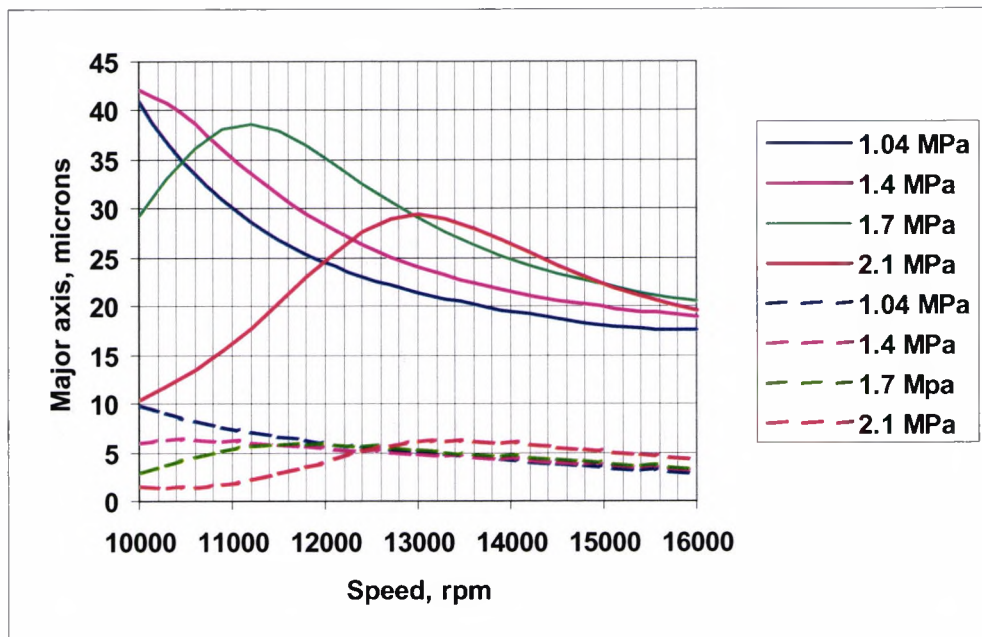


Figure 4.16C: Comparison of response at Impeller end bearing with in-phase (dashed line) and out of phase (solid line) unbalance.

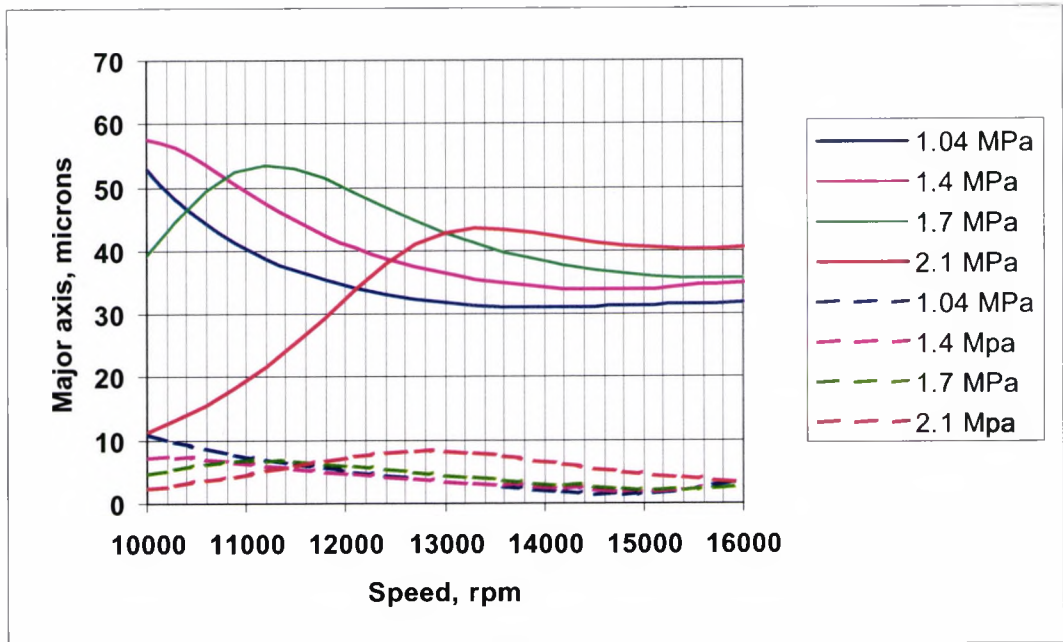


Figure 4.16D: Comparison of response at Impeller with in-phase (dashed line) and out of phase (solid line) unbalance

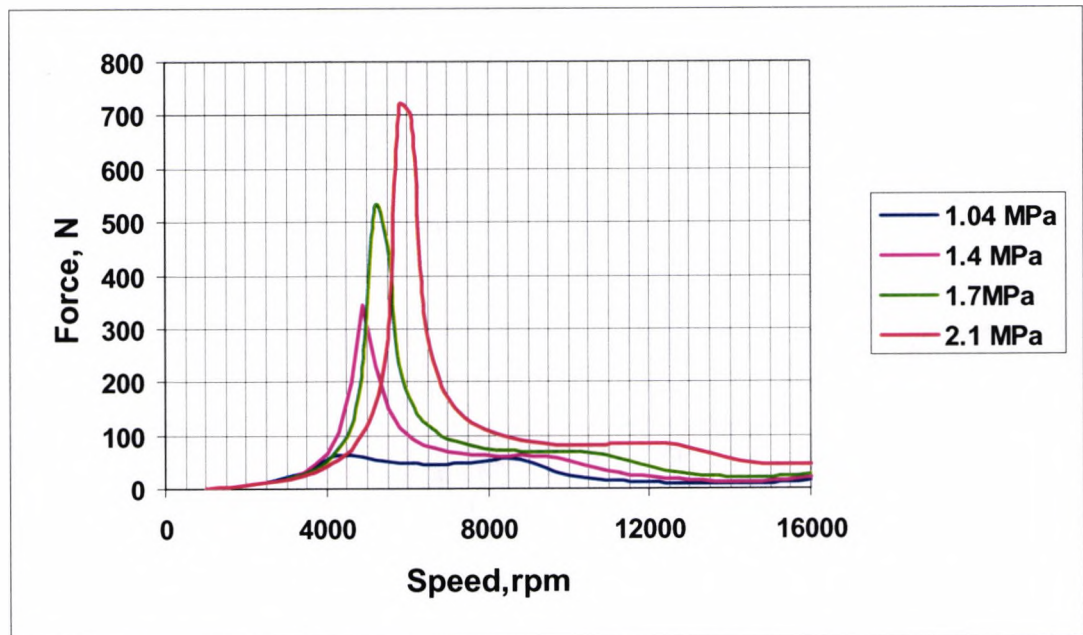
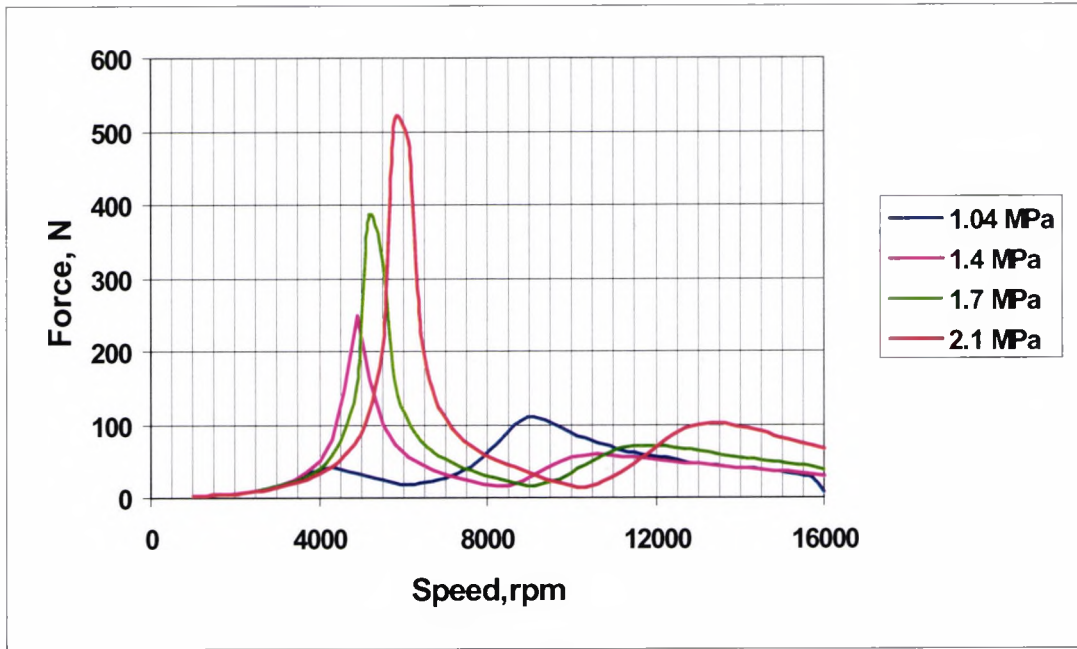
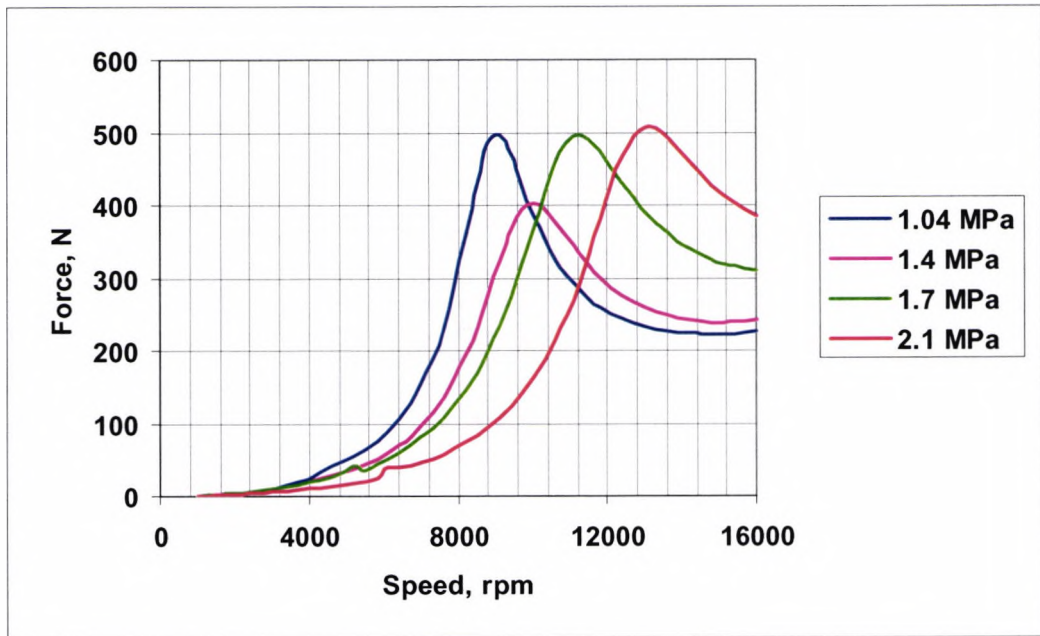


Figure 4.17A: Force at Rear bearing. In-phase unbalance



**Figure 4.17B: Force at Impeller bearing. In-phase unbalance**



**Figure 4.17C: Force at Rear bearing. Out of - phase unbalance**

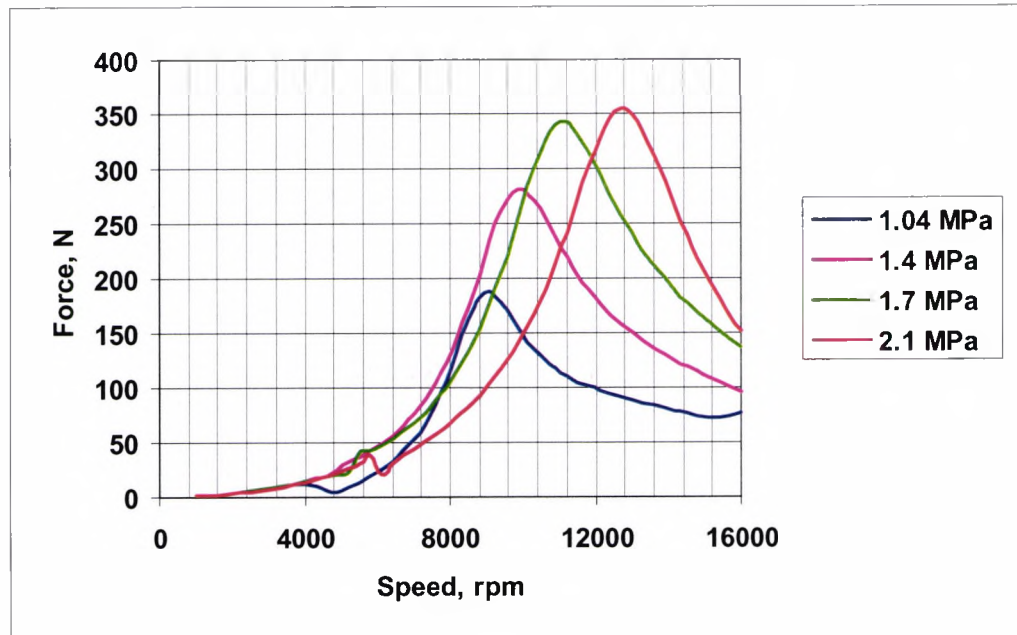


**Figure 4.17D: Force at Impeller bearing. Out of - phase unbalance**

#### **4.9. References:**

- 1) Turbomachinery Rotor dynamics  
Dara Childs
- 2) Stability and Damped Critical Speeds of a Flexible rotor in fluid-film bearings  
Lund, J. W., ASME Journal of engineering for Industry, vol 96, No 2, May 1974,  
pp 509-517
- 3) Mechanical Vibration - Balance Quality requirements of rigid rotors.  
Part 1: Determination of permissible residual unbalance  
ISO 1940/1
- 4) The mechanical balancing of flexible rotors  
ISO 5406
- 5) Centrifugal Compressors for Petrochemical Industries  
American Petrochemical Industries, API 617.
- 6) Theory Of Vibrations  
Thompson, W. T., Prentice Hall

Parameter	Nominal Clearance
Journal diameter (D), cm	3.8
Bearing length (L), cm	3.8
Bearing radial clearance, cm	0.005
Number Of Pockets	6
Pocket Depth, cm	0.02
Pocket Angle, deg	30
Land Axial Length, cm	0.76
Supply orifice diameter, cm	0.125
Shaft Vertical Position, cm	-0.0025
Supply Temperature, °C	24
Supply pressure, MPa	1.7 MPa
Exit pressure, MPa	0.35 MPa
HFC134a viscosity at 10° C, mPa.s	0.224
HFC134a Liquid density, Kg/m <sup>3</sup>	1200
Flow, lpm	15.0
Vertical Load Capacity (W), N	407
Specific Loading (W/LD)	0.282 MPa
Principal Stiffness, kN/m	18250
Cross coupled stiffness, kN/m	5500
Principal Damping, kN-sec/m	8.6
Cross coupled damping, kN-sec/m	0.29

**Table 4.1: Journal Bearing Characteristics**

**CHAPTER FOUR**  
**HYDROSTATIC BEARING TESTING**

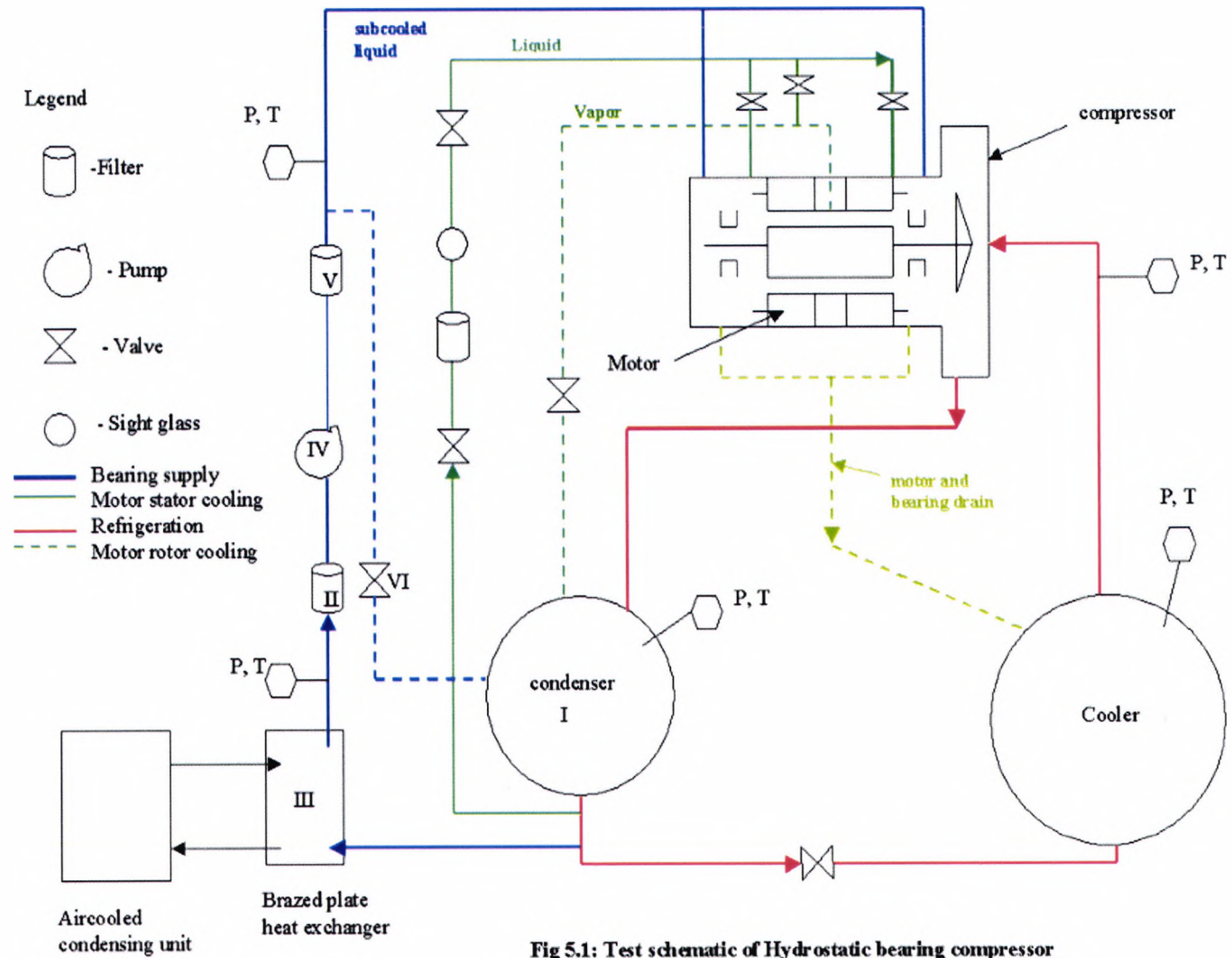
## **HYDROSTATIC BEARING TESTING**

### **5.1 Introduction**

This chapter deals with the results of vibration tests on a compressor with hydrostatic bearings. Although it was shown, in the previous chapter, that the design is marginally acceptable, a thorough understanding of the actual behaviour was deemed necessary for its validation and improvement. The tests were carried out on a 1.7MW water-cooled chiller. Their object was to correlate the vibration analysis with the measurements, specifically to determine the onset of rotordynamic instability due to the bearings. Another aim was to study the rotor response to compressor aerodynamic instability and supply pressure instability due to pump cavitation. In order to accomplish these aims, shaft vibrations were measured at stations where the clearance was lowest i.e. at the bearings and the impeller. Parts of the results of this chapter have already been presented at an international conference publication<sup>(1)</sup>.

### **5.2 Test System**

The test rig layout is shown in figure 5.1. The system consists of three refrigerant loops, one for supplying high-pressure liquid to the bearings, a second one for cooling the motor and a third one to produce chilled water. A centrifugal pump (item IV) delivers high-pressure liquid refrigerant to the bearings. The pump inlet is taken from the bottom of the condenser (item I). A filter (item II) and a heat exchanger (item III) are located upstream of the pump and downstream of the condenser. The heat exchanger, which is constructed from a series of copper coated stainless steel plates brazed together, subcools the refrigerant entering the bearings. Cold refrigerant, at 5°C, flows on one side of the plates from the air-cooled condensing system and on the other side, warm refrigerant, which leaves the condenser at 34°C, is subcooled to 10°C. The purpose of subcooling the refrigerant that is used as the lubricant is to avoid cavitation in the pump and to prevent evaporation in the bearing cavity due to any pressure drop and temperature rise due to friction.



The liquid from the pump discharge passes through a 10-micron filter (item V) before entering the bearing cavity. A refrigerant bypass valve (item VI) is used to control the bearing supply pressure. The total pressure drop from the pump to the bearings is less than 30 kPa. Refrigerant coming out of the bearings is discharged into the cooler or evaporator.

### **5.3 Instrumentation**

The principle measurements made in the test were the vibration amplitudes at the bearings and the impeller, the bearing and motor temperature and the refrigerant pressure at the pump discharge, the condenser and the cooler. A list of instruments used for making the principle measurements is given below:

<b>Name</b>	<b>Measurement</b>	<b>Make</b>	<b>Comments</b>
Displacement Probe	Measure shaft vibration	Bently Nevada	Frequency range – 10 Hz to 10 kHz, Accuracy - 2.5 $\mu\text{m}$
Iron-Constantan Thermocouple	Bearing and Motor stator temperatures	Omega, Inc	Range -50 to 200°C Accuracy - 1°C
Pressure Transducer	To measure bearing supply pressure	Viatran, Inc	Range – 0 to 3.5 MPa Accuracy - 10 kPa

The Bently-Nevada displacement probe is a non-contacting eddy current gap voltage measuring transducer and is widely used in the industry for vibration measurement. The probe is used to measure distance to any conductive material. The transducer is a flat coil of wire, located on the end of a ceramic tip. The coil is protected by 0.25 mm thick epoxy fiberglass. An RF voltage generated by the proximator drives the probe. The signal output from the proximator is a voltage proportional to the gap distance between the probe and the observed surface. The proximator requires an 18 Vdc supply. A detailed description of the probe operation, installation and readout system is given in Appendix B.

For radial vibration measurement, probes were mounted near the journal bearings and the impeller. At each axial location, two probes were installed, 90° apart in the horizontal and vertical directions. For phase angle measurement a keyphasor is required. The keyphasor is a transducer installed on a machine train to provide a voltage pulse that occurs once-per-revolution of the shaft. The keyphasor pulse provides a reference for data taken on a machine train. It is a reference mark and timer for speed and phase angle.

Due to space limitations, a keyphasor could not be mounted. The compressor speed was therefore calculated from the inverter output frequency using the formula  $120 \cdot f/P$ , where P is the number of poles. The speed given by  $120 \cdot f/P$  is known as the synchronous speed. In an induction motor, the rotor speed is less than the synchronous speed by a small percentage, which is essential for torque production. The difference between the synchronous and rotor speeds is called "slip". In a well-designed induction motor, slip varies from 0.5 to 1% of the synchronous speed. Due to the small value of the slip, it was neglected and the rotor speed was taken as the synchronous speed. In the present case where the number of poles is 2, the speed is given by 60f. Vibration data was recorded by Bently-Nevada's ADRE 208 system.

#### **5.4 Test Results**

The test procedure is outlined in appendix C. The single most important parameter for vibration measurement is the amplitude of vibration. The vibration measurement results in two orthogonal directions are presented at the front bearing, the rear bearing and the impeller. As mentioned in Section 5.3, the two directions are referred to as horizontal and vertical. Vibration measurements were carried out under steady state conditions at varying values of load, speed and supply pressure. Vibration measurements were also carried out under aerodynamically unstable operating conditions, namely those involving rotating stall. The vibration results are presented in the following format:

- 1) Spectrum plot – Fast Fourier Transform of time based signal output from the probe. This plot shows the vibration amplitude as a function of the frequency and is useful for locating the dominant frequencies.

- 2) Waterfall plot – This plot shows a succession of spectrum plots at different times. It has frequency, amplitude and time information and is useful for locating instability and resonance during start-up or coast down.
- 3) Orbit plot – This plot depicts the shaft motion and is derived from the time based signals from two orthogonal probes at a given location. It is useful to locate asymmetry in bearing stiffness. A circular orbit indicates equal stiffness in the two orthogonal directions.

## **5.5 Discussion of Test Results:**

### **5.5.1 Accuracy of test results - Effect of electrical and mechanical runout (Glitch):**

Appendix B gives a detailed account of the effect of the shaft material and temperature on the proximity probe output. For the present case, where the shaft material is steel and the temperatures are below 40°C, these two effects are not significant. The proximity probe cannot distinguish between the actual vibration and erroneous readings caused by physical and mechanical deformities in the shaft material. These erroneous readings are known collectively as glitch and are measured by rotating the shaft at slow speed where dynamic effects are negligible. At higher speeds this figure may be vectorially subtracted from the amplitude readings to give a true vibration reading. Although glitch can be electronically compensated, it is necessary to minimise it during rotor manufacture. Glitch is composed of mechanical runout and electrical runout. The specification of tight tolerances at the probe areas reduces the mechanical runout. Roller burnishing and degaussing can reduce electrical runout. In roller burnishing the probe area is rolled between hardened rollers under load for a period of 10 hours or more. Burnishing brings uniformity to the surface metallurgy. Residual magnetism in a shaft caused as a result of magnetic particle crack detection or by working in a magnetic field can produce electrical runout. A residual magnetism of 5 gauss gives an electrical runout of 12 µm. Due to time constraints, neither roller burnishing nor degaussing were carried out. The procedure of using the slow roll values to correct electronically for glitch was adopted. The following amplitude values were observed at 10 Hz:

At the Front Bearing: 45 µm

At the Rear Bearing: 45 µm

At the Impeller: 70 µm

### **5.5.2 Comparison of unbalance response amplitudes with analysis**

Figures 5.2 and 5.3 show amplitude as a function of speed at startup with 2.1 MPa supply pressure. Table (5.1) compares measured vibration parameters with calculated values based on actual unbalance presented on pages 186 to 188 in appendix A. The measured values were corrected for glitch. The main conclusions are as follows:

- 1) The critical speeds i.e the speeds corresponding to peak amplitudes, are within 15% of the calculated values. The measurements show a critical speed at 7200 rpm, which was not predicted in the analysis.
- 2) The measured amplitudes are higher than calculated response with the predicted actual unbalance. The discrepancy may be due to the combined effect of glitch, unbalance distribution, and modelling approximations.
- 3) The measured orbit in figure (5.4) shows a near circular orbit that agrees closely with the calculated ones. The circular orbit shows that the stiffness' in horizontal and vertical directions are nearly equal.

Station	Frequency (rpm)		Amplification factor		Amplitude(pk-pk), $\mu\text{m}$		
	Measured	Calculated	Measured	Calculated	Measured	Corrected	Calculated
<b>Rear Brng</b>	4300	4300	0.0	0.0	56	11	1
	5800	6100	0.0	11.3	56	11	3
	7200	no pk	5.9	no pk	51	6	no-pk
	14000	12700	3.7	3.78	64	19	13
<b>Front Brng</b>	5800	5800	0	15.26	52	7	3
	7200		4.5		50	5	
	12200	13000	0.0	3.58	46	1	20
<b>Impeller</b>	5800	5200	0	9.82	100	30	3
	7100		0	No pk	89	19	No pk
	12000	13000	2.55	3.33	140	70	33

Table 5.1: Measured vs calculated response values (actual unbalance calculations)

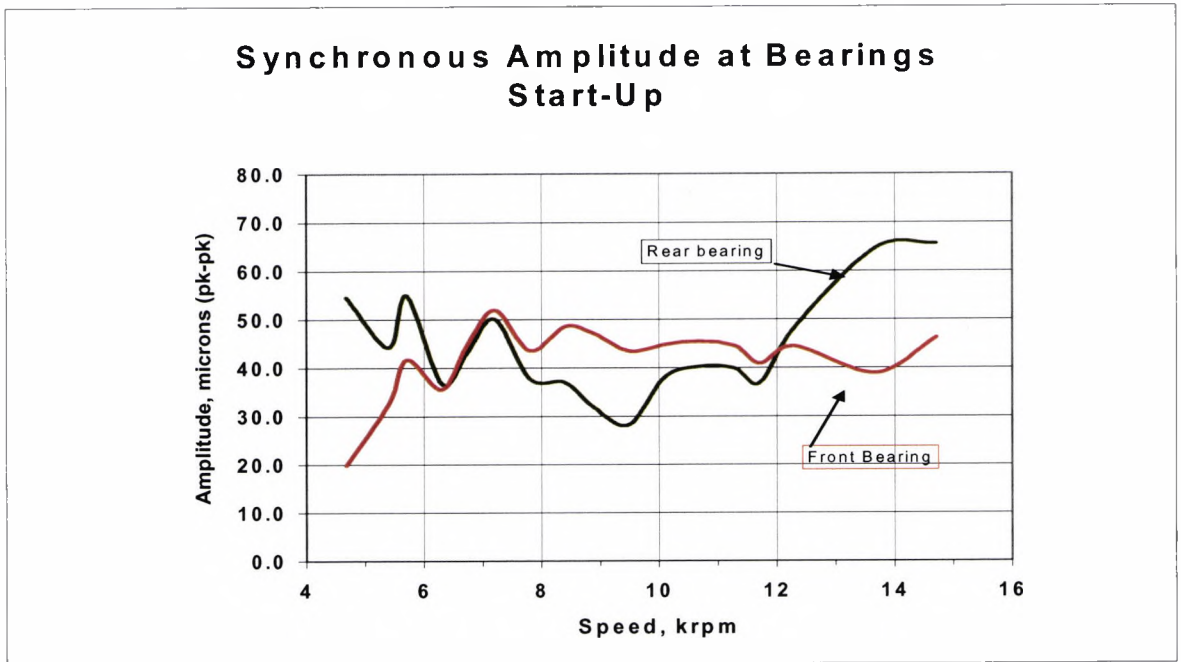


Fig 5.2: Measured rotor synchronous amplitude at bearings  
 - supply pressure 2.1 Mpa

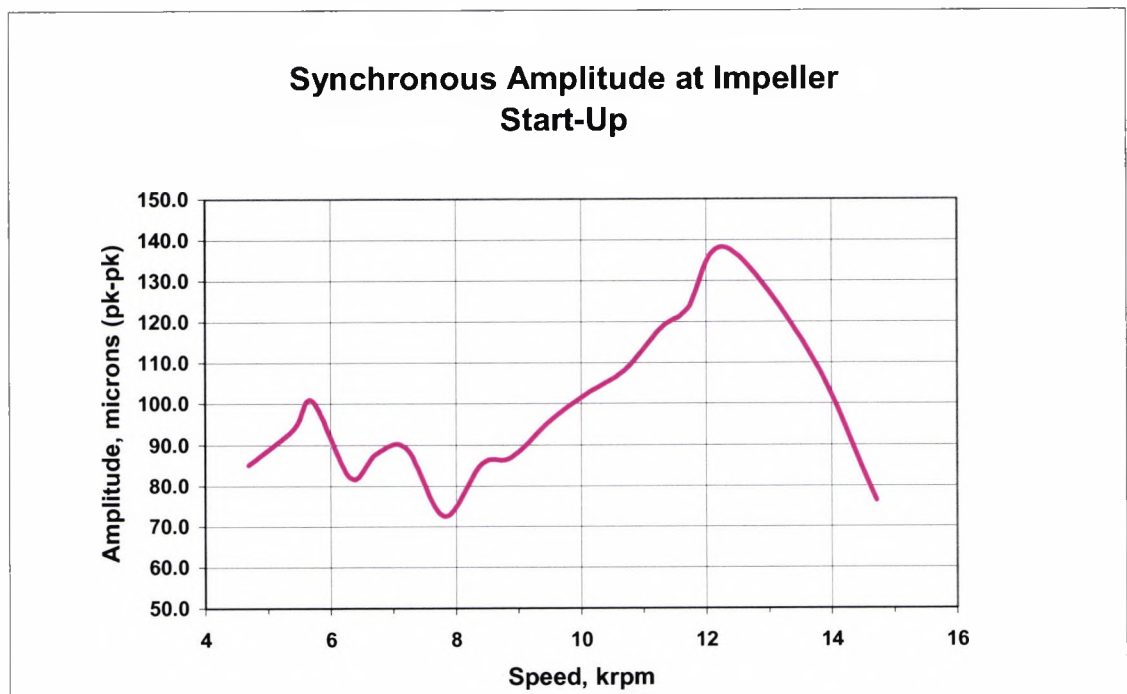


Fig 5.3: Measured rotor synchronous amplitude at impeller  
 - supply pressure 2.1 MPa

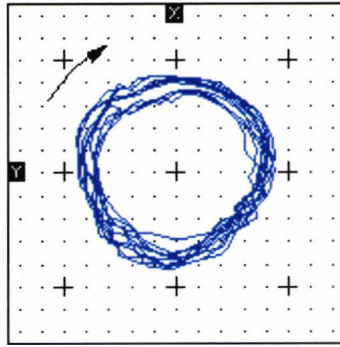


Fig 5.4 Shaft orbit near Impeller during steady state, 13200 rpm.  
scale, 25.4 microns/div

**5.5.3. Rotor Response as a function of Compressor Capacity:** The object of this test was to find out if there is an additional radial load, due to gas pressure on the impeller, acting on the bearings. Figures 5.5a and 5.5b show a spectrum plot of vibrations at the front bearing in the horizontal, X and vertical Y directions, as a function of compressor capacity at 12600 rpm and a supply pressure of 2.1 MPa. The results do not show a change in amplitude or frequency of the vibration with increase in load. The amplitude at 210 Hz is nearly equal both in the horizontal and the vertical directions, which shows that the stiffness is also nearly equal in both directions. Since, the amplitude did not change with the compressor load, it can be concluded that the higher compressor load does not change the load on the bearing. This is because the supply pressure and unbalance are the same at all three compressor loads and the vibration amplitude is a function of the bearing load, in addition to the supply pressure and unbalance. Note that the bearing load determines the dynamic properties which in turn determines the vibration amplitude. Hence, the bearing load should be the same for all three compressor load cases.

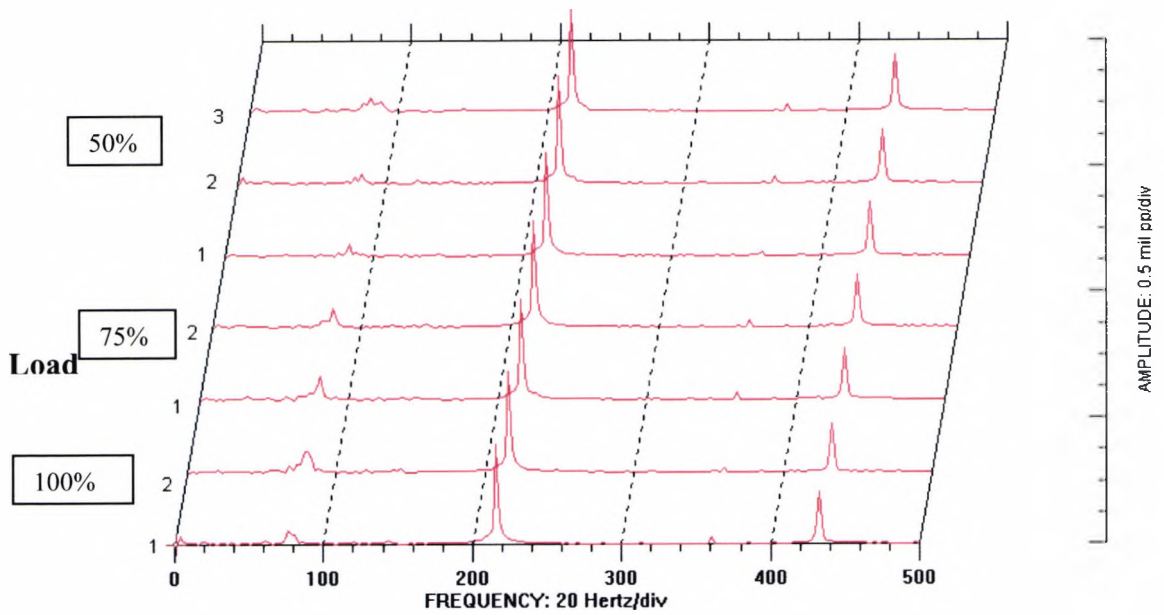


Fig 5.5a: Front bearing Horizontal vibration spectrum as a function of load  
 Speed 12 600 rpm, Supply pressure = 2.1 MPa  
 Y axis in mils pk-pk (1mil=25.4 microns)

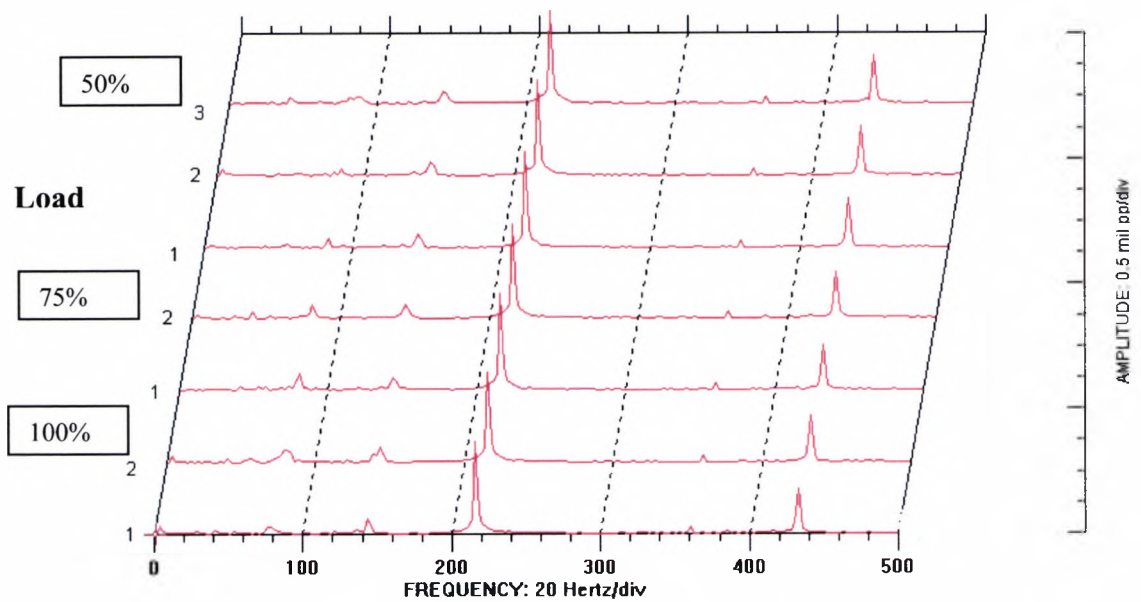


Fig 5.5b : Front bearing Vertical vibration spectrum as a function of load  
 Speed 12 600 rpm, Supply pressure = 2.1 MPa  
 Y axis in mils pk-pk (1mil=25.4 microns)

**5.5.4 Rotor Response due to Aerodynamic instability:** The rotor response was also measured under unstable operating conditions. The important instability in a centrifugal compressor is stall, a brief description of which is given below.

**Stall** occurs due to flow separation either in the diffuser or the impeller. In compressors with vane or pipe diffusers, separation occurs in the diffuser as the flow is decreased. Separation in a pipe blocks flow in that passage, resulting in excessive incidence in the adjacent pipe, which in-turn is blocked. The stalling of diffuser passages moves around the diffuser at 10 to 25% of the impeller rotating speed. The stall phenomenon is therefore referred to as rotating stall. Hence for the present compressor at 12600 rpm impeller speed, the rotating stall cell frequency should be 21 to 52 Hz.

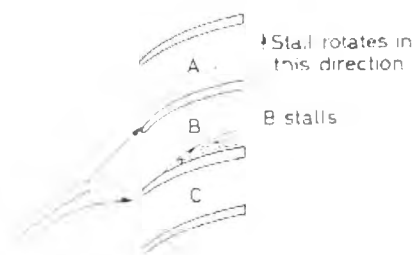


Fig 5.6: Rotating stall

#### Discussion of rotating stall

Vibration amplitude measured in rotating stall conditions, at a supply pressure of 2.1 MPa and 12600 rpm, are presented at the impeller in figures 5.7, 5.8 A and 5.8B. Similar results at the bearing locations are given in appendix D. The appearance of 42 Hz frequency during the instability shows the presence of stall. In addition to the presence of 42Hz frequency, there is also a strong 84 Hz frequency component present during rotating stall. 42 Hz is the primary or fundamental frequency of rotating stall and its second harmonic is at 84 Hz. The vibration amplitude at 84 Hz was higher than at 42 Hz. It is difficult to calculate the net radial force at the impeller tip resulting from aerodynamic effects during rotating stall. The measured vibration amplitude at stall frequency can be used to determine the magnitude of rotating stall force. The force is calculated by carrying out an asynchronous rotor response with a known forcing frequency of 84 Hz. The magnitude of the force is varied until the vibration amplitude at the impeller and bearings closely matches the

measured response. Using the above method, the stall force was calculated as 550 N. The force component due to the 42 Hz frequency can also be determined using the above procedure.

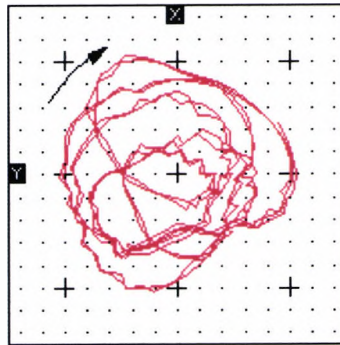


Fig 5.7: Shaft orbit near impeller during Stall, 12600 rpm, scale, 1mil/div.  
Supply pressure =2.1 MPa (1mil=25.4 microns)

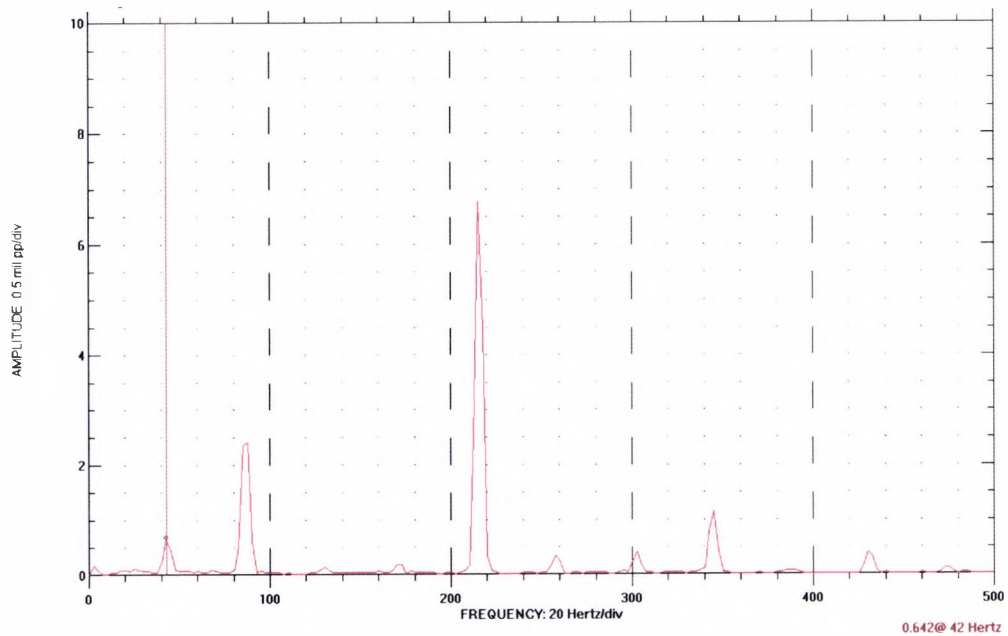


Fig5.8A: Spectrum Plot during stall, Y-direction, at Impeller.  
Supply pressure 2.1 MPa  
Y axis in mils pk-pk (1mil=25.4 microns)

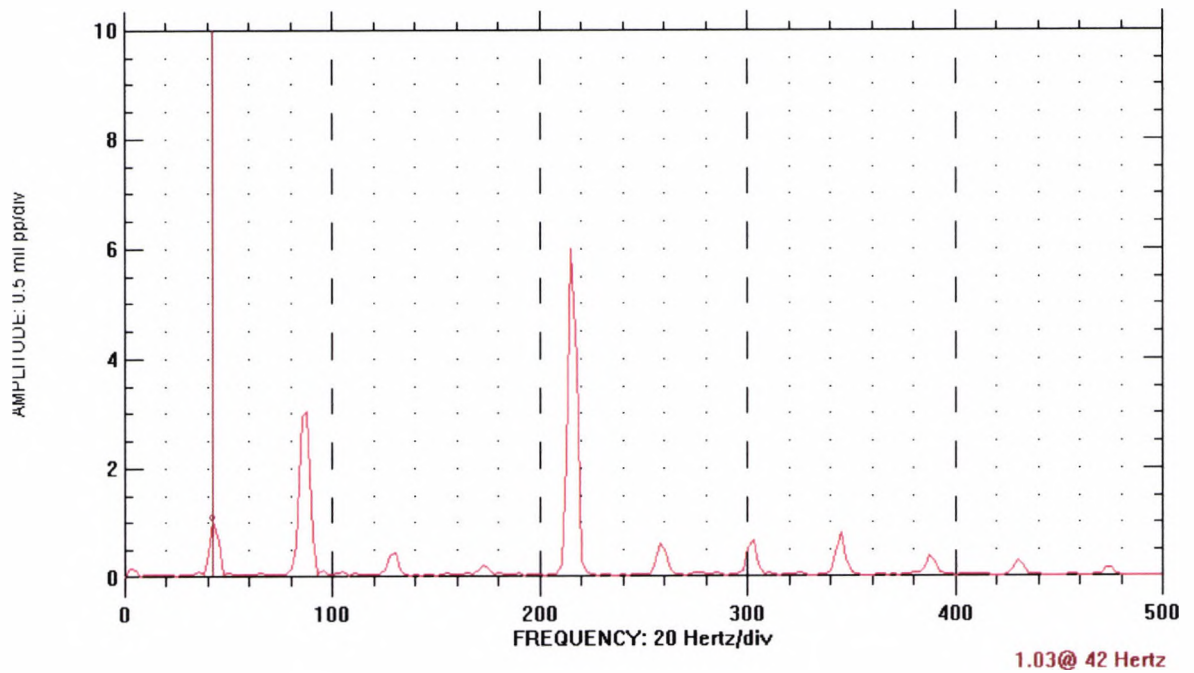


Fig5.8B: Spectrum Plot during stall, X-direction, at Impeller.  
 Supply pressure =2.1 MPa  
 Y axis in mils pk-pk (1mil=25.4 microns)

**5.5.5 Verification Of Rotor-Bearing Stability:** It was concluded, from the rotordynamic stability analysis in chapter 4, that the compressor is marginally stable but the stability deteriorates with decrease in supply pressure or increase in speed. The stability analysis was not capable of determining whether the amplitude of vibration is limited or increases without bounds. It therefore needs to be resolved whether or not the compressor can operate in the “unstable” region with a steady limited amplitude of vibration. This is now considered.

**5.5.6 Effect Of Speed on Rotor-Bearing Stability:** Fig 5.9 shows a waterfall plot of amplitude vs frequency at the front bearing as the speed varies during start up. Waterfall plots at the rear bearing and the impeller are given in appendix D. Data was taken with a lubricant supply pressure of 2.1 MPa. Note that the speed at the time intervals shown on the Y-axis is calculated from the 1X vibration frequency corresponding to the lowest vibration peak. The sub synchronous peak appears momentarily at 210 Hz (12600 rpm) before becoming strong at 243 Hz (14500 rpm). The ratio of sub synchronous to synchronous frequency is close to 0.5. The trend is the same at the rear bearing and the impeller except in magnitude. The compressor

was run at steady state at speeds of 12600 rpm to 13200 rpm to investigate the presence of instability.

Figures 5.10 and 5.11 show the spectrum plot at the front bearing during steady state operation at a lubricant supply pressure of 2.1 MPa and compressor speeds of 13200 and 12600 rpm. The sub synchronous frequency occurs at 80 Hz and the ratio of sub synchronous to synchronous frequency is 0.38. The frequency stayed at 80 Hz when the speed was increased to 13200 rpm. The amplitude was below 0.5 mil pk-pk (12.5  $\mu\text{m}$ ) at 12600 rpm and increased when the speed was increased to 13200 rpm. The compressor ran for 30 minutes at 12600 rpm without any increase in amplitude. Similar trends were observed at the rear bearing and the impeller. These results are shown in Appendix D.

The predicted whirl frequency was 99 Hz whereas that observed was 80 Hz. The difference between these values is due to inaccuracies in the calculation of bearing stiffness and damping coefficients. Though the discrepancy between the predicted and observed frequency is outside the range of 10% found in machines with hydrodynamic bearings, the ratio of observed frequency to operating speed is within typical values of 0.35 to 0.46 reported in literature for rotating equipment. The analysis did not reveal any change in the whirl frequency or logarithmic decrement value with decrease in speed. However, the experimental results show a decrease in amplitude with decrease in speed without any subsynchronous frequency below 12000 rpm.

Machining tolerances introduce misalignment in the bearings, which create a non-uniform air-gap between the motor rotor and the stator. This results in the generation of unbalanced magnetic forces which caused the 2X vibration shown in figures 5.9a and 5.9b.

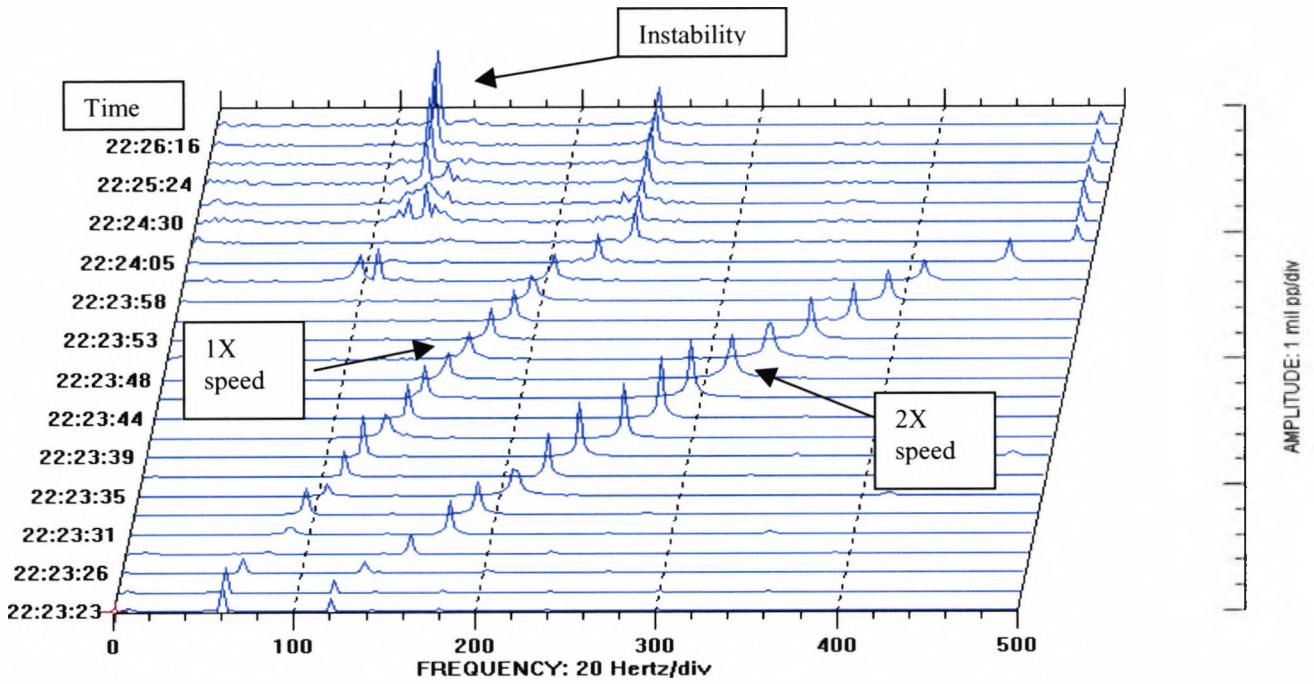


Fig 5.9A: Front Bearing, X – direction. Start Of Instability at 240 hz (14400 rpm).  
Supply pressure = 2.1 MPa. Y axis in mils pk-pk (1mil=25.4 microns)

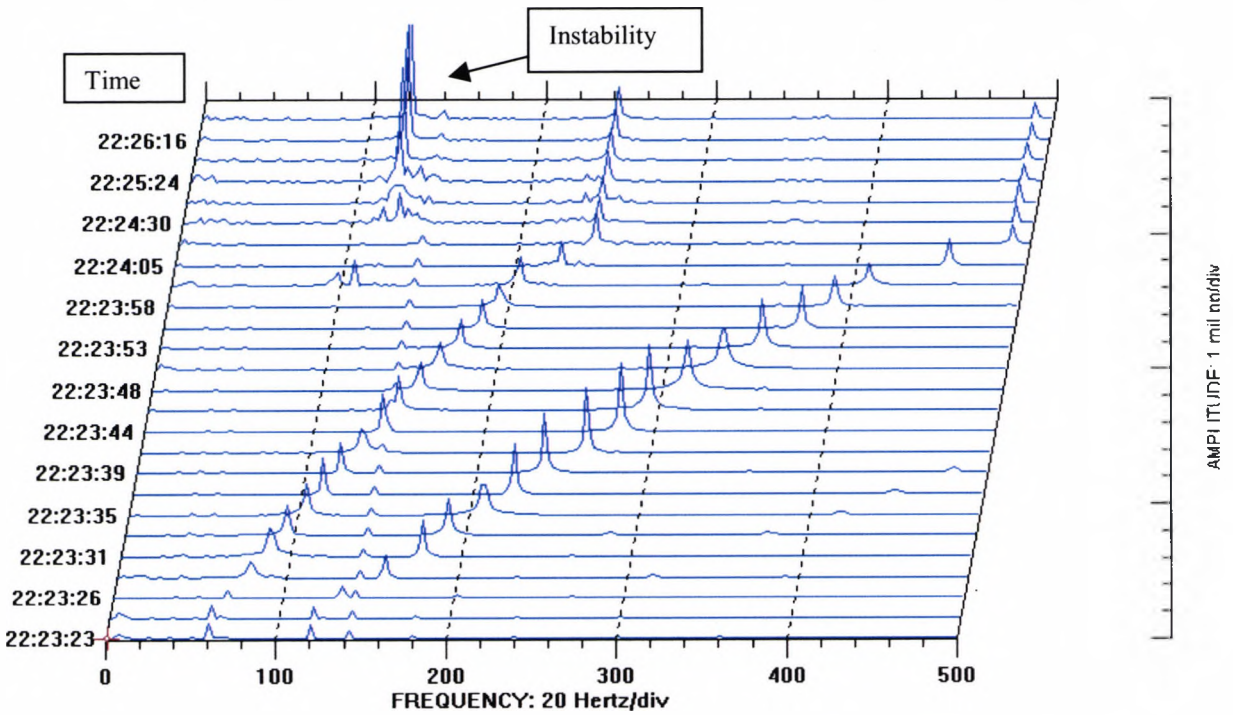
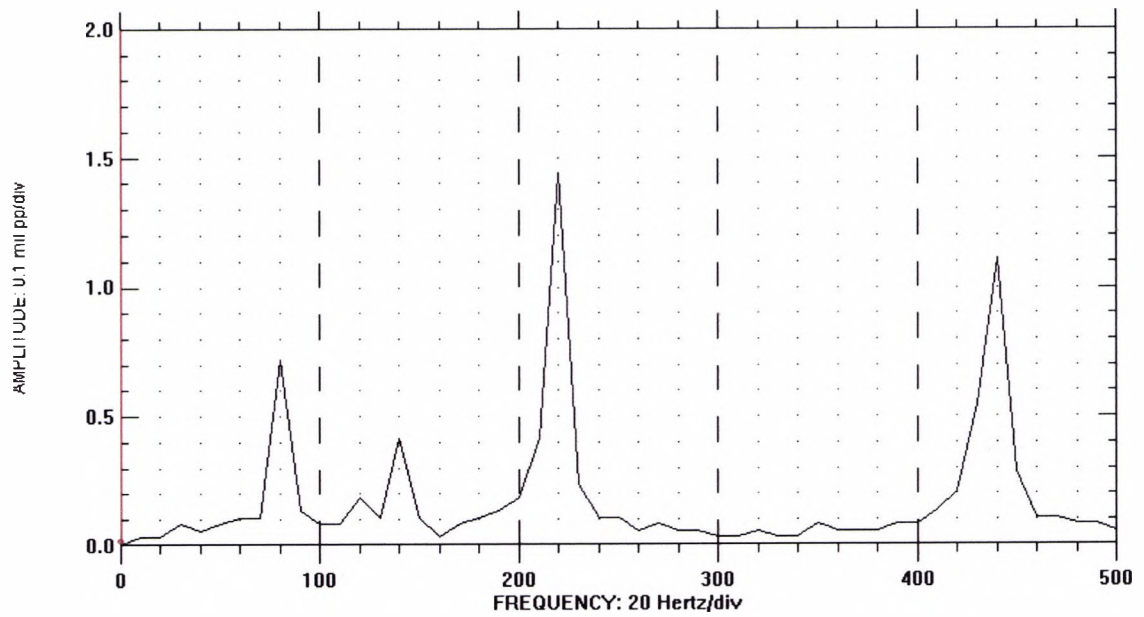
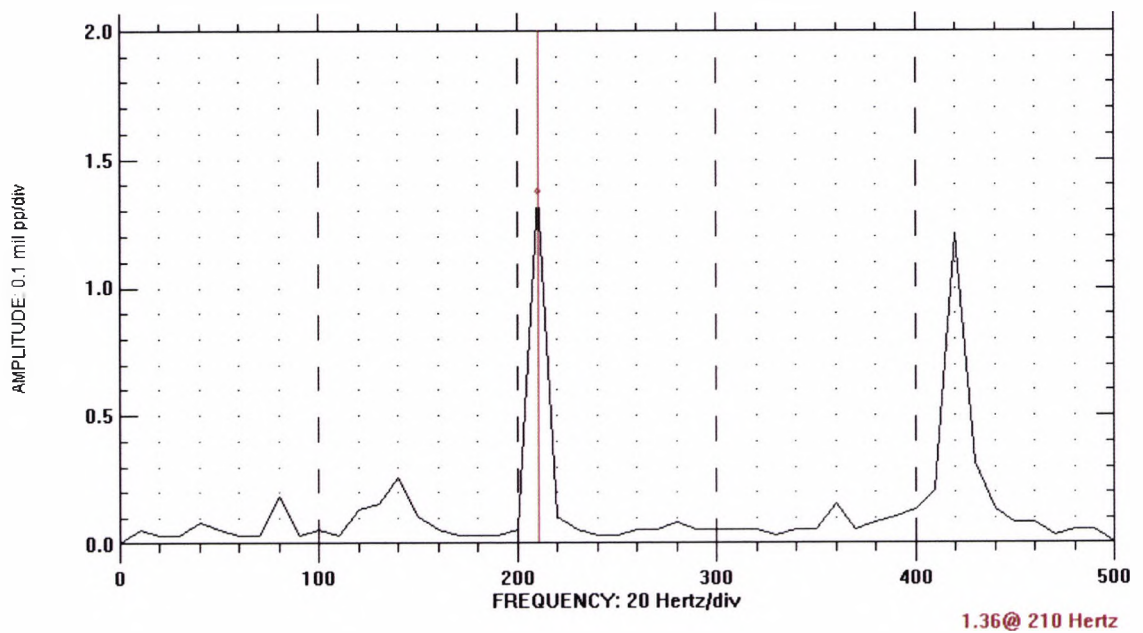


Fig 5.9B Front Bearing, Y – direction. Start Of Instability at 240 Hz (14200 rpm).  
Supply pressure = 2.1 MPa. Y axis in mils pk-pk (1mil=25.4 microns)



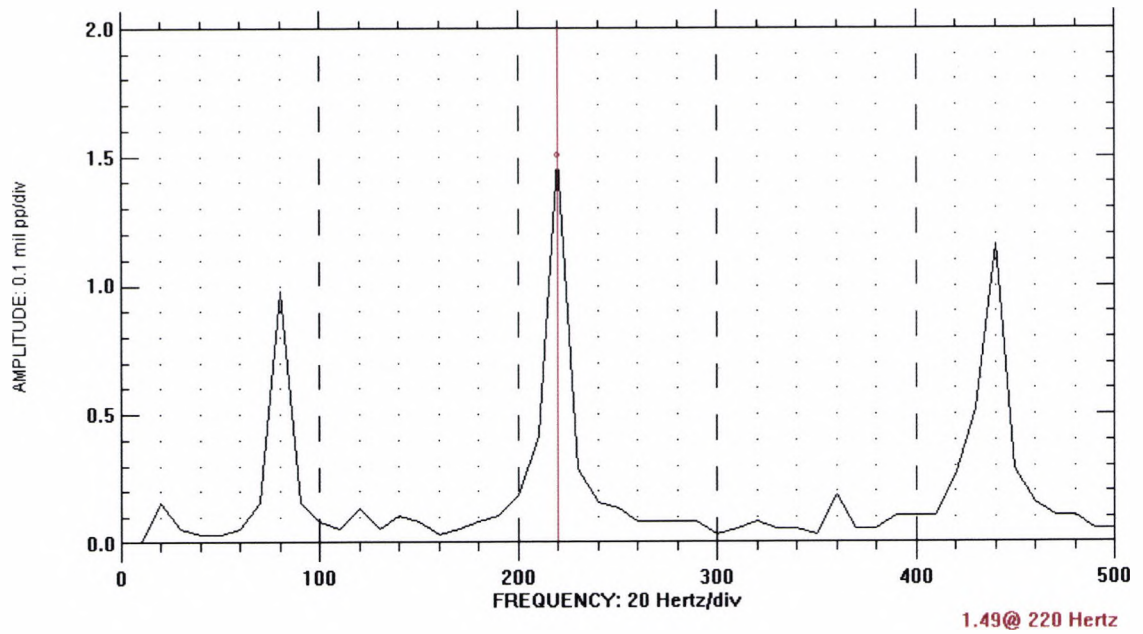
**Speed = 13200 rpm**

Fig 5.10A Subsynchronous Vibration – As a function of speed.  
 Supply Pressure = 2.1 MPa  
 Front bearing X-dir. Y axis in mils pk-pk (1mil=25.4 microns)



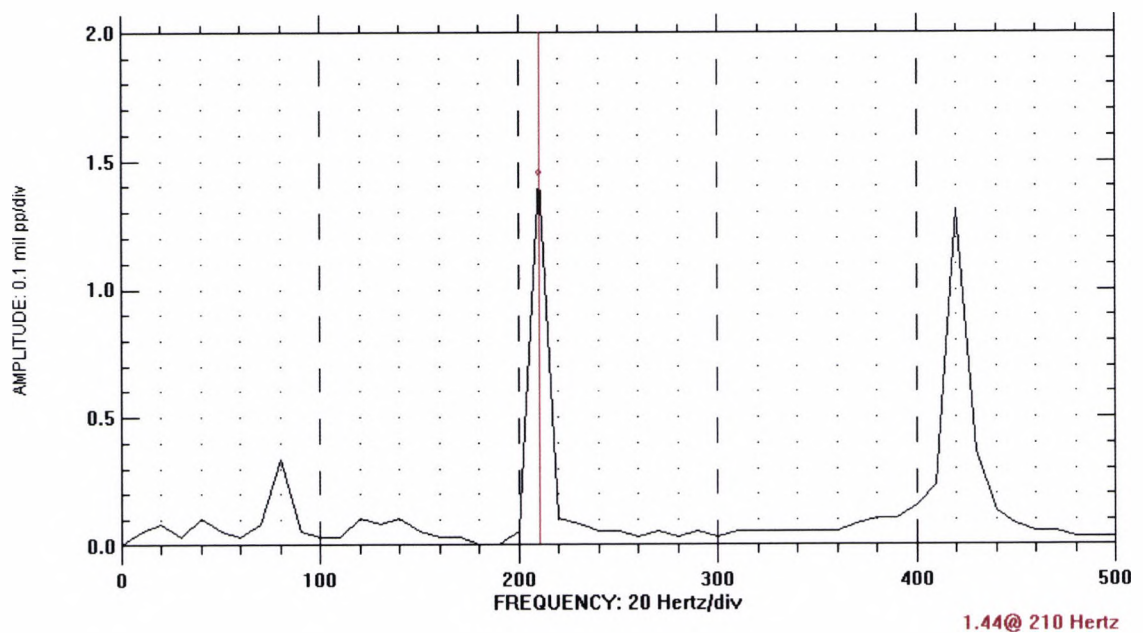
**Speed = 12600 rpm**

Fig 5.10B: Subsynchronous Vibration – As a function of speed.  
 Supply Pressure = 2.1 MPa  
 Front bearing X-dir. Y axis in mils pk-pk (1mil=25.4 microns)



Speed = 13200 rpm

Fig 5.11A: Subsynchronous Vibration – As a function of speed. Supply Pressure = 2.1 MPa  
Front bearing Y-dirn. Y axis in mils pk-pk (1mil=25.4 microns)



Speed = 12600 rpm

Fig 5.11B: Subsynchronous Vibration – As a function of speed. Supply Pressure = 2.1 MPa  
Front bearing Y-dirn. Y axis in mils pk-pk (1mil=25.4 microns)

**5.5.7 Effect of Supply Pressure on Sub Synchronous Amplitude:** Analytical predictions showed that the forward whirl instability frequency increases as the supply pressure is decreased. However, tests showed equal whirl instability frequency at 2.1 MPa and 1.7 MPa. Also, the logarithmic decremental value was predicted to decrease as the supply pressure is decreased, thus increasing the instability amplitude. The spectrum plots at 12600 rpm and supply pressure of 1.7 MPa are given in Appendix D. The table below compares the sub synchronous (80 Hz) vibration amplitude at 1.7 and 2.1 MPa. A three to six fold increase in amplitude is seen for the lower supply pressure. The vibration amplitudes at 1.7 MPa are unacceptable since they are more than the bearing minimum film thickness of 25.4 microns.

Position	Supply pressure	
	2.1 MPa	1.7 MPa
Front bearing, X	5.1	40.6
Front bearing, Y	7.6	33.
Rear bearing, X	5.1	16.5
Rear bearing, Y	5.6	16.5
Impeller, X	10.2	45.7
Impeller, Y	8.9	45.7

Table 5.2: Vibration Amplitude (peak to peak in microns) due to whirl instability as a function of supply pressure

**5.5.8 Rotor Response due to unsteady supply pressure (Pump cavitation):**

Vibration amplitudes were measured for the case when the supply pressure is unsteady due to cavitation. Figure 5.12 shows the supply pressure pulsations due to cavitation. The corresponding vibration spectrum at the front bearing before and during cavitation at 12600 rpm is shown in figures 5.13A and B. Sub synchronous vibration at 42, 84, 126 and 168 Hz can be seen. The amplitude at 84 Hz frequency is the dominant one and this frequency is close to that of whirl instability frequency of 80 Hz. During cavitation, the supply pressure is reduced thereby reducing stiffness and damping which, in turn, triggers whirl instability.

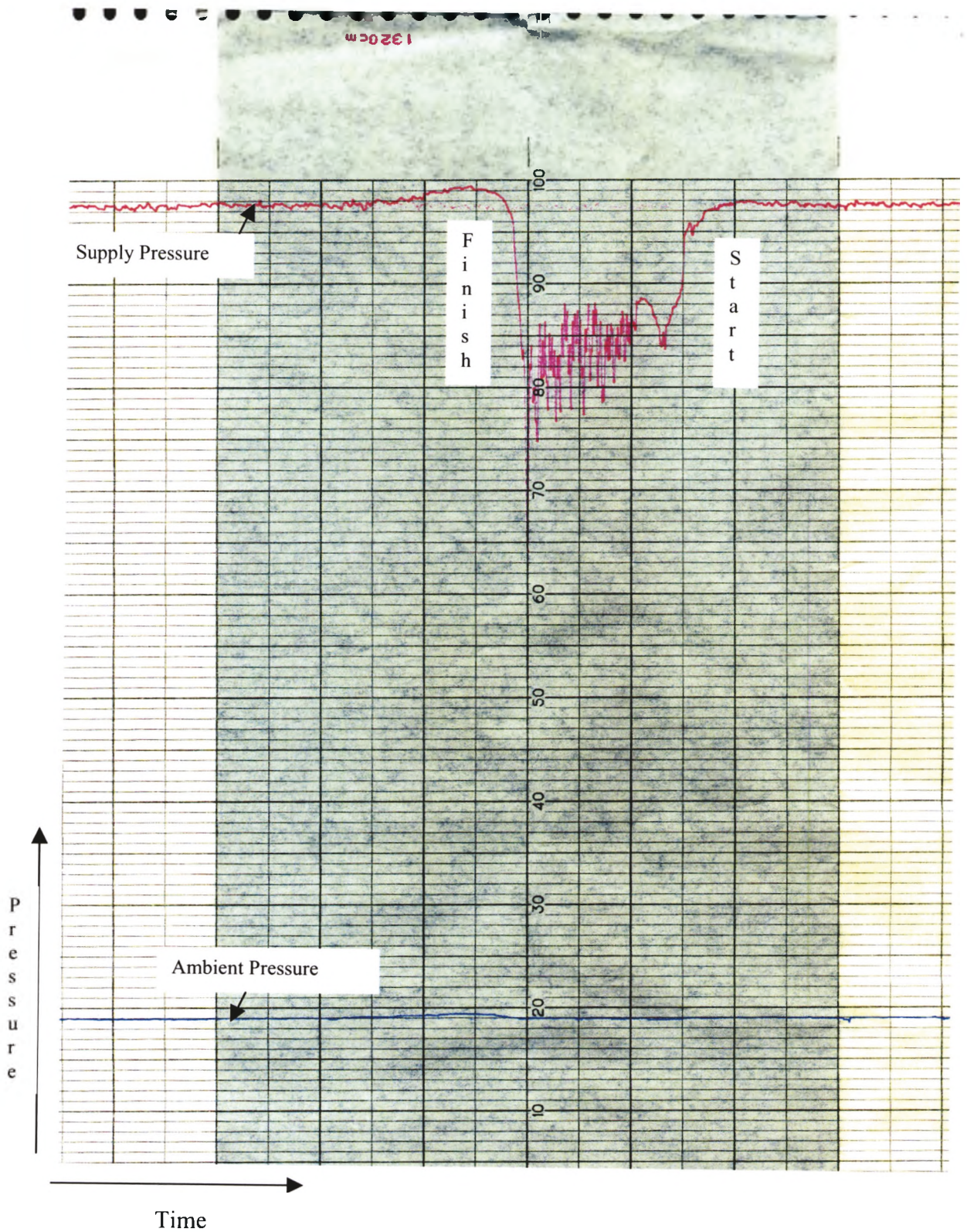


Fig 5.12: Supply Pressure During Pump Cavitation  
 Scale: Pressure - 1 div = 20 kPa  
 Time - 1mm = 3 seconds

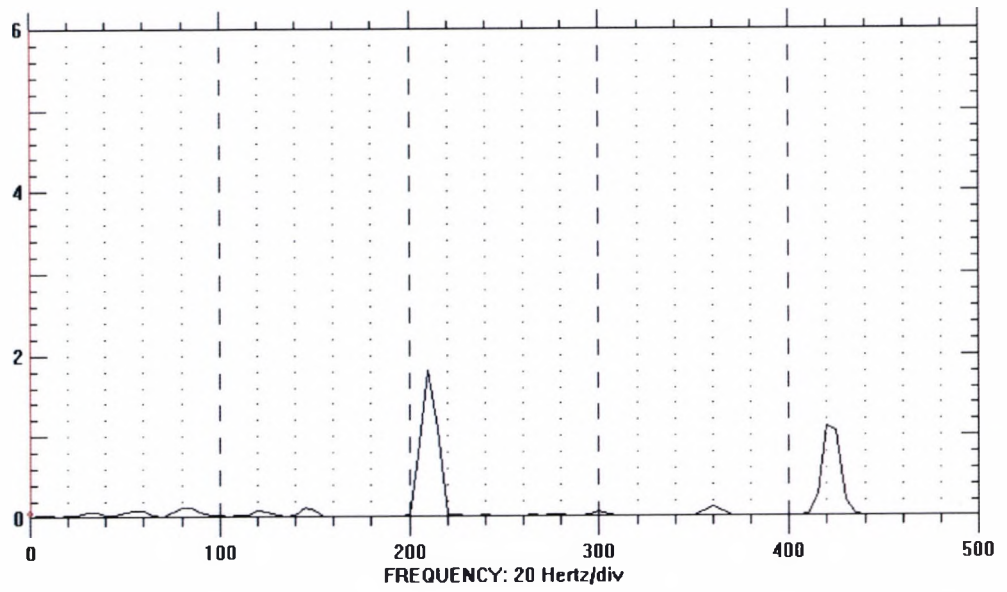


Fig 5.13A: Vibration at Front bearing, X direction before supply pressure instability due to pump cavitation

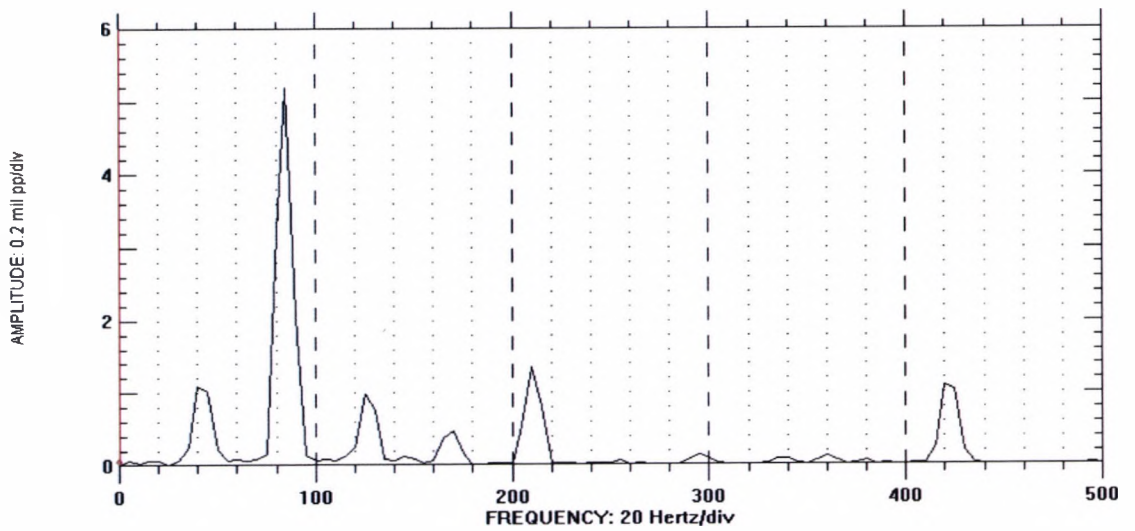


Fig 5.13B: Vibration at Front bearing, X direction - during supply pressure instability due to pump cavitation

## **5.6 Conclusions**

A hydrostatic bearing system for a low viscosity lubricant was designed and tested in an oil free centrifugal chiller. The effect of lubricant supply pressure on bearing stiffness and damping properties was determined analytically. The effect of stiffness and damping properties on the rotordynamic behaviour was studied analytically. Vibration measurements at the impeller and front bearing showed three critical frequencies whereas the calculations predicted only two critical frequencies. At the rear bearing, the measurements showed four critical frequencies whereas calculations predicted only three critical frequencies. The magnitude of the calculated frequencies is within 10% of the measured values.

As for as rotordynamic instability is concerned, the analysis predicted marginal stability at a supply pressure of 2.1 MPa and at all speeds, ranging from 1000 to 15000 rpm. However, tests have not shown any subsynchronous frequencies below 12600 rpm. Above 12600 rpm, the subsynchronous amplitude increased with speed. The vibration amplitudes attained a stable value and did not increase with time. Supply pressure plays an important role in the vibration behaviour of the rotor as it controls the bearing dynamic properties. The minimum acceptable supply pressure is 2.1 MPa. Pump cavitation results in a unsteady supply pressure and the average value of the supply pressure is low. The lower supply pressure induces whirl instability. The unsteady pressure pulsations result in lower and harmonic vibrations. The ratio of supply pressure 2.1 MPa required for stability to bearing specific loading of 0.282 MPa given in table 4.1 is 7.5.

Overall, the hydrostatic bearing system proved to be an acceptable solution for refrigerant lubricated bearings.

## **5.7 References:**

- 1) **V. M. Sishtla**, *Design and testing of an oil-free centrifugal water-cooled chiller*

IMechE, International Conference on Compressors and their systems  
Sept 1999, City University, London, UK, pp 505-522

## CHAPTER SIX

### REFRIGERANT LUBRICATED HYDRODYNAMIC BEARINGS

#### 6.1 Introduction

The previous two chapters have shown that hydrostatic bearings can be used with a low viscosity fluid. However, the auxiliary system of pump, filter and air-cooled condensing unit for subcooling makes the use of a hydrostatic bearing system expensive. As an alternative, the possibility of using a refrigerant lubricated hydrodynamic bearing is investigated in this chapter.

Figure 6.1 shows a hydrodynamic bearing with a circular shaft positioned eccentrically in a housing, such that the clearance varies around the circumference. In this case, an external pump is not needed to develop pressure in the clearance between the shaft and the housing. The pressure in a hydrodynamic bearing is generated by two events. Firstly, the rotating shaft sweeps fluid into a converging region between the shaft and the housing through the action of viscous shear forces. The local velocity profile from this effect is the Couette profile,

$$u = Uy/h, \dots\dots (6.1)$$

$$0 \leq y \leq h$$

where  $u$  is the velocity at a distance  $y$  from the housing,  $U$  is the surface velocity of the shaft and  $h$  is the clearance between shaft and housing. Both  $y$  and  $h$  are measured radially.

Note that the clearance,  $h$ , varies around the circumference of the bearing. A local flow rate due to the Couette motion is given as,

$$Q_c = \frac{1}{2} Uh \dots\dots (6.2)$$

The flow would be large where  $h$  is large and small where  $h$  is small. However, continuity demands that the overall flow rate be constant. Hence, the flow sets up a pressure gradient to supply a Poiseuille component that redistributes the fluid and maintains a constant flow rate. The positive pressure created in the converging region results in a net force on the shaft that will support load applied on the shaft. In the region downstream of 'a-a', the clearance increases and the pressure

decreases. In a refrigerant compressor, cavitation can occur in that case. The lubricating oil in a refrigerant compressor contains roughly 5 to 10% by volume of dissolved HFC134a, depending on the sump pressure and the oil temperature. If the oil pressure downstream of 'a-a', reduces below the sump pressure this dissolved gas tends to come out of solution as bubbles.

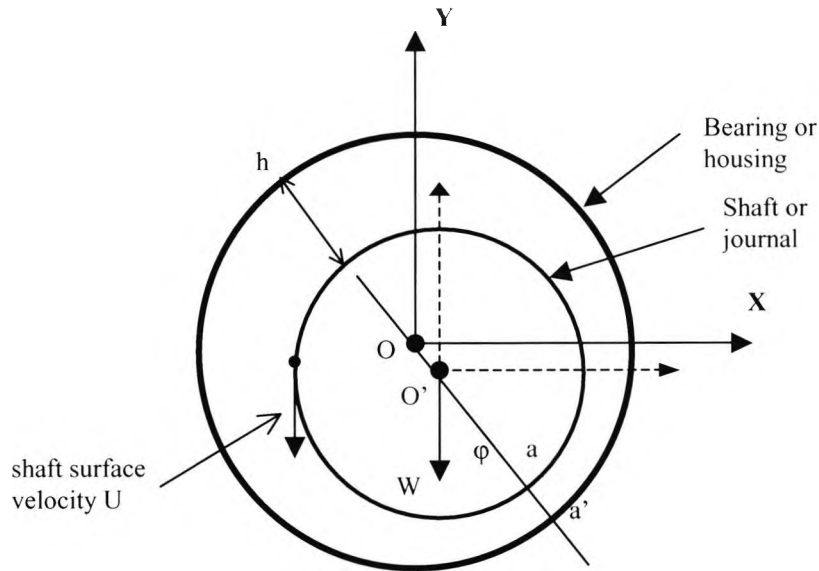


**Fig 6.1: Bearing nomenclature**

O = Bearing center, O' = Shaft center, h= clearance  
 $\phi$  = attitude angle, OO' = eccentricity = e, W= bearing load  
c = radial clearance with shaft concentric in the housing  
eccentricity ratio =  $e/c$

The lubricant pressure at the sump needs to be higher than the bearing inlet pressure to overcome the pressure drop in the piping. In a refrigeration system, the condenser pressure is higher than the evaporator pressure. By maintaining the bearing inlet pressure at slightly higher than the evaporator pressure, the pressure differential between the condenser and the evaporator can be used to supply the lubricant instead of an external pump. To avoid cavitation in the bearing, the lubricant is cooled by circulating it through the evaporator. A lubrication system diagram for refrigerant lubricated hydrodynamic bearing is shown in figure 6.2.

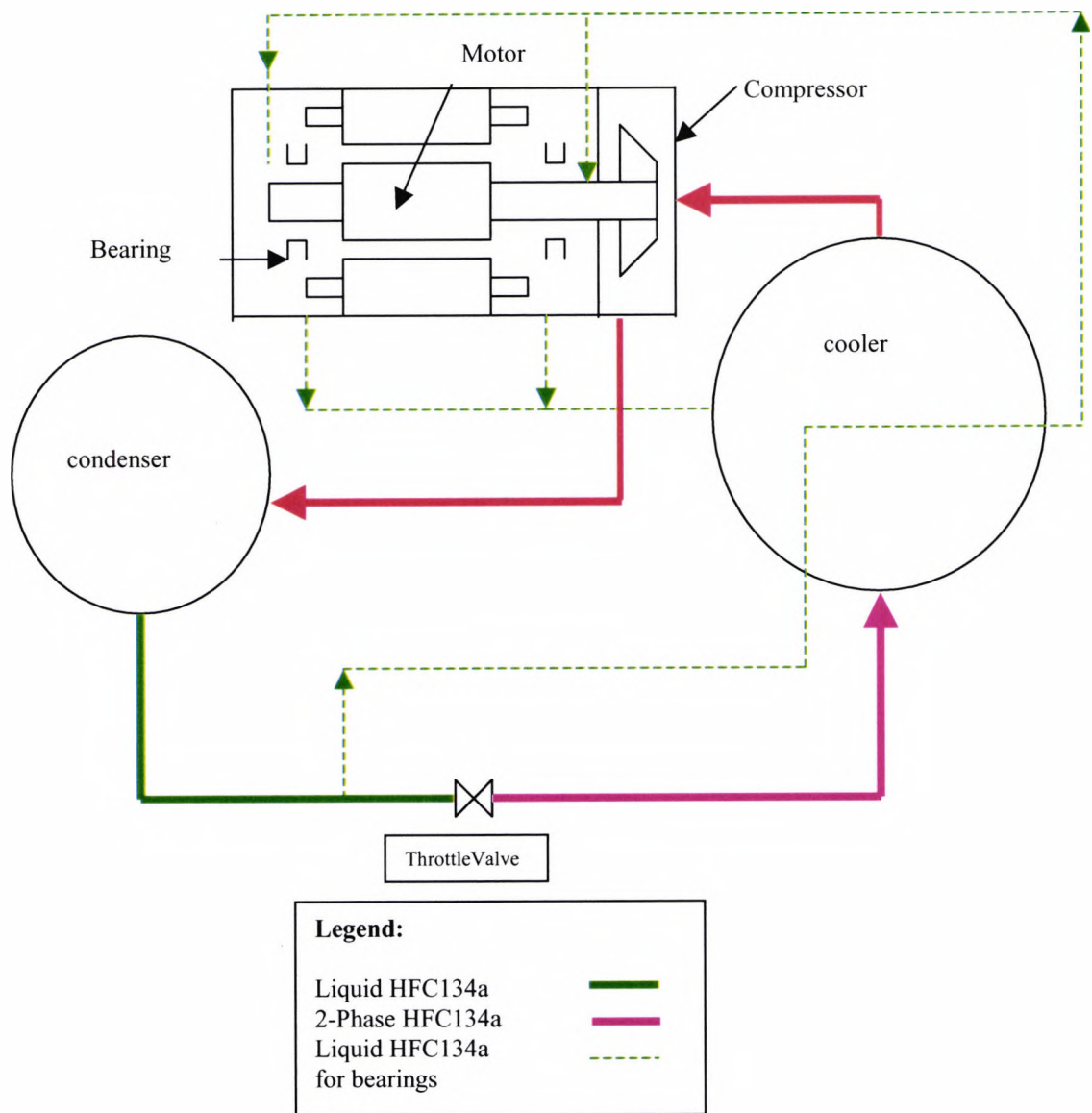


**Fig 6.2: Hydrodynamic Bearing Lubrication System**

The low viscosity of refrigerant can result in either a vortex or turbulent flow as discussed in chapter 3. The Reynolds's number based on clearance is given as:

$$Re = \frac{V C_r \rho}{\mu} \dots\dots\dots (6.3)$$

The Reynolds number and Taylor number are calculated for a bearing diameter of 50 mm, radial clearance of 0.0762 mm and HC134a viscosity of 0.224 cP. Using equation (3.3) in chapter 3, the speed corresponding to a critical Taylor number of

41.2 is 816 rpm. The speed corresponding to a Reynolds number of 2000 is 2492 rpm. Hence, Taylor vortices appear above 816 rpm and degenerate into turbulence at a speed of 2492 rpm. The Reynolds number at 14500 rpm for a synthetic oil lubricant Castrol SW32 and HFC134a lubricant is given below in Table 6.1:

Lubricant	Density kg/m <sup>3</sup>	Viscosity mPa.s (cP)	Reynolds number
Castrol SW32	900	22	116
HFC134a	1050	0.224	13344

**Table 6.1: Lubricant properties**

The above table shows that an oil lubricated bearing operates in the laminar flow regime and a HFC134a lubricated bearing operates in turbulent regime. The rest of the chapter presents a brief description of the analysis of turbulence in bearings and results are presented to show the effect of turbulence on load carrying capacity and dynamic characteristics.

The lubrication equation, also known as Reynolds equation, is a combination of the continuity and the Navier-Stokes equation with the assumption that the flow takes place in thin layers. The Reynolds equation for laminar case is shown below, while its derivation is given in appendix E.:

$$\frac{\partial}{\partial x} \left( \frac{h^3}{12\mu} \frac{\partial p}{\partial x} \right) + \frac{\partial}{\partial z} \left( \frac{h^3}{12\mu} \frac{\partial p}{\partial z} \right) = \frac{U}{2} \frac{\partial h}{\partial x} \dots\dots\dots (6.4)$$

**6.2 Turbulent Reynolds Lubrication Equation**

Turbulent flows have irregular fluctuations of velocity in all three directions. The intensity of the fluctuations is variable, but is customarily 10% or less of the mean velocity. In confined flows, turbulence may grow to cover the entire flow. Another characteristic of turbulent flows is that they entrain non-turbulent fluid, so that the extent of the turbulent region grows. The time averaged continuity and Navier-Stokes equations govern the turbulent flows. The resulting equations are derived by decomposing the velocity and pressure in the continuity and Navier-Stokes equations into time mean and fluctuating components and then time averaging them all. A

brief description of the above steps to obtain continuity and momentum equations for turbulent flow if given in Appendix F. Using the assumption that flow takes place in thin layers, the Navier–Stokes equation takes the following form:

$$\begin{aligned} \frac{\partial \bar{p}}{\partial x} &= \mu \frac{\partial^2 \bar{u}}{\partial y^2} + \frac{\partial}{\partial y}(-\rho \overline{u'v'}) \\ \frac{\partial \bar{p}}{\partial y} &= -\frac{\partial}{\partial y}(-\rho \overline{v'^2}) \quad \dots\dots\dots (6.5) \\ \frac{\partial \bar{p}}{\partial z} &= \mu \frac{\partial^2 \bar{w}}{\partial y^2} + \frac{\partial}{\partial y}(-\rho \overline{w'v'}) \end{aligned}$$

where  $\bar{u}, \bar{v}, \bar{w}$  are time averaged mean velocities and  $u', v', w'$  are the fluctuating components of velocity in the x, y and z directions and their time averaged products  $\overline{u'v'}, \overline{v'^2}, \overline{w'v'}$  the turbulent stresses. If these turbulent stresses are known, the pressure profile in the clearance region can be obtained by combining the continuity equations with the above momentum equations. Elrod and Ng<sup>(1)</sup> have used the law of wall and eddy diffusivity for the calculation of turbulent stresses. They obtained the following turbulent Reynolds equation in cartesian coordinates:

$$\frac{\partial}{\partial x} \left( \frac{h^3}{\mu} G_x \frac{\partial p}{\partial x} \right) + \frac{\partial}{\partial z} \left( \frac{h^3}{\mu} G_z \frac{\partial p}{\partial z} \right) = \frac{U}{2} \frac{\partial h}{\partial x} \quad \dots\dots\dots (6.6)$$

The derivation of the above equation is given in appendix F. Note that the above equation is similar to the laminar flow equation (6.4) with the additional factors  $G_x$  and  $G_z$  that are a function of Reynolds number based on film thickness. The values of  $G_x$  and  $G_z$  are given as:

$$\begin{aligned} \frac{1}{G_x} &= 12 + 0.0136(\text{Re})^{0.90} \\ \frac{1}{G_z} &= 12 + 0.0043(\text{Re})^{0.96} \end{aligned}$$

### **6.3 Analysis of Turbulence in the Bearing**

A bearing with a diameter of 50 mm and a length of 75 mm and a radial clearance of 0.0762 mm was analyzed with a finite difference, two-dimensional computer code<sup>(2)</sup>. The code is capable of analyzing both the laminar and turbulent regimes. The turbulence modeling was based on Elrod and Ng's formulation. The input consists of the shaft speed, the bearing geometry and the lubricant properties. The bearing geometry consists of the diameter, the length and the clearance. Lubricant properties such as viscosity and density are also part of the input. If the density is prescribed as zero, then the program treats the flow as laminar. It should be pointed out that in a compressor bearing (figure 6.3), lubricant enters radially and mixes with a small quantity of recirculating flow in a mixing chamber. A computational grid is established in the circumferential and axial directions. The code allows the pressure boundary conditions at inlet and outlet to be specified.

For a prescribed eccentricity, the code calculates the pressure distribution only in the convergent portion. However, viscous shear is accounted for in the divergent portion. The output consists of load carrying capacity, power loss, flow rate and dynamic properties as a function of eccentricity ratio (eccentricity/radial clearance).

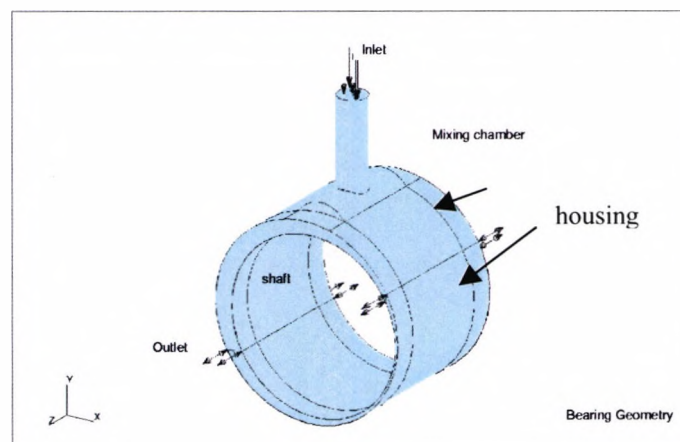


**Figure:6.3 Hydrodynamic journal bearing**

The object of the analysis was to study the effect of turbulence on the pressure distribution, power loss and dynamic characteristics. The initial analysis was carried out assuming laminar flow, followed by an analysis with turbulence. The following three cases were studied:

- 1) HFC134a lubricant – laminar flow
- 2) HFC134a lubricant – turbulent flow
- 3) Synthetic Oil (22 cP) – laminar flow

**6.3.1 Limitations of computer analysis code** The code is not capable of modeling the inlet pipe and mixing chamber. Hence, the effects of the inlet flow and the mixing chamber are not taken into account. Also, the change in pressure across the thickness of the oil film is neglected. This is what makes the analysis two-dimensional. The code assumes constant viscosity in the bearing cavity.

#### **6.4: Discussion of Results**

As shown in figure 6.4, turbulence increases the load carrying capacity. The difference in load carrying capacity between laminar and turbulent flow increases with the eccentricity ratio. The load carrying capacity as a function of film thickness is shown in figure 6.5. For a given load on the shaft, the minimum clearance is higher for turbulent flow than for laminar flow. Figure 6.6 compares the load carrying capacity of a refrigerant lubricated bearing with oil lubricant and clearly shows the larger load carrying capacity of oil due to its higher viscosity.

Figure 6.7 shows that power loss with turbulence is higher than for laminar flow. The ratio of turbulent to laminar power loss varies from 12 at a low eccentricity ratio of 0.2 to 7 at an of eccentricity ratio 0.8. This information can be used to approximately calculate the effective viscosity due to turbulence. The power loss in a hydrodynamic journal bearing at low eccentricity ratios is given as <sup>(3)</sup>:

$$P = \frac{2\pi \mu R^3 \omega^2 L}{C} \dots\dots\dots (6.7)$$

where  $R$  =shaft radius,  $\omega$  = shaft angular velocity ,  $L$  = bearing length,  $C$ =bearing radial clearance,  $\mu$  = dynamic viscosity

For the same angular velocity and bearing geometry, the power loss is proportional to viscosity. Since the power loss for turbulent refrigerant case is 12 times that of the laminar case, the effective viscosity with turbulence is 12 times that of the dynamic viscosity of HFC 134a .

Dynamic properties are presented in figures (6.8) and (6.9). The stiffness and damping values are higher for a bearing with turbulent flow. The higher stiffness raises the natural frequency of the rotor and higher damping results in lower vibration amplitudes.

### **6.5 Conclusion**

The results presented show a marked improvement in bearing performance with turbulence. Based on the power loss comparison between turbulent and laminar flows, the effective viscosity for turbulent flow is calculated as twelve times that of the dynamic viscosity of HFC134a. Because load carrying capacity is strongly affected by turbulence, it is necessary to model the flow field inside the bearing accurately. The finite difference code used for the analysis in this chapter has several limitations as pointed out in section 6.3.1. In the next chapter, flow inside a bearing is analyzed using a 3-D computational fluid dynamic (CFD) code that models variable viscosity, mixing chamber, inlet flow and the pressure across the film thickness.

### **6.6 References:**

- 1) Elrod, H.G., Ng, C.W., *A Theory Of Turbulent Fluid Films and its application to Bearings*, Trans ASME Journal Of Lubrication Technology, July 1967, pp 347 – 362.
- 2) Franklin Institute Research Laboratory, *Cylindrical Fluid-Film bearing Program – HYJURN*.
- 3) Khonsari, M.M, Booser, E.R., *Bearing Design and Lubrication*, John Wiley & Sons, Inc, pp 124.

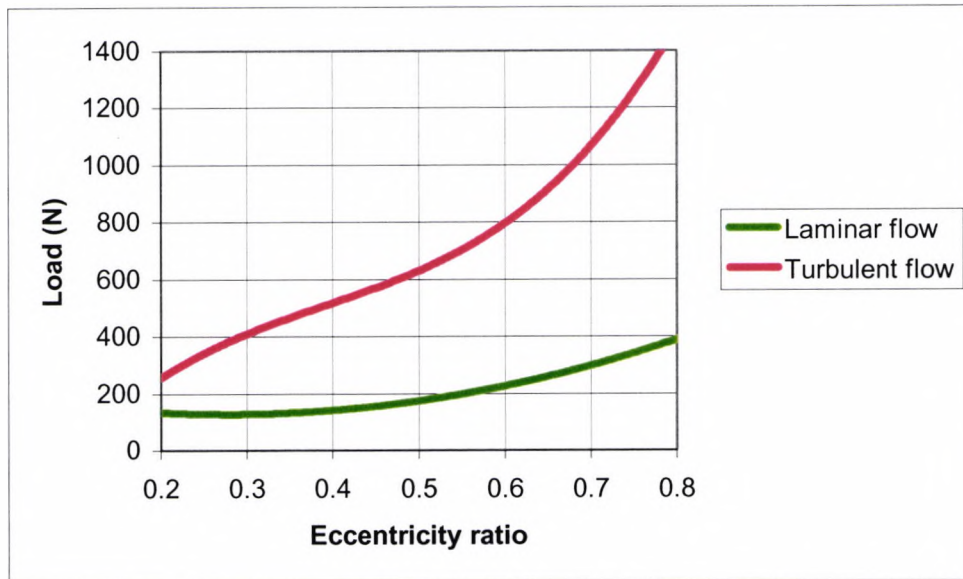


**Fig 6.4: Load Vs Eccentricity ratio  
Lubricant - HFC134a liquid**

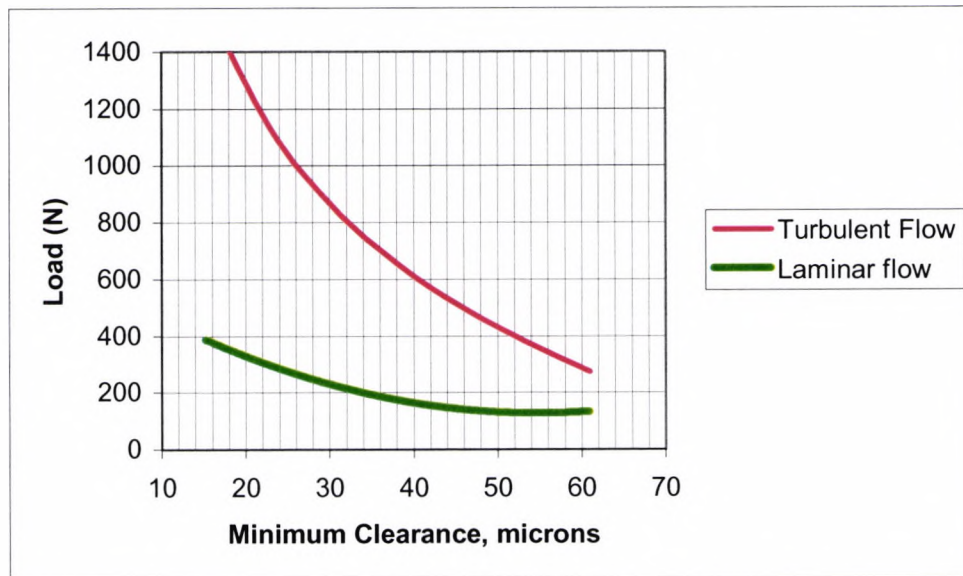


**Fig 6.5: Load Vs Minimum clearance  
Lubricant - HFC134a liquid**

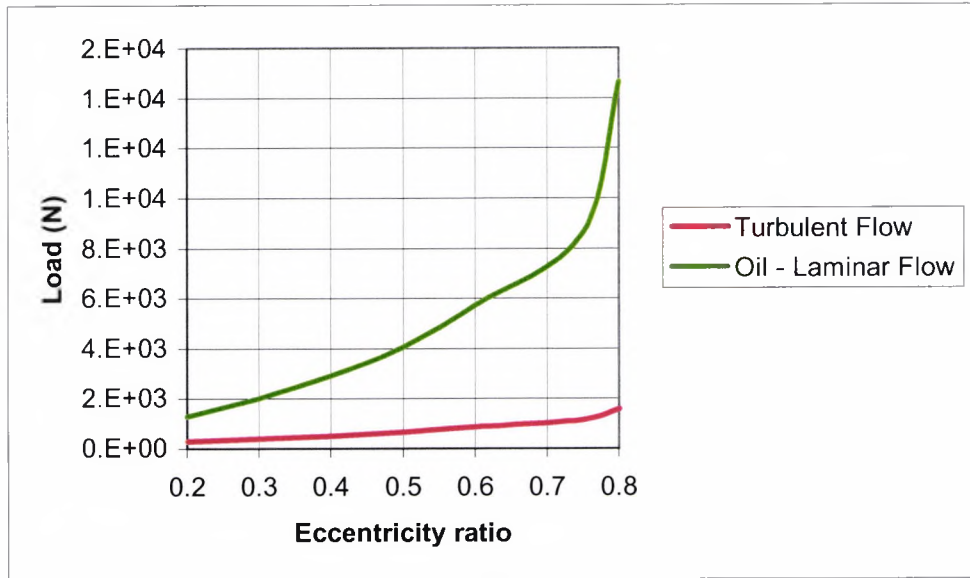


**Fig 6.6: Load vs Eccentricity ratio, with lubricant HFC134a - Turbulent flow and Oil - Laminar flow**

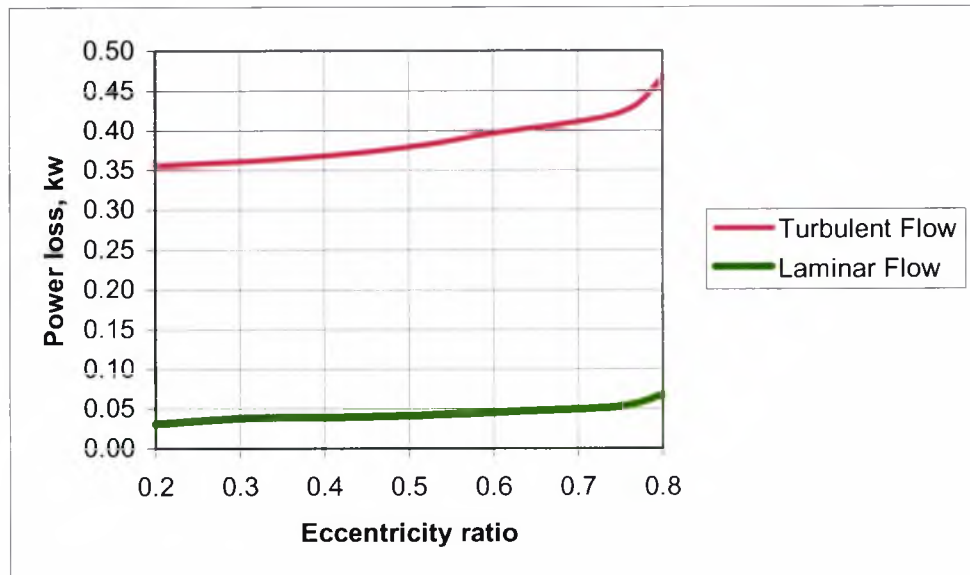


**Fig 6.7: Power Loss Vs Eccentricity ratio  
Lubricant - HFC134a liquid**

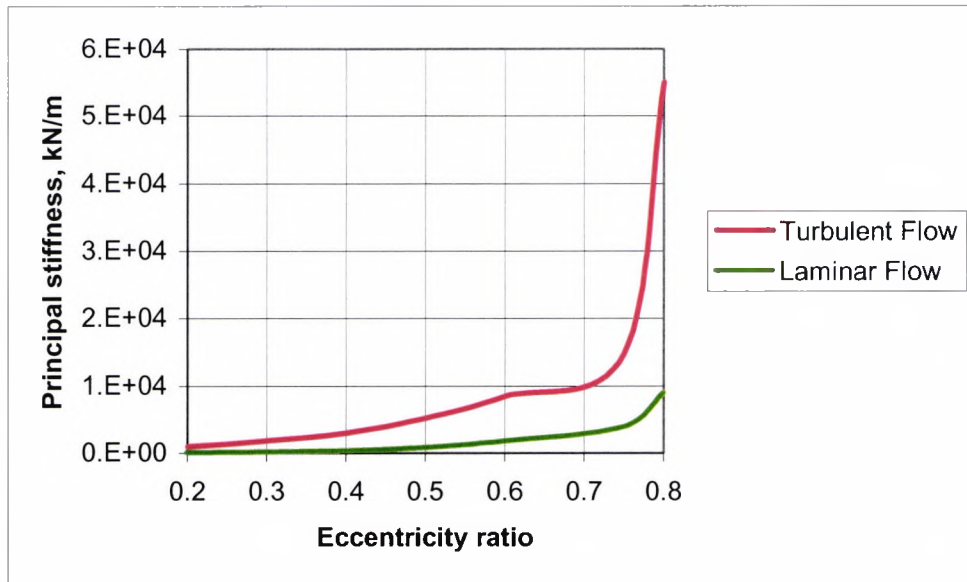


**Fig 6.8: Stiffness Vs Eccentricity ratio**  
**Lubricant - HFC134a liquid**

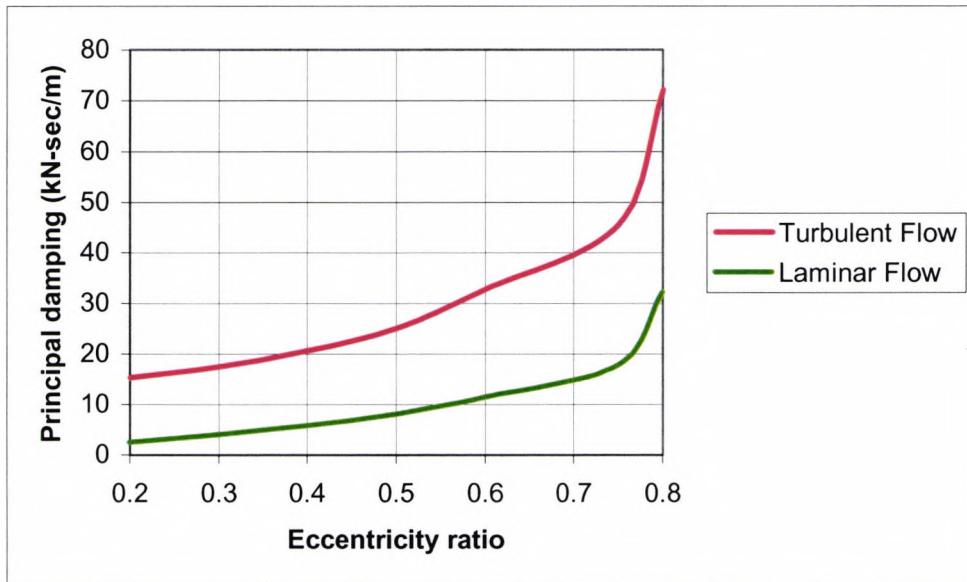


**Fig 6.9: Damping Vs Eccentricity ratio**  
**Lubricant - HFC134a liquid**

## CHAPTER SEVEN

### COMPUTATIONAL FLUID DYNAMICS ANALYSIS OF FLOW IN HYDRODYNAMIC BEARINGS

#### 7.1 Introduction:

Existing methods of bearing analysis as described in chapter 6, solve the Reynolds equation, in the region between the shaft and the bearing, as a two-dimensional model. The analysis is carried out using a computer program based on the finite difference method. The grid is made up of points in the circumferential and axial directions at a mean radius. The grid is consistent with the development of the Reynolds equation, wherein; pressure and velocity variation in the radial direction is neglected. The input, which is fairly simple and straightforward, consists of bearing geometric parameters and lubricant properties. Geometric parameters consist of the shaft diameter, length, radial clearance and eccentricity. In cases where the bearing surface is circumferentially split into more surfaces or pads, the angular extent of each surface is specified. Lubricant properties such as density, viscosity and specific heat, as a function of temperature, are also specified. The solution or output consists of mass flow, power loss, stiffness and damping coefficients.

The main advantage of this method is its simplicity. However, it has the following shortcomings:

- 1) The effects of inlet flow and inlet geometry are not taken into account.
- 2) The effect of fluid inertia is not accounted for.
- 3) The effect of pressure variation in the radial direction is neglected.
- 4) The variation of viscosity with temperature is neglected.

To investigate the effects of variable viscosity, inlet geometry, inlet flow and the pressure across the film thickness flow a three-dimensional computational fluid dynamics (CFD) code was used. CFD analysis was carried out to study the effect of three different turbulence models on the circumferential pressure distribution in the clearance region, the pressure distribution across the thickness of the film, to identify regions of cavitation and to modify the geometry to eliminate cavitation. The pressure distribution and load carrying capacity were compared between the 3-

D CFD model and a 2-D model analyzed with the finite difference code described in chapter 6.

## **7.2 CFD Analysis:**

Computational Fluid Dynamics is a numerical solution method. The continuous, multidimensional fluid domain is discretized into small elements. This process results in a replacement of the continuous domain by a number of grid points. The differential equations of motion of the continuous domain are approximated by algebraic finite difference equations at the grid points. The process allows an approximate solution of otherwise unsolvable differential equations. The steps involved are:

- 1) Selection of a mathematical model that best describes the physics of the problem
- 2) Discretization method to solve the mathematical equations
- 3) Procedure for numerical grid generation
- 4) Solution method
- 5) Convergence Criteria

A brief description of the above steps is given in appendix G. The analysis was carried out using a finite volume based CFD code, CFX, developed by AEA Technology. The type of boundary conditions and turbulent modeling in CFX is presented below:

**7.2.1 Boundary Conditions:** The CFX computer program allows six types of boundary conditions:

- Inlet
- Outlet
- Opening
- Wall
- Symmetry Plane
- Periodic pair

**Inlet:** An inlet boundary condition is used where it is known that the flow is directed into the domain. The options available for value at the inlet are the normal speed, the Cartesian velocity components, the total pressure and the mass flow rate. The program allows two options for specifying the turbulence quantities, the intensity and the length scale specification. The turbulence quantities can be set either to default or user defined values.

**Outlet:** An outlet boundary condition is used where it is known that the flow is directed out of the domain. The program allows specification of uniform static pressure, average static pressure, normal speed out, Cartesian velocity components and mass flow rate.

**Opening:** An opening is used where it is not known whether the flow is in or out of the domain. This feature allows flow recirculation at the boundary. The program allows specification of pressure and Cartesian velocity components. When the pressure is specified, it is taken as the total pressure based on the normal component of velocity for flow into the domain.

**Wall:** Walls are solid impermeable boundaries to fluid flow. Walls allow the permeation of heat flux into and out of the domain. Walls are the default boundary condition; any surfaces not part of an existing boundary condition will be automatically grouped into a default wall boundary. There are three options for the influence of a wall boundary on the flow, namely:

- a) No-slip stationary - No-slip and zero velocity at the wall
- b) Free-slip - Shear stress at the wall is zero and wall friction effects do not retard the velocity of the fluid near the wall.
- c) No-slip moving – Non-zero wall velocity with no-slip condition. With this option a relative velocity can be specified which exists between the wall boundary and a reference coordinate frame.

For simulations of turbulence models, one can describe the wall surface as being smooth or rough. For rough walls, the height of roughness is specified in the input.

### **7.3 Turbulent Flow Modeling**

The problem here is that of predicting interaction between a Couette flow and a pressure flow. Couette flow is a simple shear flow that exists in the annulus between two concentric cylinders, when one is turned and the other is held stationary. Pressure flow is a pressure-induced fluid motion such as would take place between stationary walls. In an actual bearing, where the shaft is displaced from its central position, the pressure varies both circumferentially and axially. For laminar flow in bearings, linear superposition is possible and axial flow is independent of the shaft speed. This is not the case for turbulent flow.

Turbulent analysis of simple geometries is in itself quite complex. In bearings, this is further complicated by the fact that the flow is nonplanar and that axial and circumferential pressure gradients exist. Another problem is an increased tendency for cavitation in the diverging region of the bearing due to the larger pressure drop associated with turbulent flow.

In the treatment of turbulent flow, the number of variables exceeds the number of equations. For example, for three-dimensional bearings the relations between the fluctuating components and the time-averaged velocities must be established before a rational analysis can be attempted. The presence of a varying pressure gradient along the flow channel is one of the two differences between the types of turbulent flow investigated experimentally and the turbulent flow in bearings. The other difference is the fact that in a bearing there is no planar flow and axial velocity components vary continuously within the bearing clearance.

Turbulent flow is governed by the unsteady Navier-Stokes equations. Turbulence generally involves length scales much smaller than the smallest finite volume mesh, which can be practically used in a numerical analysis. To resolve the features of the flow at this level directly would require, even in the simplest cases, an extremely large number of small mesh elements. This method of modeling turbulence flow is referred to as direct numerical simulation (DNS). Although direct numerical simulation is possible for very few simple cases, for most cases it is not performed due to practical limits of computer memory and processor speed. To enable the

effects of turbulence to be predicted, a large amount of CFD research has concentrated on methods that make use of turbulence models. Turbulence models have been specifically developed to account for the effects of turbulence without recourse to a prohibitively fine mesh. In general, turbulence models seek to modify the governing equations by inclusion of additional terms or equations to account for turbulence effects.

With respect to a time scale much larger than that of turbulent fluctuations, turbulent flow could be said to exhibit average characteristics, with an additional time varying, fluctuating component. For example, a velocity component may be divided into an average and a time varying component, and replaced into the unsteady Navier-Stokes equation. In doing this, however, the new ensemble averaged equations include terms containing products of the fluctuating quantities, which act like viscous stresses in the fluid. These terms, called turbulent or Reynolds' stresses, are difficult to determine and so become further unknowns.

To determine the turbulent stresses additional equations are required to close the full set of flow equations and these equations define the type of turbulence model. A number of models have been developed that can be used to approximate turbulence. Some have very specific applications, while others can be applied to a wider class of flows with a reasonable degree of confidence. Turbulence models can be divided into two broad categories, eddy viscosity models and Reynolds stress models.

**7.3.1 Turbulence models:**

**Eddy Viscosity model** This model suggests that turbulence consists of small eddies which are continuously forming and dissipating and in which the Reynolds stresses are assumed to be proportional to the mean velocity gradients. The effect of the Reynolds stress contribution is then described by the addition of a turbulence component of viscosity so that

$$\mu_{\text{eff}} = \mu + \mu_t \dots\dots (7.1)$$

where  $\mu_{\text{eff}}$  is the effective viscosity,  $\mu$  is the molecular viscosity and  $\mu_t$  is the turbulent viscosity. Dimensional analysis shows that:

$$\mu_t = C_p \nu L \dots\dots(7.2)$$

where  $C$  is a constant,  $\rho$  is the density,  $v$  is the mean velocity and  $L$  is the length

CFX has two eddy viscosity models:

- 1) Zero Equation: In its simplest description, turbulence can be characterized by two parameters; its kinetic energy or a velocity and a length scale. In mixing length models, kinetic energy is determined from the mean velocity and length is a prescribed function of the coordinates. This model computes a global value of  $\mu_t$  from the mean velocity and a geometric length scale using an empirical formula. Because no additional transport equations are solved, these are termed 'zero equation'. Accurate prescription of length is possible for simple flows but not for separated or highly three-dimensional flows. Simple to implement and use, zero equation models approximate results very quickly, and provide a good initial guess for simulations using more advanced turbulence models.
  
- 2) Two equation  $k$ - $\epsilon$  model: Since a minimum description of turbulence quantities requires at least a velocity and length scale, a model which derives the needed quantities from two such equations is a logical choice. In almost all such models, an equation for the turbulent kinetic energy,  $k$ , determines the velocity scale. The choice for length is based on the observation that in turbulent equilibrium flows, those in which rates of production and destruction of turbulence are in near-balance, the dissipation,  $\epsilon$ , kinetic energy,  $k$  and length  $L$  are related by:

$$\epsilon \approx k^{3/2}/L \dots\dots\dots (7.3)$$

This idea is based on the fact that, at high Reynolds numbers, there is a cascade of energy from the largest eddies to the smallest eddies and that the energy transferred to the smallest eddies is dissipated. Equations for  $k$  and  $\epsilon$  are derived from the Navier-Stokes equations. The  $k$ - $\epsilon$  model is a significant advance over zero equation models for it calculates turbulence viscosity locally and preserves flow history effects.

**Reynolds stress models** These models do not use the eddy viscosity concept, but use transport equations for the individual Reynolds Stresses. The Reynolds stress

model transport equations are solved for the individual stress components. Reynolds stress models are more suited for flows with strong curvature, separation or swirl

**7.3.2 Treatment of Flow Near a Wall:** Under certain turbulent flow conditions, such as fully developed, and attached flow, the velocity profile near a wall assumes a characteristic shape. This boundary layer profile tends to contain a region where the velocity profile is logarithmic and universally expressible in terms of the wall shear stress. The assumed applicability of this profile provides a means to compute the wall shear stress as a function of the velocity at a given distance from the wall numerically. The mathematical basis is called a ‘wall function’ and its logarithmic nature gives rise to the well known ‘log law of the wall’. The advantage of the wall function approach is that the high gradient shear layers near the wall can be modeled with a relatively coarse mesh yielding substantial savings in CPU time and storage. The alternative is to resolve the details of the boundary layer profile with the mesh fully, but this requires a prohibitively fine mesh and a correspondingly large number of nodes.

Very close to the wall, the profile changes from logarithmic to linear i.e similar to that of laminar flow. This innermost region is called the laminar sublayer. To complete the mathematical description of the boundary layer, the logarithmic function is merged with a linear one. All turbulence models in CFX use wall functions. The analysis calculates a dimensionless distance from the wall,  $y^+$  that is used to check the validity of the wall function for a given mesh. The wall function approximation is valid only for values of  $y^+$  between 10 and 1000. Values of  $y^+$  greater than 1000, indicate that the mesh near the wall region is too coarse and will require subsequent refinement. Conversely values less than 10 indicate that the mesh is too refined close to the wall, and the wall function model does not adequately span the laminar sub-layer region of the boundary layer. Minimum, maximum and average values of  $y^+$  are written at the end of output file.  $y^+$  is defined as

$$y^+ = y \frac{\rho}{\mu} \left( \frac{\tau}{\rho} \right)^{\frac{1}{2}} \dots\dots\dots (7.4)$$

(Where  $y$  is the distance from the wall,  $\rho$  is the fluid density,  $\mu$  is the fluid viscosity, and  $\tau$  is the fluid shear stress)

## **7.4 Refrigerant Lubricated Hydrodynamic Bearing - Geometry and Analysis**

### **Model**

The geometric parameters of the bearing considered are as follows:

Diameter = 50.8 mm

Length = 75 mm

Radial clearance = 75  $\mu\text{m}$

X, Y Coordinates of shaft position = 38.1  $\mu\text{m}$ , 38.1  $\mu\text{m}$

Eccentricity ratio = 0.707

Shaft speed = 14 500 rpm

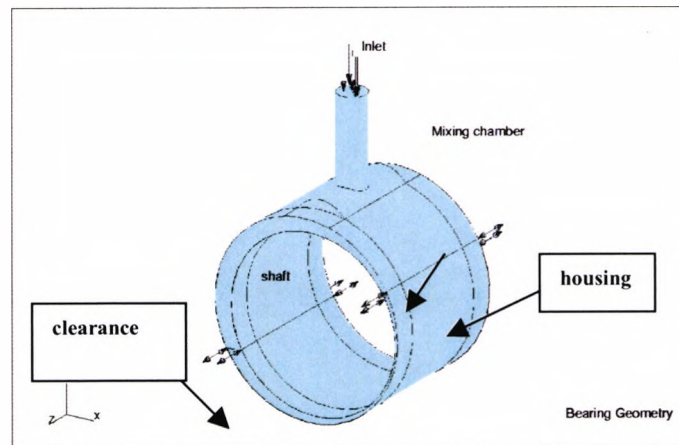
Direction of rotation - clockwise as shown in Fig (7.1) end view, confirms the right handed coordinated system

The model is shown in figure 7.1. The small clearance between the bearing and the shaft posed problems for the CFX mesh generator. Fortunately, however, CFX is capable of importing a mesh from a variety of external mesh generators. The mesh was generated using the finite element package ANSYS and was exported to CFX. An automatic mesh generation feature in ANSYS was used to generate the elements. The clearance space between the shaft and the bearing was meshed using hexahedral elements. The mesh generator used tetrahedral elements to mesh the inlet pipe and the mixing chamber. Tetrahedral meshes are known to be less accurate for turbulent flows than for laminar. Since the flow in the inlet pipe and mixing chamber is laminar, a tetrahedral mesh will not create inaccuracies. The details of the computational mesh are shown in Table 1 below:

Radial divisions	Circumferential divisions	Axial divisions	Nodes
4	200	25	29172
7	300	25	72261
10	450	25	128886
13	550	25	250092

**Table 7.1: Details of the computational mesh**

The clearance space was modeled with 4, 7 10 and 13 layers of elements. Figure 7.2 shows the 128886 node mesh in three parts, the overall mesh, the detailed mesh in the inlet region and in the clearance space. The pressure distribution was calculated at three different sections as shown in Figure 7.3, located at mid plane (section A-A), and at axial distance 1 cm from mid plane (section B-B) and 2.5 cm from mid plane (section C-C).



Isometric View

Side View

End View

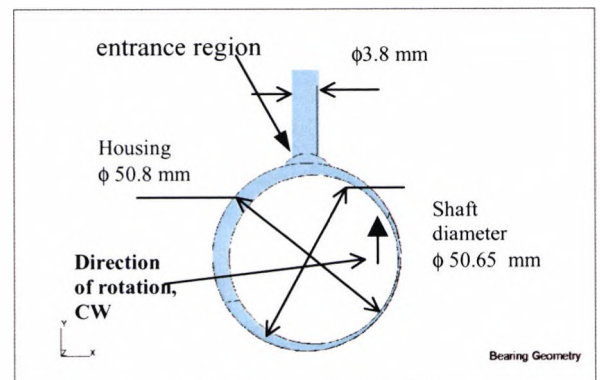
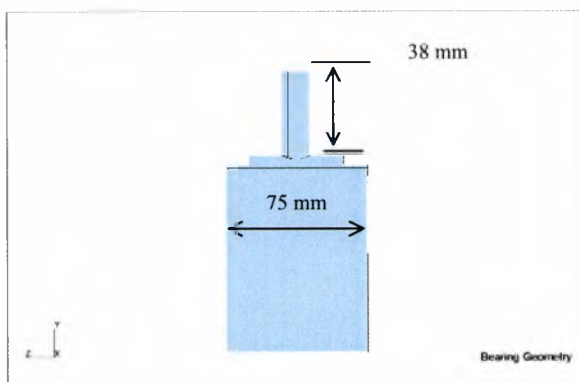
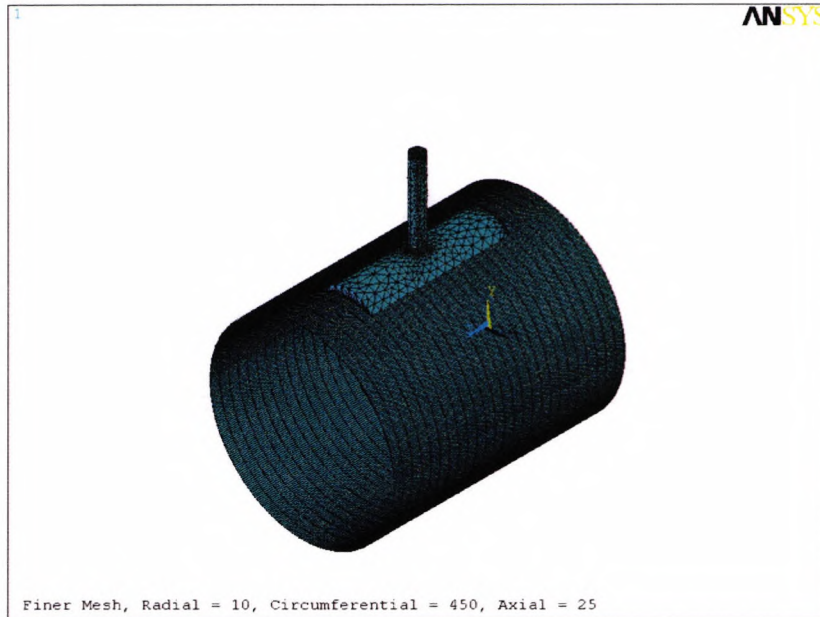
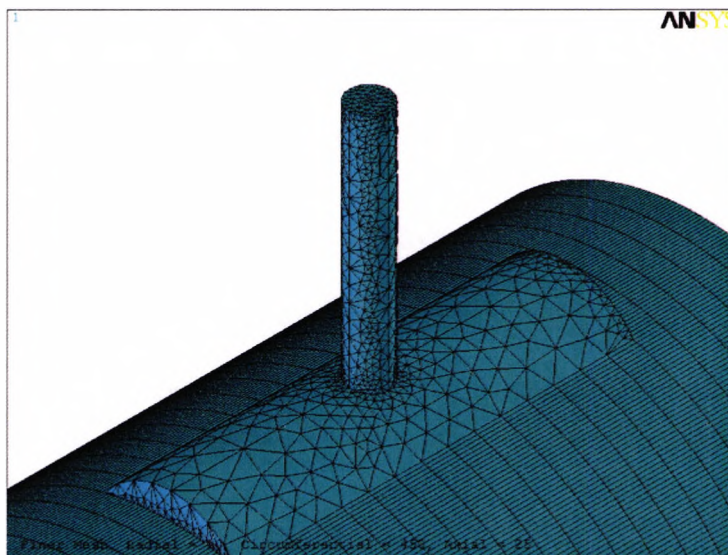


Fig (7.1) Bearing geometry with shaft



**Fig 7.2a: Overall Mesh, 128886 nodes**



**Fig 7.2b: Mesh in the inlet region**

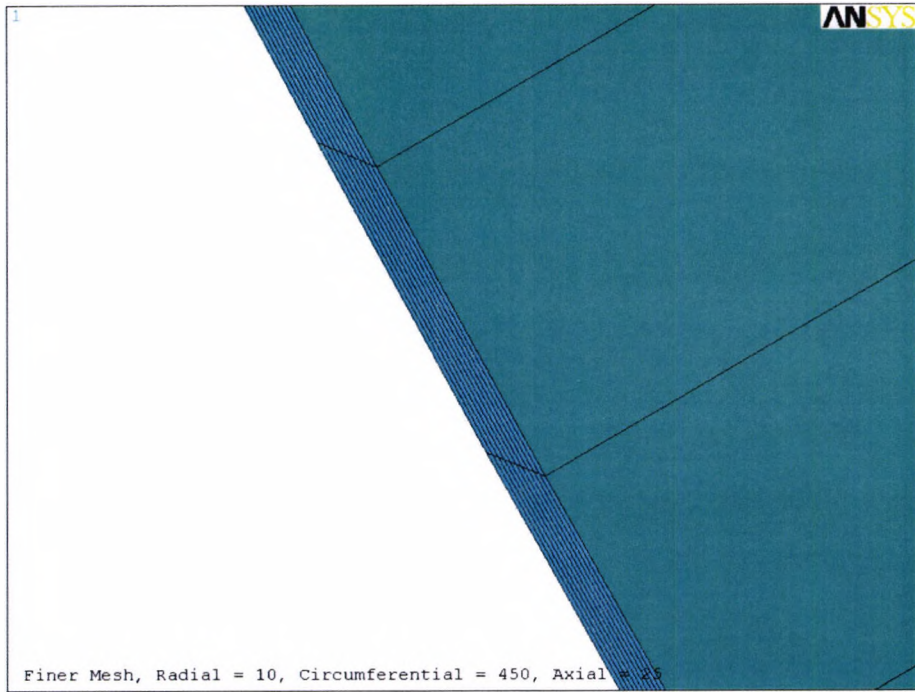


**Fig 7.2c: Mesh in the clearance region**

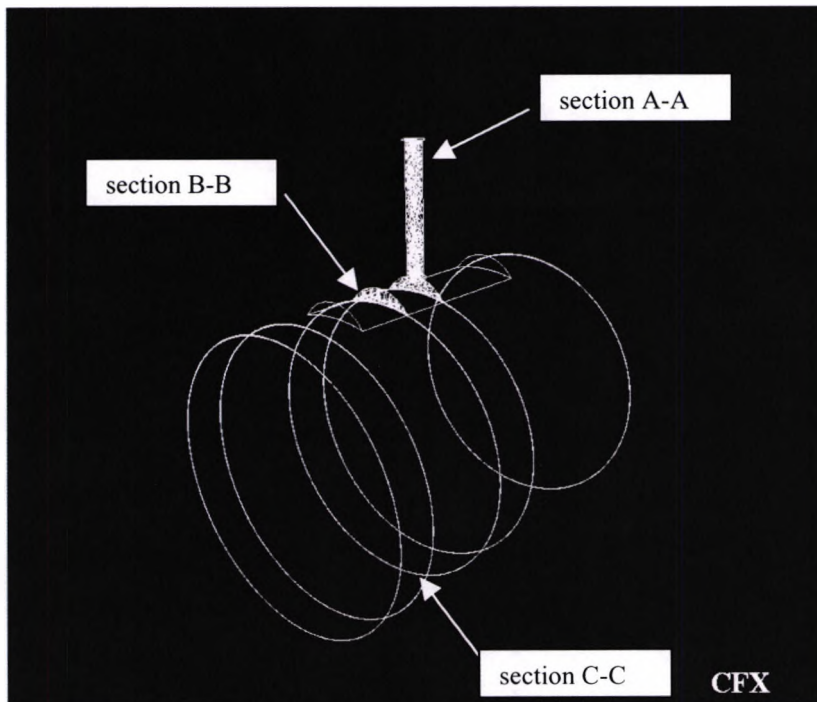


**Fig 7.3: Locations of results sections**

### **7.5: Analytical procedure**

The bearing was analyzed with the following boundary conditions:

Inlet total pressure = 563 kPa,

Outlet pressure = 387 kPa

Shaft = No slip rotating wall,

with surface velocity of 38 m/sec corresponding to a rotational speed of 14500 rpm.

Housing = No slip stationary wall.

Dynamic viscosity at 15°C= 0.224 mPa -sec

A typical temperature rise for oil lubricated journal bearings in a refrigeration compressor is 15°C. Table 2 below shows the viscosity variation of lubricants over a normal operating range of temperatures. For HFC134a, the variation in viscosity is 20% but for oil the viscosity variation is 85%. Due to the small variation of viscosity for HFC134a, the initial analysis was carried out assuming it to be constant. Note that the temperature rise in the bearing with HFC134a will be lower than 15°C due to its viscosity being lower than that of oil. Hence, the viscosity variation for HFC134a will be even smaller than 20%. The effect of viscosity variation on the load carrying capacity is presented at the end of this chapter for the final bearing design.

Lubricant	Dynamic Viscosity (mPa-sec)	
HFC134a	0.239 @10°C	0.198 @25°C
Oil (68 cst+5%HFc134a)	24 @55°C	13@70°C

**Table 7.2: Lubricant viscosity at operating temperatures**

The inlet pressure is based on a condenser saturation temperature of 25°C with an assumed pressure drop of 100 kPa from the condenser to the bearing inlet. The outlet pressure is set at 35 kPa above the evaporator saturation pressure corresponding to 5° C. Initial values for all solved variables need to be set in CFX. Initial conditions give the solver a flow field from which to start its calculations. Convergence is more rapidly achieved if a sensible initial guess is provided. However, the final results will not be affected by the initial guess. For

incompressible laminar flows, the default values provided by the program were found to be adequate. For turbulent incompressible flows, the default values did not always result in a converged solution. Convergence could not be obtained for computations with the zero equation, k- $\epsilon$  and Reynolds stress turbulence models. First solving the laminar case and using the results of that solution as initial values for the turbulent analysis successfully overcame this convergence problem.

**7.5.1 Mesh Density Optimization:** The results of a CFD analysis depend upon the mesh density or the number of nodes defining the computational domain. The results should converge to a grid-independent size value. The selection of the right number of nodes is a trade-off between computational time and accuracy. The “correct” node number is arrived at by performing analyses with different node numbers until the variation in results are within an acceptable limit. Since the peak pressure in the clearance is a measure of the load carrying capacity, it was chosen as the variable for establishing the mesh density. A maximum variation of 10% in peak pressure between two mesh sizes with a node number ratio of 2, was selected as the criterion. Four different mesh sizes were analyzed with the Reynolds stress turbulence model. The peak pressure and computational times are shown in Table 3 below. Figure 7.4 shows the pressure distribution across section A-A. The change in peak pressure between 128886 nodes and 250092 is less than 10%. Due to the lower CPU time, the 128886-node mesh was selected for further analysis. Also, note that the  $y^+$  values are within the limits of 10 and 1000, as specified in section 7.3.2.

Number of nodes	Peak pressure (kPa)	Percent change	Average $y^+$		cpu time (sec)
			Shaft	Wall	
29172	1138		79	75	1000
72261	1347	18.4	49	63	2172
128886	1529	13.5	36	37	4325
250092	1624	6.2	31	35	8256

**Table 7. 3: Summary of results with different mesh densities**

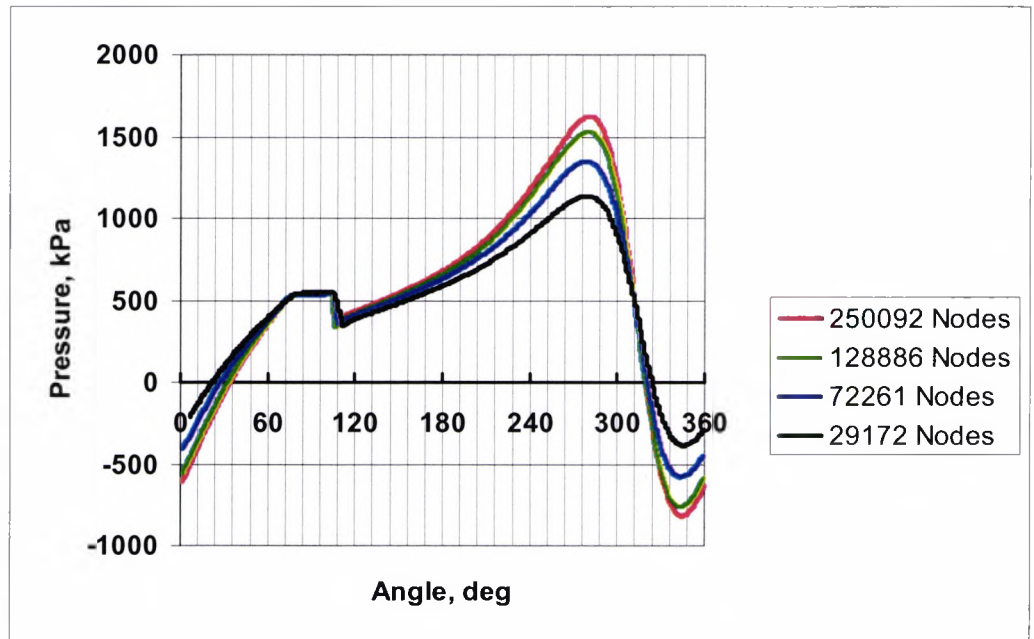


**Fig 7.4: Pressure distribution for Reynolds stress model at section A-A with four different mesh sizes**

**7.5.2 Turbulence Model Selection:** The turbulent models specified in section 7.3, can be used in any given flow. However, depending on the flow physics one model may give more accurate results than the other. Also, computation times can vary significantly from the simple zero equation to the complex Reynolds stress models. There is always a trade-off between accuracy and computation time. In a bearing, the effect of the turbulence models on the pressure distribution has not been studied previously. Analysis was carried out with the zero equation,  $k-\epsilon$  and Reynolds stress turbulence models. Results of the pressure distribution at section A-A are shown in Figure 7.5. The variation in pressure distribution between the different turbulence models is small. The computation time for the zero equation solution is 3850 seconds compared to 4325 seconds for the Reynolds stress solution. Hence, by using the zero equation solution, a small savings in computational time can be gained without losing accuracy.

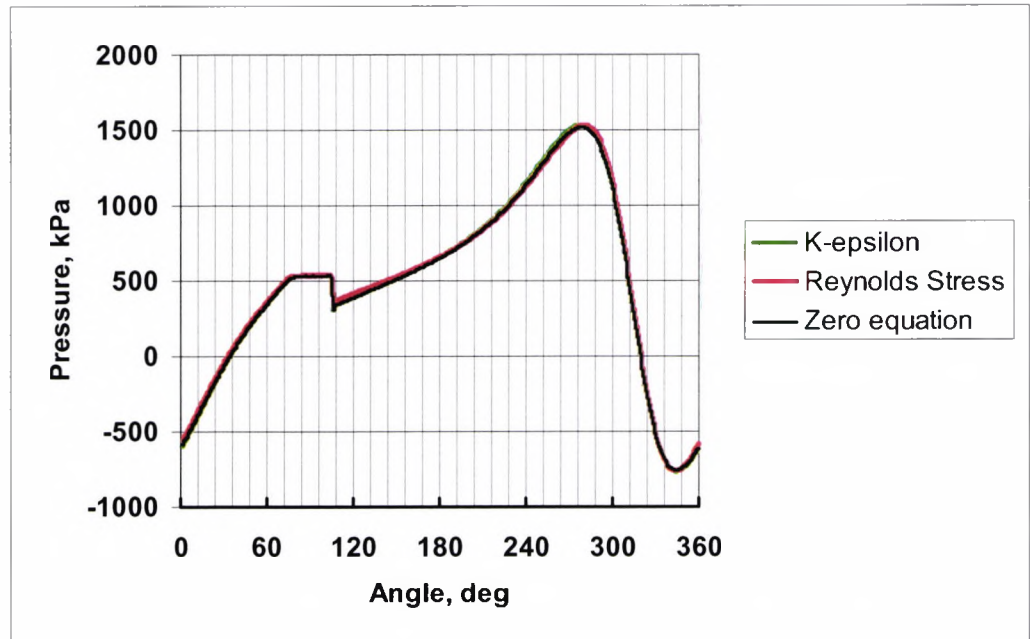
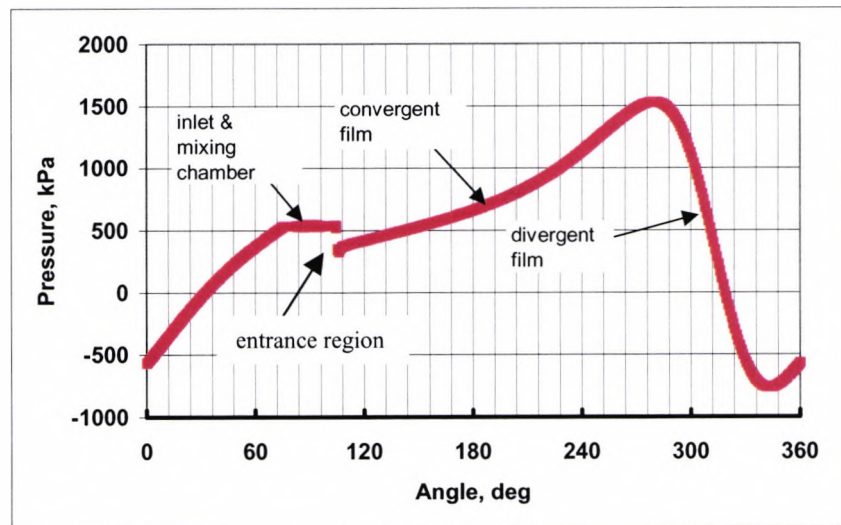


**Fig 7.5: Pressure distribution at section A-A with three different turbulence models**

### 7.6 Discussion of results

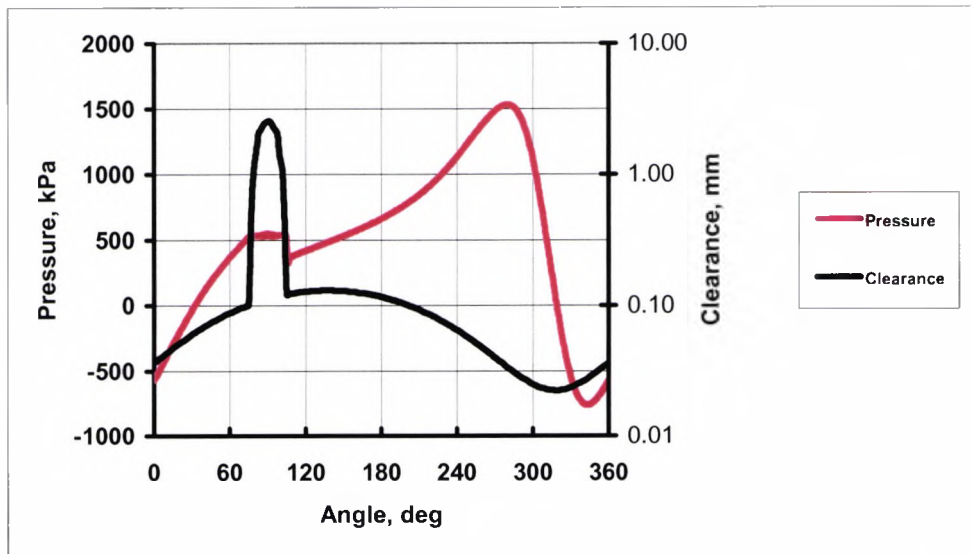
The main object of the analysis was to determine the pressure distribution in the clearance space and to compare the 3-D CFD analysis results with those of the existing 2-D bearing analysis program. For a particular eccentricity of the shaft in a bearing, integration of the pressure distribution around the shaft yields the bearing load carrying capacity. A typical pressure distribution around the clearance region at section A-A is shown in Figure 7.6. The shape of the pressure profile shows an increase of pressure in the convergent clearance region and a pressure decrease in the divergent clearance region. Also, the entrance section shows a sudden reduction in pressure, which is attributed to the decrease in area from the mixing chamber to the small clearance region between the shaft and the bearing housing. Pressures less than saturation pressure (calculated at inlet temperature), indicate a potential for cavitation. The negative pressure in the divergent region, downstream of the minimum clearance in section A-A, indicates a definite potential for cavitation.

The variation of pressure across the film thickness, around the circumference other than the entrance region, is less than 2% of the mean pressure. The low variation of pressure across the film thickness supports the assumption that the flow in a bearing can be treated as two-dimensional. For the sake of clarity, all the subsequent pressure plots will show only the average pressure distribution.



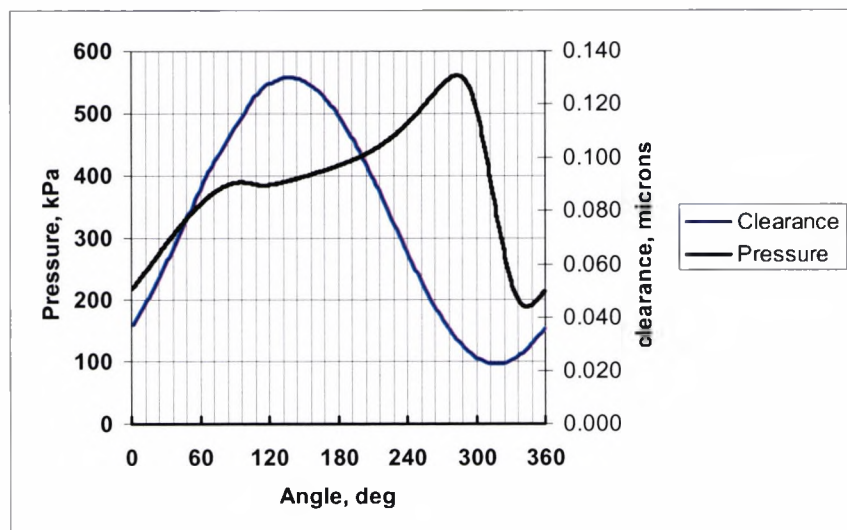
**Fig 7.6: Pressure distribution at Section A-A, Reynolds Stress model, 128886 nodes**

The pressure drop in the entrance region, in Figure 7.6, is 200 kPa. Figure 7.7 shows the distribution of clearance and pressure at section A-A. Figure 7.1 identifies the entrance region. This is the region in which there is transition from the mixing chamber to the low clearance region in the direction of flow. The pressure drop in the entrance region coincides with the large change in the clearance.



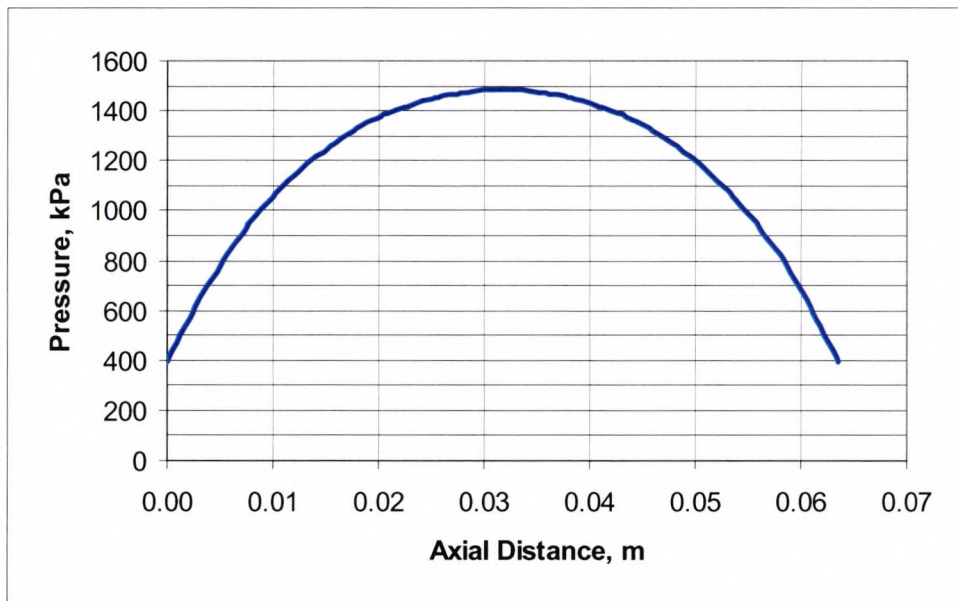
**Fig 7.7 Pressure and clearance distribution at Section A-A, Reynolds Stress model, 128886 nodes**

Figure 7.8 shows pressure distribution and clearance at section C-C. The gradual change in clearance results in a gradual pressure variation without the sudden pressure drop experienced at section A-A.



**Fig 7.8: Pressure and clearance distribution at section C-C, Reynolds Stress model, 128886 nodes**

The axial variation of maximum pressure is shown in figure 7.9. The maximum pressure occurs in the middle of the bearing and the pressure variation is symmetric about the middle of the bearing. This result shows that by applying a symmetry boundary condition at the mid plane, only one half of the bearing needs to be analyzed. This would save considerable computation time. The other reason for symmetry is the equal pressures at both outlets. If the outlet pressures are not equal, then one needs to analyze the complete bearing geometry.



**Fig 7.9: Axial distribution of maximum pressure, Reynolds Stress model, 128886 nodes**

Figure 7.10 shows a raster plot of the axial and circumferential pressure distribution in the bearing.

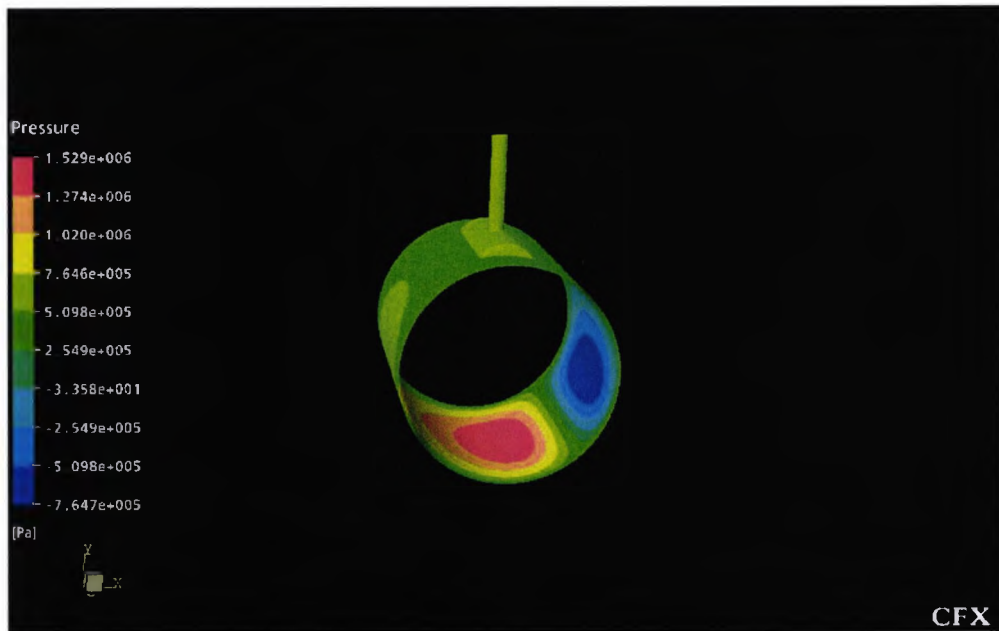


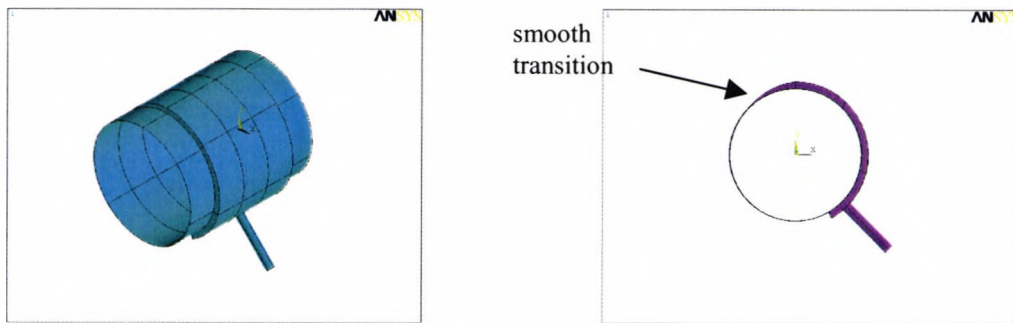
**Fig 7.10: Pressure distribution for Reynolds Stress Model – 128886 nodes**

The results presented thus far identified two sources of potential problems

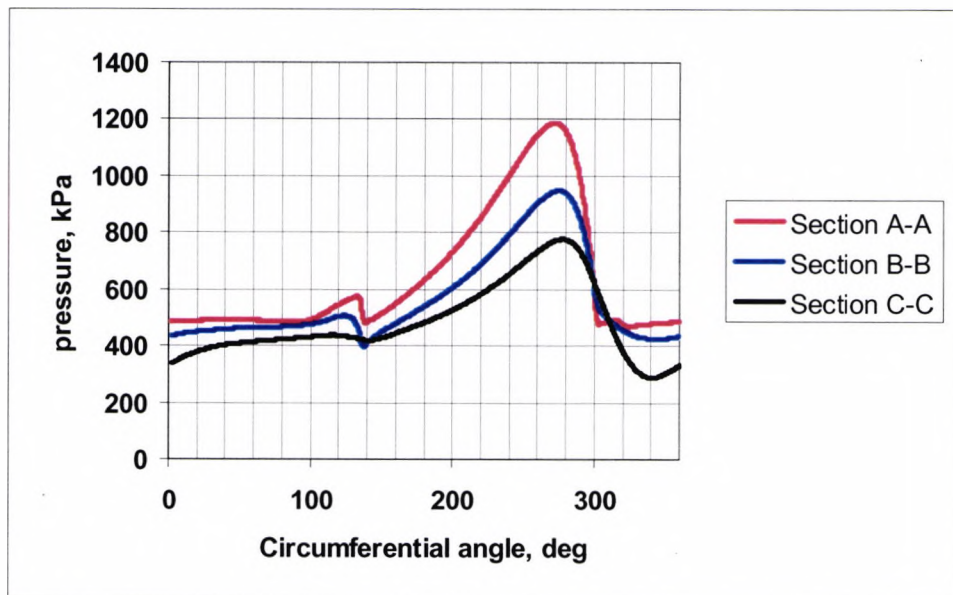
- 1) large pressure drop in the entrance region – which can lead to cavitation and loss of load carrying capacity
- 2) negative pressure regions – a source of cavitation

Figure 7.11 shows a bearing that was designed to minimize both of the above mentioned effects. The noticeable features are the location of the inlet a few degrees downstream of the maximum pressure, a wide groove extending from the inlet to the start of the convergent region and a smooth transition from the wider groove to the small clearance section. The bearing inlet is located at 315 deg and the mixing groove extends from 300 deg to 120deg. The mesh consists of 10 layers across the film thickness with 138652 nodes. Results of pressure distribution are shown in figure 7.12. The results clearly show absence of negative pressure. However, the

pressure in section C-C falls below the inlet pressure due to the absence of the groove. One way to overcome the problem is to extend the groove axially to minimize the cavitation region. Figure 7.13 shows a reduction of pressure drop in the entrance region, from 200 to 75 kPa.



**Fig 7.11: Grooved bearing with smooth transition, radial sections = 10, circumferential sections = 450, Axial section = 25, Nodes =137630**



**Fig 7.12: Pressure distribution in grooved bearing**

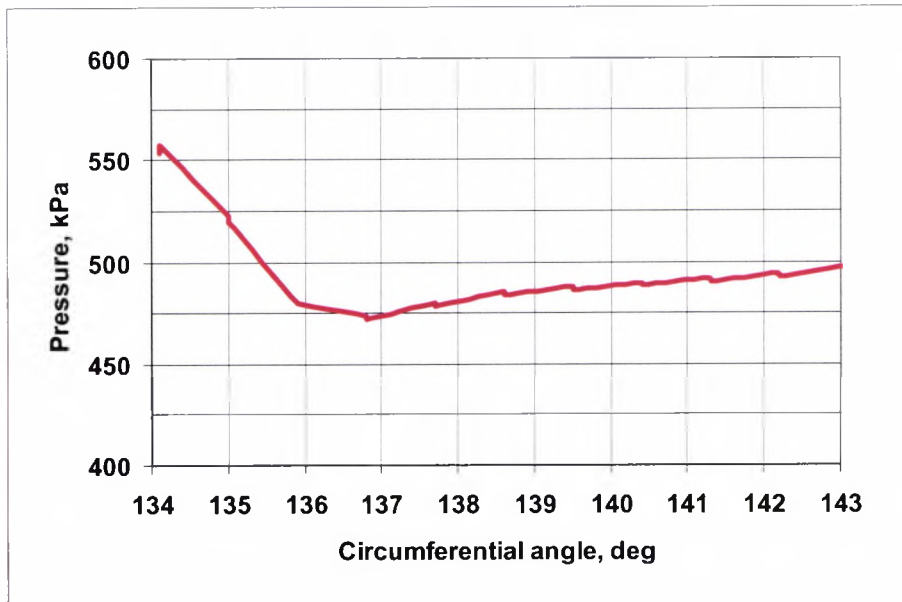


**Fig 7.13: Pressure drop in the transition region at section A-A**

**7.6.1 Comparison with simple zero-equation finite difference code:**

The bearing shown in Figure 7.1 was analyzed with the simple 2-D, zero equation finite difference code. As mentioned in chapter 6, the 2-D code cannot model the flow in the inlet pipe and the mixing chamber. A comparison of solutions of the CFD and 2-D simple finite difference analysis codes at section A-A is shown in Fig 7.14. The 2-D simple code does not account for the pressure drop in the entrance region. Also, in the convergent region, higher pressures are estimated by the CFD. Note that the result of the 2-D analysis was with the optimized mesh density. Also a similar comparison of estimates of the axial distribution of peak pressures is shown in Figure 7.15. Due to symmetry about the mid plane, results of one half the length of the bearing are shown. Similar trends can be inferred from figure 7.16 for a grooved bearing. The simple finite difference code predicts lower peak pressures all along the bearing length.

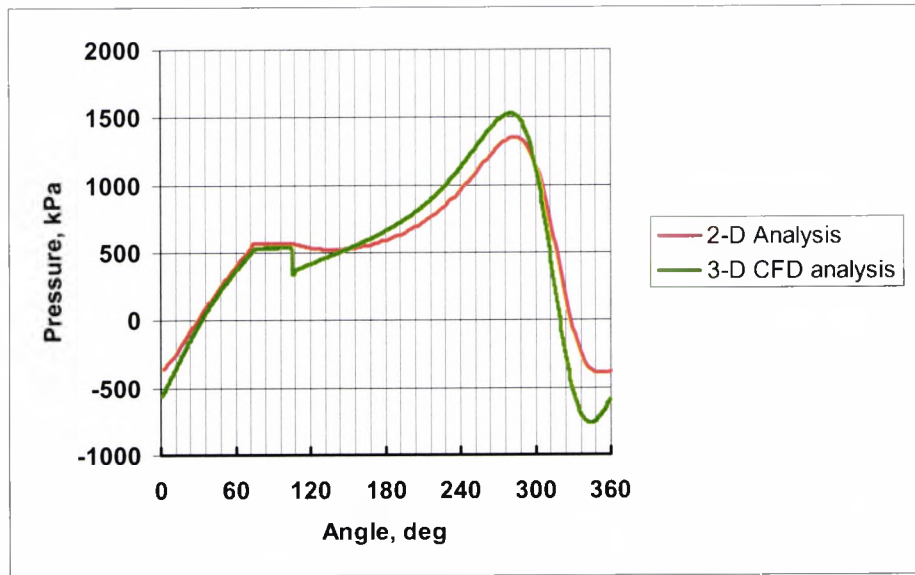


**Fig 7.14: Comparison of pressure distribution with CFD and 2-D Zero equation finite difference code, Section A-A**

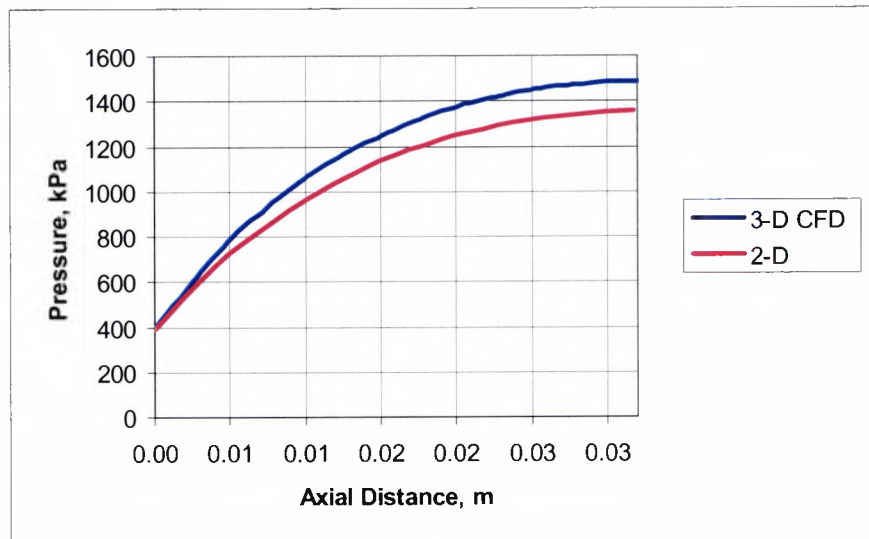


**Fig 7.15: Axial pressure distribution with CFD and 2-D Zero equation finite difference code**

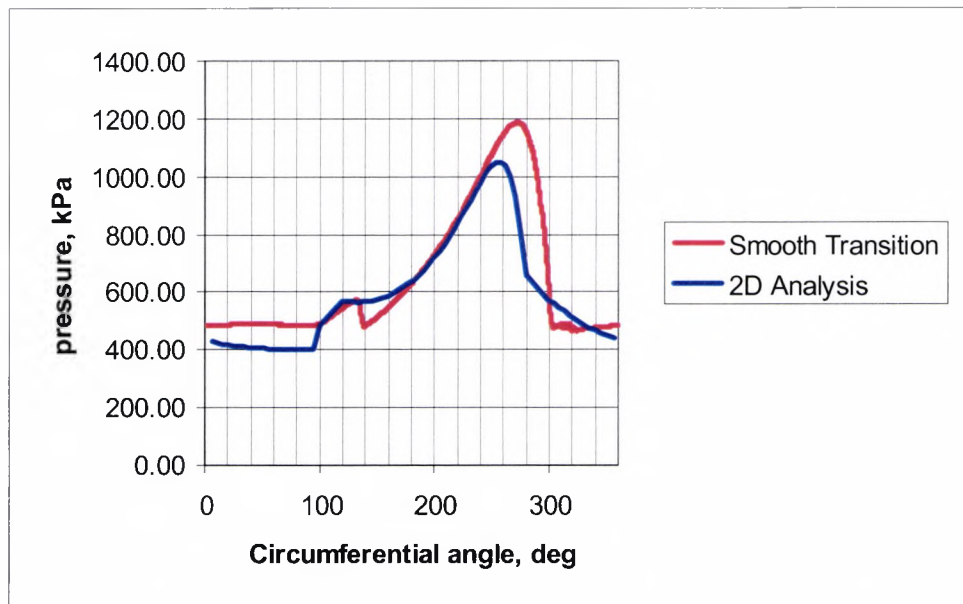


**Fig 7.16: Comparison of pressure distribution with CFD and 2-D Zero equation finite difference code, grooved bearing**

A comparison of load carrying capacity estimates is given in Table 4. The complete 3-D CFD analysis predicts an 18% higher load carrying capacity than the simple code. Table 4 also presents results of load carrying capacity with viscosity variation taken into account. The peak pressure and load carrying capacity variation is less than 1%. Hence, analysis with assumed constant viscosity is adequate.

Case	Top inlet		Grooved bearing	
	Load (N)	Peak pressure (kPa)	Load	Peak pressure (kPa)
3-D CFD	2185	1529	941	1186
2-D Finite difference	1837	1354	860	1050
3-D CFD, viscosity variation			952	1195

**Table 7. 4: Comparison CFD and simple finite difference code results**

Finally, using the dynamic properties calculated by the simple finite difference code, an unbalance response analysis of the compressor rotor described in chapter 3 was carried out with grooved hydrodynamic bearings. Unbalances of 33 g-mm at the

motor end planes and 35 gm-mm at the impeller were applied. The unbalances at the motor end planes are in the same phase and that at the impeller is 180 deg out of phase with those at the motor end planes. The results of the estimates of the amplitude of vibration for hydrostatic (supply pressure of 2.1 MPa) and hydrodynamic bearings are shown in figure 7.19. The critical speeds identified by peak vibration amplitudes in the hydrostatic bearings are not present in the hydrodynamic bearings. The stiffness of both the bearings are comparable. However, the damping of the hydrodynamic bearings is much higher and results in well damped modes.

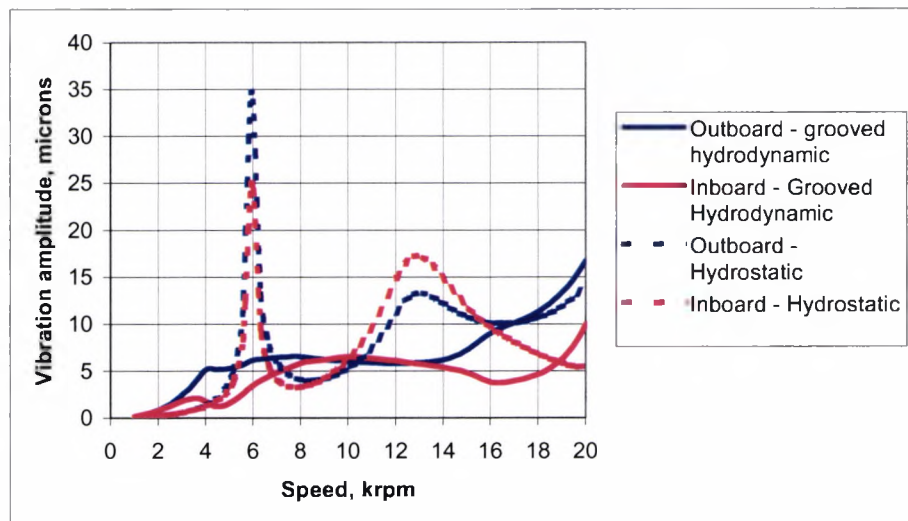


**Figure 7.17: Comparison of amplitude of vibration between hydrostatic and hydrodynamic bearings.**

**7.7 Conclusion:** CFD analysis was used to calculate pressure distribution in a hydrodynamic bearing. The analysis showed a positive slope of pressure or pressure rise in the convergent region and a negative slope or decreasing pressure in the divergent region. The difference in magnitude of pressure in the clearance region with three different turbulence models is very small. Analysis showed a significant pressure drop at the transition region between the mixing chamber and the small clearance region. The analysis was successfully used to design a bearing that has reduced pressure drop at the transition region and is free of negative pressures. CFD

analysis predicted 13% higher peak pressure than the 2-D model. CFD analysis also predicted 9 to 18% higher load carrying capacity than the simple finite difference code. The larger percent increase is for full bearing and the smaller one for grooved bearing. For a refrigerant lubricated bearing, the assumption of constant viscosity results in a negligible penalty in the load carrying capacity.

## **CHAPTER EIGHT**

### **SUMMARY, CONCLUSIONS AND RECOMMENDATIONS**

#### **FOR FURTHER WORK**

##### **8.1 Summary**

The study is divided into two parts. In the first part, a procedure was developed for designing a refrigerant lubricated hydrostatic bearing for a centrifugal compressor operating at 14500 rpm. The procedure establishes key parameters to obtain maximum load carrying capacity and dynamic properties to avoid dangerous rotor vibrations. A hydrostatic bearing compressor was designed and tested to prove the procedure.

Hydrodynamic bearings are easy to manufacture and their system is simplified by the absence of the need for an external pump. The relative motion between the shaft and the bearing generates the pressure required to support an external load. The second part is devoted to the modeling of turbulence in hydrodynamic bearings. A literature survey showed that much of the work on turbulent flow modeling in a hydrodynamic bearing was carried out before the mid 1970's. In recent years, computational fluid dynamics was successfully used to model complex turbulent flows. However, there was little work done in applying these models to analyze flow in bearings. The present work applied computational fluid dynamic analysis to hydrodynamic bearing flow.

##### **8.2 Conclusions**

The main findings can be summarized as follows:

- 1) By utilizing the procedure outlined in this thesis, oil-free refrigerant compressors of the centrifugal type can be built to operate at high speeds, for optimum aerodynamic performance, with externally pressurized hydrostatic bearings. Such compressors could be driven by high-speed motor to reduce bearing loads. Two-phase flow in the bearings can be avoided by maintaining the bearing discharge pressure at 50 to 60 kPa above the evaporator pressure and cooling the

supply refrigerant to 5° C below the saturation temperature corresponding to the discharge pressure.

- 2) In a hydrostatic bearing, three key parameters were found to influence load carrying capacity and dynamic properties. They are the orifice diameter, the radial clearance and the external pressure. An orifice diameter/radial clearance ratio was found for the highest load carrying capacity. The ratio is a weak function of the number of pockets. For a six-pocket bearing the ratio is 20 and for a four-pocket design it is 25.
- 3) To avoid rotor instability, the ratio of supply pressure to bearing specific loading ( $W/LD$ ) should be greater than 7.5.
- 4) Negative logarithmic decrement values upto 0.1 will not result in high compressor vibrations.
- 5) In the operating range of 10 000 to 14500 rpm, to keep the vibrations at bearings below 25% of the film thickness, the supply pressure should be greater than 2.1 MPa.
- 6) CFD analysis of hydrodynamic bearing has confirmed that the pressure distribution is independent of the turbulence models assumed for small clearances.
- 7) Pressure variation across the film thickness is less than 2% of the mean value. Hence, the assumption of neglecting pressure variation in radial direction seems to be valid.
- 8) CFD analysis was successfully applied to locate the inlet passage in a position to remove the low pressure region which causes cavitation.
- 9) CFD analysis has shown higher-pressure in the clearance area than the existing simple 2-D finite difference analysis method. The load carrying capacity derived from CFD analysis is 9 to 18% higher than that obtained from a simple 2-D finite difference code. This results in a smaller size bearing.
- 10) Compressors with hydrodynamic bearings showed lower peak vibration amplitudes than those with hydrostatic bearings.

### **8.3 Recommendations for further work**

The present work has opened up research possibilities in several areas. The following are a few worth considering for further research:

1. The main drawback of hydrostatic bearings is the requirement of costly high-pressure pump. Larger hydrostatic bearings should be designed and tested with lower supply pressures. The bearing diameter can be increased up to the motor shaft diameter.
2. Experimental analysis of turbulent hydrodynamic bearings should be carried out to validate results of CFD analysis.
3. CFD analysis of hydrodynamic bearings should be extended to calculate stiffness and damping. The CFD analysis in the present study was carried out for a steady state position of the bearing. Unbalance in the shaft causes the shaft to whirl around the steady state position. This type of shaft motion causes the bearing clearance to change continuously. Hence, CFD packages with moving mesh capabilities should be investigated.
4. Rolling element bearings are another option that needs to be investigated. The main obstacle for using oil-free refrigerant is the rusting of the bearings due to moisture in the system. Also, the low viscosity of refrigerant results in a thin lubricant film, less than  $1\mu\text{m}$ . In order to operate in the full film region, the combined surface finish of the race and the balls or rollers should be less than  $0.1\mu\text{m}$ . At present ceramic bearings are capable of achieving such high surface finishes and are also resistant to rusting.

## **APPENDIX A**

### **Results of Unbalance Response Analysis**

This appendix shows output plots from the unbalance analysis program ROTBRG.

- 1) Supply pressure 1.04 MPa - Figure 1A to Figure 1K
- 2) Supply pressure 1.4 MPa - Figure 2A to Figure 2K
- 3) Supply pressure 1.7 MPa - Figure 3A to Figure 3K
- 4) Supply pressure 2.1 MPa - Figure 4A to Figure 4K
- 5) Supply pressure 1.7 MPa - Figure 5A to Figure 5E for actual unbalance case
- 6) Supply pressure 2.1 MPa - Figure 6A to Figure 6K for actual unbalance case

Magnitude of unbalance

- a) Cases 1 to 4: Motor rotor 79.5 gm-mm per plane, Impeller 16 gm-mm
- b) Cases 4 and 6: Motor rotor 33.5 gm-mm, impeller – 34.5 gm-mm

The station numbers (STA) and corresponding location is as follows:

Station 3 – Near bearing opposite to impeller

Station 14 – Near bearing close to impeller

Station 4 – Motor rotor end opposite to impeller

Station 9 – Motor rotor near impeller

Station 20 – Impeller center of gravity

The bearing force plot shows, magnitude and phase angle in mutually perpendicular X and Y directions.

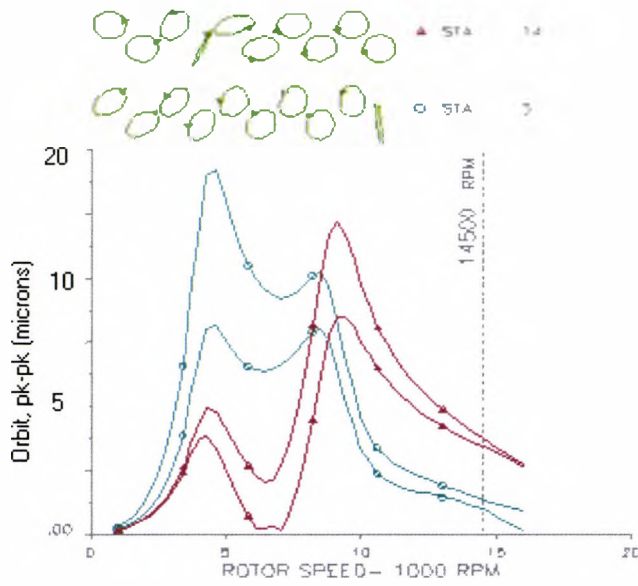


Figure 1A: Synchronous Response with in-phase unbalance - Amplitude at Bearings

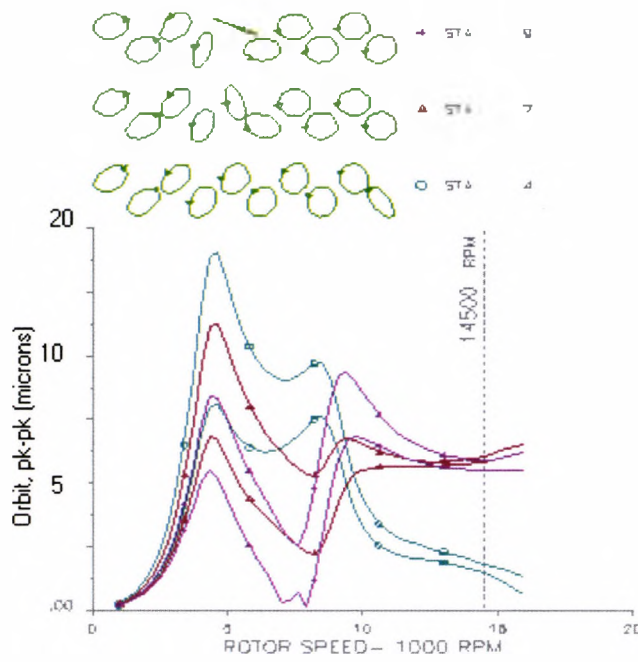


Figure 1B: Synchronous Response with in-phase unbalance - Amplitude at Motor

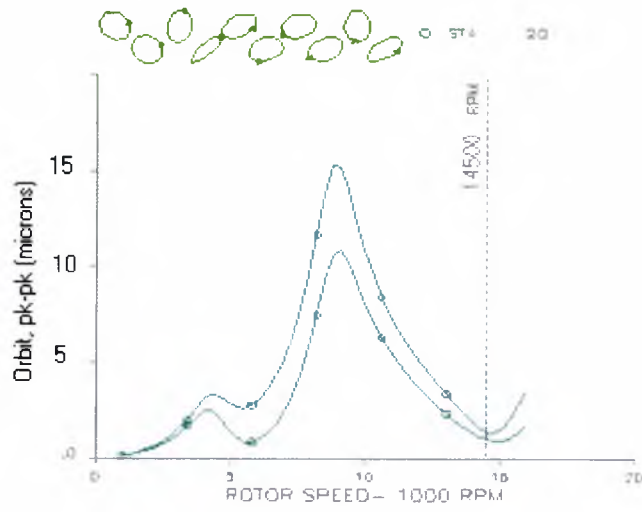


Figure 1C: Synchronous Response with in-phase unbalance - Amplitude at Impeller

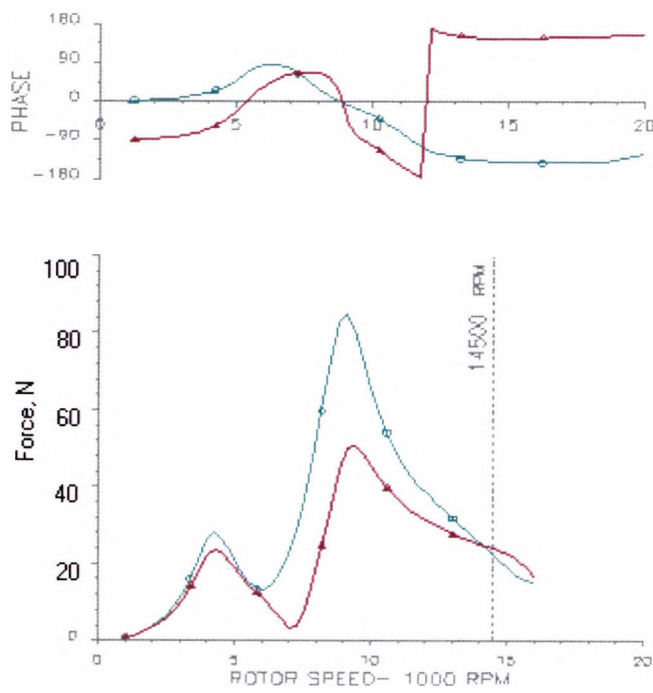
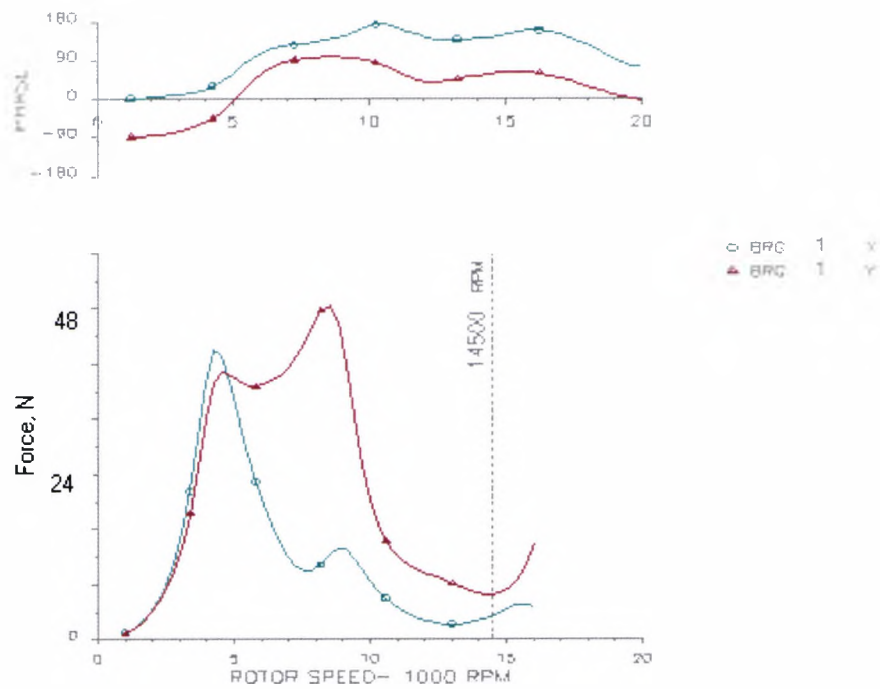


Figure 1D: Synchronous Response with in-phase unbalance - Force at Front Bearing



**Figure 1E: Synchronous Response with in-phase unbalance - Force at at Rear Bearing**

**Unbalance in-phase, ISO 1940**

AMPLIF FACTOR BASED ON MAJOR ORBIT

STATION	PK NO	RPM	AMPLIF FACTOR
3	1	4600.00	2.04
3	2	8500.00	1.45
4	1	4600.00	2.05
4	2	8500.00	1.44
7	1	4600.00	2.25
7	2	9400.00	.00
9	1	4300.00	2.37
9	2	9400.00	2.90
14	1	4300.00	2.68
14	2	9100.00	4.33
20	1	4300.00	.43
20	2	8800.00	4.53

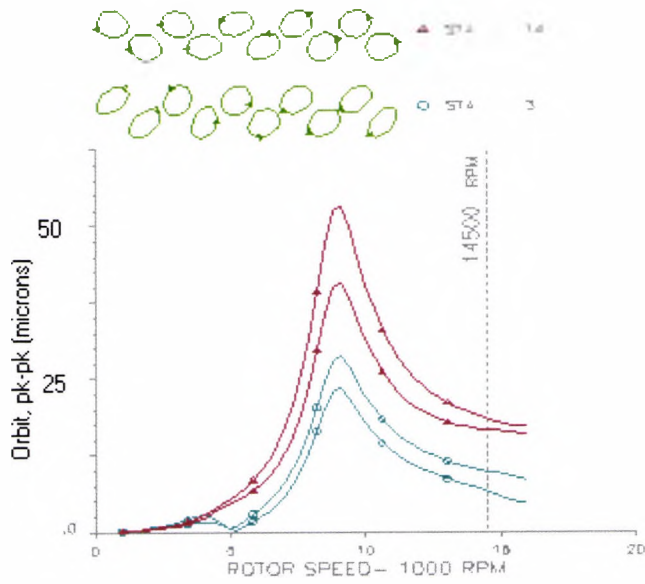


**Figure 1F: Synchronous Response with out of -phase unbalance - Amplitude at Bearings**

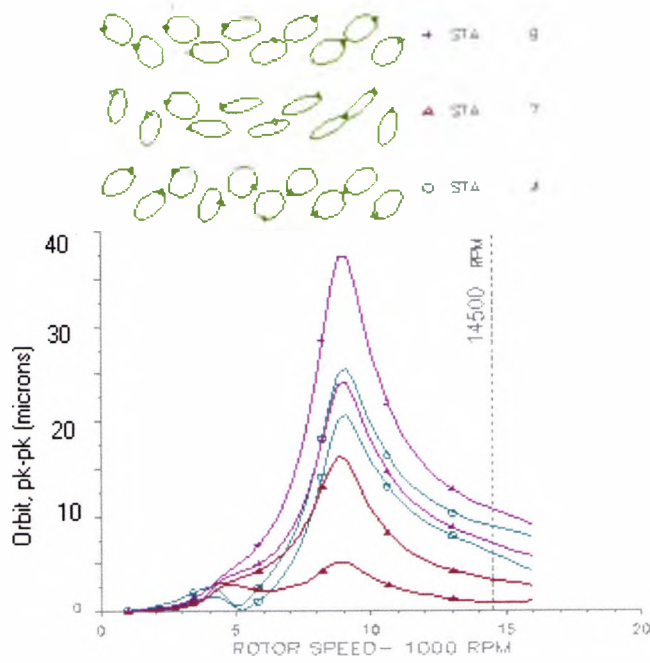


**Figure 1G: Synchronous Response with out of -phase unbalance - Amplitude at Motor**

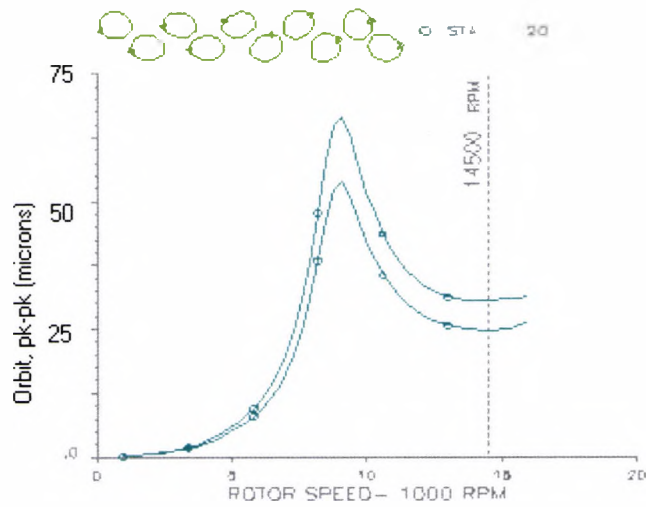


Figure 1H: Synchronous Response with out of-phase unbalance - Amplitude at Impeller

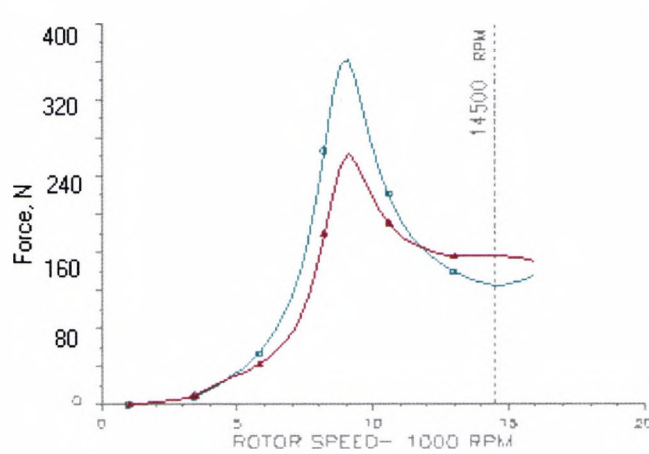
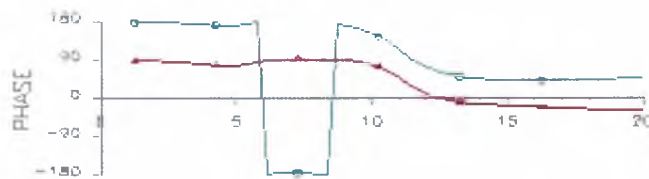
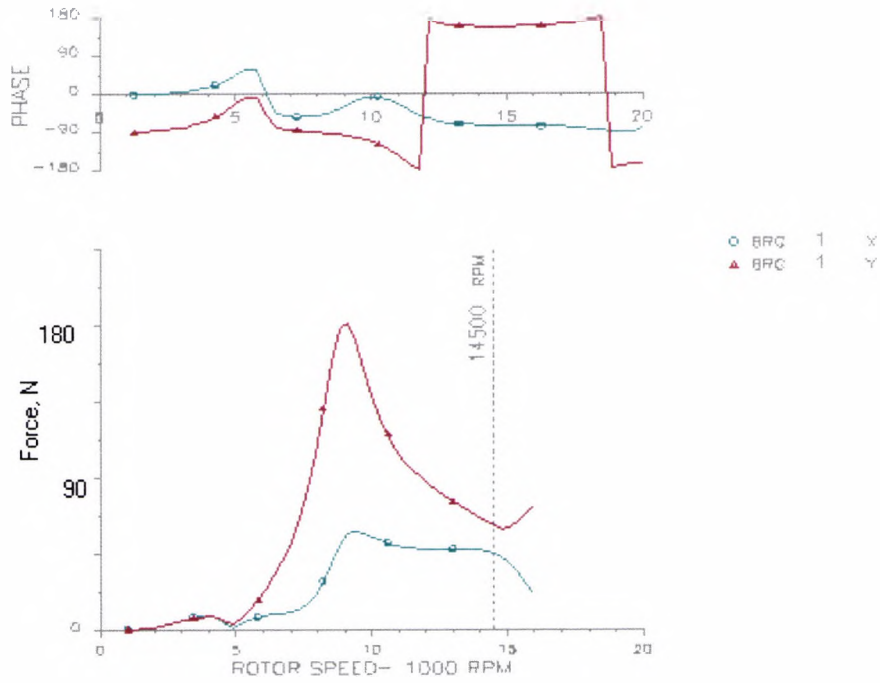


Figure 1J: Synchronous Response with out of-phase unbalance - Force at Front Bearing



**Figure 1K: Synchronous Response with out of -phase unbalance - Front at Rear Bearing**

**Unbalance out-of phase, ISO 1940**

AMPLIF FACTOR BASED ON MAJOR ORBIT

STATION	PK NO	RPM	AMPLIF FACTOR
3	1	4000.00	3.40
3	2	9100.00	4.36
4	1	4000.00	3.41
4	2	9100.00	4.36
7	1	8800.00	4.57
9	1	9100.00	4.52
14	1	9100.00	4.42
20	1	9100.00	4.26

XR3 High SPEED direct drive compressor xr3hspdm3.in  
 60 Hz, Hydrostatic Bearings, 200 psi, unbalance in-phase, ISO 1940  
 Unbalance response

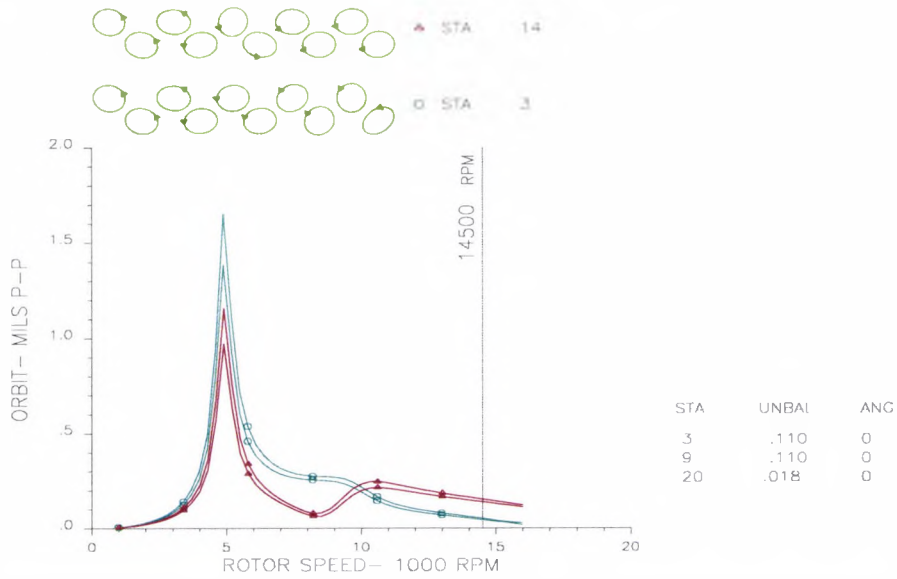


**Fig (2A): Synchronous Response with in - phase unbalance - Amplitude at Bearings**

XR3 High SPEED direct drive compressor xr3hspdm3.in  
 60 Hz, Hydrostatic Bearings, 200 psi, unbalance in-phase, ISO 1940  
 Unbalance response

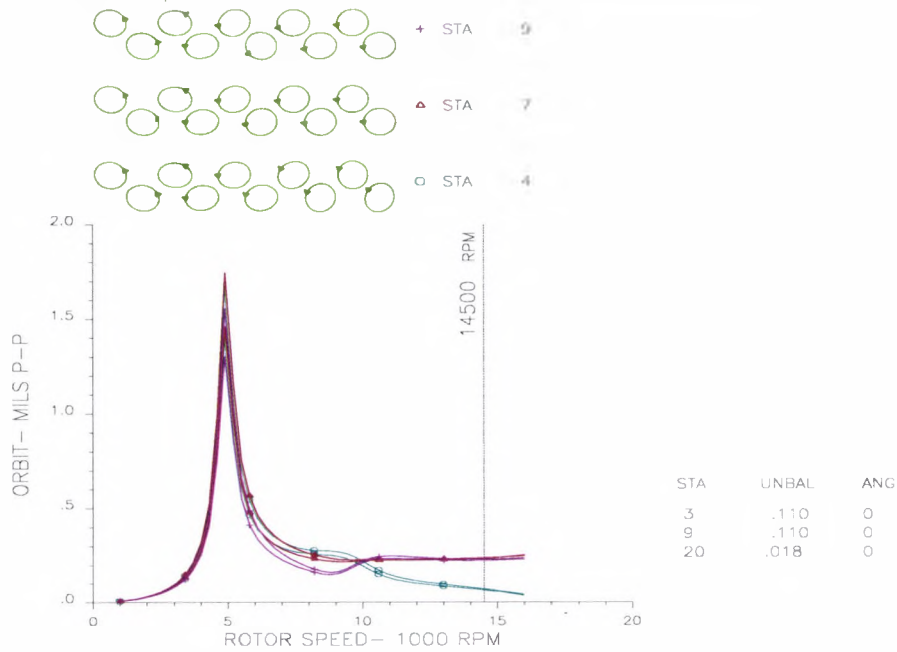


**Fig (2B): Synchronous Response with in - phase unbalance - Amplitude at Motor**

XR3 High SPEED direct drive compressor xr3hspdm3.in  
 60 Hz, Hydrostatic Bearings, 200 psi, unbalance in-phase, ISO 1940  
 Unbalance response

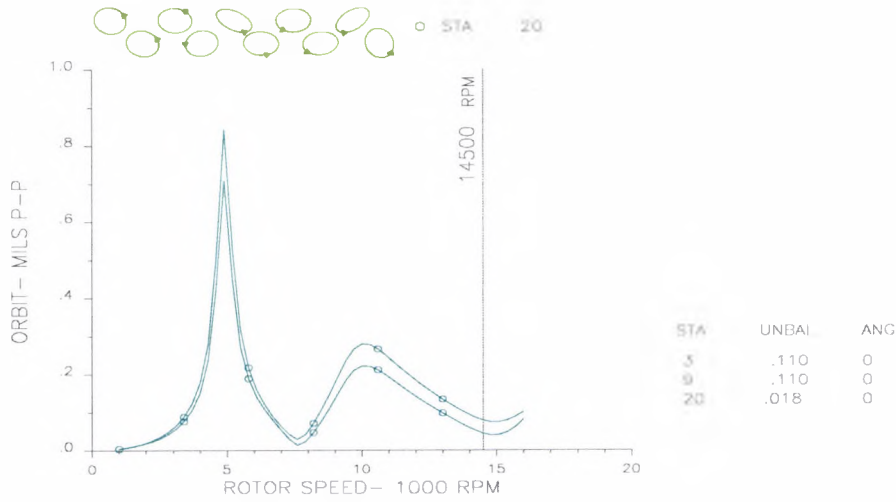


**Fig (2C): Synchronous Response with in - phase unbalance - Amplitude at Impeller**

XR3 High SPEED direct drive compressor xr3hspdm3.in  
 60 Hz, Hydrostatic Bearings, 200 psi, unbalance in - phase, ISO 1940  
 Unbalance response

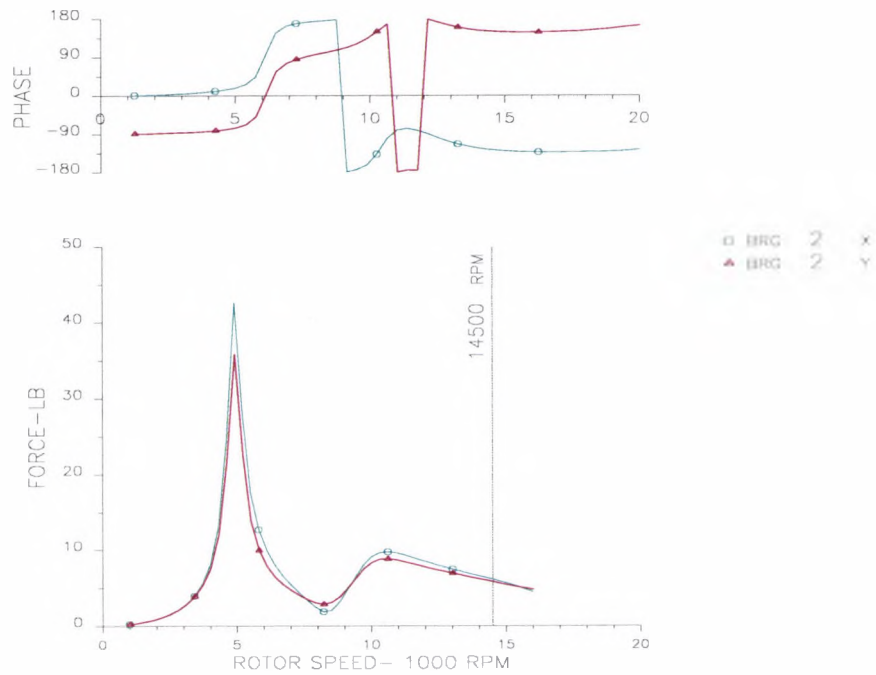


**Fig (2D): Synchronous Response with in - phase unbalance - Force at Front Bearing**

XR3 High SPEED direct drive compressor xr3hspdm3.in  
 60 Hz, Hydrostatic Bearings, 200 psi, unbalance in-phase, ISO 1940  
 Unbalance response

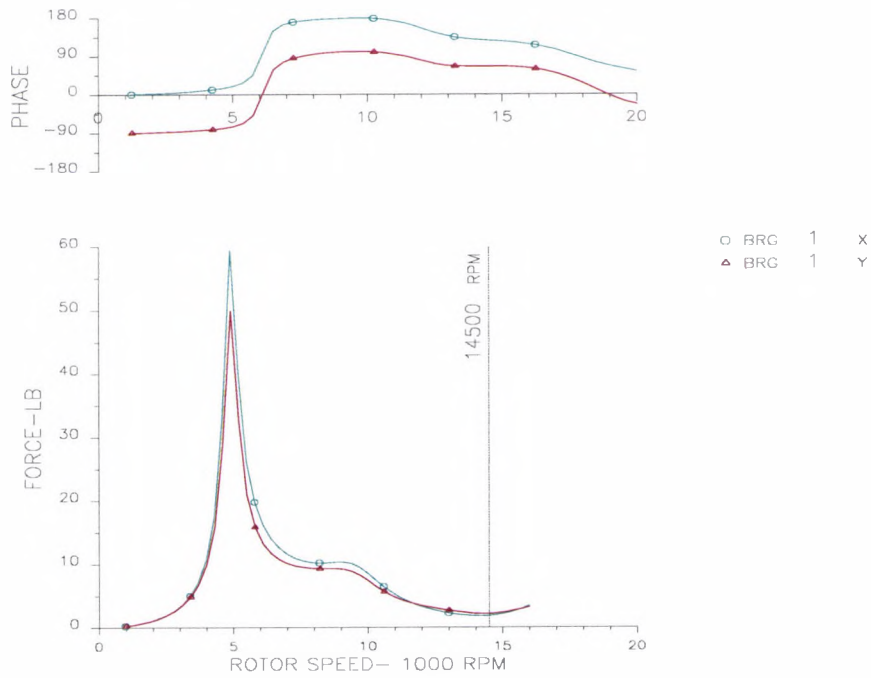


**Fig (2E): Synchronous Response with in - phase unbalance - Force at Rear Bearing**

**Unbalance in-phase, ISO 1940.**

**AMPLIFICATION FACTOR BASED ON MAJOR ORBIT**

STATION	PK NO	RPM	AMPLIF FACTOR
3	1	4900.00	10.46
4	1	4900.00	10.46
7	1	4900.00	10.47
7	2	10900.00	.00
9	1	4900.00	10.53
9	2	10900.00	.00
14	1	4900.00	10.64
14	2	10600.00	2.59
20	1	4900.00	10.78
20	2	10000.00	3.81

XR3 High SPEED direct drive compressor xr3hspdm31.in  
 60 Hz, Hydrostatic Bearings, 200 psi, unbalance out of-phase, ISO 1940  
 Unbalance response

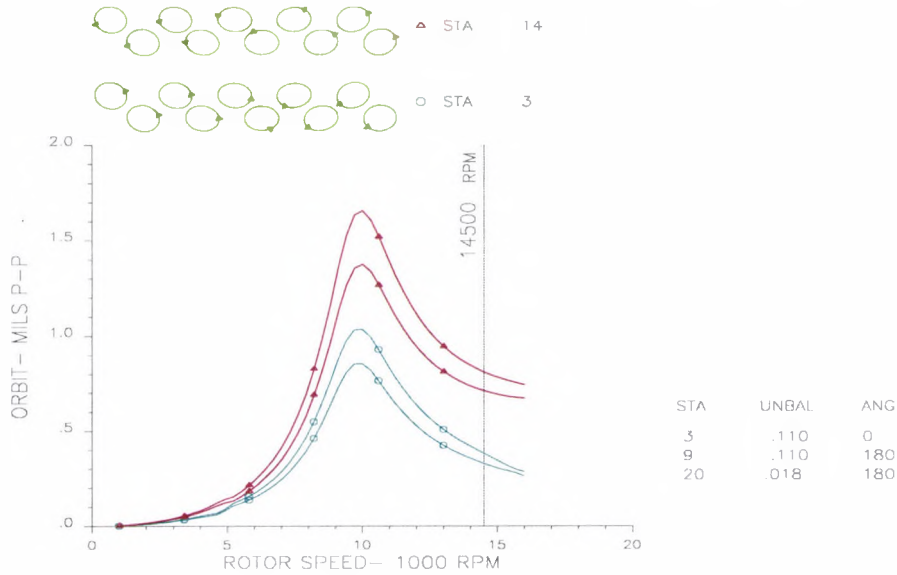


**Fig (2F): Synchronous Response with out of - phase unbalance - Amplitude at Bearings**

XR3 High SPEED direct drive compressor xr3hspdm31.in  
 60 Hz, Hydrostatic Bearings, 200 psi, unbalance out of-phase, ISO 1940  
 Unbalance response

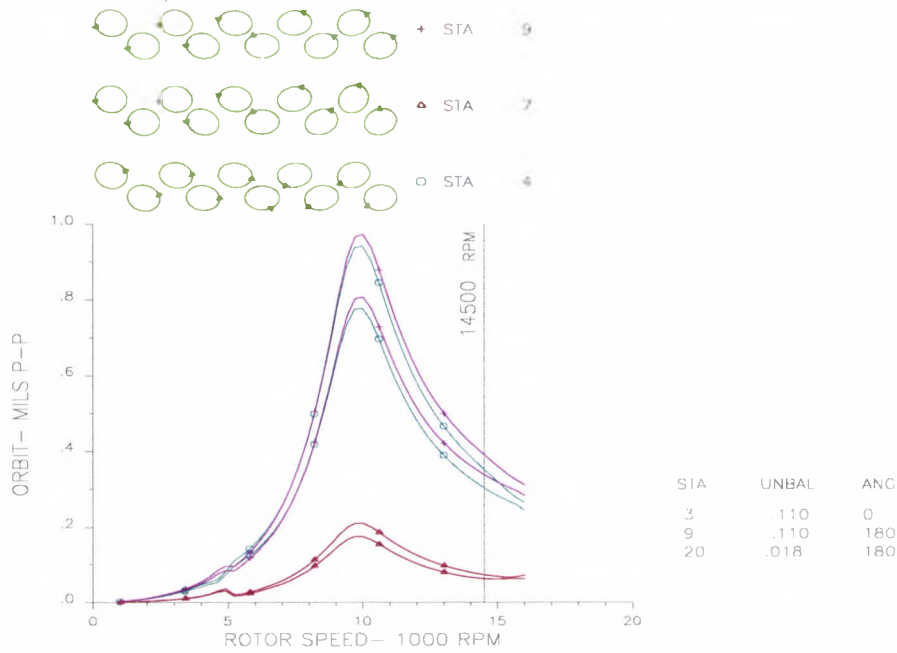


**Fig (2G): Synchronous Response with out of - phase unbalance - Amplitude at Motor**

XR3 High SPEED direct drive compressor xr3hspdm31.in  
 60 Hz, Hydrostatic Bearings, 200 psi, unbalance out-of-phase, ISO 1940  
 Unbalance response

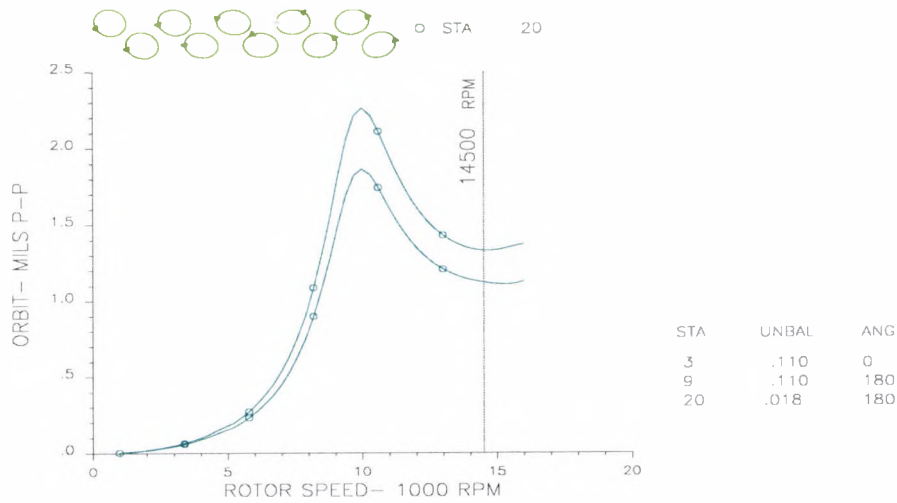


Fig (2H): Synchronous Response with out of - phase unbalance - Amplitude at Impeller

XR3 High SPEED direct drive compressor xr3hspdm31.in  
 60 Hz, Hydrostatic Bearings, 200 psi, unbalance out-of-phase, ISO 1940  
 Unbalance response

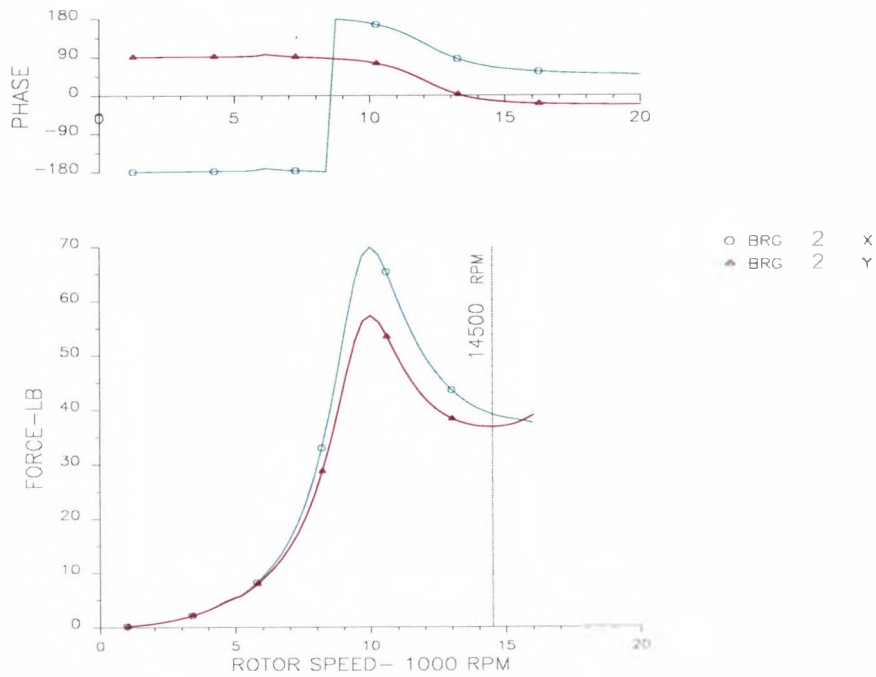
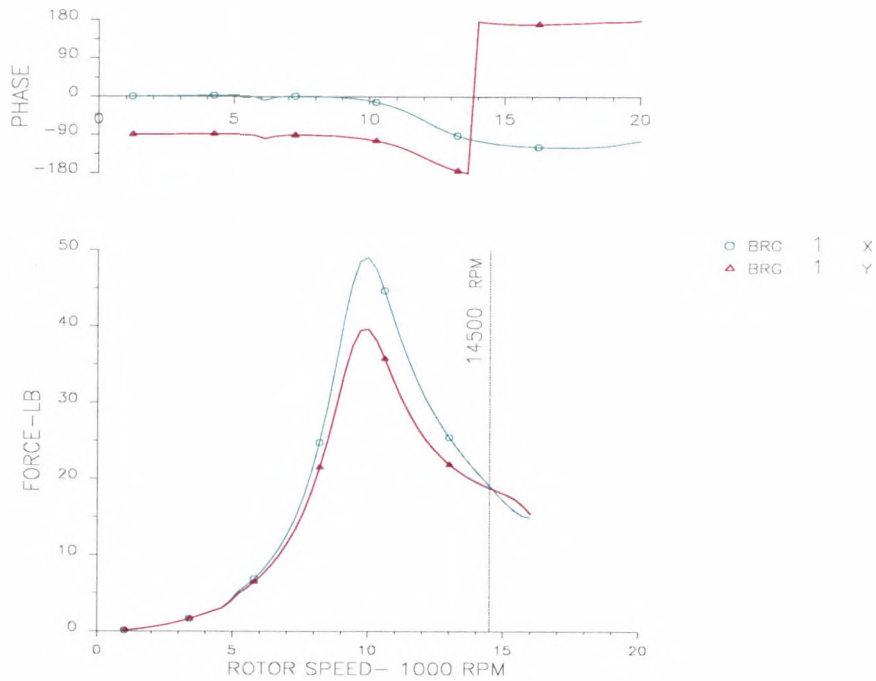


Fig (2J): Synchronous Response with out of - phase unbalance - Force at Front Bearing

XR3 High SPEED direct drive compressor xr3hspdm31.in  
 60 Hz, Hydrostatic Bearings, 200 psi, unbalance out of-phase, ISO 1940  
 Unbalance response



**Fig (2K): Synchronous Response with out of - phase unbalance - Force at Rear Bearing**

**Unbalance out of-phase, ISO 1940.**  
**AMPLIFICATION FACTOR BASED ON MAJOR ORBIT**

STATION	PK NO	RPM	AMPLIF FACTOR
3	1	10000.00	3.65
4	1	10000.00	3.64
7	1	4900.00	7.14
7	2	9700.00	3.64
9	1	4900.00	.00
9	2	10000.00	3.59
14	1	10000.00	3.40
20	1	10000.00	3.11

XR3 High SPEED direct drive compressor xr3hspdm1.in  
 60 Hz, Hydrostatic Bearings, 250 psi, Unbalance in-phase, ISO 1940  
 Unbalance response

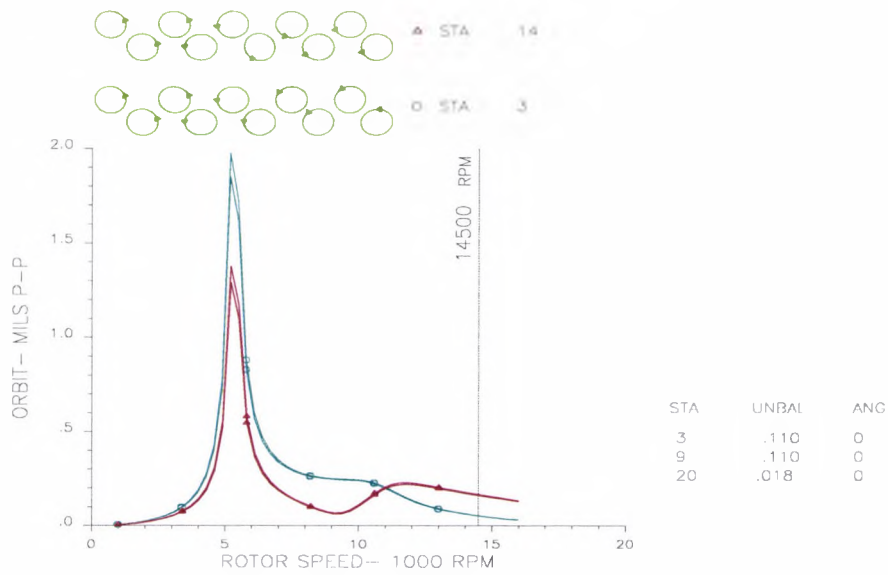


**Fig (3A): Synchronous Response with in- phase unbalance - Amplitude at Bearings**

XR3 High SPEED direct drive compressor xr3hspdm1.in  
 60 Hz, Hydrostatic Bearings, 250 psi, Unbalance in-phase, ISO 1940  
 Unbalance response

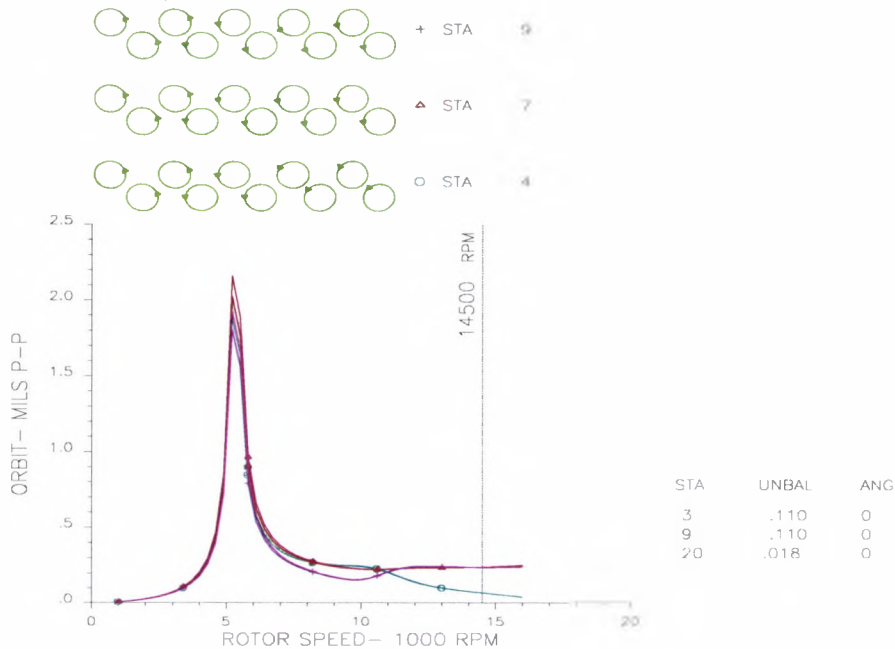


**Fig (3B): Synchronous Response with in- phase unbalance - Amplitude at Motor**

XR3 High SPEED direct drive compressor xr3hspdm1.in  
 60 Hz, Hydrostatic Bearings, 250 psi, Unbalance in-phase, ISO 1940  
 Unbalance response

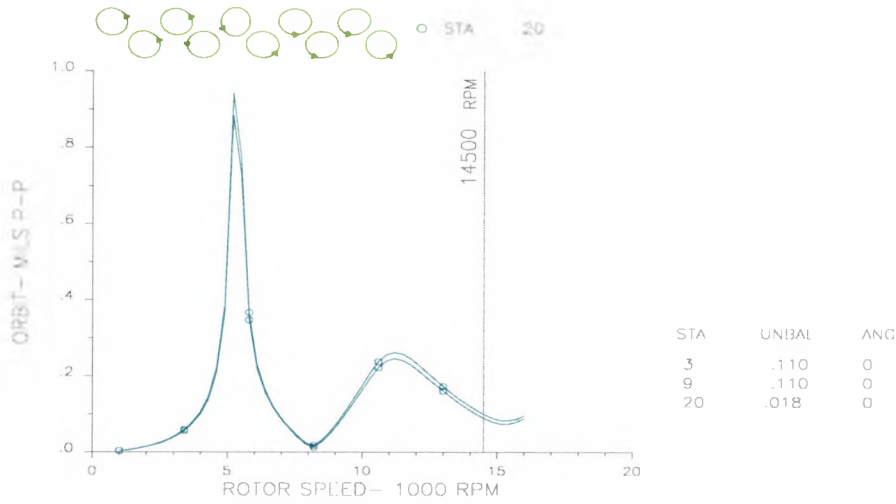


**Fig (3C): Synchronous Response with in- phase unbalance - Amplitude at Impeller**

XR3 High SPEED direct drive compressor xr3hspdm1.in  
 60 Hz, Hydrostatic Bearings, 250 psi, Unbalance in-phase, ISO 1940  
 Unbalance response

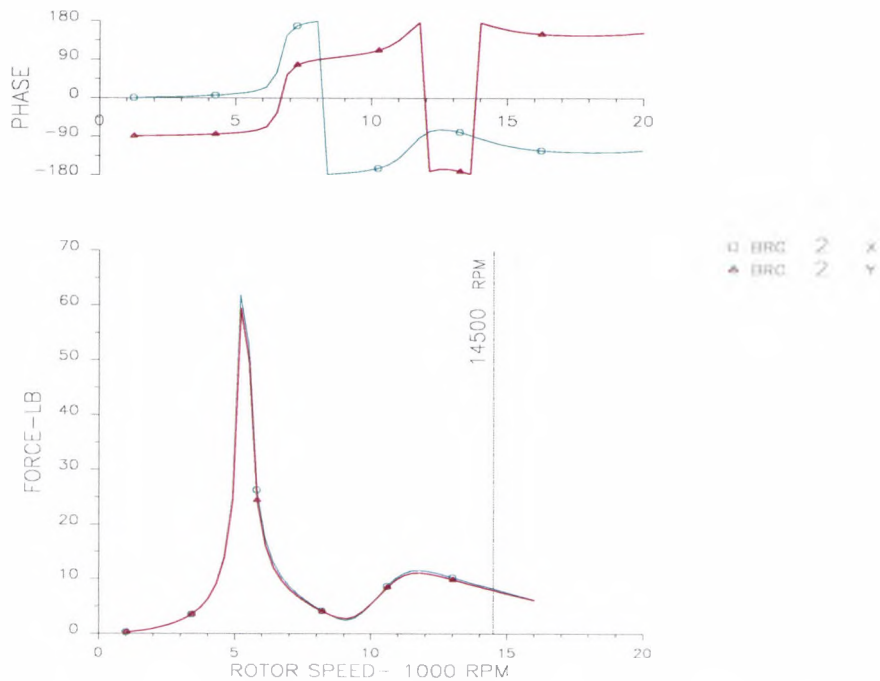


**Fig (3D): Synchronous Response with in- phase unbalance - Force at Front Bearing**

XR3 High SPEED direct drive compressor xr3hspdm1.in  
 60 Hz, Hydrostatic Bearings, 250 psi, Unbalance in-phase, ISO 1940  
 Unbalance response

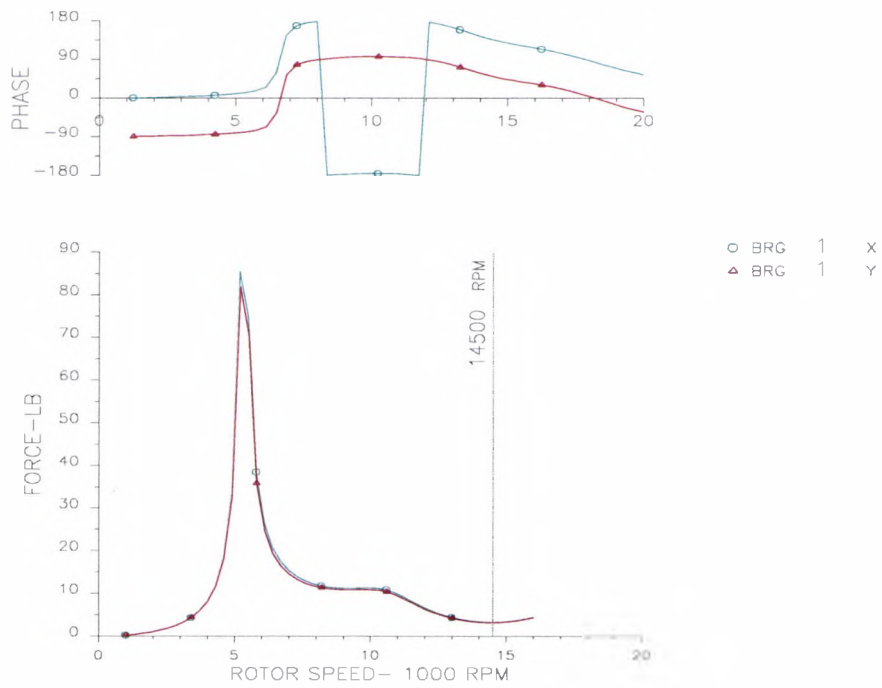


**Fig (3E): Synchronous Response with in- phase unbalance - Force at Rear Bearing**

XR3 High SPEED direct drive compressor xr3hspdm12.in  
 60 Hz, Hydrostatic Bearings, 250 psi, Unbalance opposite phase, ISO 1940  
 Unbalance response

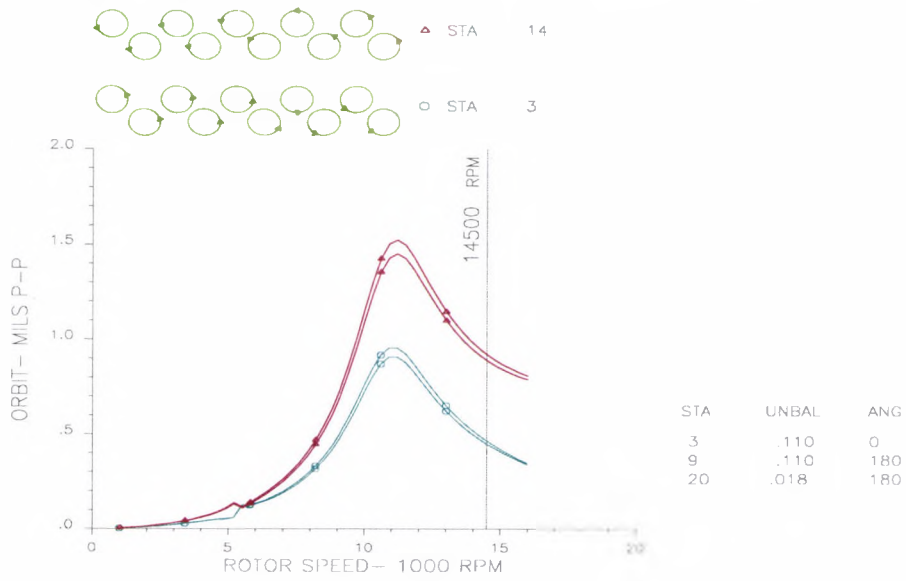


**Fig (3F): Synchronous Response with out of - phase unbalance - Amplitude at Bearings**

XR3 High SPEED direct drive compressor xr3hspdm12.in  
 60 Hz, Hydrostatic Bearings, 250 psi, Unbalance opposite phase, ISO 1940  
 Unbalance response

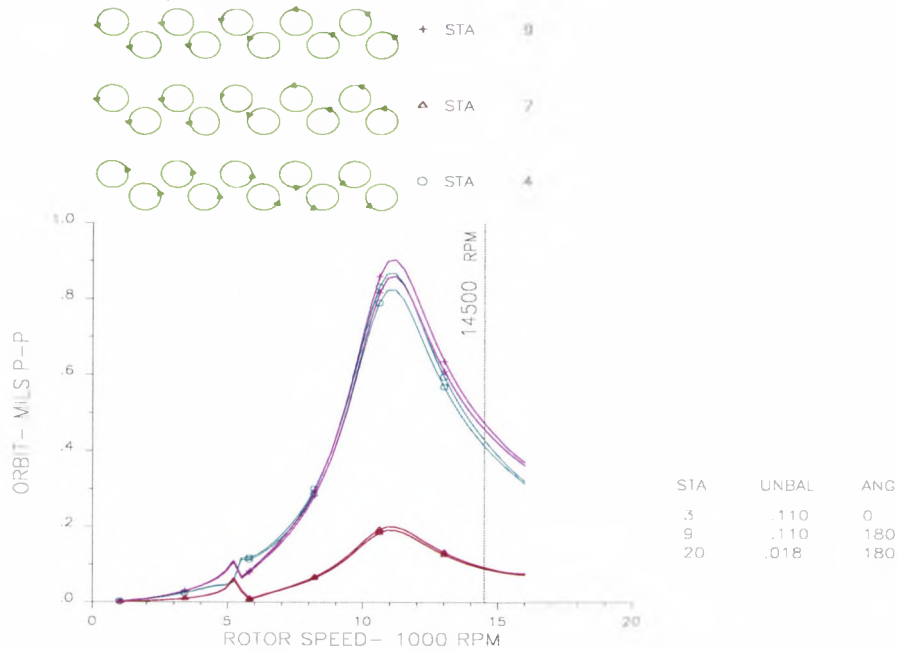


**Fig (3G): Synchronous Response with out of - phase unbalance - Amplitude at Motor**

XR3 High SPEED direct drive compressor xr3hspdm12.in  
 60 Hz, Hydrostatic Bearings, 250 psi, Unbalance opposite phase, ISO 1940  
 Unbalance response

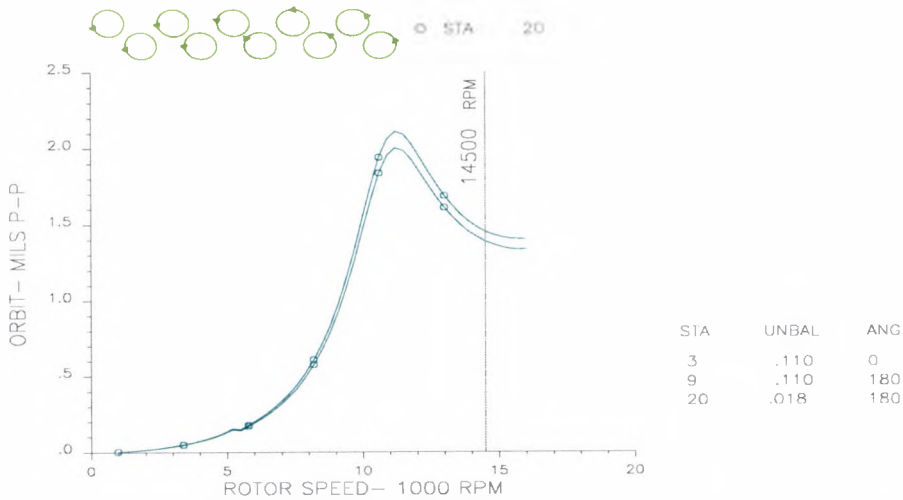


**Fig (3H): Synchronous Response with out of - phase unbalance - Amplitude at Impeller**

XR3 High SPEED direct drive compressor xr3hspdm12.in  
 60 Hz, Hydrostatic Bearings, 250 psi, Unbalance opposite phase, ISO 1940  
 Unbalance response

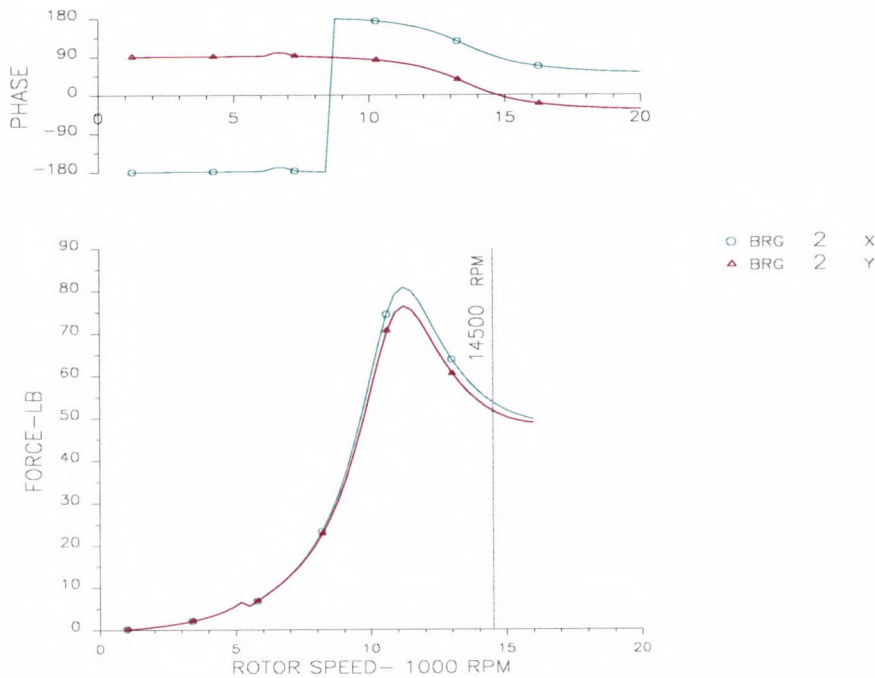


**Fig (3J): Synchronous Response with out of - phase unbalance - Force at Front Bearing**

XR3 High SPEED direct drive compressor xr3hspdm12.in  
 60 Hz, Hydrostatic Bearings, 250 psi, Unbalance opposite phase, ISO 1940  
 Unbalance response

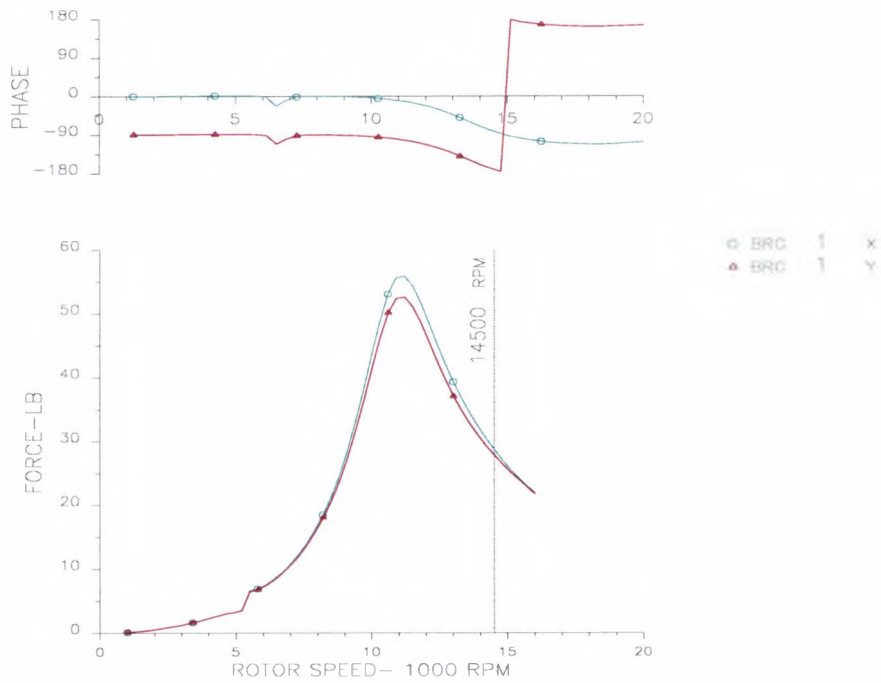


**Fig (3K): Synchronous Response with out of - phase unbalance - Force at Rear Bearing**

XR3 High SPEED direct drive compressor xr3hspdm2.in  
 60 Hz, Hydrostatic Bearings, 300 psi, unbalance in-phase, ISO 1940  
 Unbalance response

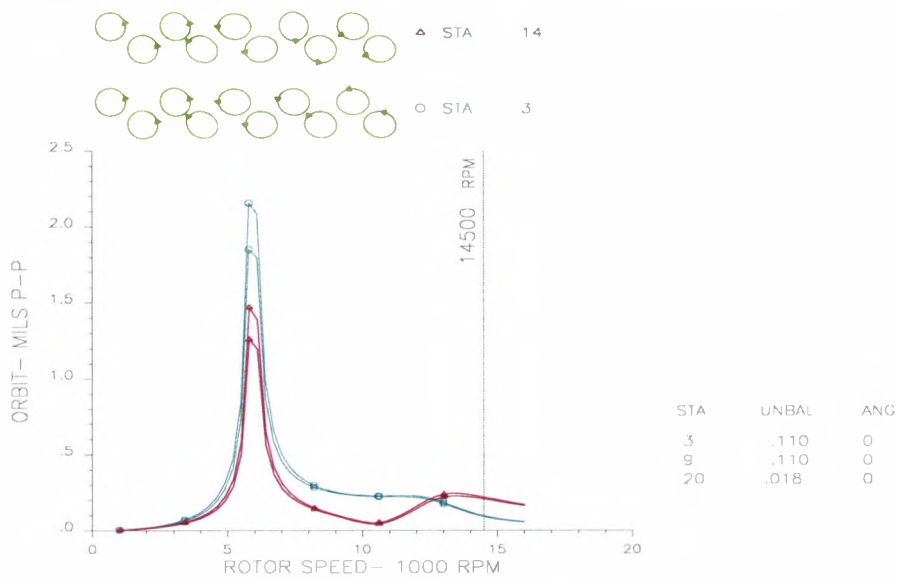


**Fig (4A): Synchronous Response with in- phase unbalance - Amplitude at Bearings**

XR3 High SPEED direct drive compressor xr3hspdm2.in  
 60 Hz, Hydrostatic Bearings, 300 psi, unbalance in-phase, ISO 1940  
 Unbalance response

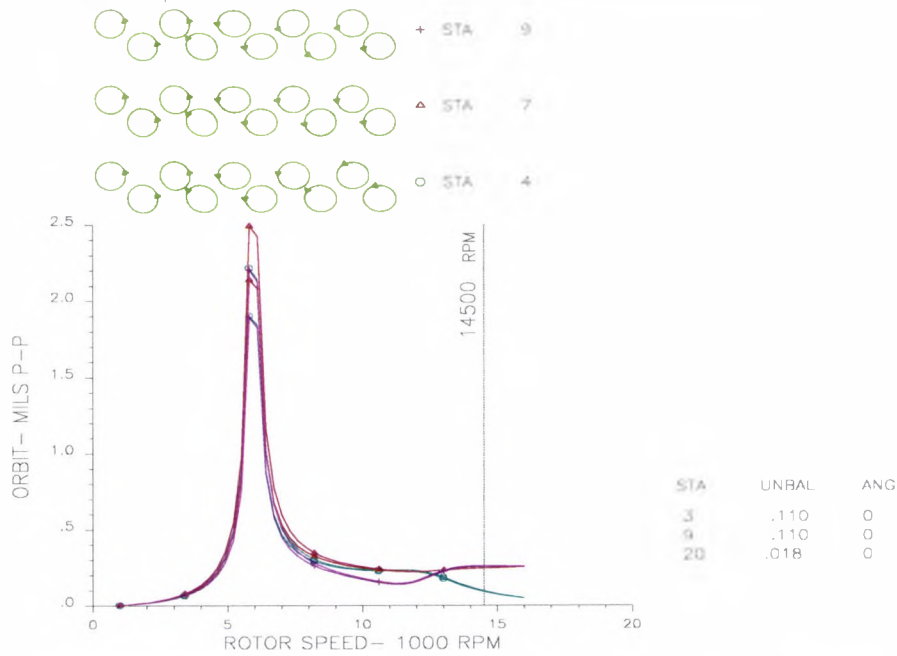


**Fig (4B): Synchronous Response with in- phase unbalance - Amplitude at Motor**

XR3 High SPEED direct drive compressor xr3hspdm2.in  
 60 Hz, Hydrostatic Bearings, 300 psi, unbalance in-phase, ISO 1940  
 Unbalance response

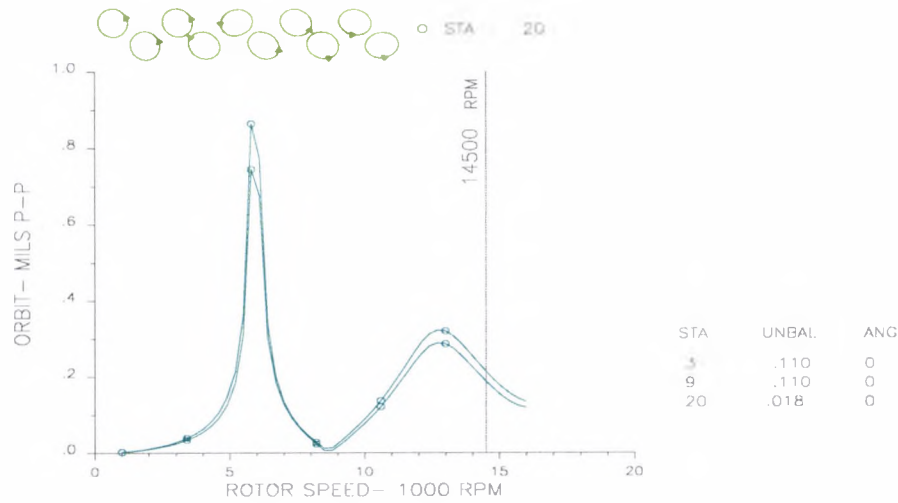


**Fig (4C): Synchronous Response with in- phase unbalance - Amplitude at Impeller**

XR3 High SPEED direct drive compressor xr3hspdm2.in  
 60 Hz, Hydrostatic Bearings, 300 psi, unbalance in-phase, ISO 1940  
 Unbalance response

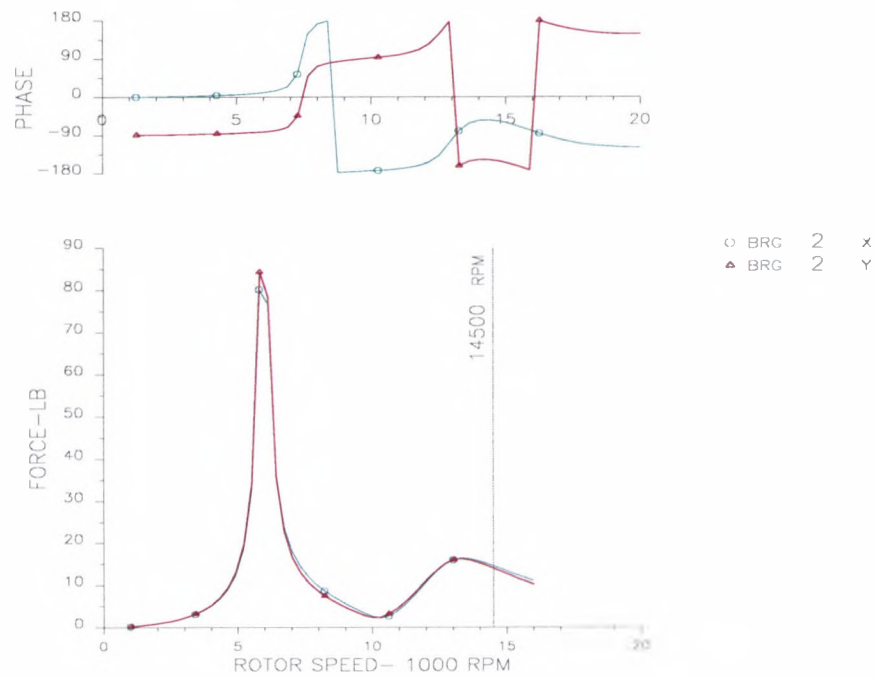


**Fig (4D): Synchronous Response with in- phase unbalance - Force at Front Bearing**

XR3 High SPEED direct drive compressor xr3hspdm2.in  
 60 Hz, Hydrostatic Bearings, 300 psi, unbalance in-phase, ISO 1940  
 Unbalance response

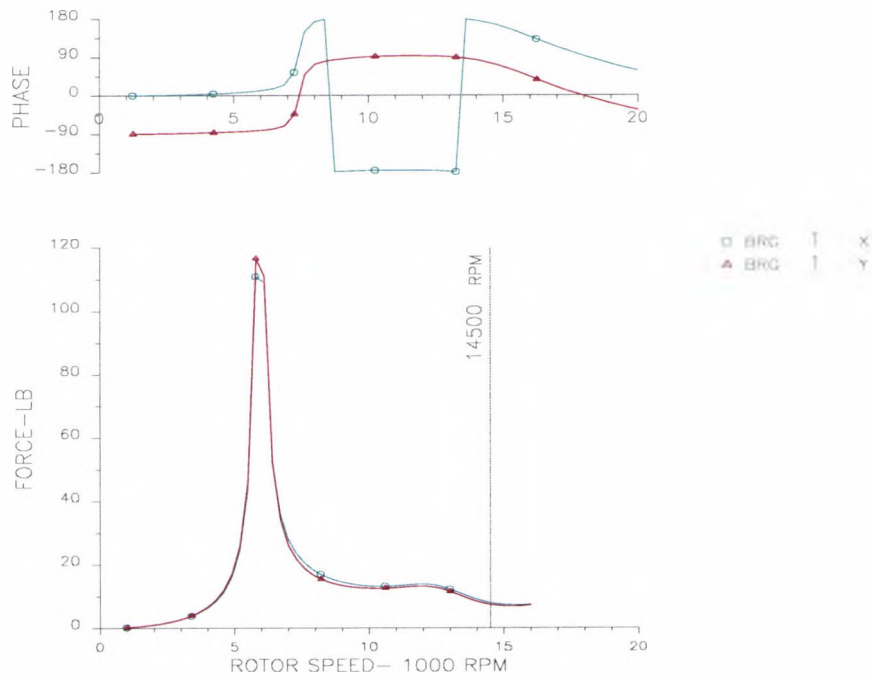


**Fig (4E): Synchronous Response with in- phase unbalance - Force at Rear Bearing**

**Unbalance in-phase, ISO 1940.**  
**AMPLIFICATION FACTOR BASED ON MAJOR ORBIT**

STATION	PK NO	RPM	AMPLIF FACTOR
3	1	5800.00	9.68
3	2	11500.00	1.27
4	1	5800.00	9.67
4	2	11500.00	1.28
7	1	5800.00	9.64
9	1	5800.00	9.71
9	2	14500.00	.00
14	1	5800.00	9.86
14	2	13300.00	3.57
20	1	5800.00	10.29
20	2	12700.00	4.52

XR3 High SPEED direct drive compressor xr3hspdm21.in  
 60 Hz, Hydrostatic Bearings, 300 psi, Opposite Phase unbalance  
 Unbalance response

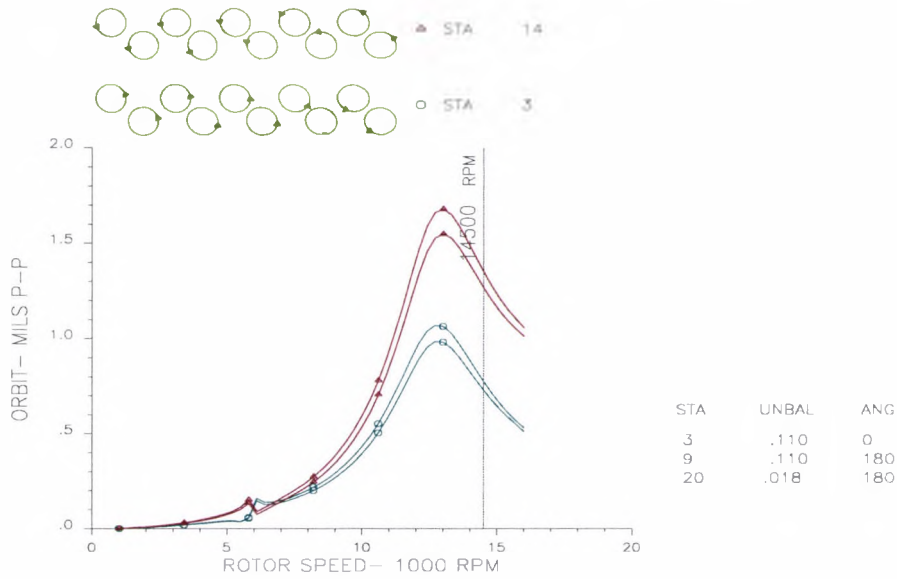


**Fig (4F): Synchronous Response with out of - phase unbalance - Amplitude at Bearings**

XR3 High SPEED direct drive compressor xr3hspdm21.in  
 60 Hz, Hydrostatic Bearings, 300 psi, Opposite Phase unbalance  
 Unbalance response

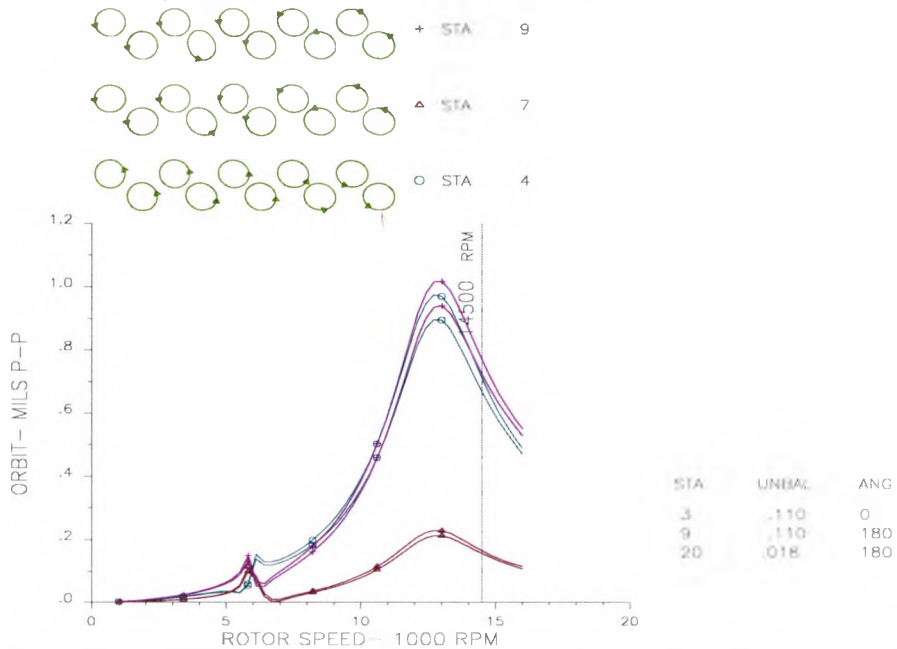


**Fig (4G): Synchronous Response with out of - phase unbalance - Amplitude at Motor**

XR3 High SPEED direct drive compressor xr3hspdm21.in  
 60 Hz, Hydrostatic Bearings, 300 psi, Opposite Phase unbalance  
 Unbalance response

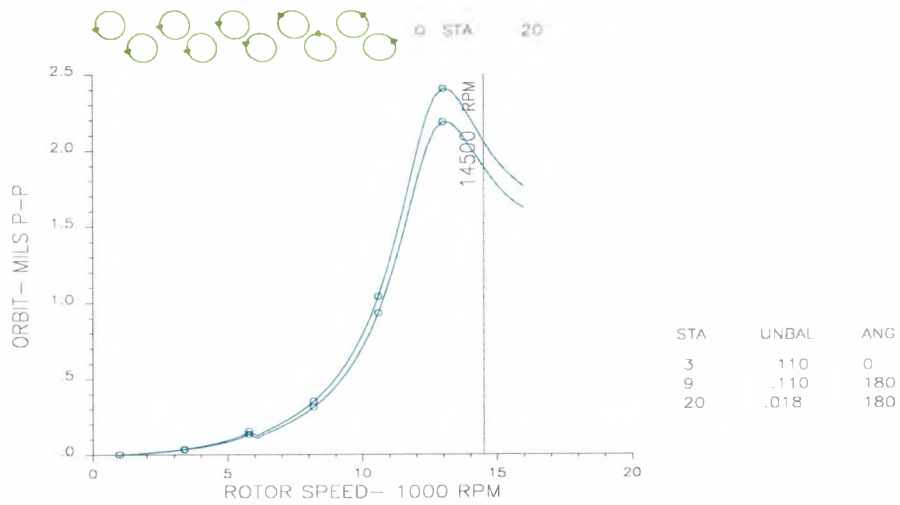


**Fig (4H): Synchronous Response with out of - phase unbalance - Amplitude at Impeller**

XR3 High SPEED direct drive compressor xr3hspdm21.in  
 60 Hz, Hydrostatic Bearings, 300 psi, Opposite Phase unbalance  
 Unbalance response

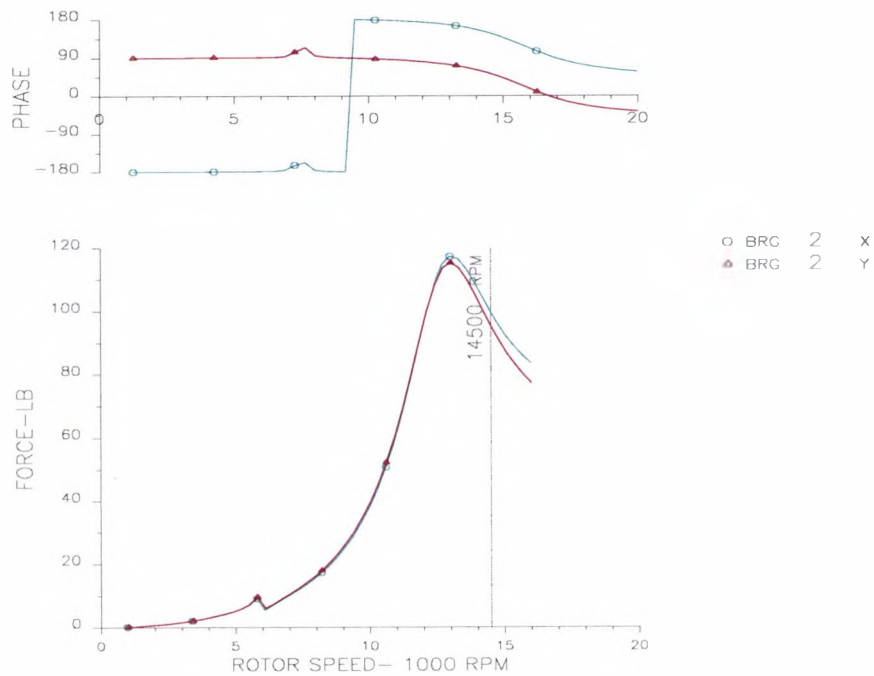


**Fig (4J): Synchronous Response with out of - phase unbalance - Force at Front Bearing**

XR3 High SPEED direct drive compressor xr3hspdm21.in  
 60 Hz, Hyarostatic Bearings, 300 psi, Opposite Phase unbalance  
 Unbalance response

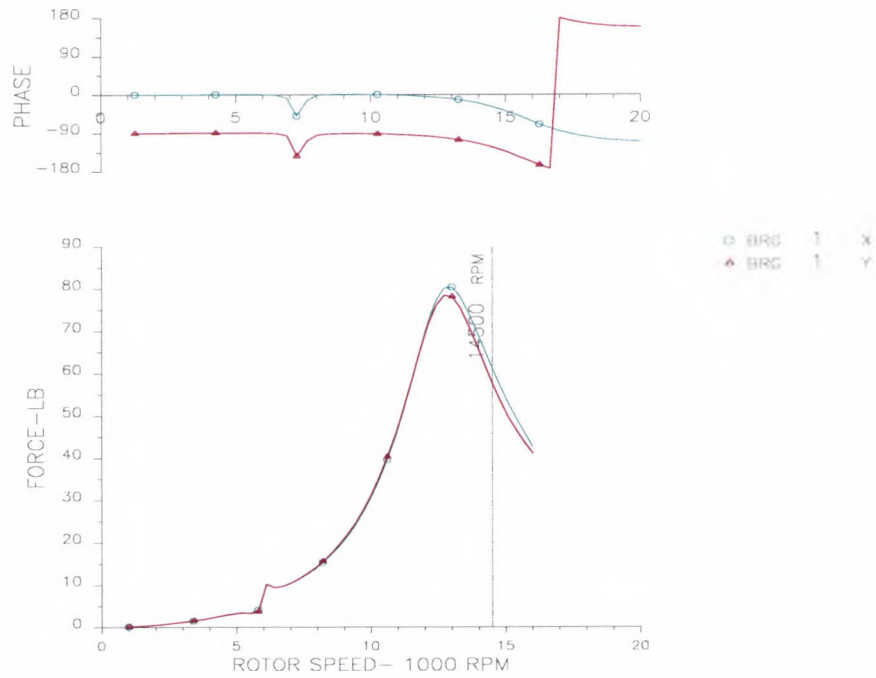


**Fig (4K): Synchronous Response with out of - phase unbalance - Force at Rear Bearing**

**Unbalance out-of-phase**  
**AMPLIF FACTOR BASED ON MAJOR ORBIT**

STATION	PK NO	RPM	AMPLIF FACTOR
3	1	5200.00	.00
3	2	6100.00	.00
3	3	12700.00	3.92
4	1	5200.00	.00
4	2	6100.00	.00
4	3	12700.00	3.90
7	1	5800.00	11.92
7	2	12700.00	4.00
9	1	5800.00	14.30
9	2	13000.00	3.88
14	1	5800.00	9.85
14	2	13000.00	3.52
20	1	5800.00	.00
20	2	13000.00	.00

### Actual unbalance case

The residual unbalance of the test motor rotor was obtained by balancing the machine readout. Similarly for the impeller, the residual unbalance was obtained from the balancing machine. Unfortunately, the angular position was not noted in both cases. Hence, the amount of residual unbalance in all the balancing planes is known, but not their angular orientation. This case is referred to as actual unbalance and the results of the response analysis for 1.7Mpa and 2.1Mpa are shown in figures 5A through 5E and 6A through 6E. The unbalance at the rear bearing end balancing plane is opposite to that at the front bearing end plane and the impeller.

XR3 High SPEED direct drive compressor xr3hspdm12.in  
 60 Hz, Hydrostatic Bearings, 250 psi, Unbalance opposite phase, actual value  
 Unbalance response

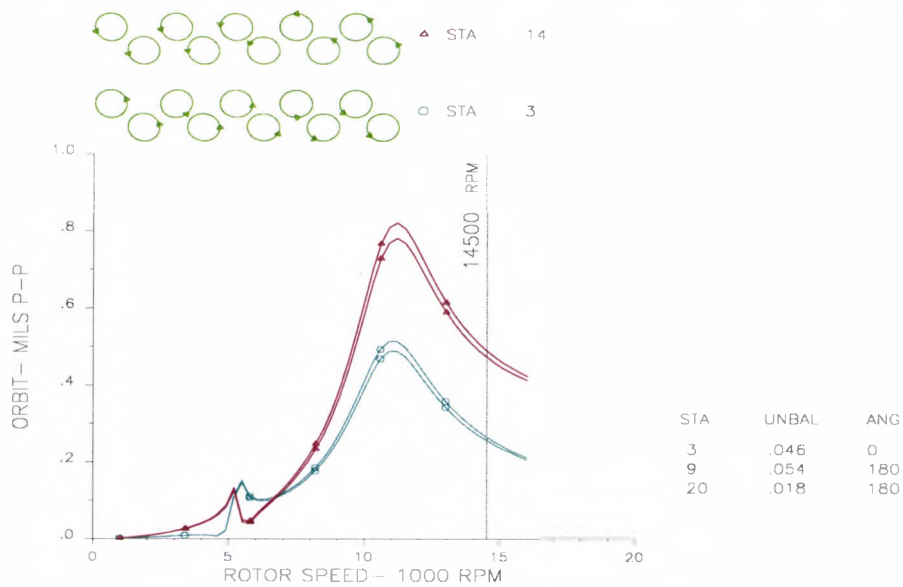


**Fig (5A): Synchronous Response with out of - phase unbalance - Amplitude at Bearings, Actual Unbalance – supply pressure 1.7MPa**

XR3 High SPEED direct drive compressor xr3hspdm12.in  
 60 Hz, Hydrostatic Bearings, 250 psi, Unbalance opposite phase, actual value  
 Unbalance response

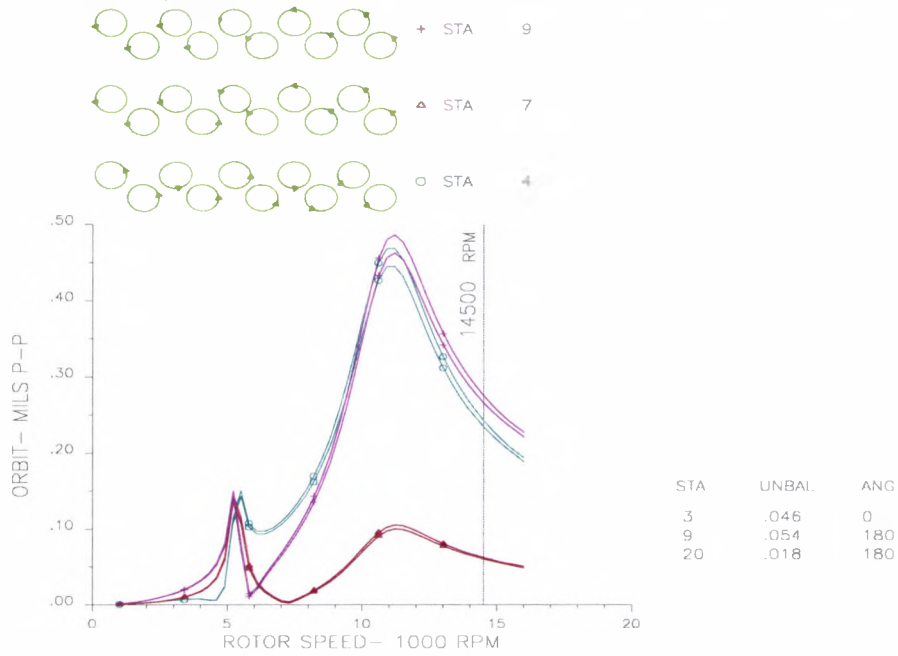


**Fig (5B): Synchronous Response with out of - phase unbalance - Amplitude at Impeller, Actual Unbalance – Supply pressure 1.7MPa**

XR3 High SPEED direct drive compressor xr3hspdm12.in  
 60 Hz, Hydrostatic Bearings, 250 psi, Unbalance opposite phase, actual value  
 Unbalance response

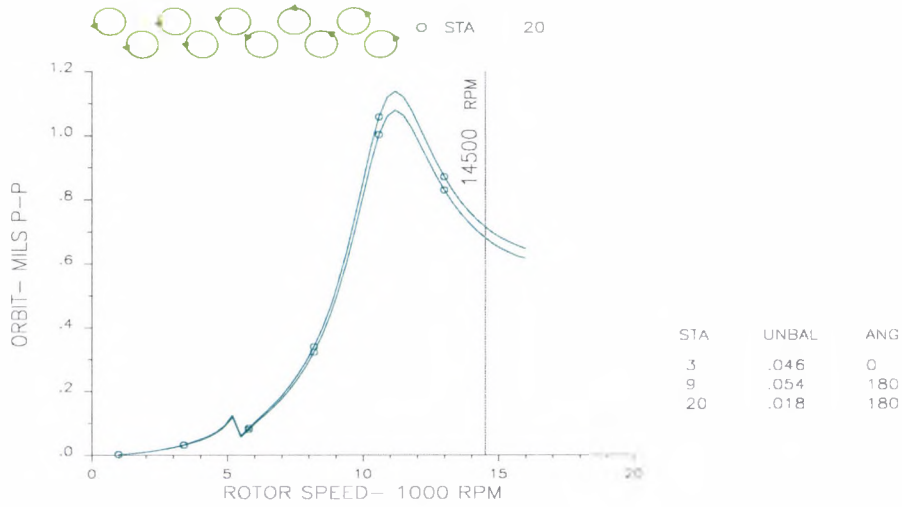


**Fig (5C): Synchronous Response with out of - phase unbalance - Amplitude at Impeller, Actual Unbalance - supply pressure 1.7MPa**

XR3 High SPEED direct drive compressor xr3hspdm12.in  
 60 Hz, Hydrostatic Bearings, 250 psi, Unbalance opposite phase, actual value  
 Unbalance response

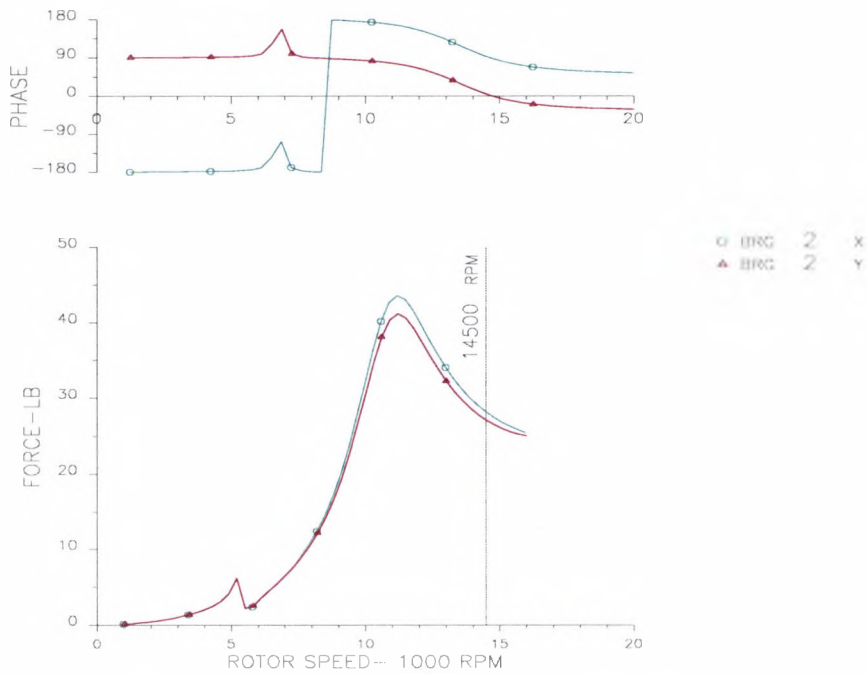


**Fig (5D): Synchronous Response with out of - phase unbalance - Force at Front Bearing Actual Unbalance - supply pressure 1.7MPa**

XR3 High SPEED direct drive compressor xr3hspdm12.in  
 60 Hz, Hydrostatic Bearings, 250 psi, Unbalance opposite phase, actual value  
 Unbalance response

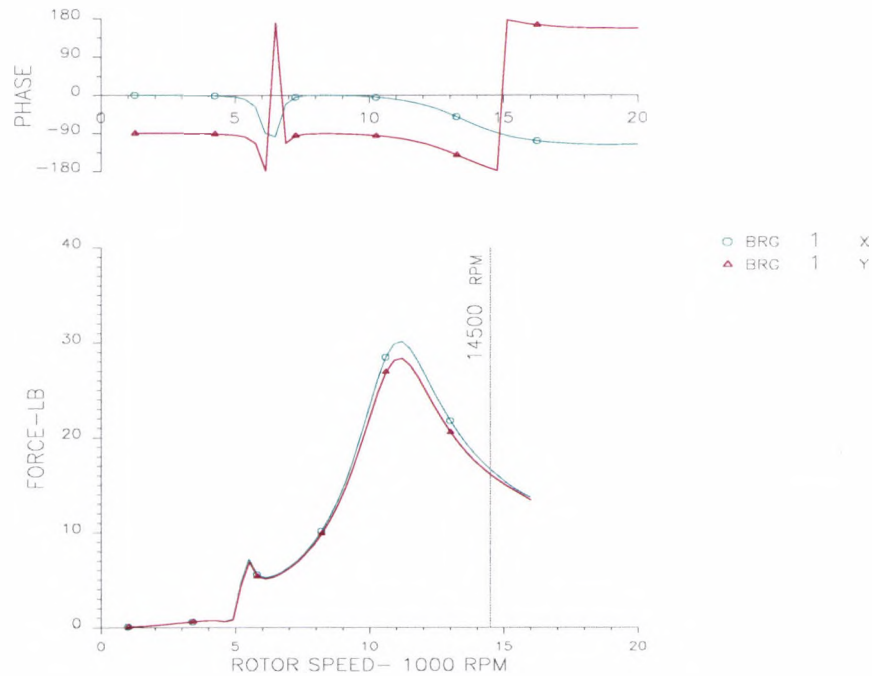


**Fig (5E): Synchronous Response with out of - phase unbalance - Force at Rear Bearing, Actual Unbalance - supply pressure 1.7MPa**

**Unbalance opposite phase, actual value**  
**AMPLIF FACTOR BASED ON MAJOR ORBIT**

STATION	PK NO	RPM	AMPLIF FACTOR
3	1	4000.00	.00
3	2	5500.00	7.63
3	3	11200.00	3.48
4	1	3700.00	.00
4	2	5500.00	8.56
4	3	11200.00	3.47
7	1	5200.00	10.22
7	2	11200.00	3.29
9	1	5200.00	13.92
9	2	11200.00	3.36
14	1	5200.00	13.53
14	2	11200.00	3.23
20	1	5200.00	9.82
20	2	11200.00	3.08

XR3 High SPEED direct drive compressor xr3hspdm22.in  
 60 Hz, Hydrostatic Bearings, 300 psi, Opposite Phase unbalance, actual unbalance  
 Unbalance response

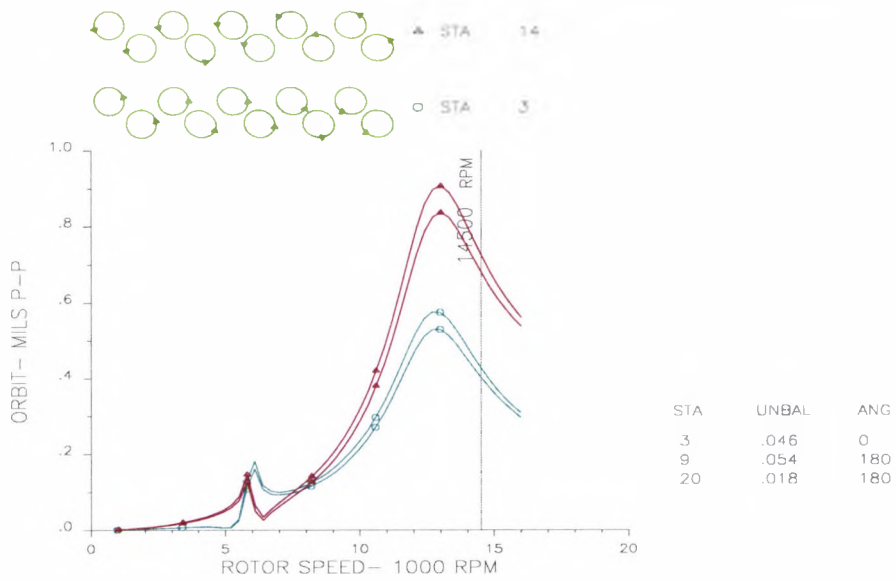


**Fig (6A): Synchronous Response with out of - phase unbalance - Amplitude at Bearings, Actual Unbalance - supply pressure 2.1MPa**

XR3 High SPEED direct drive compressor xr3hspdm22.in  
 60 Hz, Hydrostatic Bearings, 300 psi, Opposite Phase unbalance, actual unbalance  
 Unbalance response

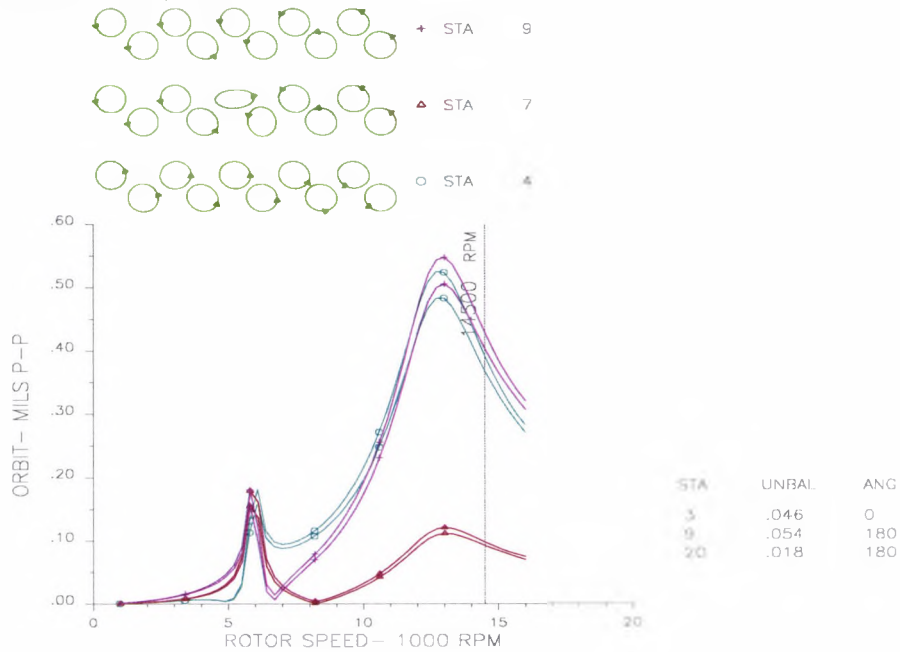


**Fig (6B): Synchronous Response with out of - phase unbalance - Amplitude at Motor Actual Unbalance- supply pressure 2.1MPa**

XR3 High SPEED direct drive compressor xr3hspdm22.in  
 60 Hz, Hydrostatic Bearings, 300 psi, Opposite Phase unbalance, actual unbalance  
 Unbalance response

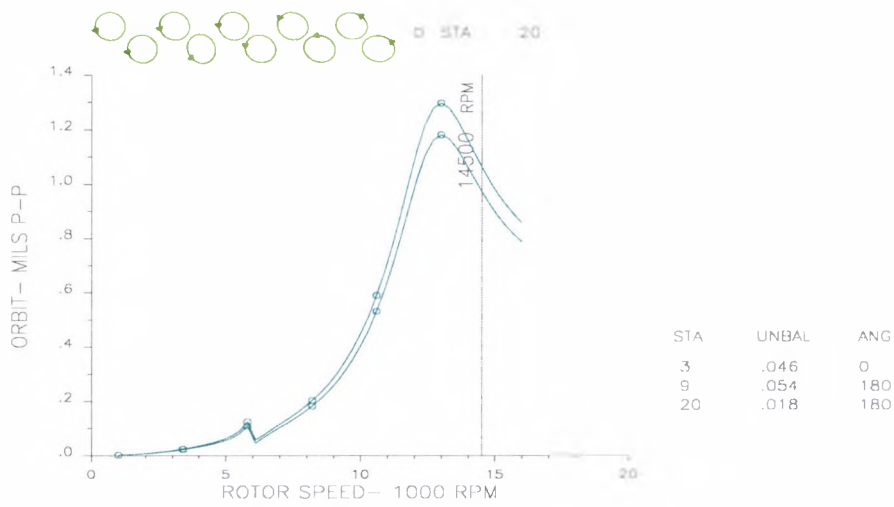


**Fig (6C): Synchronous Response with out of - phase unbalance - Amplitude at Impeller, Actual Unbalance- supply pressure 2.1MPa**

XR3 High SPEED direct drive compressor xr3hspdm22.in  
 60 Hz, Hydrostatic Bearings, 300 psi, Opposite Phase unbalance, actual unbalance  
 Unbalance response

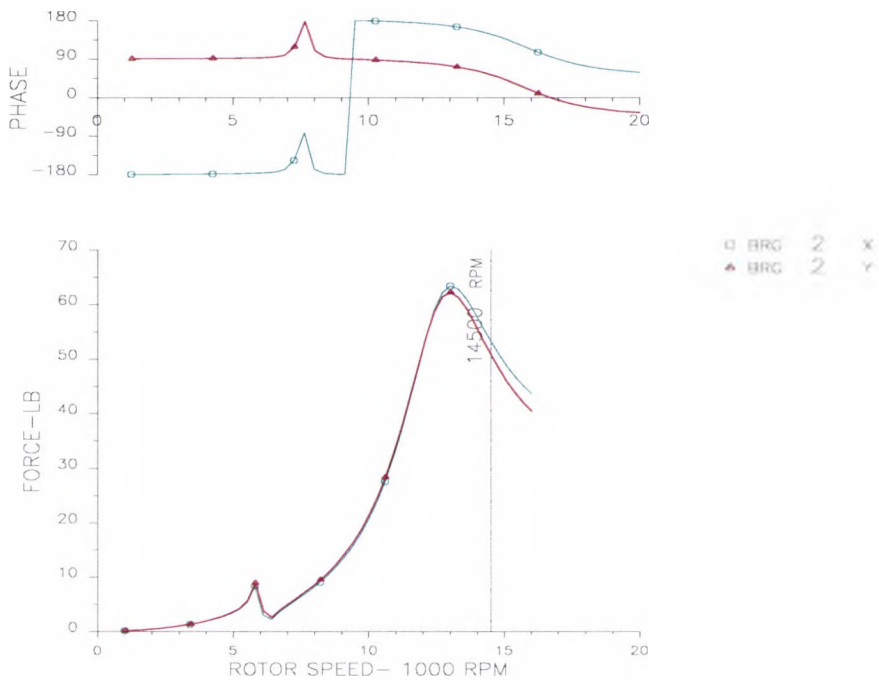


**Fig (6D): Synchronous Response with out of - phase unbalance - Force at Front Bearing, Actual Unbalance- supply pressure 2.1MPa**

XR3 High SPEED direct drive compressor xr3hspdm22.in  
 60 Hz, Hydrostatic Bearings, 300 psi, Opposite Phase unbalance, actual unbalance  
 Unbalance response

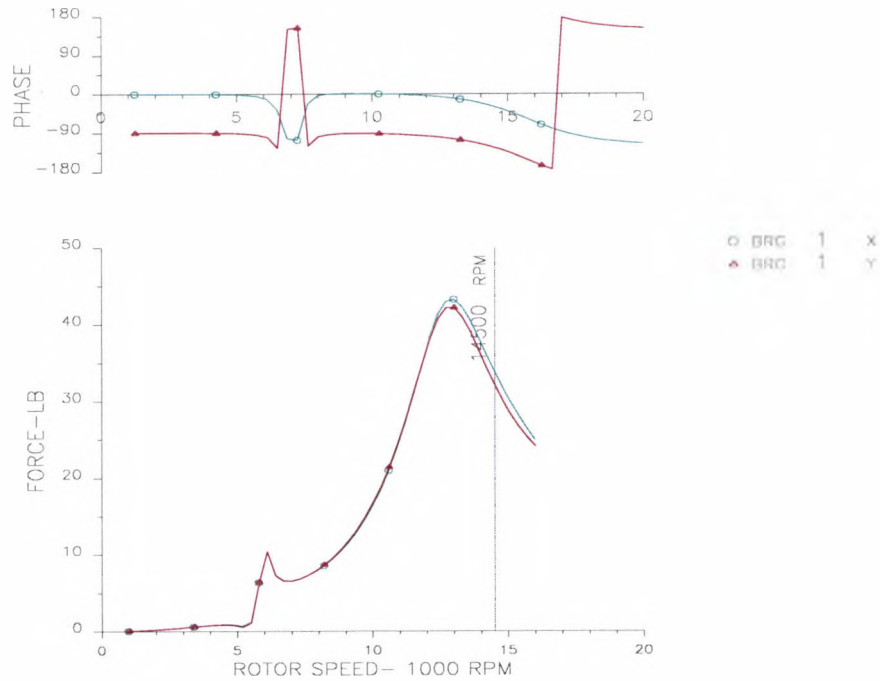


**Fig (6E): Synchronous Response with out of - phase unbalance - Force at Rear Bearing, Actual Unbalance- supply pressure 2.1MPa**

**Unbalance out-of Phase, actual unbalance magnitude**  
**AMPLIF FACTOR BASED ON MAJOR ORBIT**

STATION	PK NO	RPM	AMPLIF FACTOR
3	1	4300.00	.00
3	2	6100.00	11.30
3	3	12700.00	3.78
4	1	4000.00	2.30
4	2	6100.00	11.07
4	3	12700.00	3.78
7	1	5800.00	10.27
7	2	13000.00	3.72
9	1	5800.00	13.16
9	2	13000.00	3.75
14	1	5800.00	15.26
14	2	13000.00	3.58
20	1	5800.00	11.70
20	2	13000.00	3.33

## **APPENDIX B**

### **Shaft vibration measurement**

#### **B1 Introduction**

This appendix gives a description of the operation of vibration probes used in bearing testing. The appendix also shows test results at all three locations, namely front and rear bearing and impeller during stall, bearing instability conditions. A brief write-up on the effect of electromagnetic forces, the source of the 2X vibration, is given at the end.

#### **B2 Vibration measurement - Proximity probe**

The main parameters of vibration measurement are amplitude, frequency and phase angle. Amplitude can be expressed as displacement, velocity or acceleration. Velocity and acceleration can be calculated from displacement and frequency. For rotor vibrations the important criterion is to avoid rubbing between the stationary and the rotating components. Hence, displacement measurement is widely used as a vibration measurement parameter. A non-contacting eddy current probe, Model 7200, manufactured by Bently-Nevada, was used for the displacement measurement in the test programme.

Bently-Nevada eddy current probes are widely used in the industry for vibration measurement. The non-contacting eddy current probe is a gap voltage measuring transducer. It is used to measure distance and change in distance from any conductive material. The transducer is a flat coil of wire, located on the end of a ceramic tip. The coil is protected by 0.25 mm thick epoxy fiberglass and is not visible. An RF voltage generated by a proximator drives the probe. The signal output from the proximator is a voltage proportional to the gap distance between the probe and the observed surface. The proximator requires an 18 VDC supply.

## **Basic Operation**

**Static Gap Measurement:** The -18Vdc from the power supply is applied at the proximator input terminals. The proximator converts this voltage into an RF signal, which is applied to the probe through a coaxial cable. The probe coil radiates this signal into the surrounding area as a magnetic field. If there is no conductive material to intercept the magnetic field, there is no loss of RF signal. Because, the magnetic field is only affected by conductive material, any non-conductive material in the gap does not affect the eddy current field.

When a conductive surface approaches the probe tip, eddy currents are generated on the surface of the material and power is absorbed. As the surface comes closer to the probe tip, more power is absorbed, until the gap is approximately 380  $\mu\text{m}$ , when the total energy radiated by the probe is absorbed by the conductive surface, and the maximum power is lost. The gap of 380  $\mu\text{m}$  is typical for steel surfaces, it varies due to the differences in conductivity of other materials. The proximator measures the RF voltage envelope and provides a DC signal output equal to the negative peaks of the envelope. The DC voltage output from the proximator is directly measured by a voltmeter.

## **Peak to Peak motion and Average gap measurement**

If the observed surface is moving and changing the gap distance, the RF envelope is not constant, but varies in direct proportion to the peak-to-peak movement of the observed surface. The proximator output signal contains two pieces of information:

- a) Average DC voltage (average gap distance)
- b) AC voltage (dynamic motion)

The AC voltage component will indicate the vibration on both sides of the average gap. The output signal contains the vibration amplitude, frequency and phase information. The peak -to-peak amplitude is the total distance that a shaft will vibrate i.e, from the farthest to the closest distance to the probe. The dynamic signal is read by a Bently Data Acquisition System, ADRE 208.

## **Linear Range Of the Probe**

The probe has a linear range of between 630 to 2000  $\mu\text{m}$ . Within the probe linear range, the voltage output from the proximator is directly proportional to the probe gap. The static gap is set midway in the linear range. A scale factor of 200 millivots per 25  $\mu\text{m}$  is the industry standard for the calibration of eddy current probes. The frequency response is linear from 10 Hz to 10 kHz. The maximum frequency of interest from unbalance response and oil whirl instability is 300 Hz.

## **Factors affecting the probe output**

### **Observed materials**

The calibration scale factor of an eddy current probe is dependent upon the conductivity of the observed surface. The industry standard, the American Petroleum Institute, and Bently Probe Proximators are calibrated to observe 4140 steel. Most steels have the same, or nearly the same, conductivity and therefore the same calibration factor. Aluminum has a higher conductivity than steel and consumes less power at a given gap and therefore produces a higher voltage output at the proximator. In the present study, the probes were used against 4140 steel at the bearings and the impeller.

### **Effect Of Probe Temperature**

Probe temperature will also effect the range limits of the probe but to a much less degree than differences in materials. The probe output decreases with increase in temperature, From room temperature to 100°C, there is no appreciable change.

### **Effect Of Probe Tip Diameter**

The range of a probe is approximately proportional to the probe tip diameter. Eddy current probes do not measure a surface area equal to the diameter of the tip. There is a cone effect as the probe actually radiates laterally, in addition to straight ahead. This approximates a 45° divergence from the tip. The observed area is approximately equal to the probe tip diameter, plus 2x the probe gap. A 7.62 mm diameter tip at a typical 25 mm gap will see an area approximately equal to  $7.62+(2 \times 1.25)= 10.12$  mm in diameter.

## APPENDIX C

### Hydrostatic Bearing Compressor Test setup & Procedure

#### C1: Chiller System Description

The test schematic is shown in figure (5.1). The system consists of three refrigerant loops,

- 1) Bearing lubrication loop, supplying liquid to bearings,
- 2) Motor cooling loop, refrigerant for motor cooling. The motor cooling loop is split into two, a liquid line cooling the end turns of stator and a vapor line cooling rotor to reduce windage losses.
- 3) Vapor compression cycle to produce chilled water.

#### C.1.1 Bearing Lubrication loop ( Fig 1, blue color)

The bearing lubrication loop provides high-pressure refrigerant to the bearings. A centrifugal pump (IV) is used to provide required high pressure. The pump inlet is taken from bottom of condenser (I). A filter (II) and a heat exchanger (III) are located upstream of the pump. The heat exchanger, for subcooling the refrigerant, is a brazed plate type with cold refrigerant on one side and refrigerant from condenser on the other side. The purpose of subcooling refrigerant for lubrication is to avoid cavitation in the pump and evaporation in bearing cavity due to pressure drop or high temperature. An air-cooled condensing unit supplies the cold refrigerant required for subcooling the lubrication refrigerant. Liquid from pump discharge passes through a filter (V) before entering the bearing cavity. A refrigerant bypass valve (4) is used to control the bearing supply pressure. Care is taken to ensure low-pressure drop in the whole system. Refrigerant discharge from bearings enters into the evaporator.

#### C.1.2 Motor Cooling Loop (Fig 1: green color)

The motor is cooled by refrigerant from the condenser. The major sources of heat generation in a motor are located at the air gap, space between stator inside diameter

and rotor outside diameter, and at the end turns. The heat generation in the air gap is due to windage or shear. The air gap can be cooled either by vapor or by liquid from the condenser. To minimize windage losses, air gap is cooled by refrigerant vapor. The heat generation in the end turns is due to  $I^2R$  losses, where I is the current in amps and R the resistance in ohms. The end turns are cooled by liquid refrigerant from condenser. In order to ensure that liquid does not enter the air gap, drains are placed at each end and at the bottom of the housing. Drain line from both ends are connected to the evaporator.

### **C.1.3 Vapor Compression loop** ( Fig 1: red color)

Liquid from condenser (I) enters, after isenthalpic throttling across valve (VI), the evaporator (VII). Chilled water returning from the air handler (not shown) is cooled by the latent heat of boiling refrigerant. Vapor from the evaporator enters the centrifugal compressor (VIII). High-pressure gas from compressor is condensed into liquid in the condenser. The condenser water picks up the total heat i.e the heat removed from chilled water and the heat added by compression. The heat is rejected into the atmosphere by means of a cooling tower.

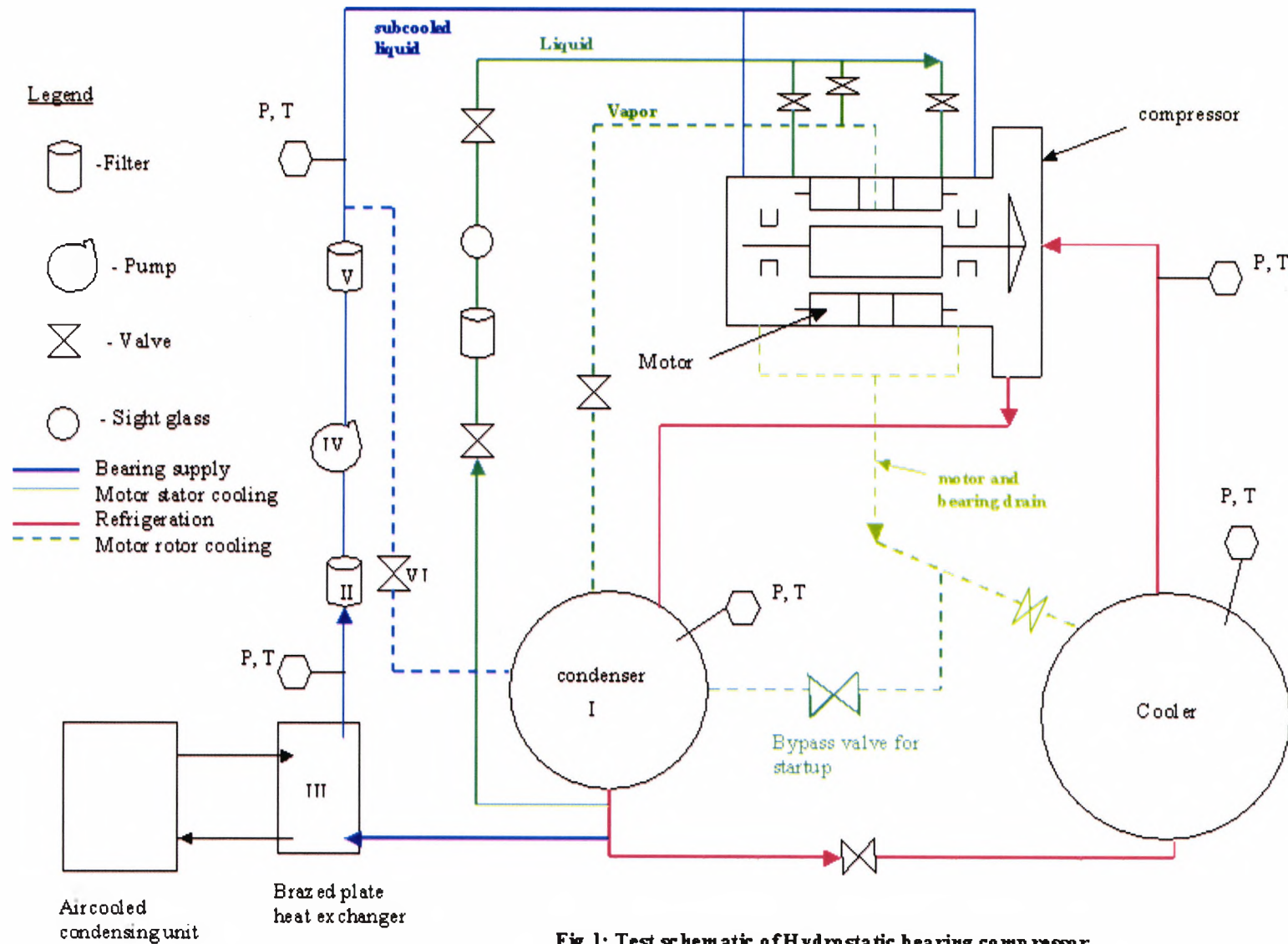
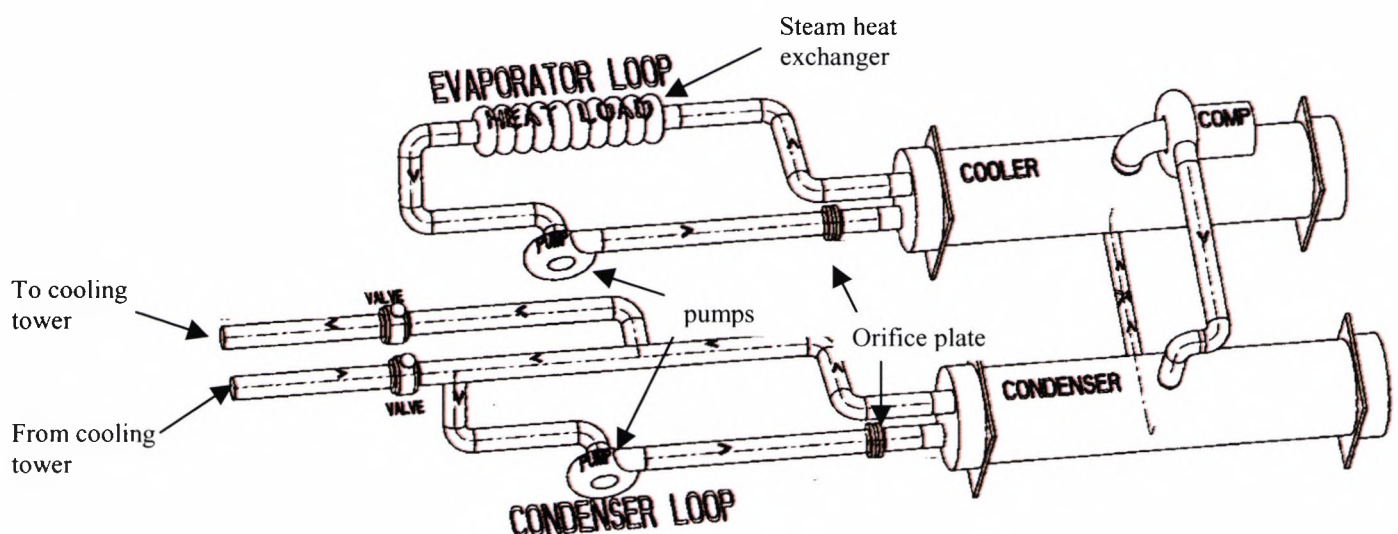


Fig 1: Test schematic of Hydrostatic bearing compressor

## C2: Test Cell Description

Testing was carried out in a 500-ton water cooled chiller. The objective is to demonstrate feasibility of hydrostatic bearings using liquid HFC134a for centrifugal compressors in water-cooled chiller. Mechanical performance characteristics such as shaft vibrations, motor and bearing temperatures were measured under different load and speed conditions. Data on compressor aerodynamic and inverter performance was also collected.

The chiller is placed in a test cell (Figure 2) consisting of two separate water loops one on evaporator side and the other on condenser side. Water flow rates in both the loops can be varied from 200 to 1600 gpm. Building heat load is simulated by addition of heat to the cooler inlet water. A steam heat exchanger is used for this purpose. A pneumatic control valve controls steam flow to the heat exchanger. The condenser water circuit consists of a closed loop through the test chiller and cooling tower (not shown) and a side branch used to add makeup water. Control valves are provided to regulate amount of water going back to and returning from cooling tower. Condenser inlet water temperature control is accomplished by a water exchange that occurs when a controlled valve releases water back to the tower. An equivalent amount of cold water through the supply valve replaces the hot water and is mixed with the remaining closed loop water to obtain the desired condenser inlet temperature.



**Fig 2: Water chiller Test Loop**

The refrigerant saturation temperature in the cooler is few degrees below the leaving chilled water temperature. The temperature difference between leaving chilled water and refrigerant saturation temperature is a function of the tube surface area, heat transfer characteristics of the tube and heat flux. The water temperature change across the cooler is a function of water flow rate and heat rejection. For a well-designed evaporator, the leaving temperature difference is between 0.25 to 0.5 °C. The condenser saturation temperature is 0.25 to 0.5 °C above the leaving condenser water temperature. The corresponding saturation pressures in the cooler and condenser establish the pressure ratio across the compressor.

### **C2.1: Chiller Startup**

The first step in the startup process is to establishing lubricant supply at correct pressure and temperature. The magnitude of lubricant supply pressure is controlled by the position of the bypass valve, VI and the supply temperature is controlled by the refrigerant flow, from the air-cooled unit, to the brazed plate heat exchanger, iii. Refrigerant pump is started with the bypass valve VI set to wide open position. The bypass valve, VI, is then closed to obtain the required supply pressure to bearings. Also, before starting the pump, the valve on the cooler side of the motor/bearing drain line is closed and the valve on the condenser side is set to wide open position. This will maintain the liquid level in the condenser which otherwise will accumulate in cooler. Before starting the compressor, the lubricant supply pressure to the bearings is adjusted to a minimum value of 1.8 Mpa by the bypass valve. Lubricant temperature is maintained at 5C by the air-cooled unit. The motor cooling liquid supply lines is set to 50% open position. The compressor is brought to 60% of full speed. After reaching a steady state, the valve in the motor drain line on condenser side is closed and the valve to cooler is adjusted to maintain a motor cavity pressure at 0.1 Mpa above cooler pressure.

During startup process, the entering condenser water temperature is maintained around 20°C and leaving chilled water temperature controller is set to 5°C. At any given speed, changing the entering condenser water temperature varies the compressor operating condition.

### **C2.2 Compressor Surge and Stall:**

Stall is a instability caused by separation of flow inside the compressor, mainly in diffuser passages. Severe stall leads to compressor surge that is characterized by flow reversal from condenser to cooler. Surge also results in an intermittent low frequency noise generation. In a motor driven compressor, surge results in current fluctuations down to zero due to unloading caused by flow reversal. Compressor is brought into surge by raising the entering condenser water temperature until a low frequency noise is heard or a wide fluctuation in magnitude of current is observed. As mentioned before, stall is a precursor to surge and is characterized by low frequency pressure pulsations in the discharge line. Compressor stall occurs at 1 to 2 deg below surge. Hence, setting entering condenser water temperature 1 to 2 deg below the temperature at which surge occurs can bring compressor into stall. This method is followed whenever dynamic pressure transducers are not present at the impeller discharge. It should be pointed out that a compressor can run indefinitely in stall provided the resultant force and hence shaft vibrations are below acceptable levels. The same is not true for compressor surge, since it causes instability in the system that affects the leaving chilled temperature.

### **C2.3 Refrigerant Pump cavitation:**

This is achieved by reducing the subcooling and or by closing the valve upstream of pump (valve is not shown in the schematic). Cavitation also results in severe vibration of the pump and an increase in noise.

Figures 3 through 15 show both test setup and internal components of the compressor.

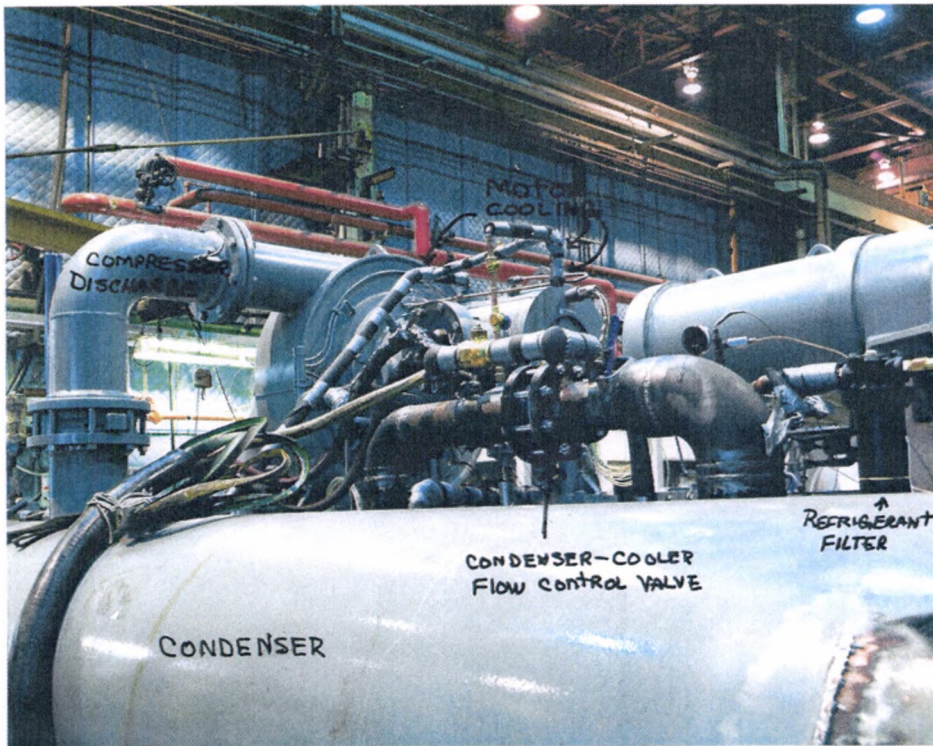


**Figure 3: Compressor discharge side view**

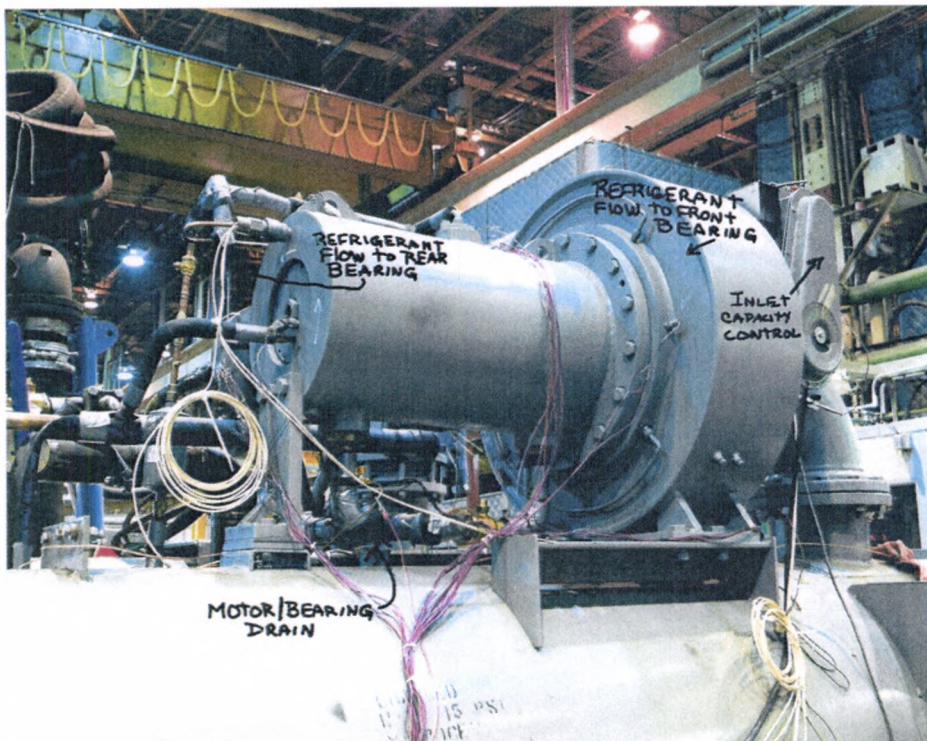


**Figure 4: Compressor front side**

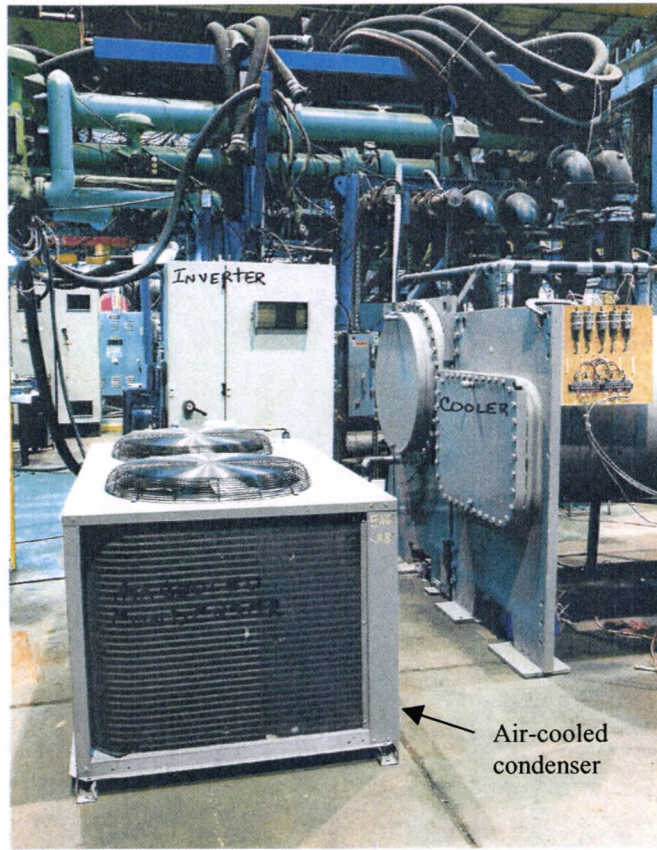


**Figure 5: Chiller system components – Inverter and Air-cooled condenser shown**

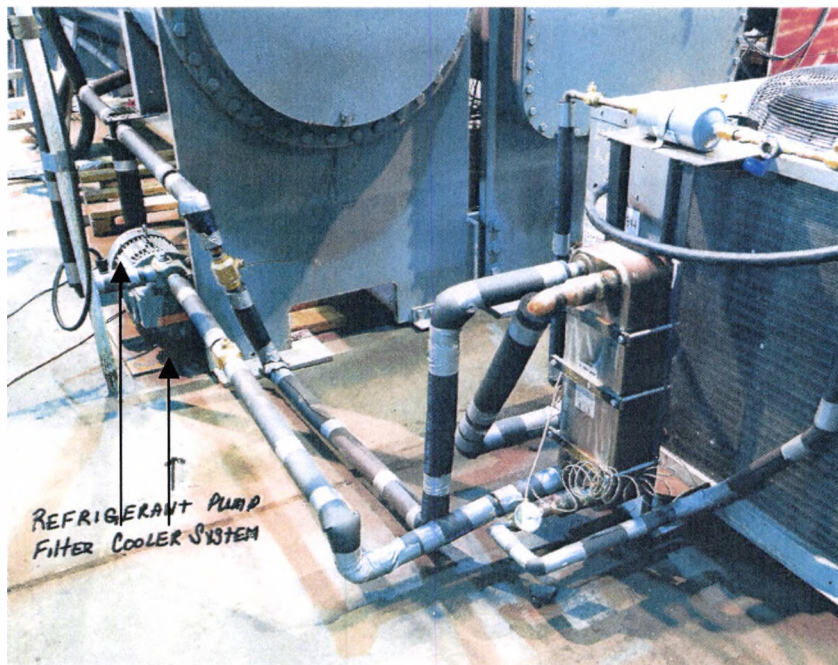


**Figure 6: Chiller system components – Refrigerant pump and filter shown**



**Figure 7: Data collection system – Pressure Transducers, temperature chart recorders and Vibration acquisition**

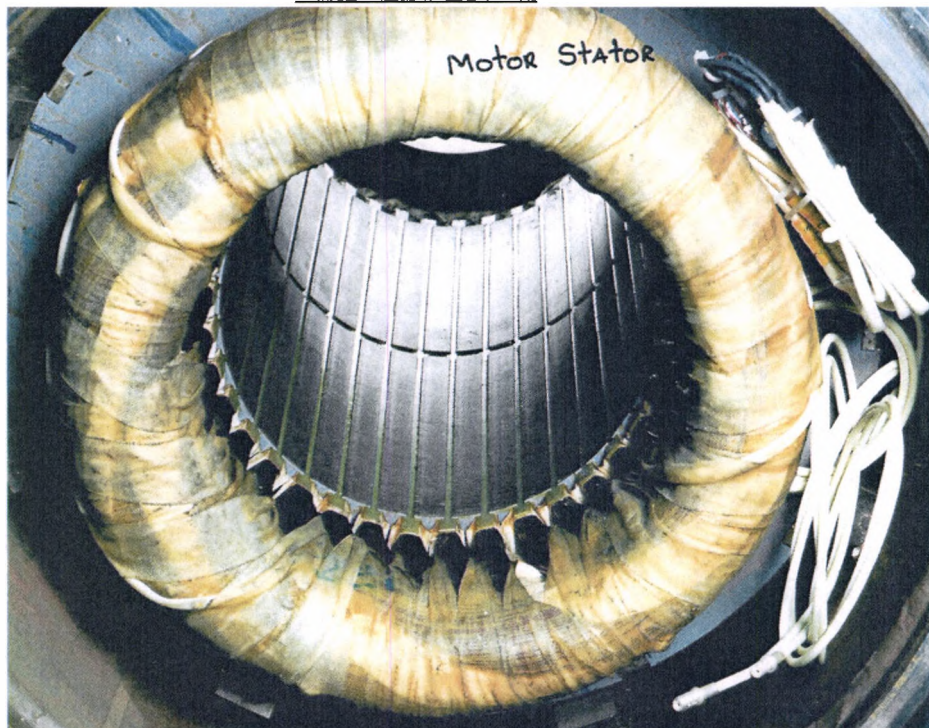


**Fig 8: High Speed Motor Stator**

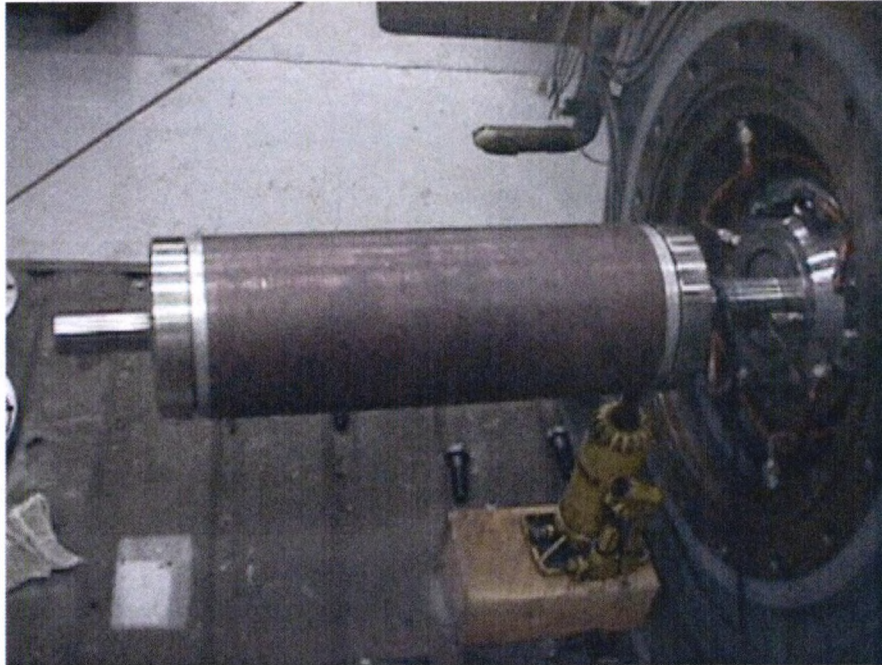


**Fig 9: High Speed motor rotor**

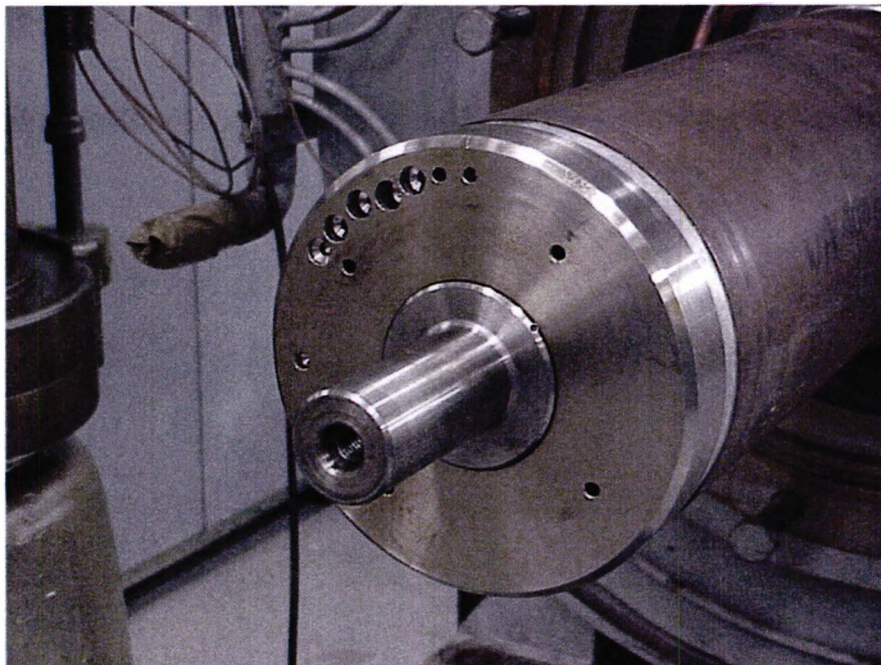


**Fig 10: Balancing holes in the rotor end ring**

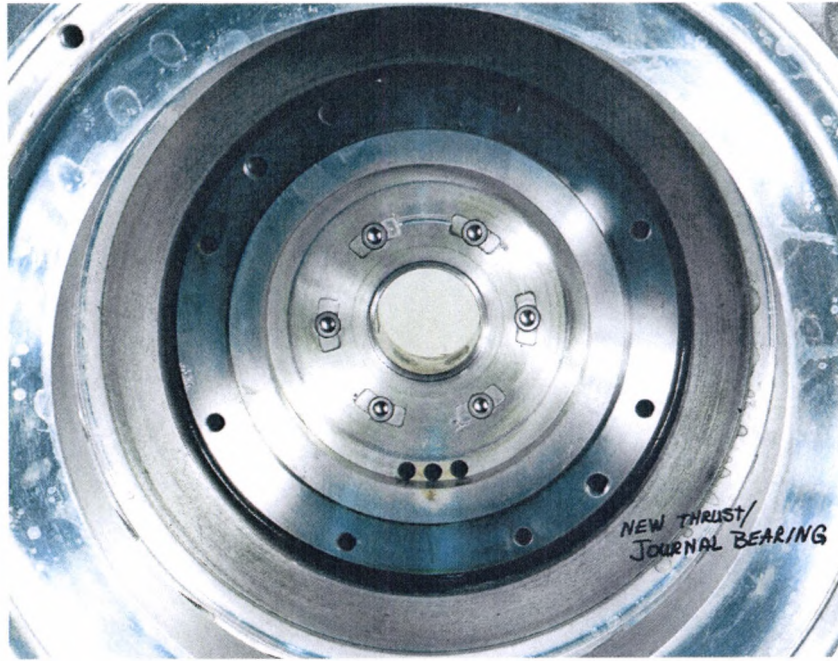


**Figure 11: Impeller side journal and thrust bearing**

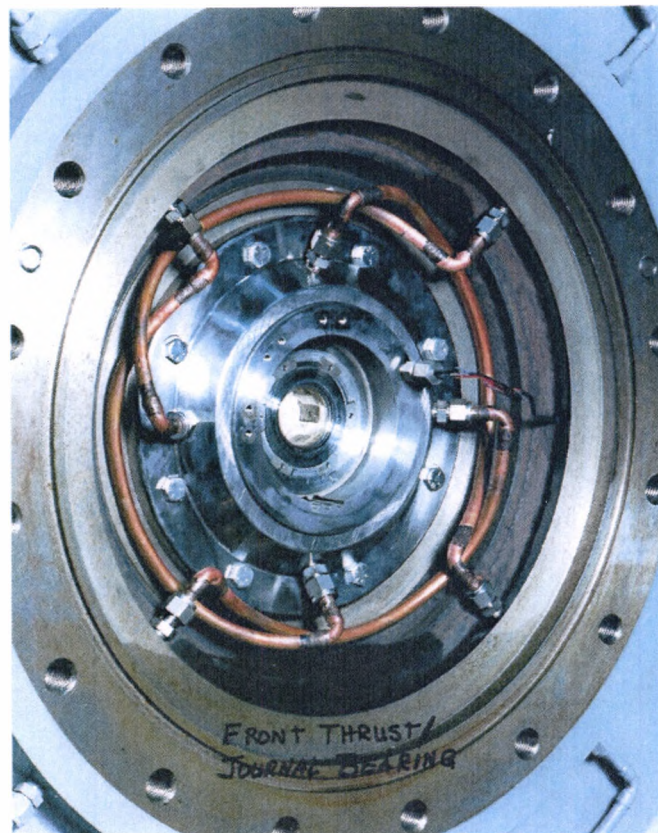


**Figure 12: Refrigerant piping to bearings**

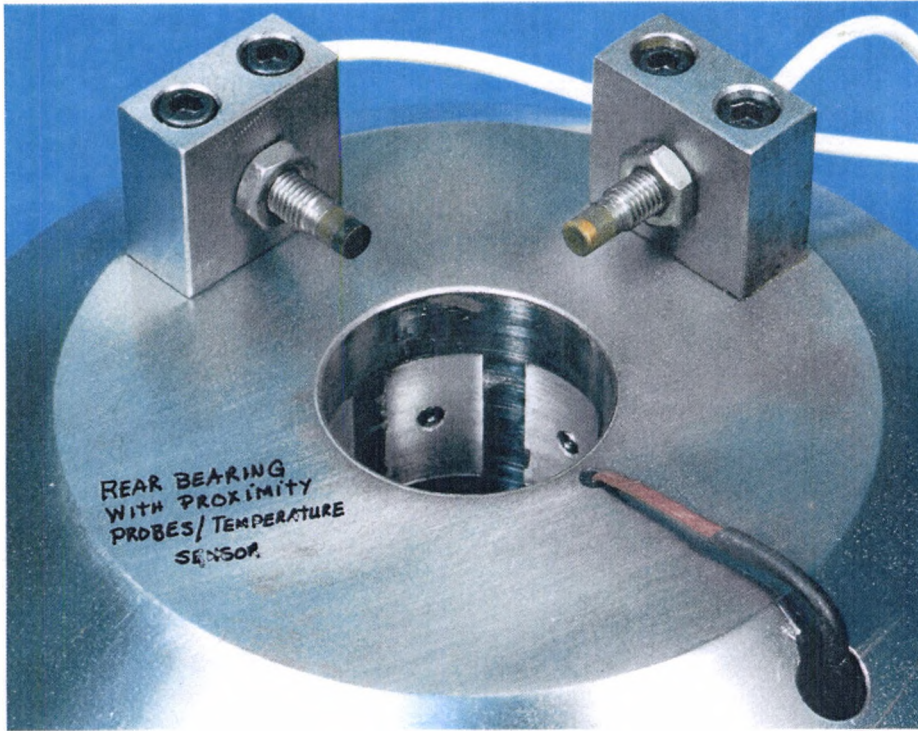


**Figure 13: Proximity probes and temperature sensor in motor end bearing**

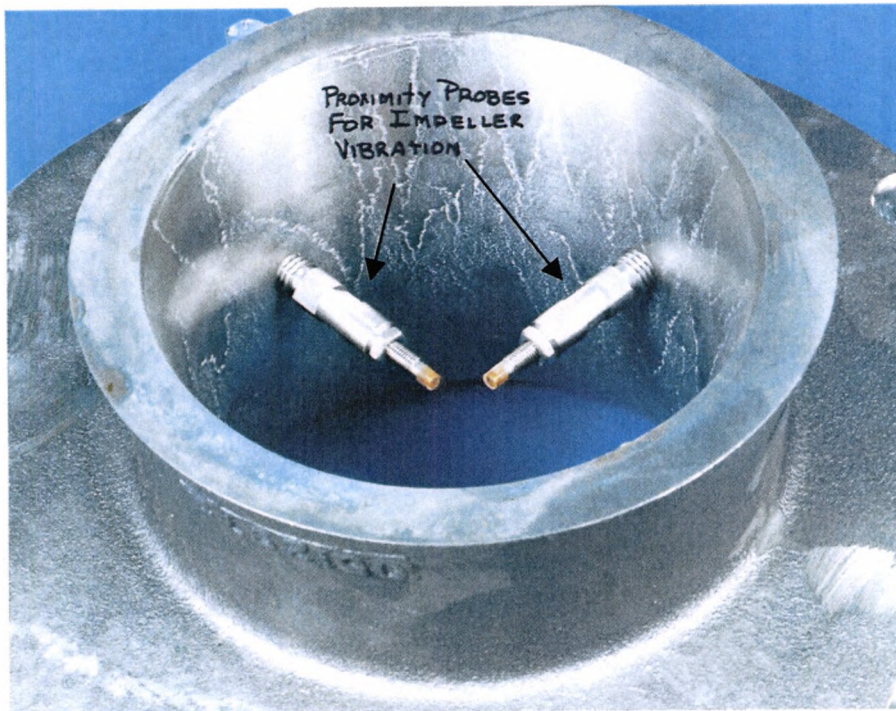


**Figure 15: Proximity probes in shroud for measuring impeller vibrations, impeller not shown**

## APPENDIX D

### Test results of Hydrostatic bearing

#### D1: Vibration Amplitude during compressor stall

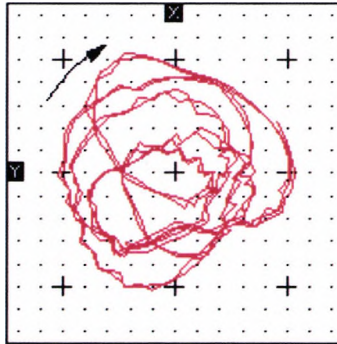


**Fig 1: Impeller orbit during Stall, 13200 rpm, scale, 1mil/div.  
Supply pressure =2.1 Mpa.  
(1mil=25.4 microns)**

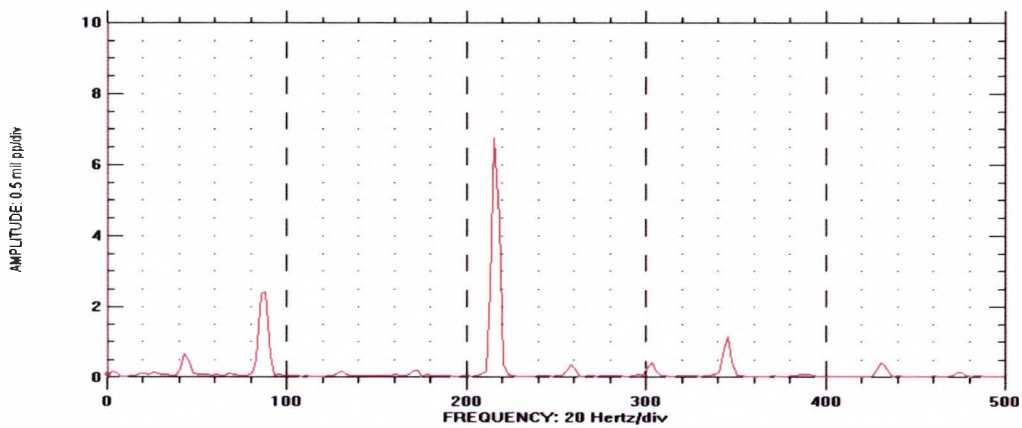


**Fig 2: Spectrum Plot before Stall, X-direction, at Impeller.  
Supply pressure 2.1 Mpa  
Y axis in mils pk-pk (1mil=25.4 microns)**

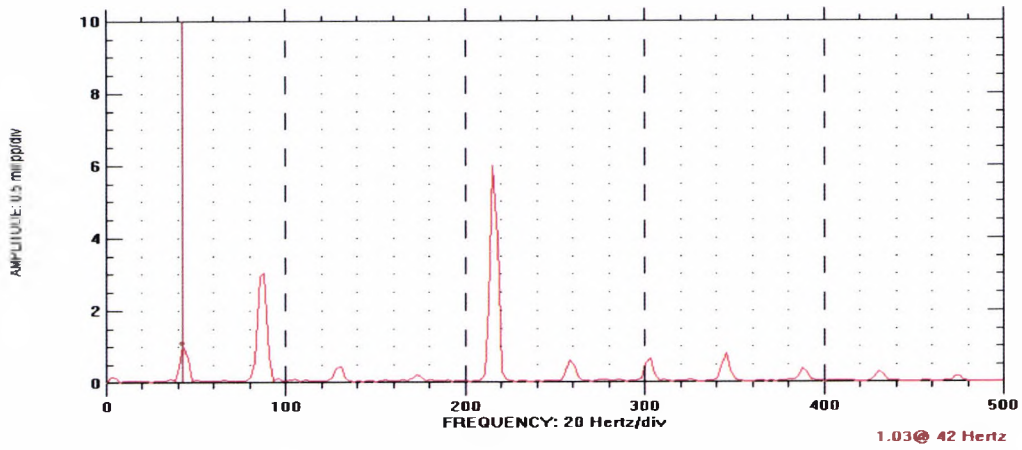


**Fig 3: Spectrum Plot during Stall, X-direction, at Impeller**  
**Supply pressure =2.1 MPa**  
 Y axis in mils pk-pk (1mil=25.4 microns)

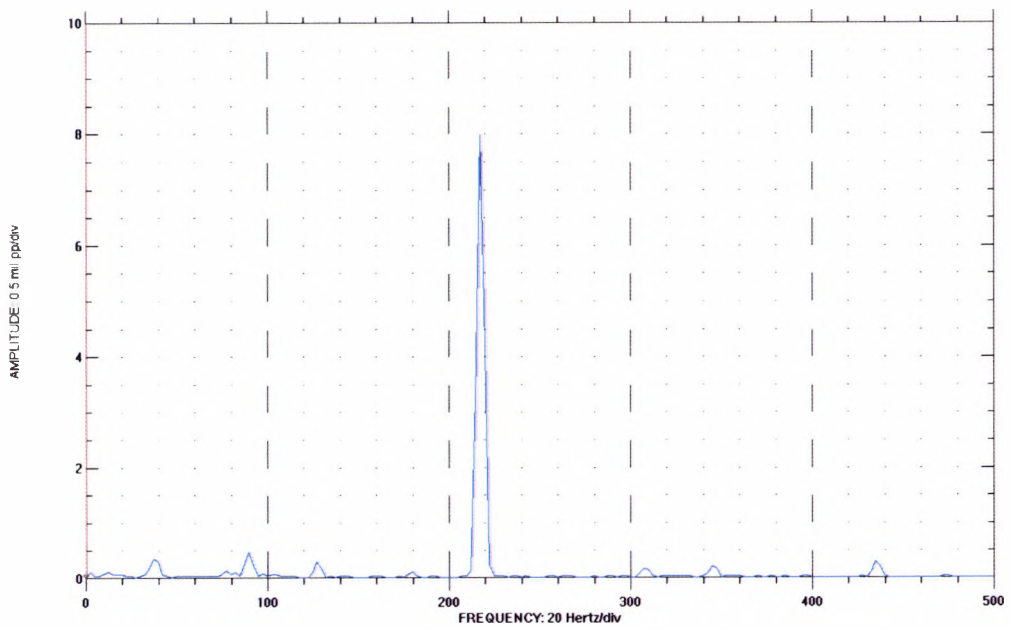


**Fig 4: Spectrum Plot before stall, Y-direction, at Impeller**  
**Supply pressure 2.1 MPa**  
 Y axis in mils pk-pk (1mil=25.4 microns)

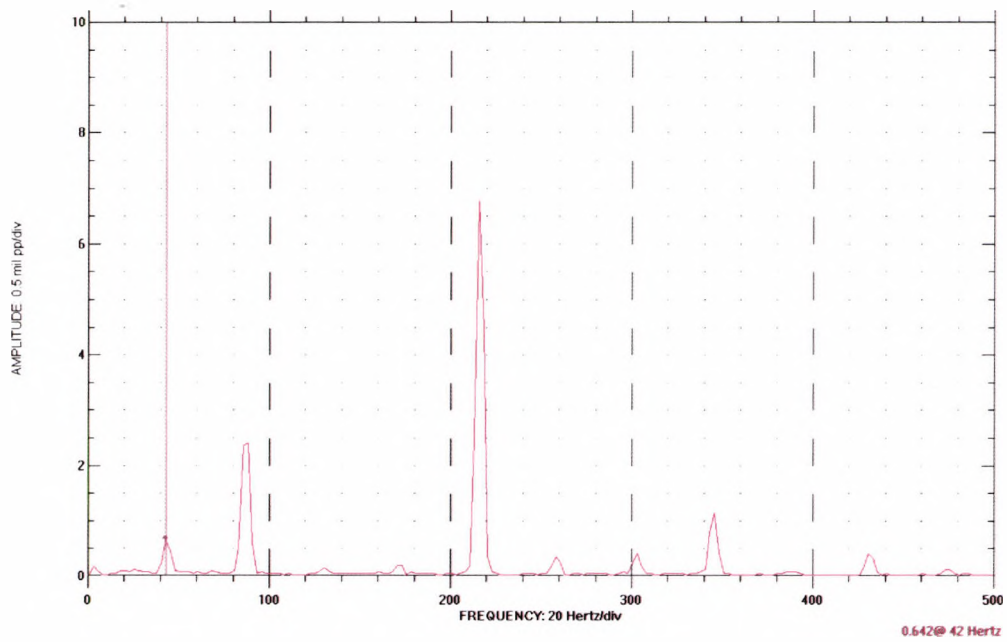


**Fig 5: Spectrum Plot during stall, Y-direction, at Impeller**  
**Supply pressure 2.1 Mpa**  
 Y axis in mils pk-pk (1mil=25.4 microns)

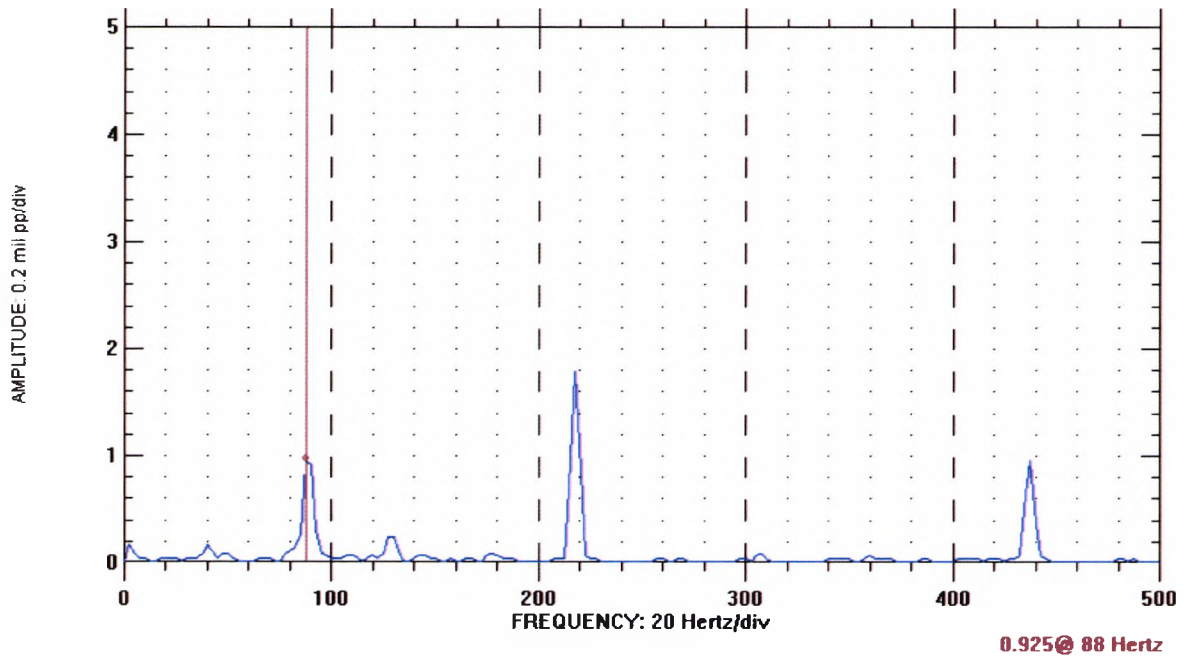


**Fig 6: Front bearing X-direction, before stall**  
**Supply pressure 2.1 MPa**  
 Y axis in mils pk-pk (1mil=25.4 microns)

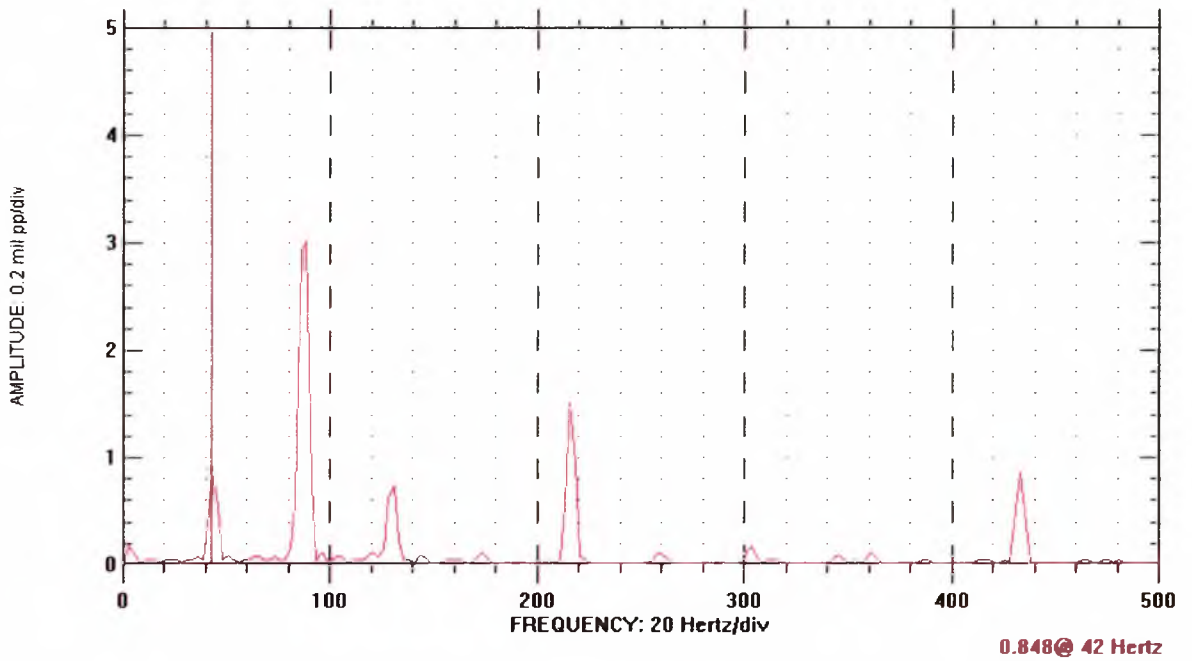


**Fig 7: Front bearing X-direction, during stall**  
**Supply pressure 2.1 MPa**  
 Y axis in mils pk-pk (1mil=25.4 microns)

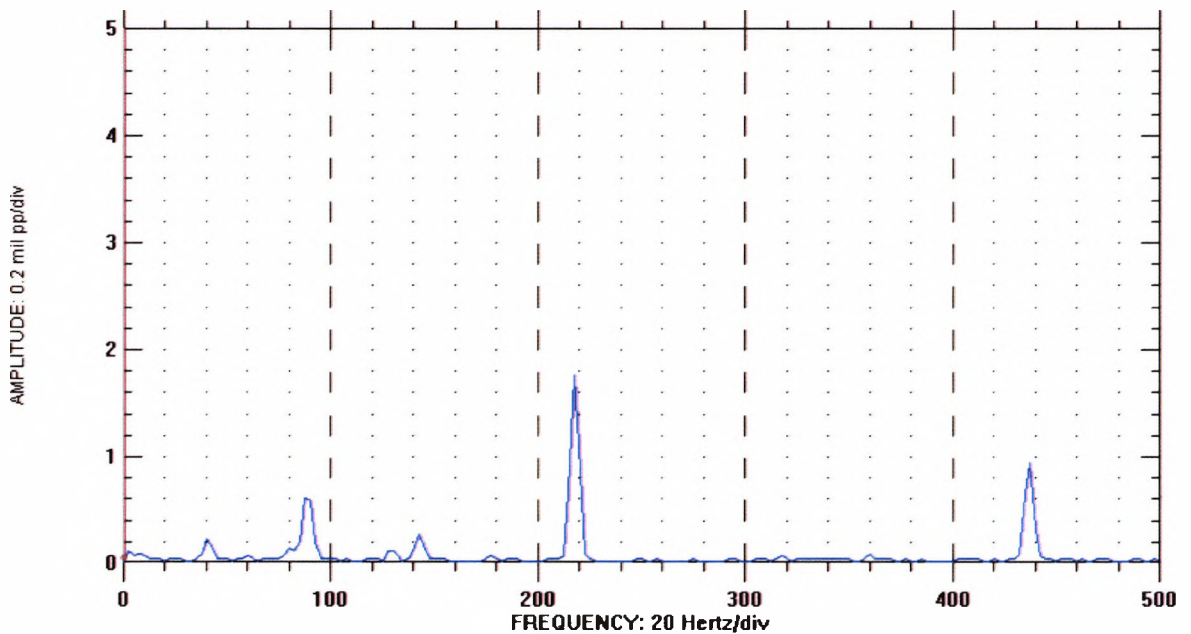


**Fig 8: Front Bearing Y-direction before stall**  
**Supply pressure 2.1 MPa**  
 Y axis in mils pk-pk (1mil=25.4 microns)

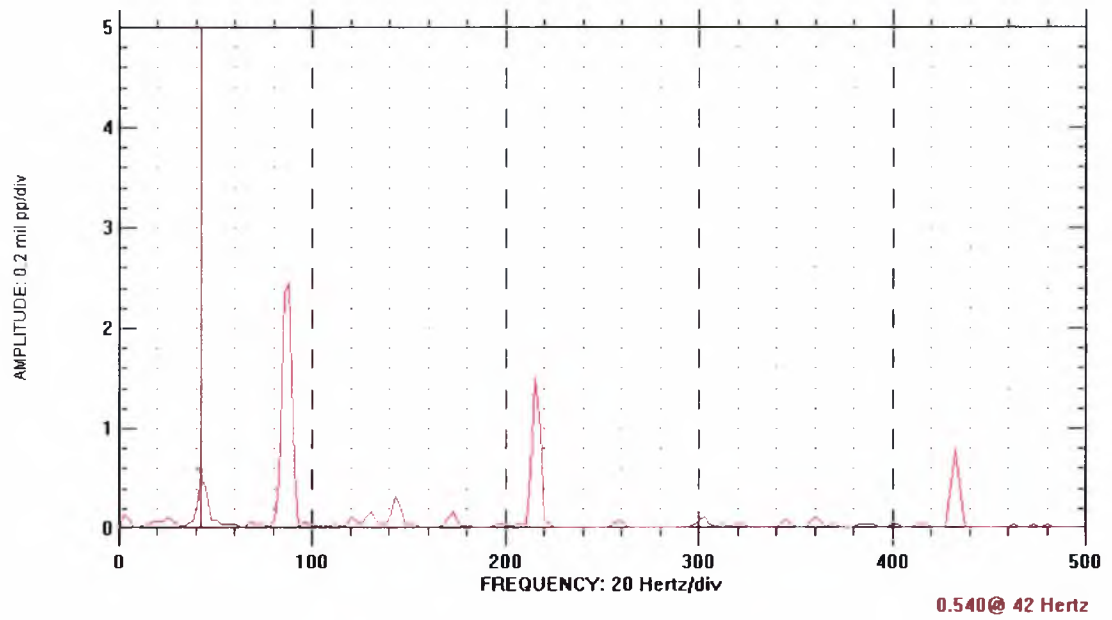


**Fig 9: Front bearing during stall, Y-direction**  
**Supply pressure 2.1 Mpa**  
 Y axis in mils pk-pk (1mil=25.4 microns)

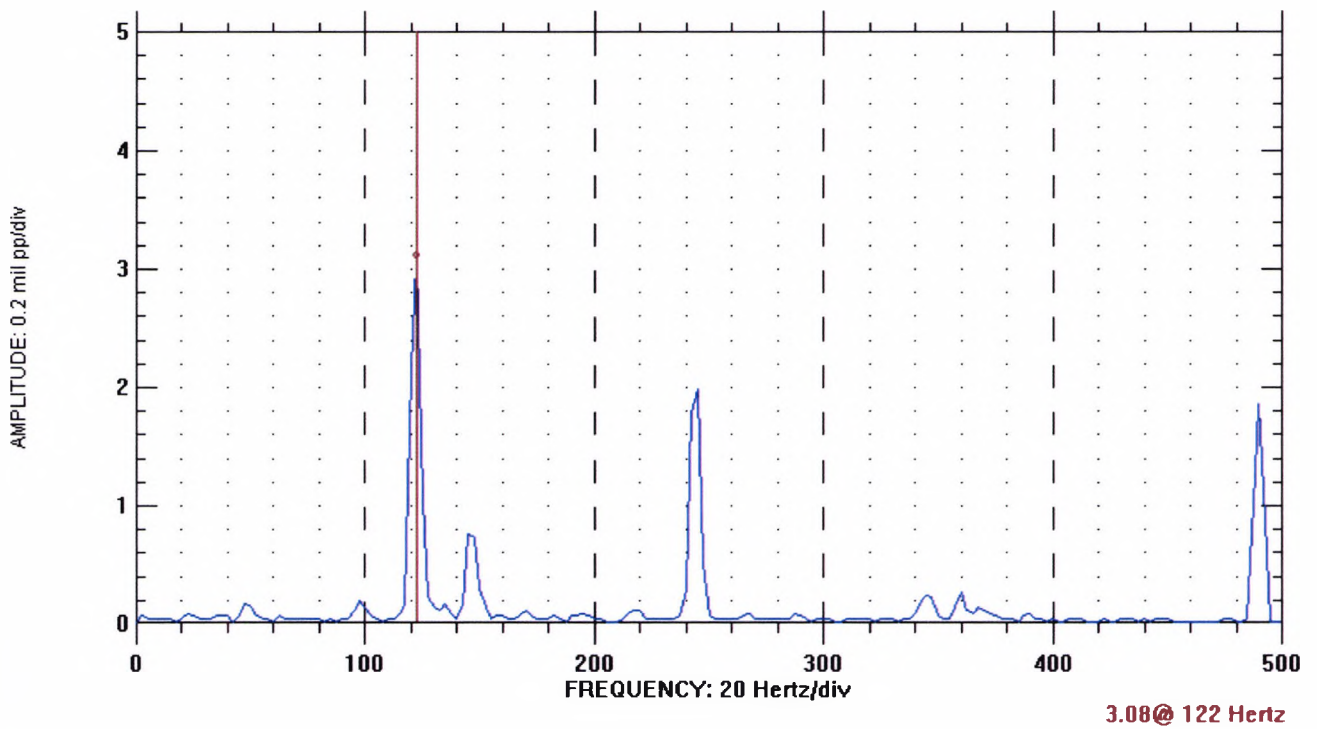


**Fig 10: Rear Bearing X-direction, before stall**  
**Supply pressure 2.1 Mpa**  
 Y axis in mils pk-pk (1mil=25.4 microns)

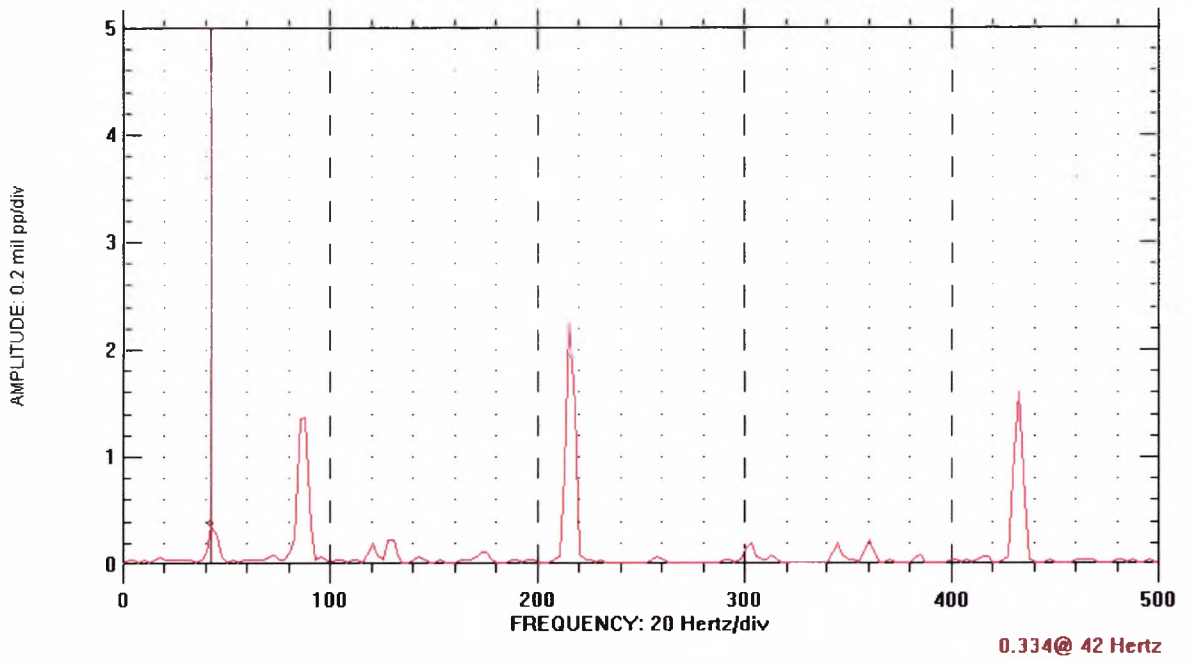


**Fig 11: Rear Bearing, X-direction, during stall**  
**Supply Pressure 2.1 MPa**  
 Y axis in mils pk-pk (1mil=25.4 microns)

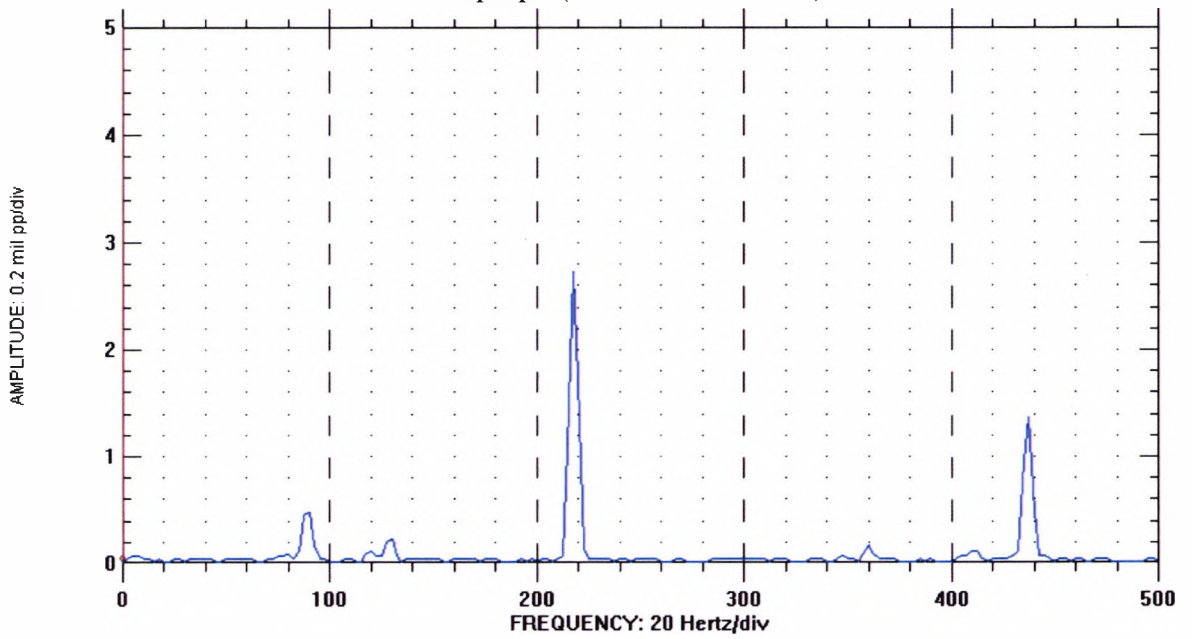


**Fig 12: Rear Bearing Y-direction before stall**

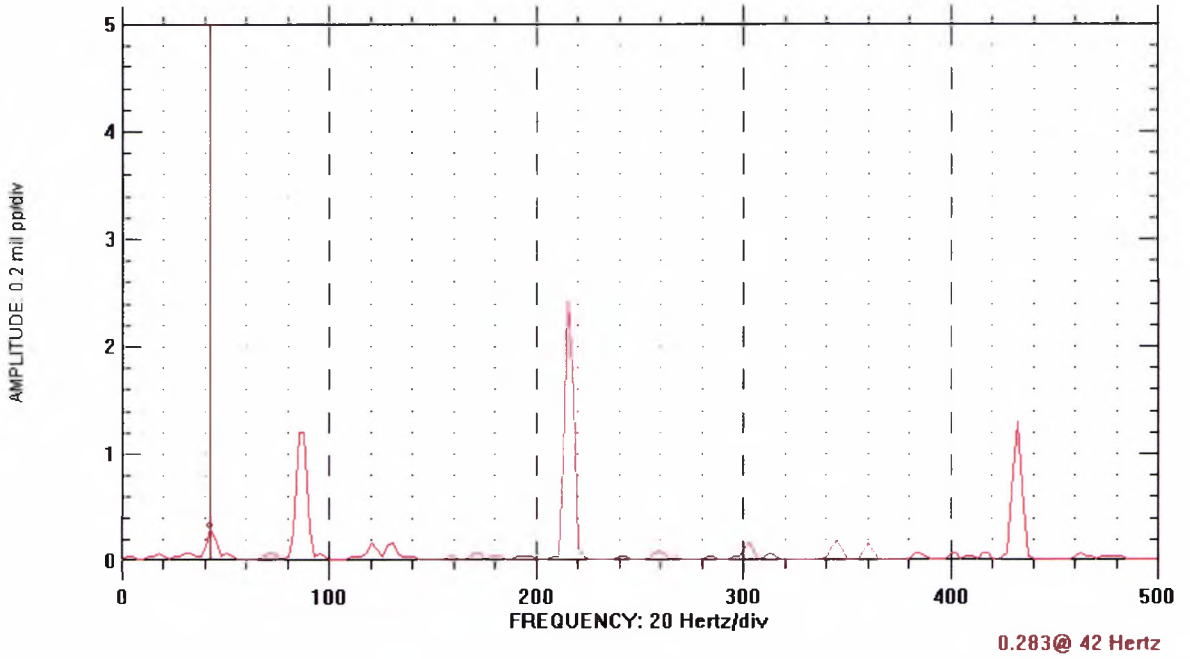


**Fig 13: Rear Bearing Y direction during stall**  
**Supply pressure 2.1 MPa**  
 Y axis in mils pk-pk (1mil=25.4 microns)

**D2:Vibration amplitude during bearing instability**

**Startup**

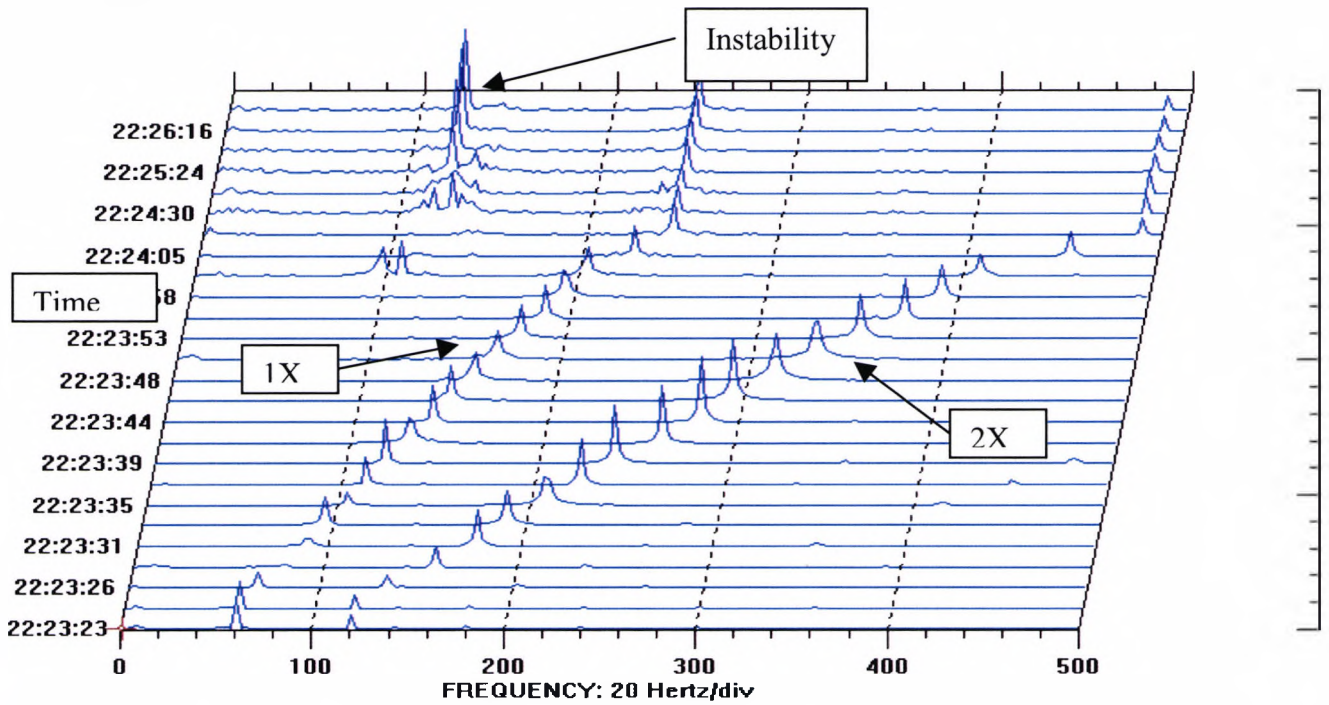


**Fig 14: Front Bearing, X – direction. Start Of Instability at 14200 rpm.**  
**Supply pressure = 2.1 Mpa.**  
 Y axis in mils pk-pk (1mil=25.4 microns)

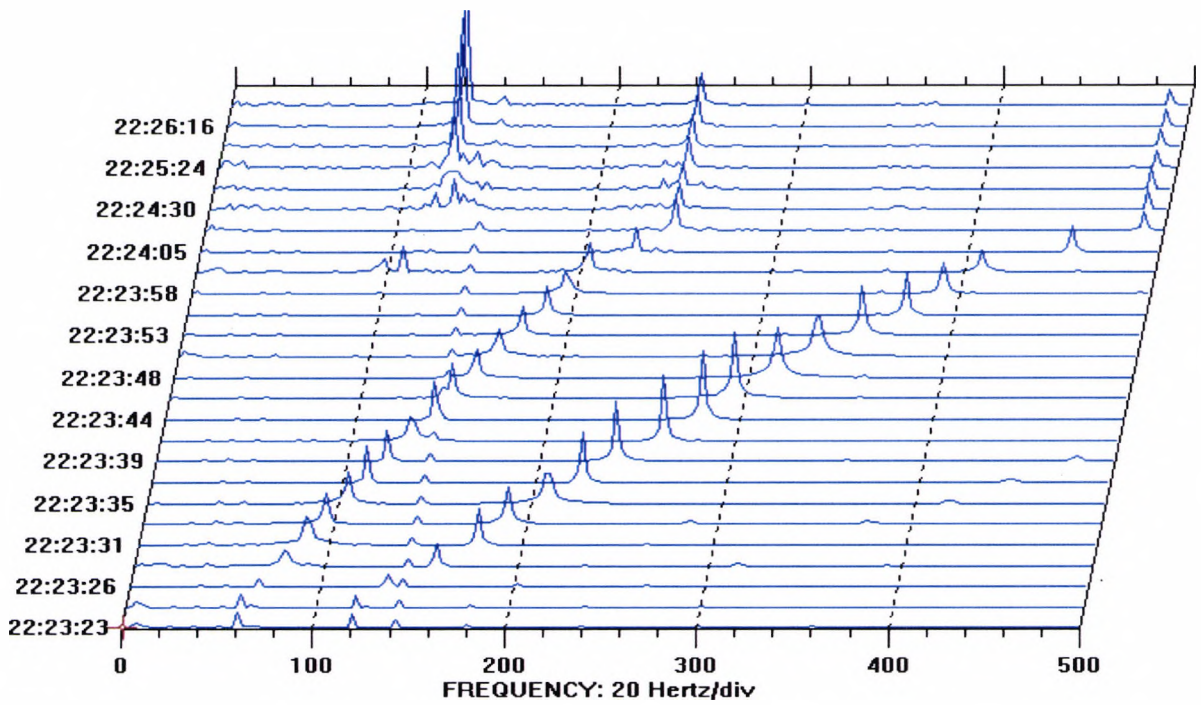


**Fig 15: Front Bearing, Y – direction. Start Of Instability at 14200 rpm.**  
**Supply pressure = 2.1 Mpa.**  
 Y axis in mils pk-pk (1mil=25.4 microns)

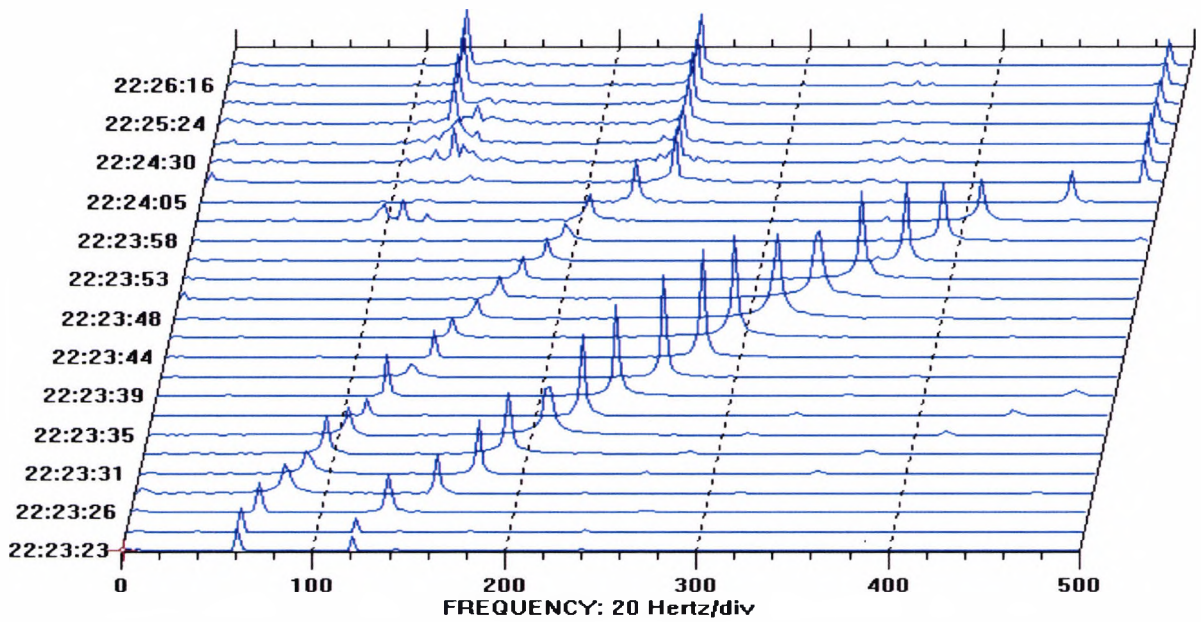


**Fig 16: Rear Bearing, X – direction. Start Of Instability at 14200 rpm.**  
**Supply pressure = 2.1 Mpa**  
 Y axis in mils pk-pk (1mil=25.4 microns)

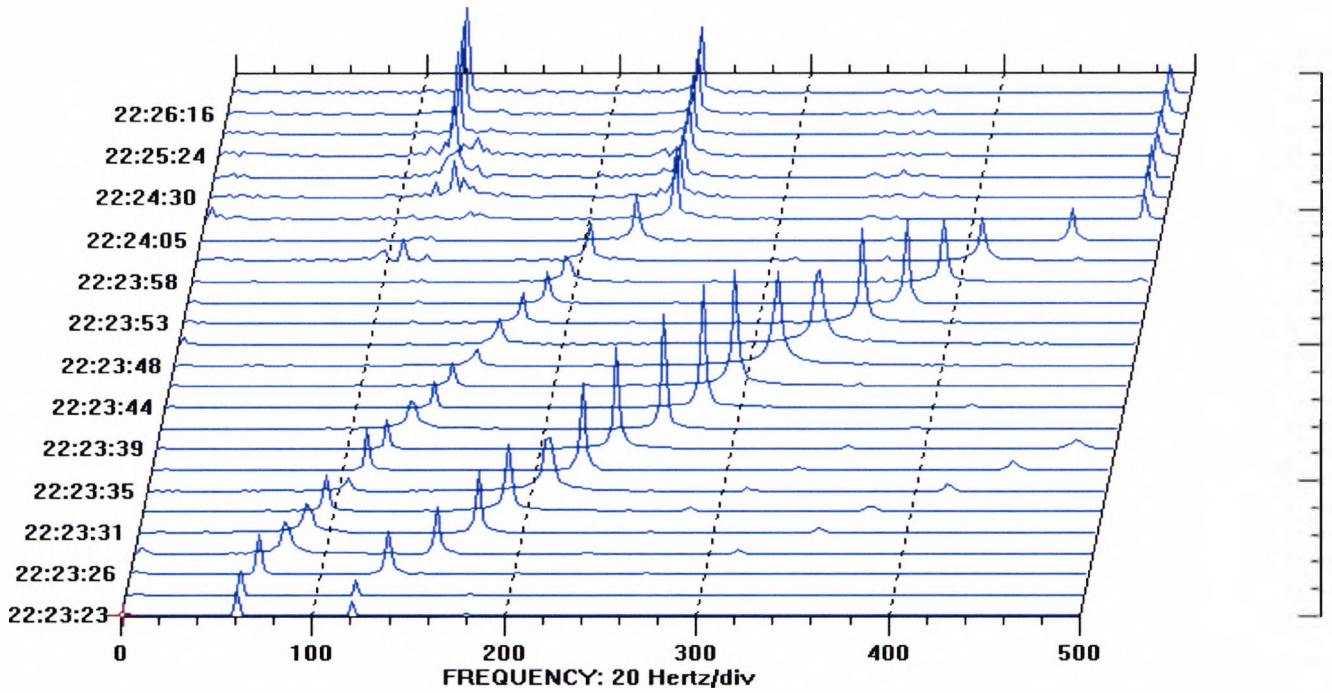


**Fig 17: Rear Bearing, Y – direction. Start Of Instability at 14200 rpm.**  
**Supply pressure = 2.1 MPa**  
 Y axis in mils pk-pk (1mil=25.4 microns)

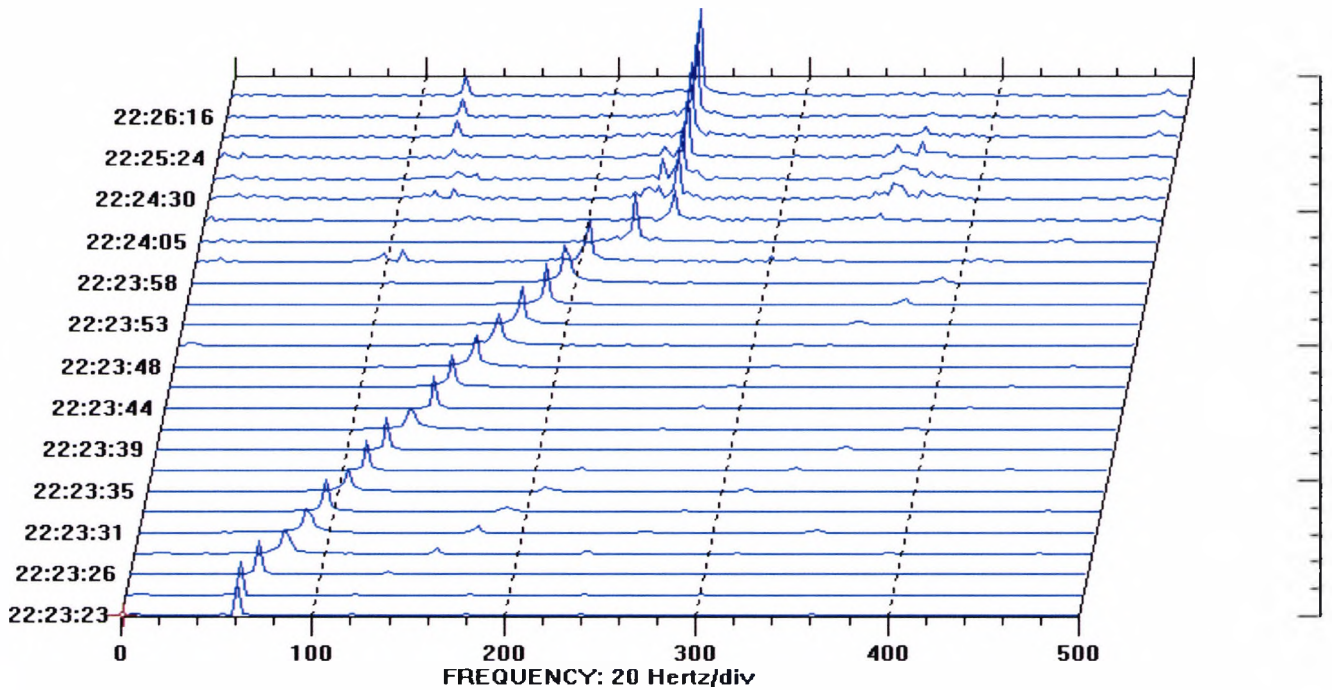


**Fig 18: Impeller, X – direction. Start Of Instability at 14200 rpm.**  
**Supply pressure = 2.1 MPa**  
 Y axis in mils pk-pk (1mil=25.4 microns)

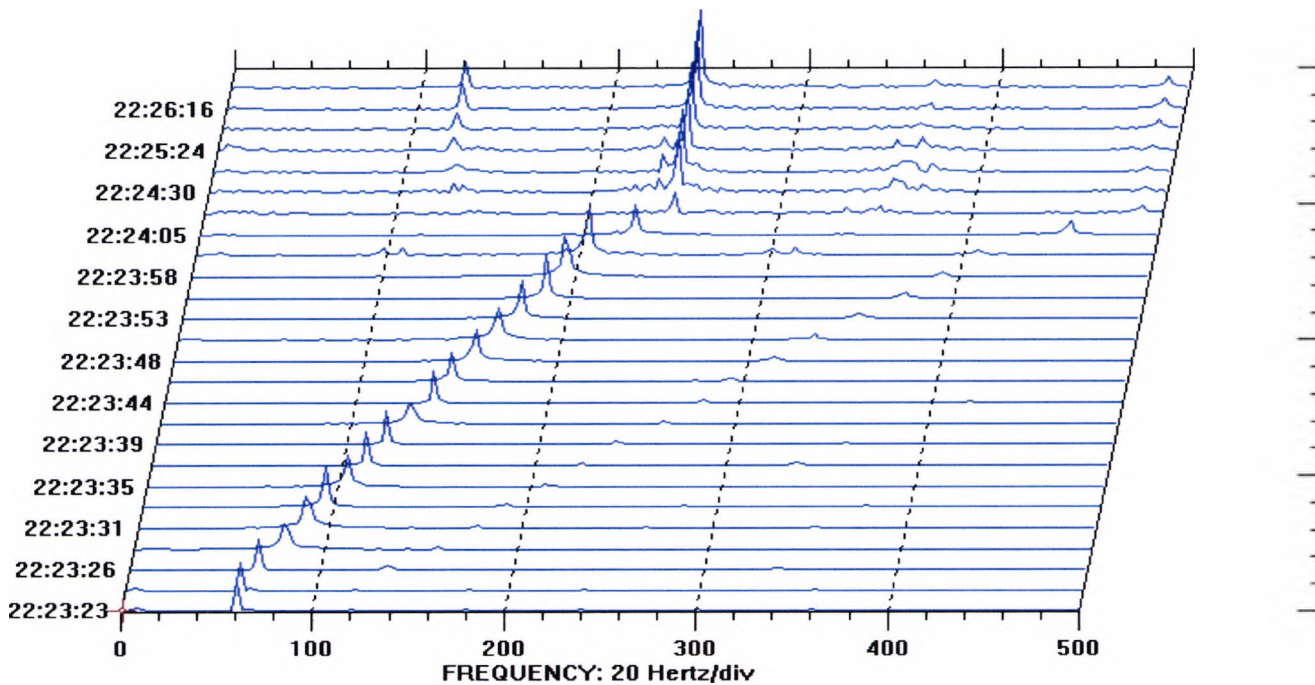
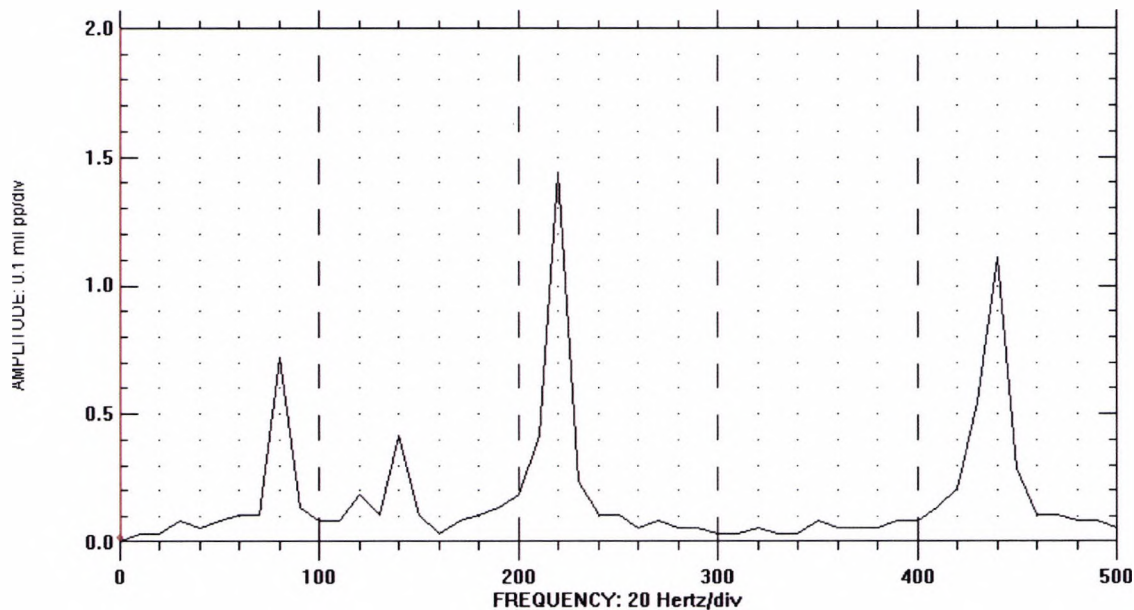


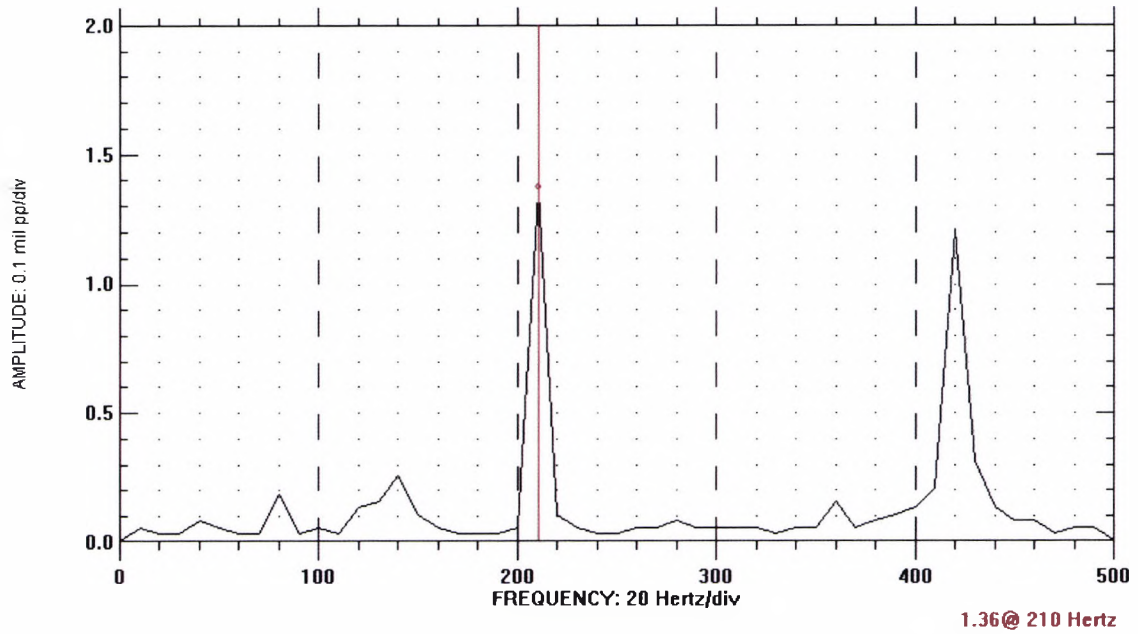
**Fig 19: Impeller, Y – direction. Start Of Instability at 14200 rpm.**  
**Supply pressure = 2.1 MPa**  
 Y axis in mils pk-pk (1mil=25.4 microns)

**Effect Of Speed**



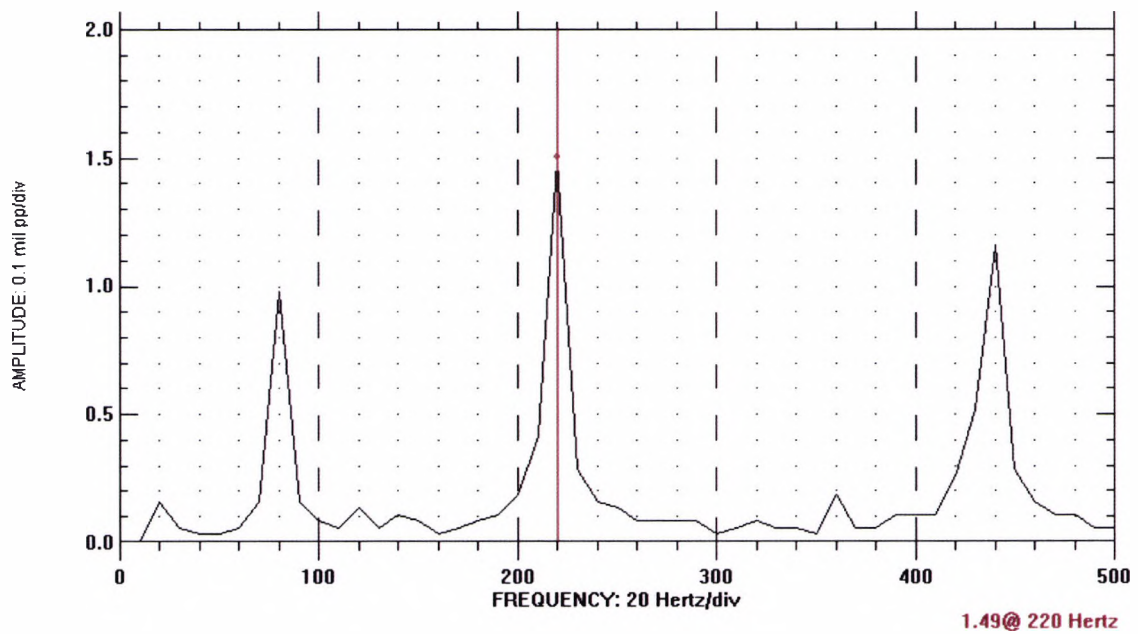
**20(A) Speed = 13200 rpm**

**Fig 20(A): Subsynchronous Vibration – As a function of speed.**  
**Supply Pressure = 2.1 MPa**  
 Front bearing X-dir. Y axis in mils pk-pk (1mil=25.4 microns)

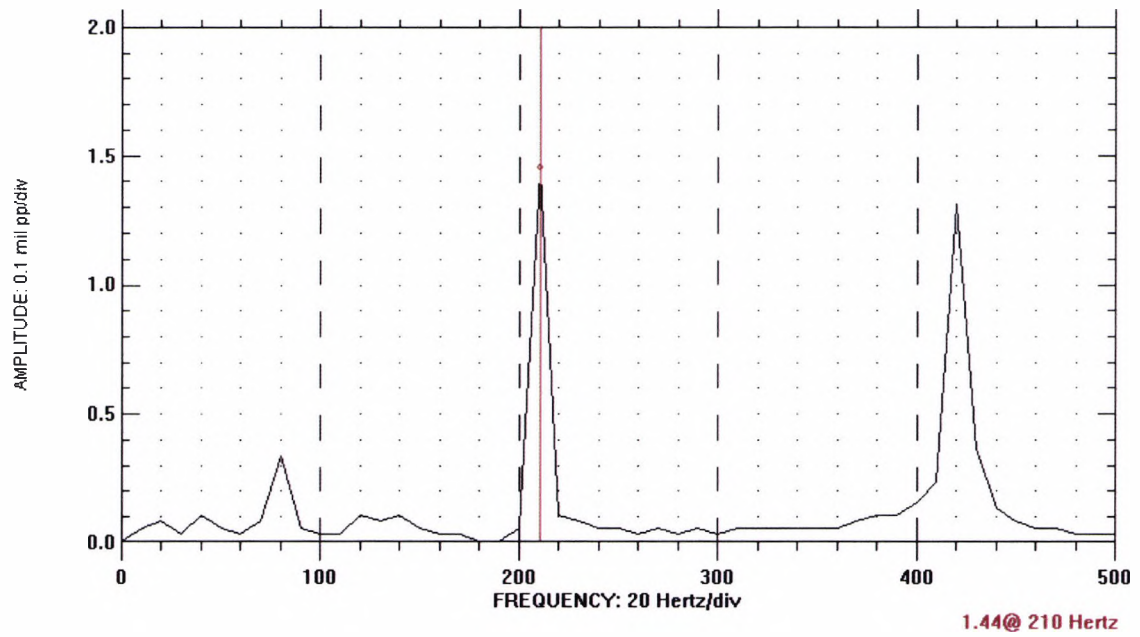


**20(B) Speed = 12600 rpm**

**Fig 20(B): Subsynchronous Vibration – As a function of speed.  
 Supply Pressure = 2.1 MPa  
 Front bearing X-dir. Y axis in mils pk-pk (1mil=25.4 microns)**



**20(C) Speed = 13200 rpm**

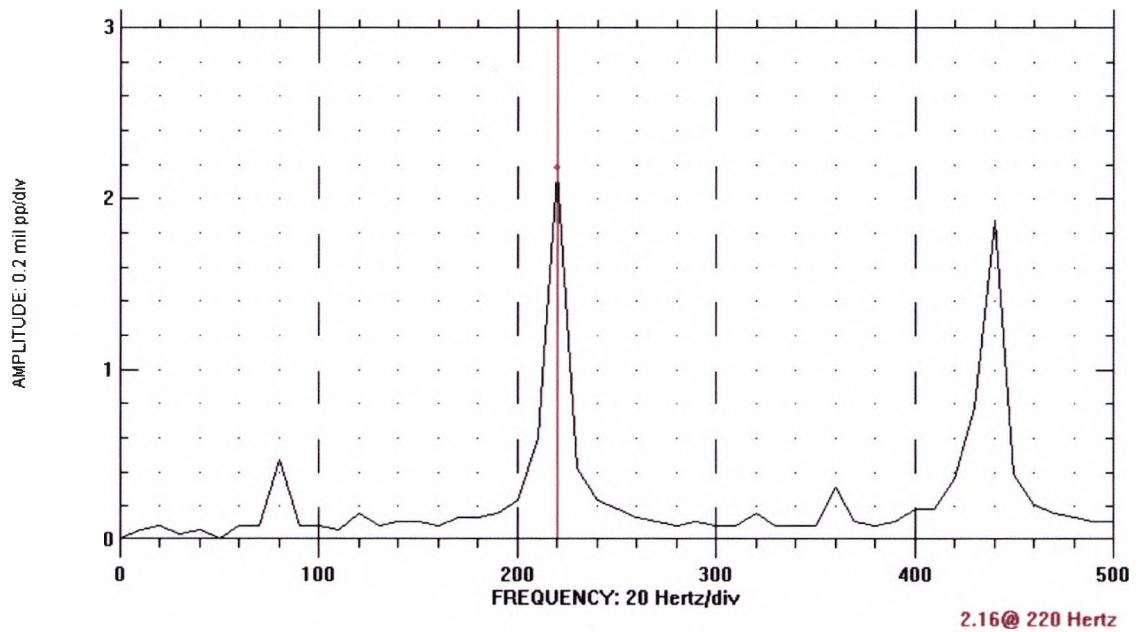


**20(D) Speed = 12600 rpm**

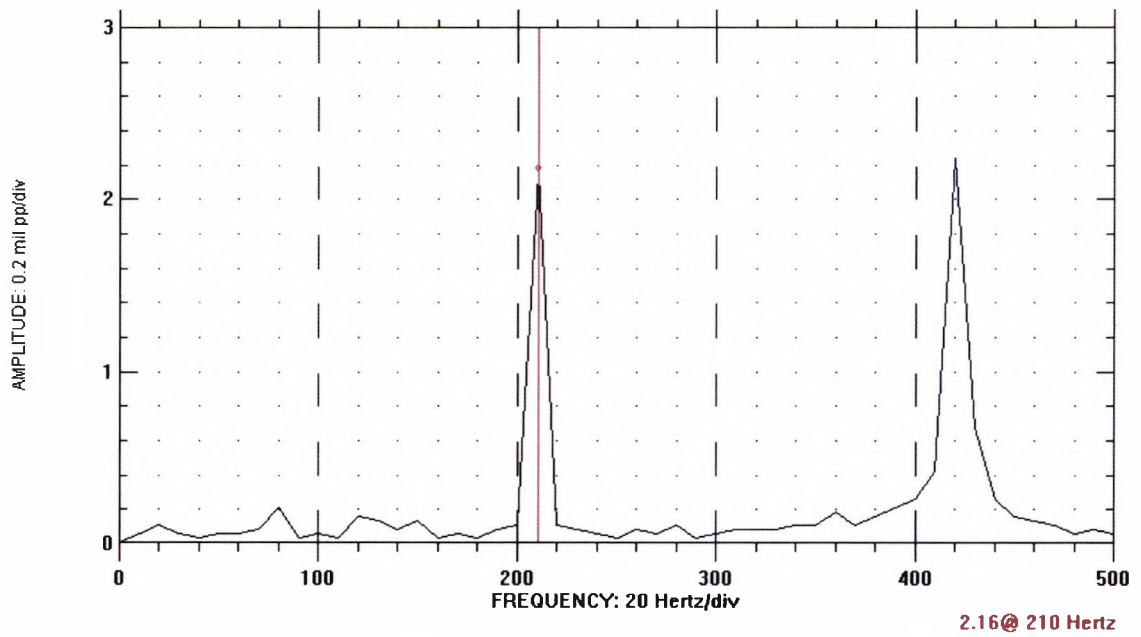
**Fig 20(D): Subsynchronous Vibration – As a function of speed.**

**Supply Pressure = 2.1 MPa**

Front bearing Y-dirn. Y axis in mils pk-pk (1mil=25.4 microns)



**20(E): Speed = 13200 rpm**



**20(F): Speed = 12600 rpm**

**Fig 20(F): Subsynchronous Vibration – As a function of speed.  
Supply Pressure = 2.1 MPa  
Rear bearing X-dir. Y axis in mils pk-pk (1mil=25.4 microns)**

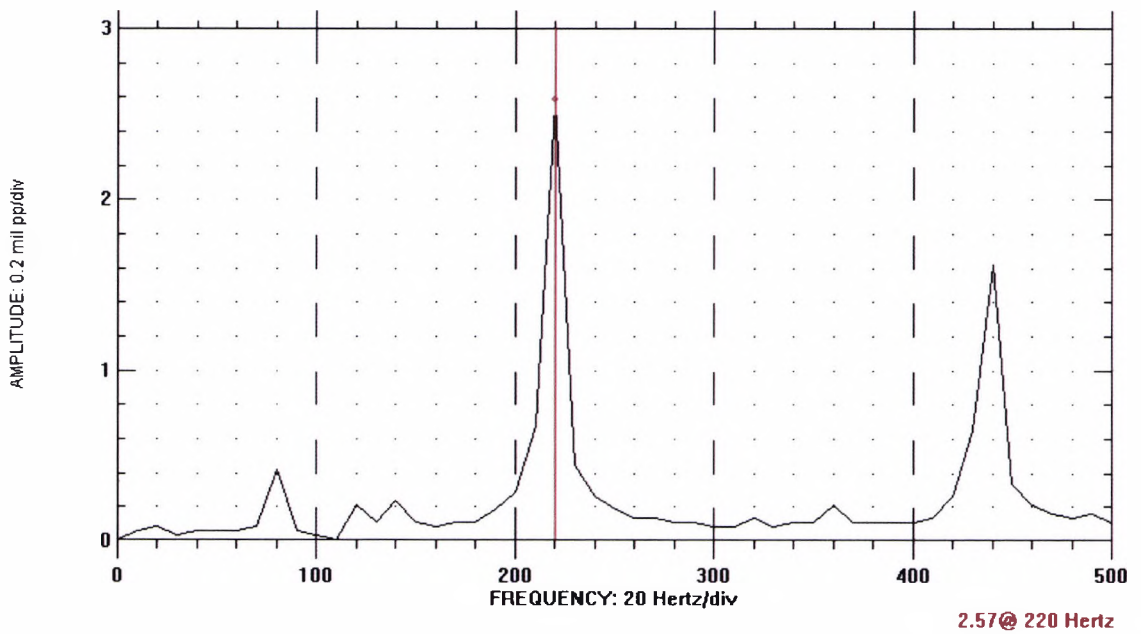
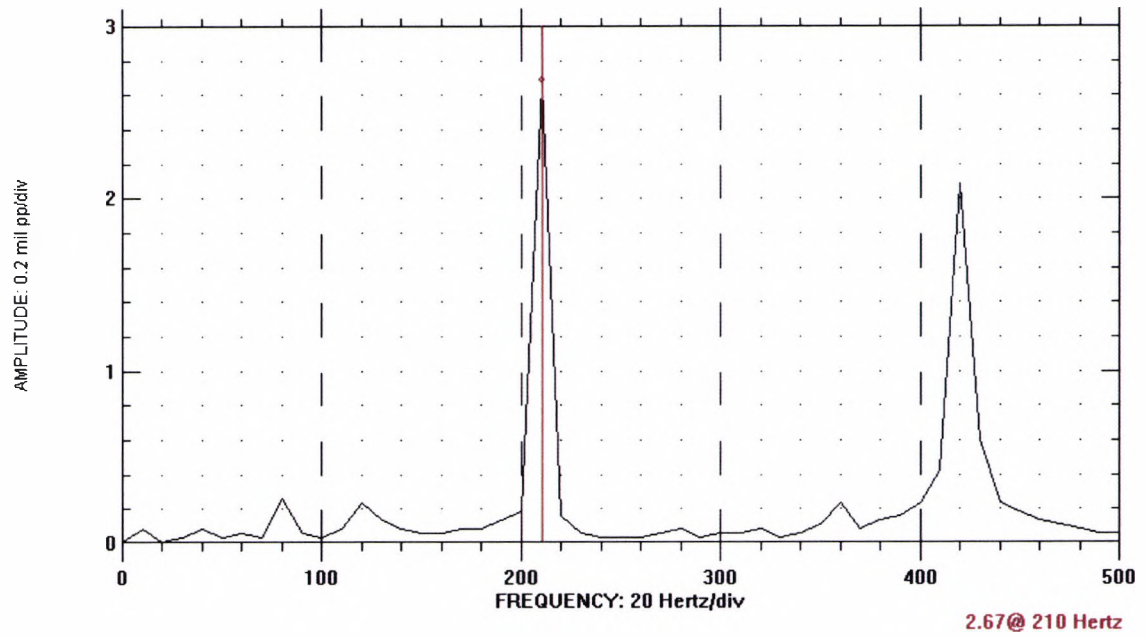


**Fig 20(G): Speed = 13200 rpm**

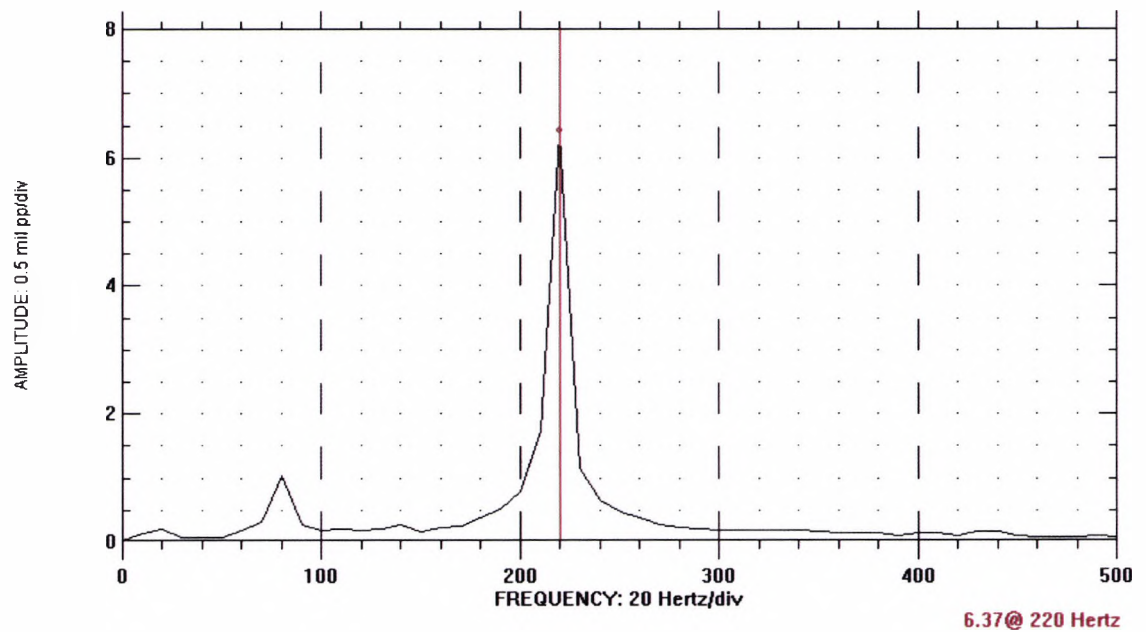


**20(H) Speed = 12600 rpm**

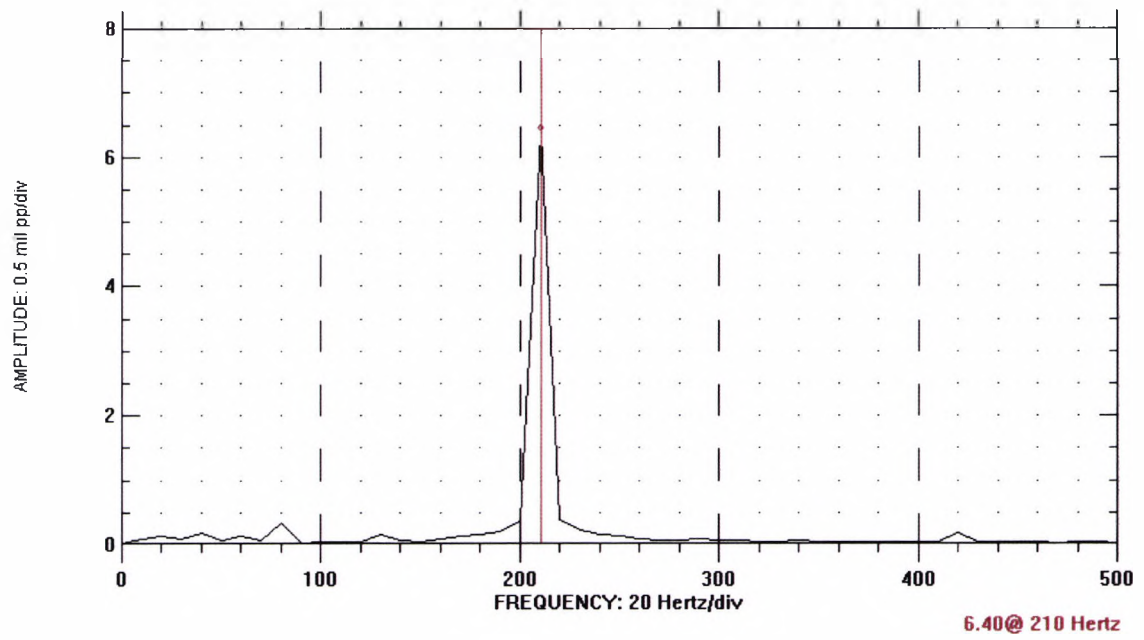
**Fig 20(H): Subsynchronous Vibration – As a function of speed.**

**Supply Pressure = 2.1 MPa**

Rear bearing Y-dir. Y axis in mils pk-pk (1mil=25.4 microns)

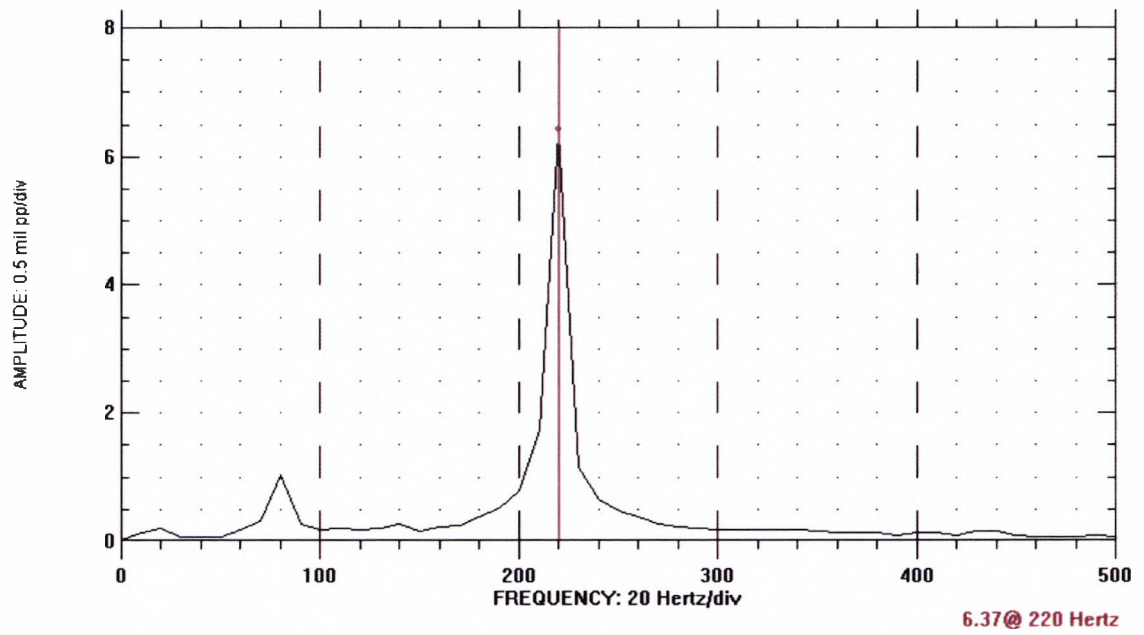


**20(J) Speed = 13200 rpm**



**20(K) Speed = 12600 rpm**

**Fig 20(K): Subsynchronous Vibration – As a function of speed.  
 Supply Pressure = 2.1 MPa  
 Impeller X-dirn. Y axis in mils pk-pk (1mil=25.4 microns)**



**20(L) Speed = 13200 rpm**

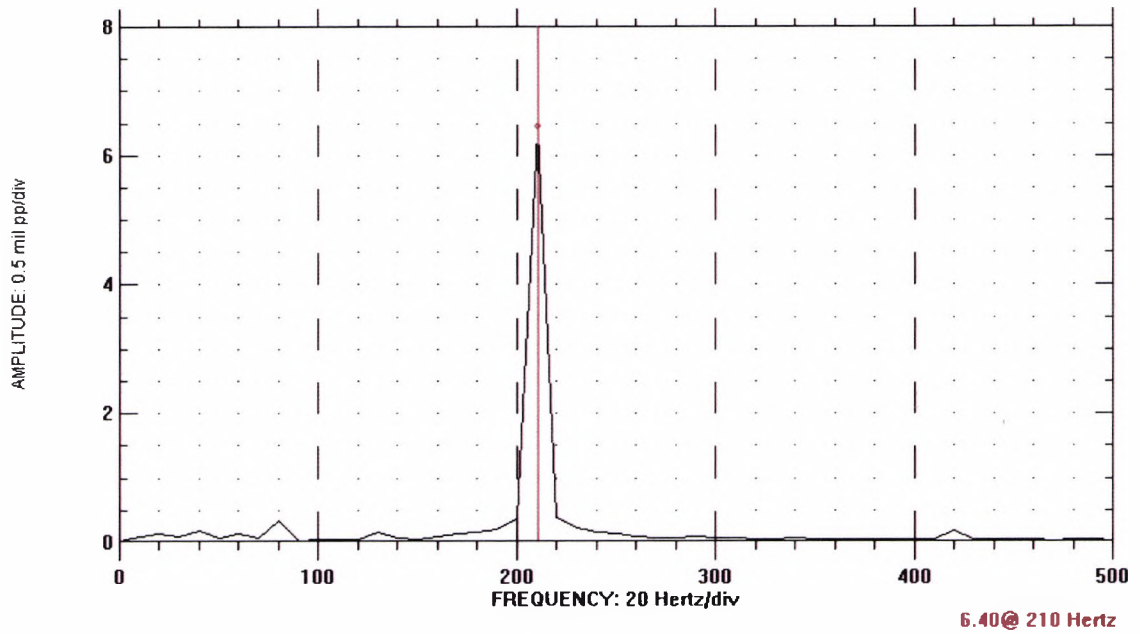


**Fig 20(M) Speed = 12600 rpm**

**Fig 20(M): Subsynchronous Vibration – As a function of speed.**

**Supply Pressure = 2.1 MPa**

Impeller Y-dirn. Y axis in mils pk-pk (1mil=25.4 microns)

### Effect Of supply pressure

Position	Supply pressure	
	2.1 MPa	1.7 MPa
Front bearing, X	0.2	1.6
Front bearing, Y	0.3	1.3
Rear bearing, X	0.2	0.65
Rear bearing, Y	0.22	0.65
Impeller, X	0.4	1.8
Impeller, Y	0.35	1.8

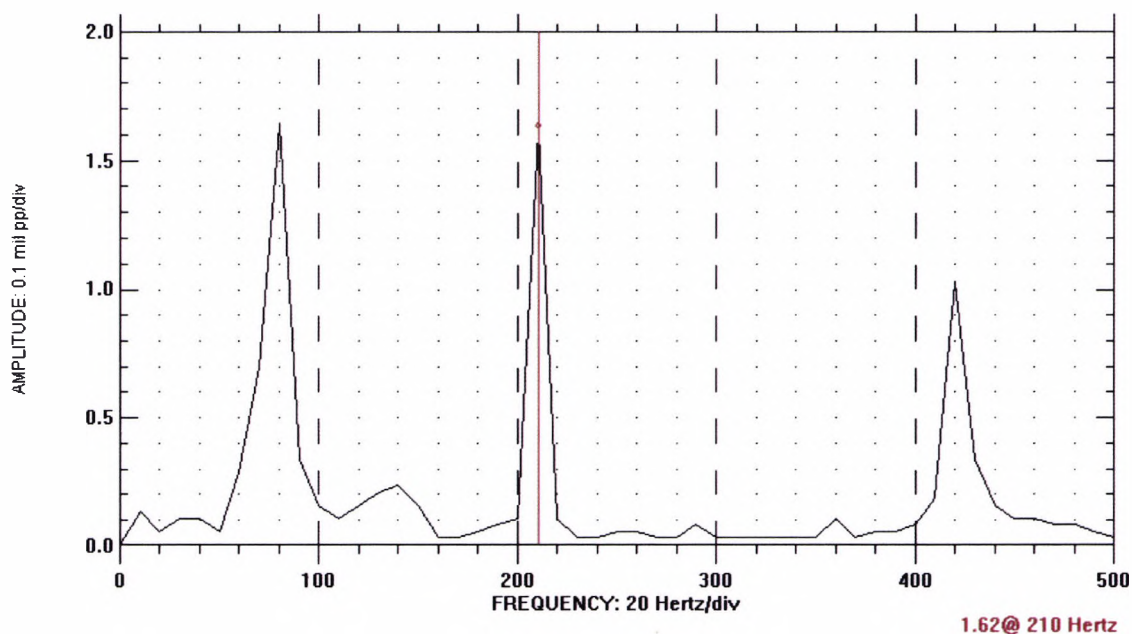


**Fig 21(A): Subsynchronous Vibration at Supply Pressure = 1.7 MPa,  
Speed = 12600 rpm  
Front Bearing X-direction. Y axis in mils pk-pk (1mil=25.4 microns)**

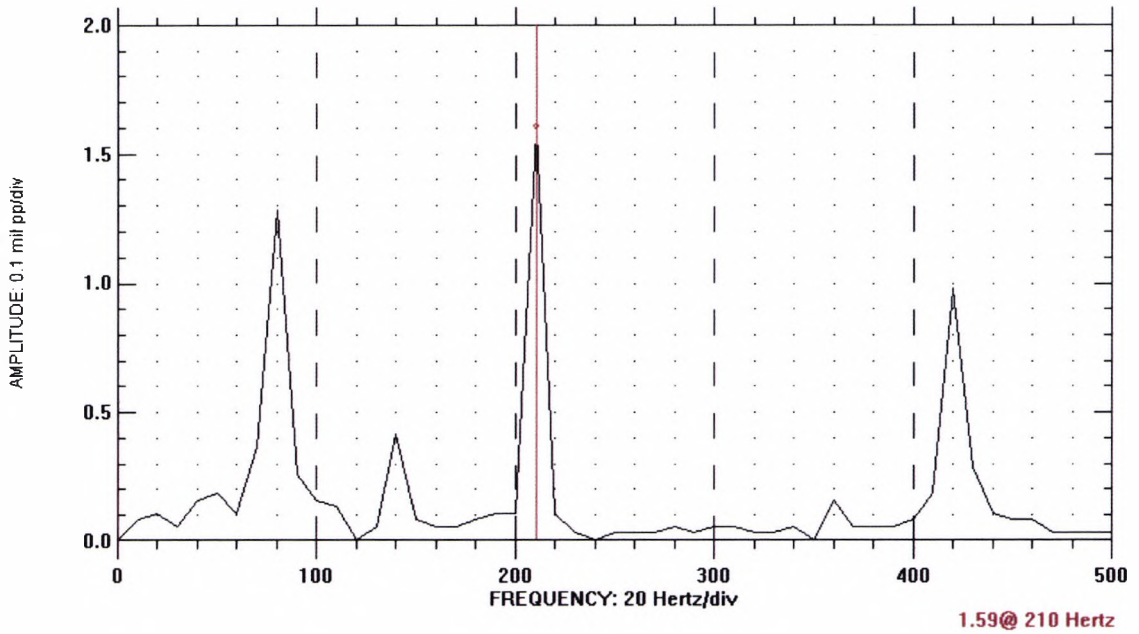


**Fig 21(B): Subsynchronous Vibration at Supply Pressure = 1.7 MPa,  
Speed = 12600 rpm**  
Front Bearing Y-direction. Y axis in mils pk-pk (1mil=25.4 microns)

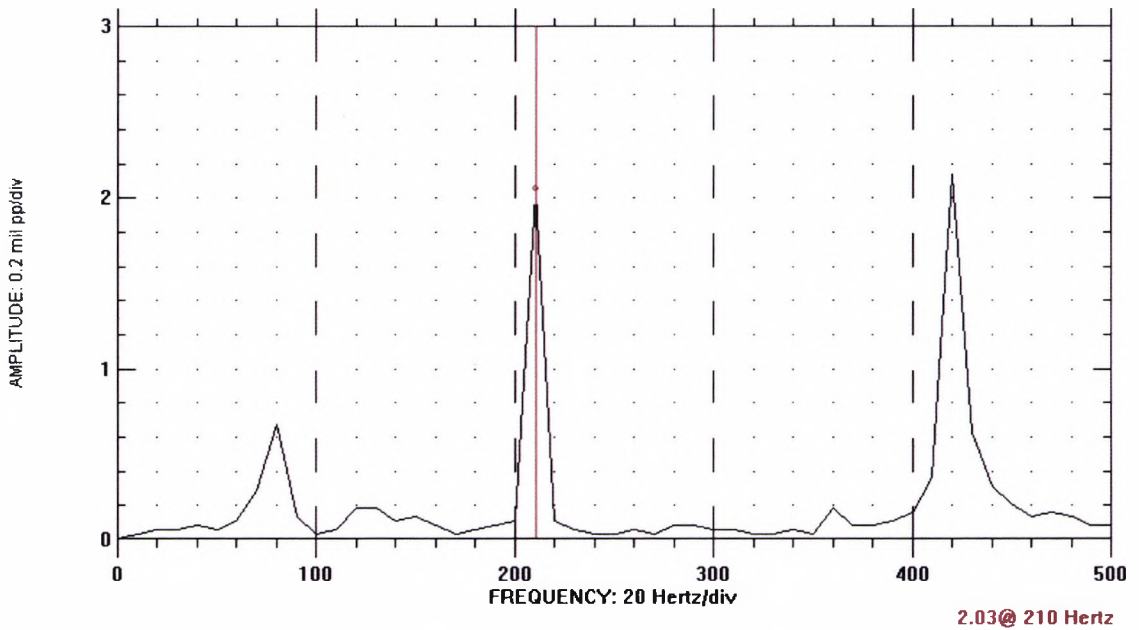


**Fig 21(C): Subsynchronous Vibration at Supply Pressure = 1.7 MPa,  
Speed = 12600 rpm**  
Rear Bearing X-direction. Y axis in mils pk-pk (1mil=25.4 microns)

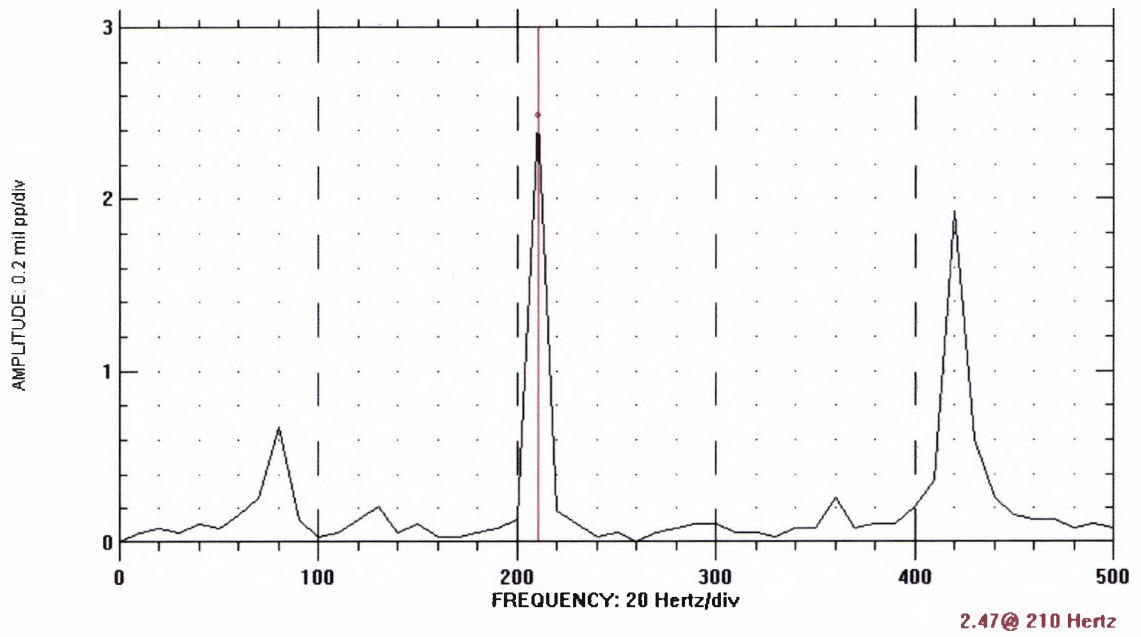


**Fig 21(D): Subsynchronous Vibration at Supply Pressure = 1.7 MPa,  
Speed = 12600 rpm  
Rear Bearing Y-direction. Y axis in mils pk-pk (1mil=25.4 microns)**

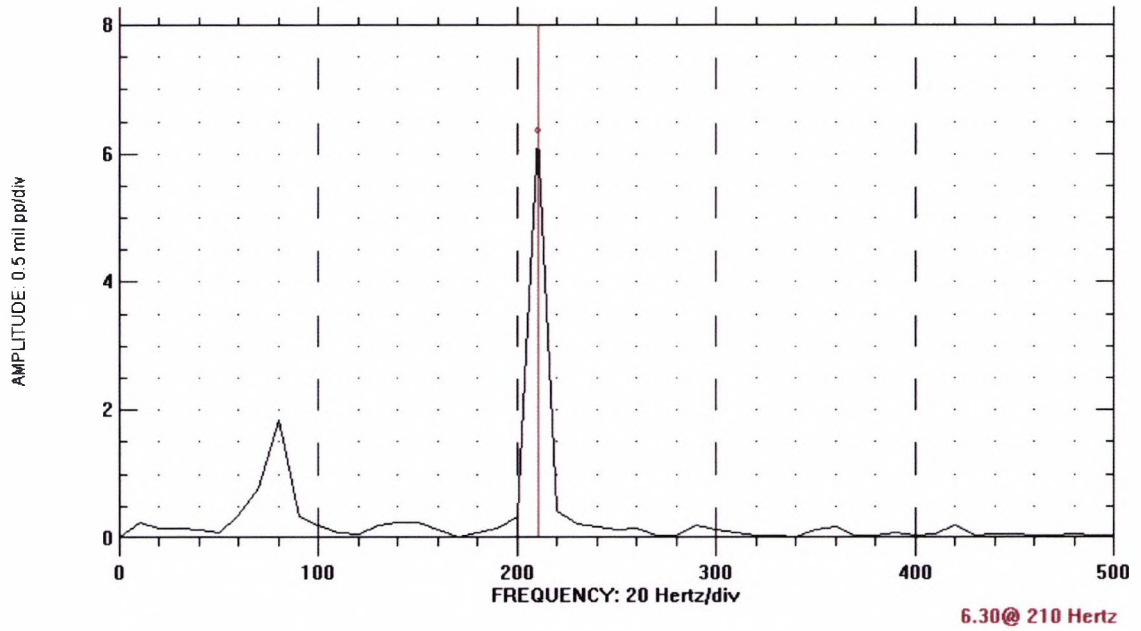


**Fig 21(E): Subsynchronous Vibration at Supply Pressure = 1.7 MPa,  
Speed = 12600 rpm  
Impeller X-direction. Y axis in mils pk-pk (1mil=25.4 microns)**

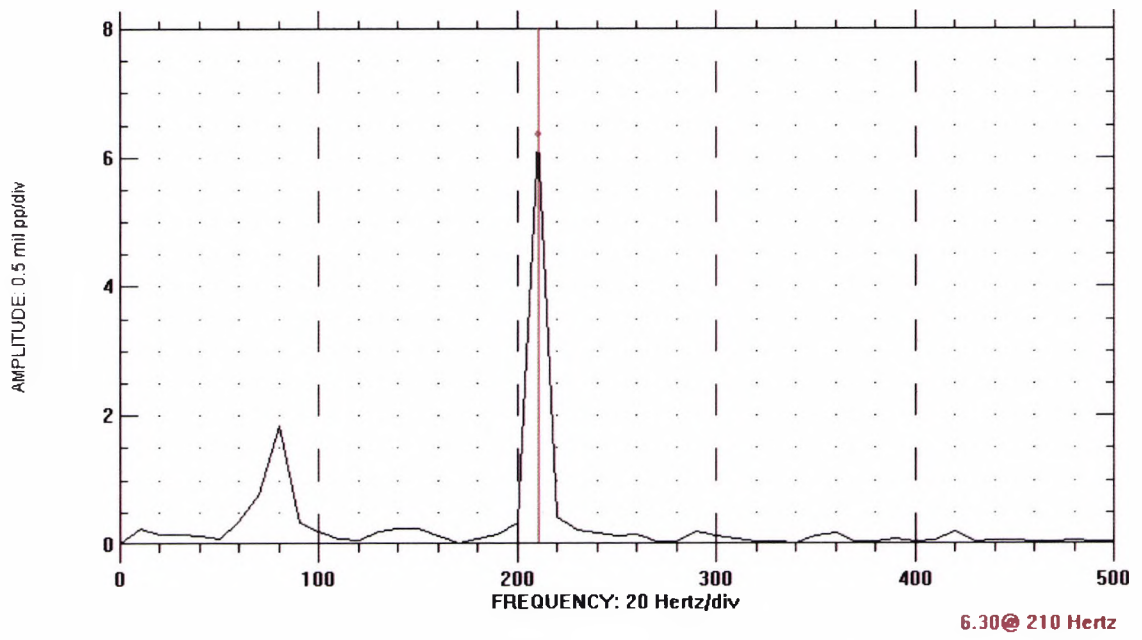


**Fig 21(F): Subsynchronous Vibration at Supply Pressure = 1.7 MPa,  
Speed = 12600 rpm**  
Impeller Y-direction. Y axis in mils pk-pk (1mil=25.4 microns)

**Rotor Response to unsteady supply pressure (Pump cavitation)**

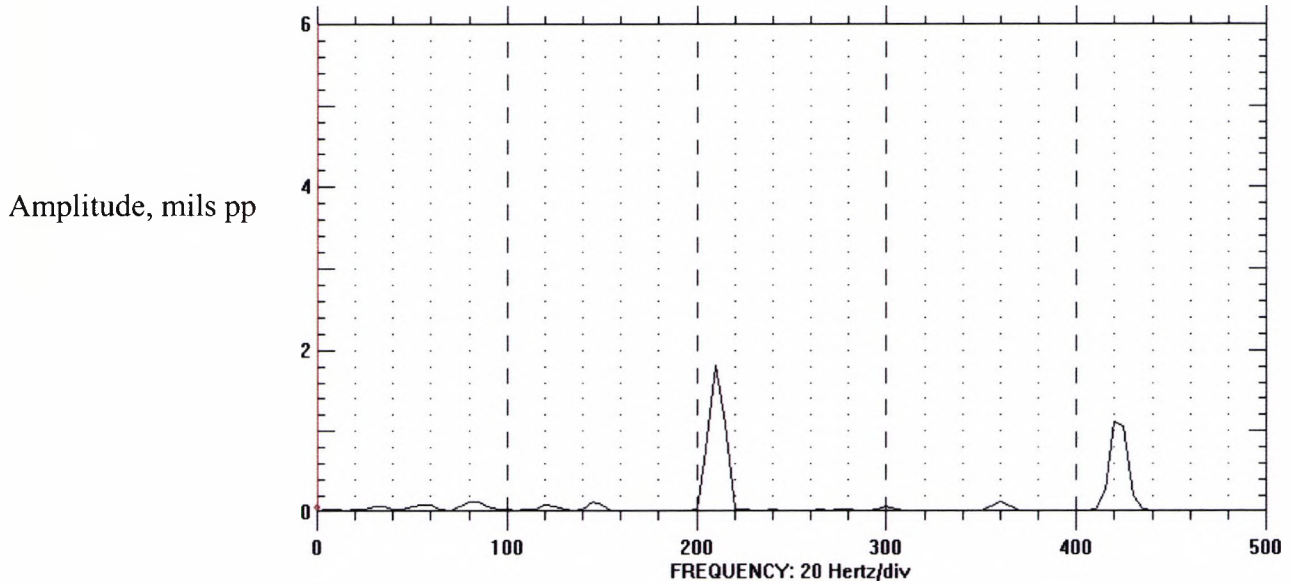


**Fig 22(A): Vibration at Front bearing, X direction  
before supply pressure instability due to pump cavitation**

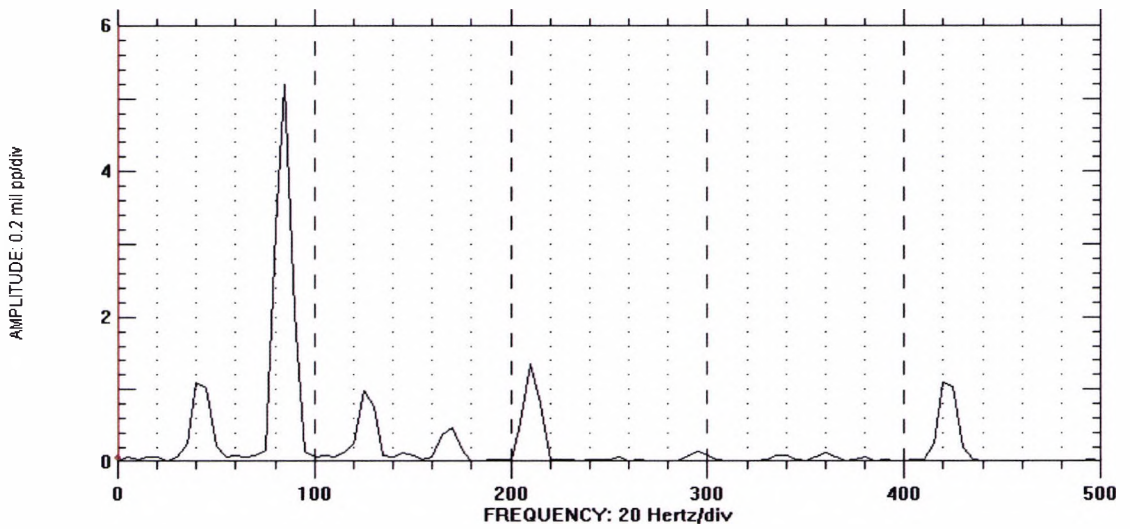


**Fig 22(B): Vibration at Front bearing, X direction  
during supply pressure instability due to pump cavitation**

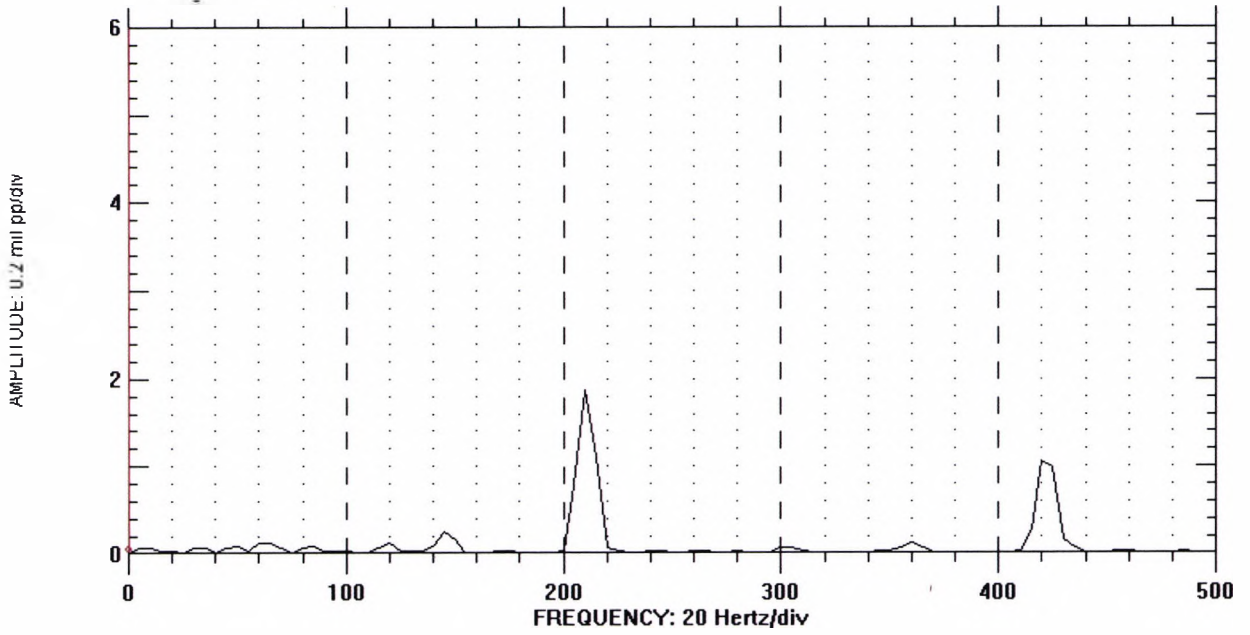


**Fig 22(C): Vibration at Front bearing, Y direction,  
before supply pressure instability due to pump cavitation.**  
Y axis in mils pk-pk (1mil=25.4 microns)

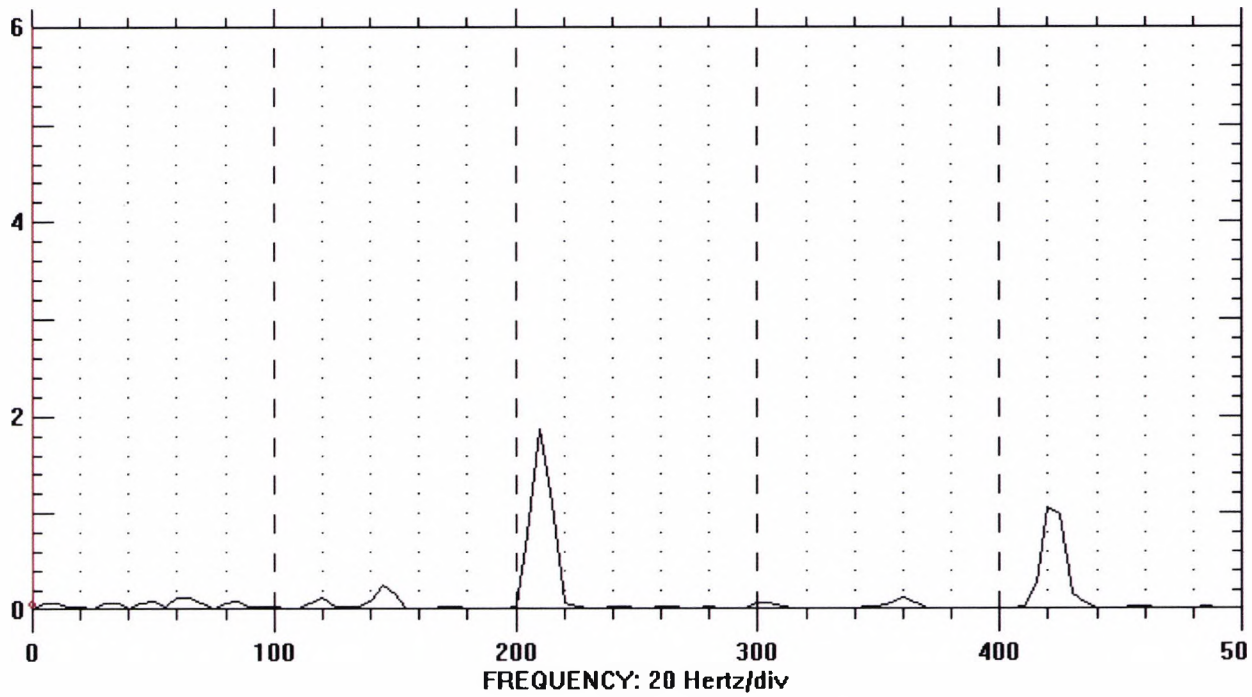


**Fig 22(D): Vibration at Front bearing, Y direction,  
during supply pressure instability due to pump cavitation.**  
Y axis in mils pk-pk (1mil=25.4 microns)

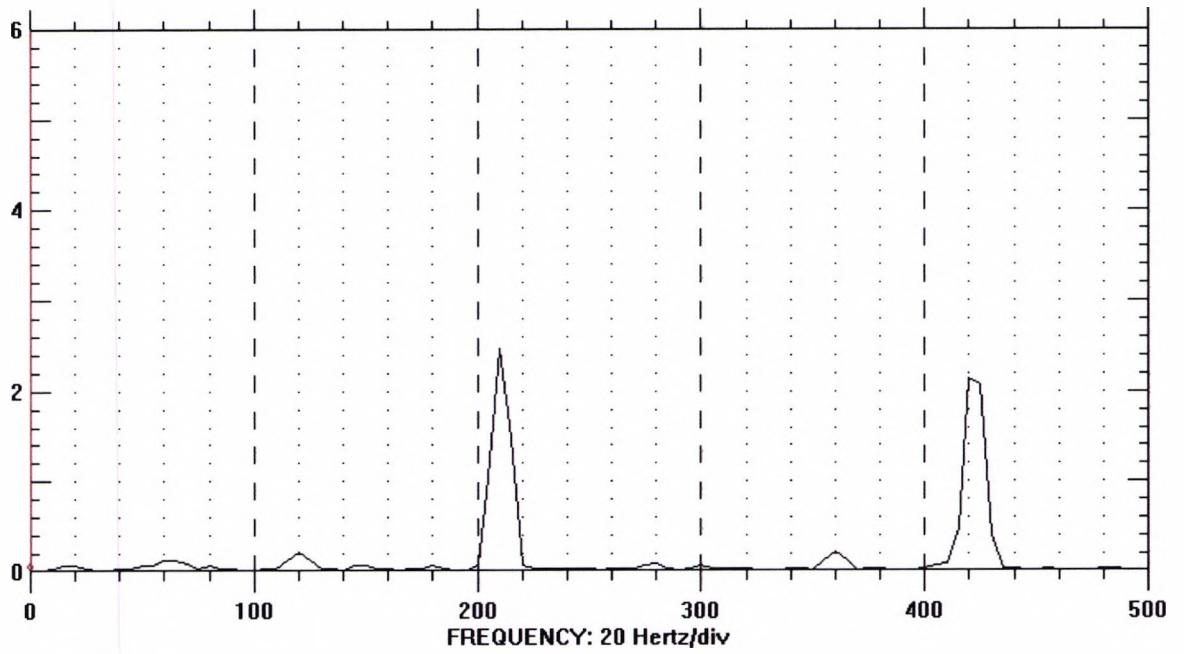


**Fig 22(E): Vibration at Rear bearing, X direction,  
before supply pressure instability due to pump cavitation.**  
Y axis in mils pk-pk (1mil=25.4 microns)

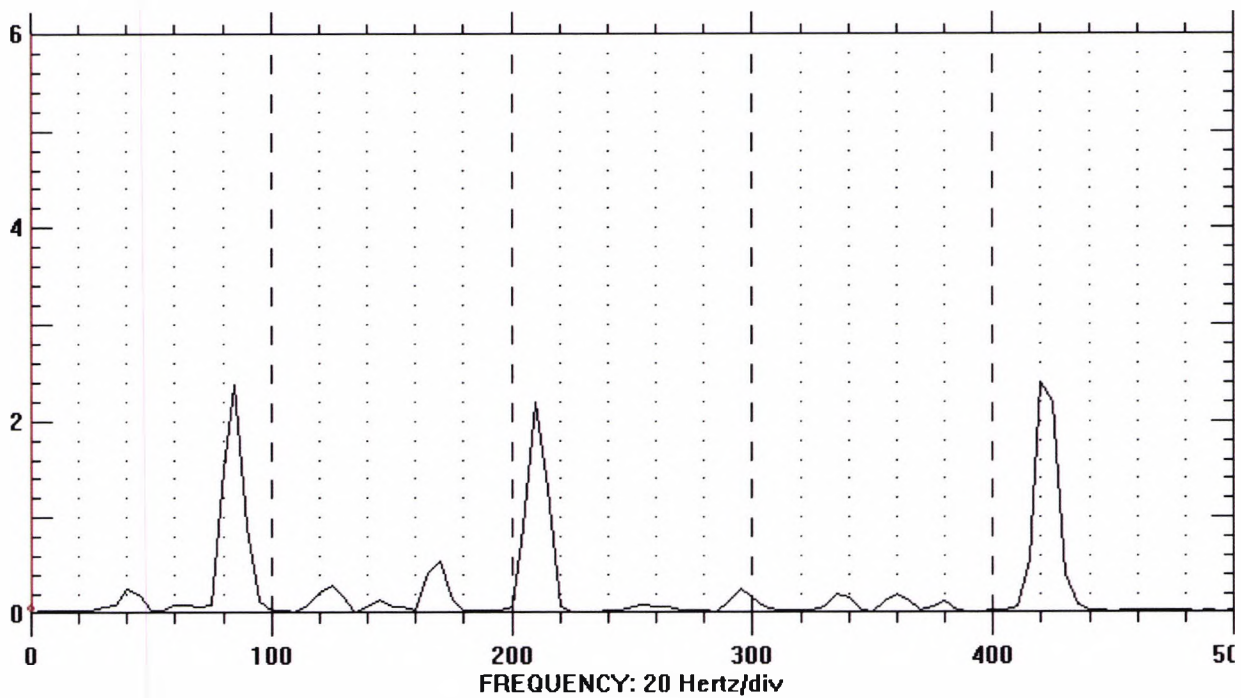


**Fig 22(F): Vibration at Rear bearing, X direction  
during supply pressure instability due to pump cavitation.**  
Y axis in mils pk-pk (1mil=25.4 microns)

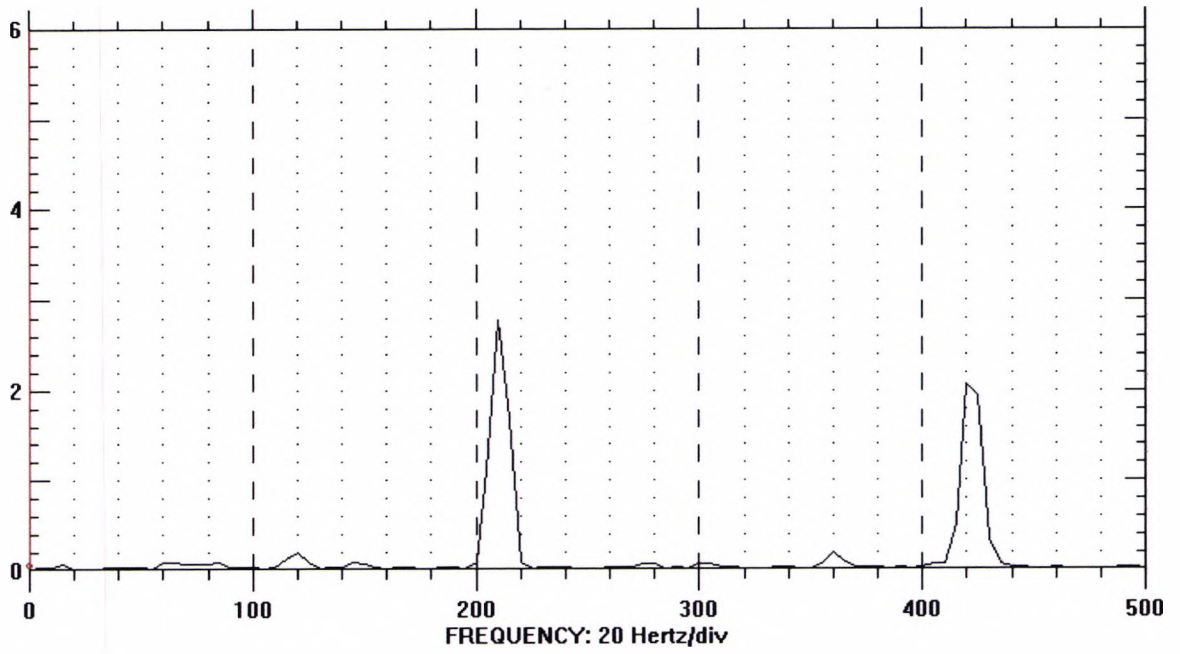


**Fig 22(G): Vibration at Rear bearing, Y direction  
before supply pressure instability due to pump cavitation.**  
Y axis in mils pk-pk (1mil=25.4 microns)

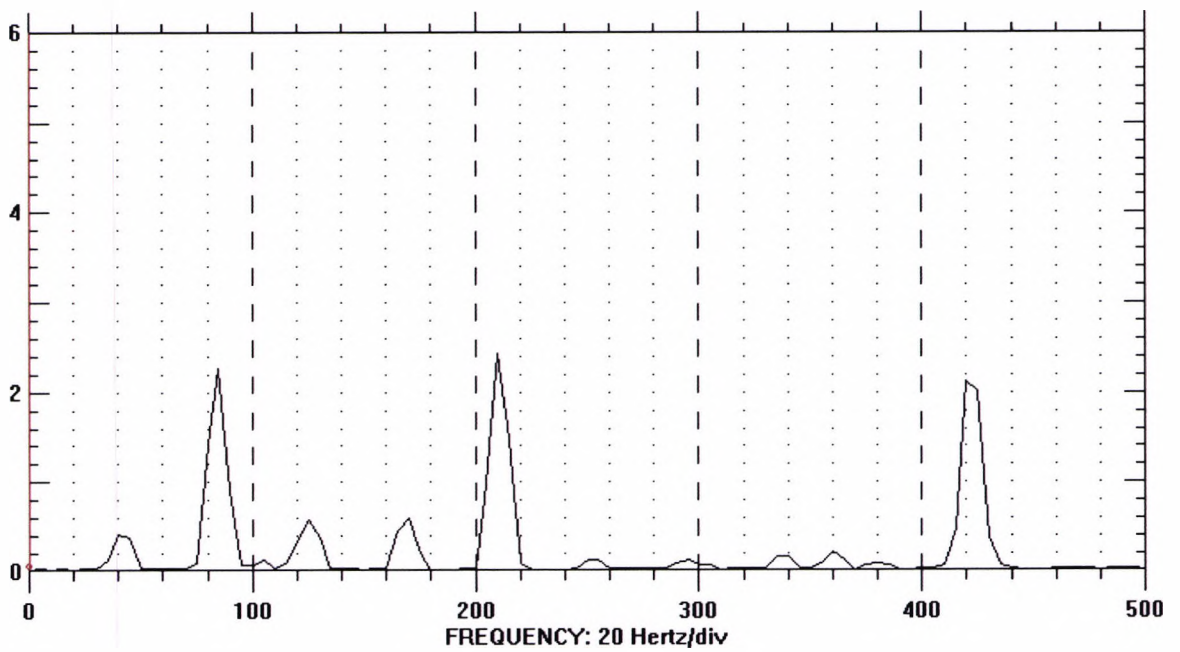


**Fig 22(H): Vibration at Rear bearing, Y direction  
during supply pressure instability due to pump cavitation**

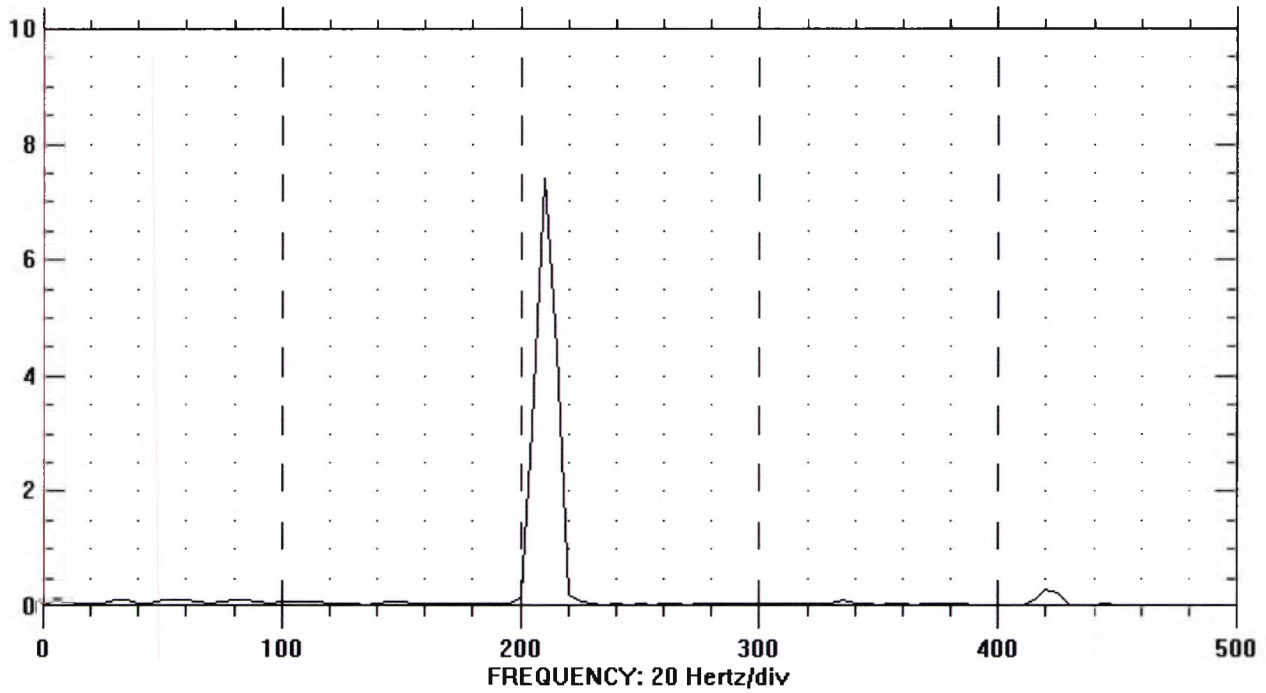


**Fig 22(J): Vibration at Impeller, X direction  
before supply pressure instability due to pump cavitation.**  
Y axis in mils pk-pk (1mil=25.4 microns)

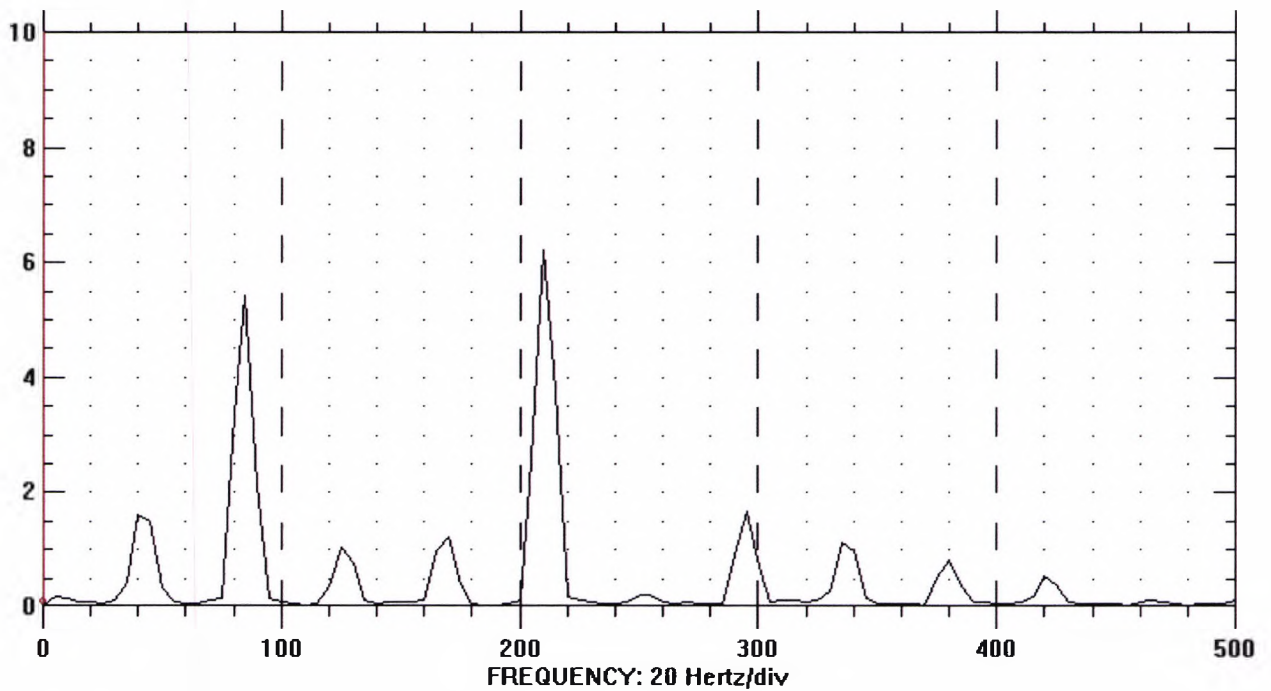


**Fig 22(K): Vibration at Impeller, X direction  
during supply pressure instability due to pump cavitation.**  
Y axis in mils pk-pk (1mil=25.4 microns)

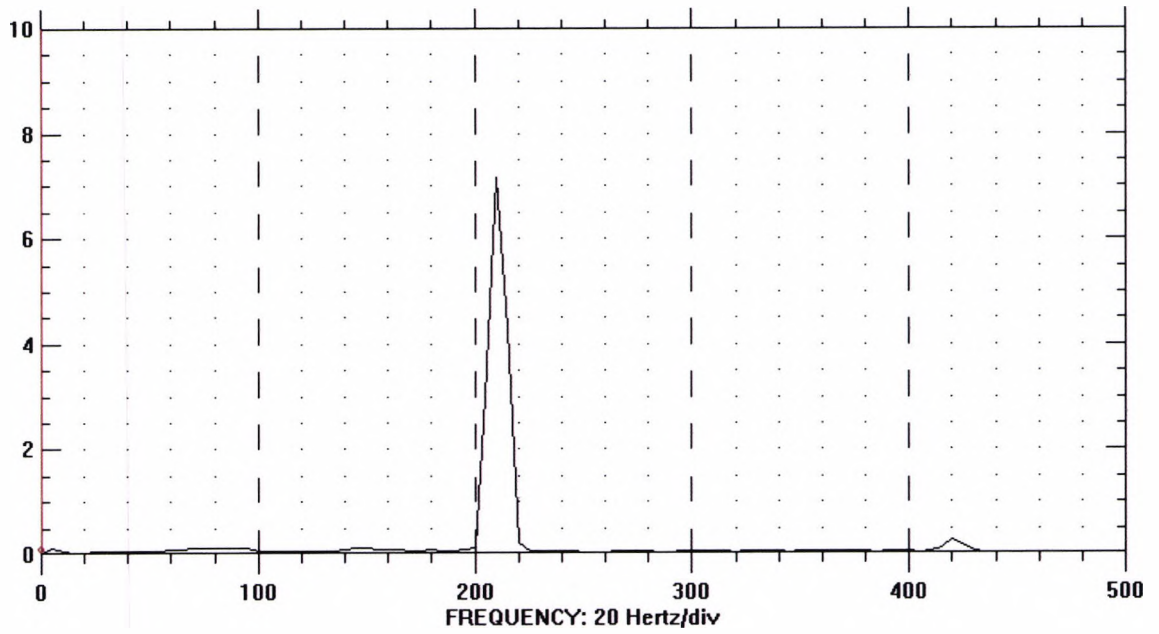


**Fig 22(L): Vibration at Impeller, Y direction  
before supply pressure instability due to pump cavitation.**  
Y axis in mils pk-pk (1mil=25.4 microns)

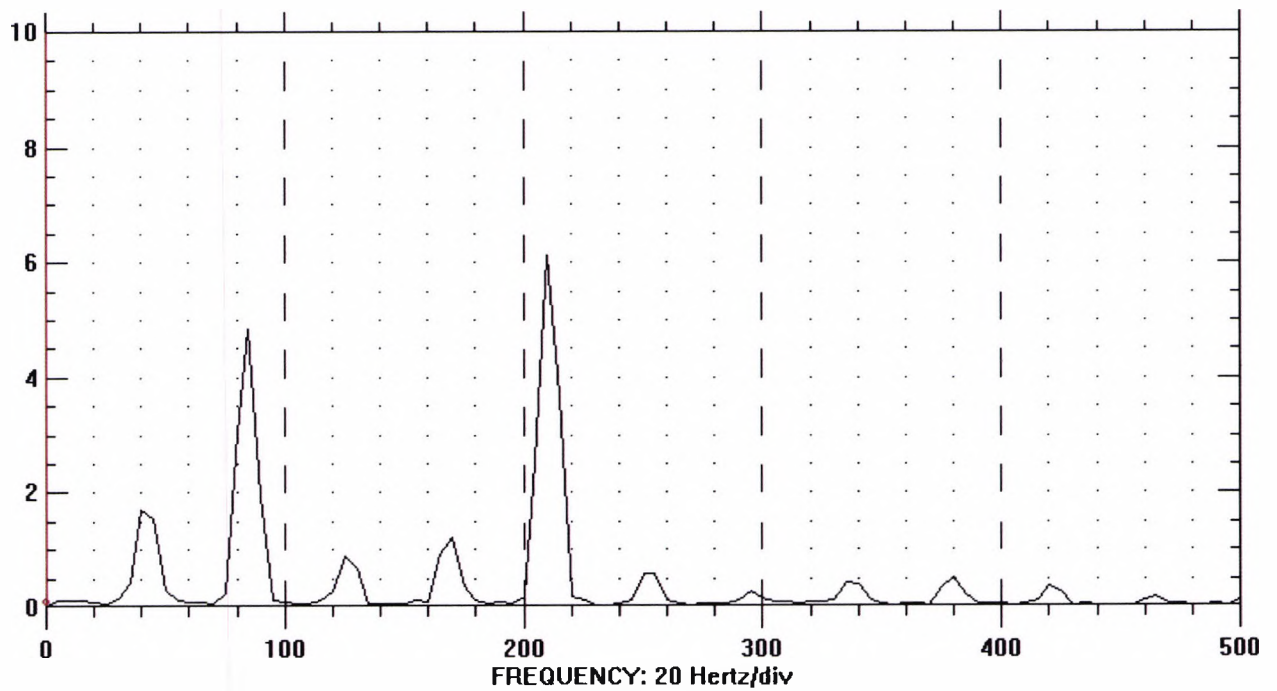


**Fig 22(M): Vibration at Impeller, Y direction  
during supply pressure instability due to pump cavitation.**  
Y axis in mils pk-pk (1mil=25.4 microns)

### **Effect of the Unbalanced Magnetic field – The Source of 2X Vibration**

The stator winding produces three phases of sine wave magnetic fields from the three power phases. This electrical input is summed to give a single sine wave magnetic field in the air gap, forming a north pole and south pole at any instant of time. The resultant flux field rotates at a frequency equal to that of the inverter power supply. Torque is generated in an induction motor by the relative slipping condition between the rotating electromagnetic field and the rotor cage. It is this slipping relationship which induces a counter electromagnetic field in the rotor to drive the resisting machine load. Since the magnetic field and the two poles are rotating at the supply frequency, any point in the air gap. these poles will pass at a frequency rate of twice the supply frequency. A radial magnetic pull occurs across the air gap at these poles, acting between the rotor and stator to give the major force acting on the motor.

The flux density is not really a continuous sine wave variation in the air gap, but has discrete steps of flux increase formed by the individual stator slots. Each slot adds an additional step increase in flux at the air gap, giving an approximate sine wave variation. The rotor bars also add stepwise variations in the flux density, since the rotor tooth alignment also affects the flux flow across the air gap. Since both of these variations are almost step increases, very high frequency "slot" forces and substantial harmonics are generated.

Asymmetry in the magnetic field due to unequal air gaps caused by misalignment in bearings and machining tolerances, gives rise to a radial force proportional to the size of the air gap. For a shaft whirling about an equilibrium position, the air gap reaches a minimum position four times, twice each in the horizontal and vertical positions. Hence the frequency of the unbalanced magnetic pull is twice that of the speed of rotation. The force contains two parts, a constant part and a time varying force with twice the rotational speed. The constant part is present when the rotor equilibrium position is eccentric with respect to the stator housing. The unbalanced magnetic force is proportional to the square of flux density. For small eccentricities

and whirl amplitudes, the flux density is inversely proportional to the air gap. For the present motor construction, the air gap is 1 mm and based on the tolerances between various fits and bearing film thickness, the eccentricity is 0.125mm. The constant force was modeled as a negative spring and an asynchronous analysis was carried out to match the amplitude at 2x the frequency. A force equal to 2600 kN at motor was required to match the observed amplitude of 2.5 mils (63 $\mu$ m) at 26400 cpm.

All the vibration spectra show an amplitude at twice the running frequency. By observing the coast down waterfall plot given in Figure (4.12A-D), it can be seen that the 2x vibration disappears when the power is shut off. This establishes that the source of twice the vibration frequency is an electrical phenomenon. Another electrical source is the harmonics present in the input voltage waveform.

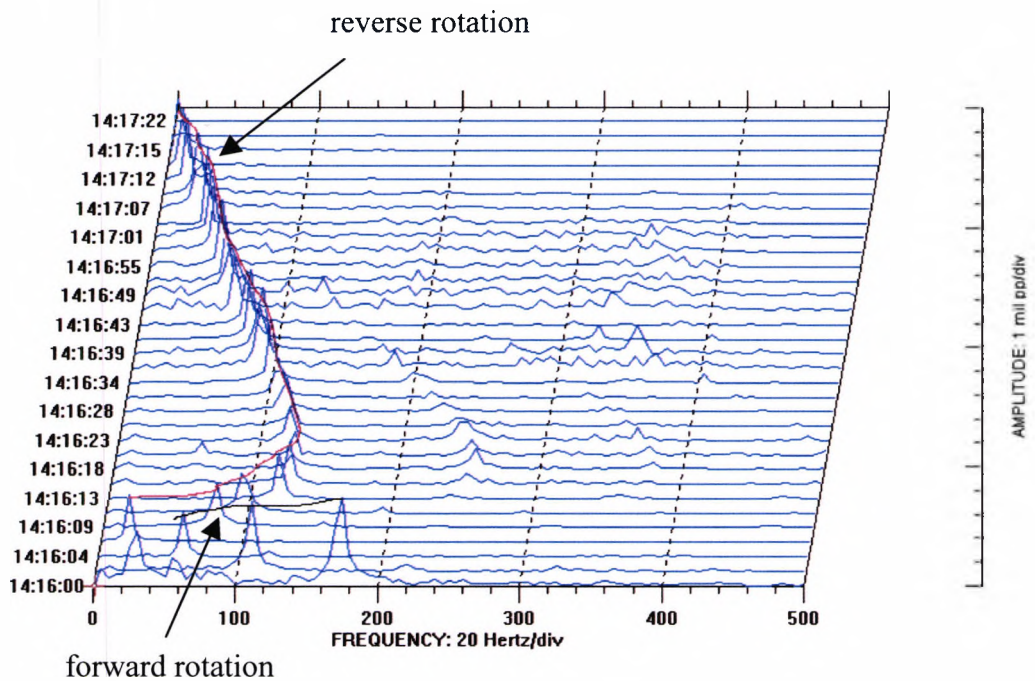


**Fig 23(A): Coast down Waterfall plot at Impeller, X direction.**  
Y axis in mils pk-pk (1mil=25.4 microns)

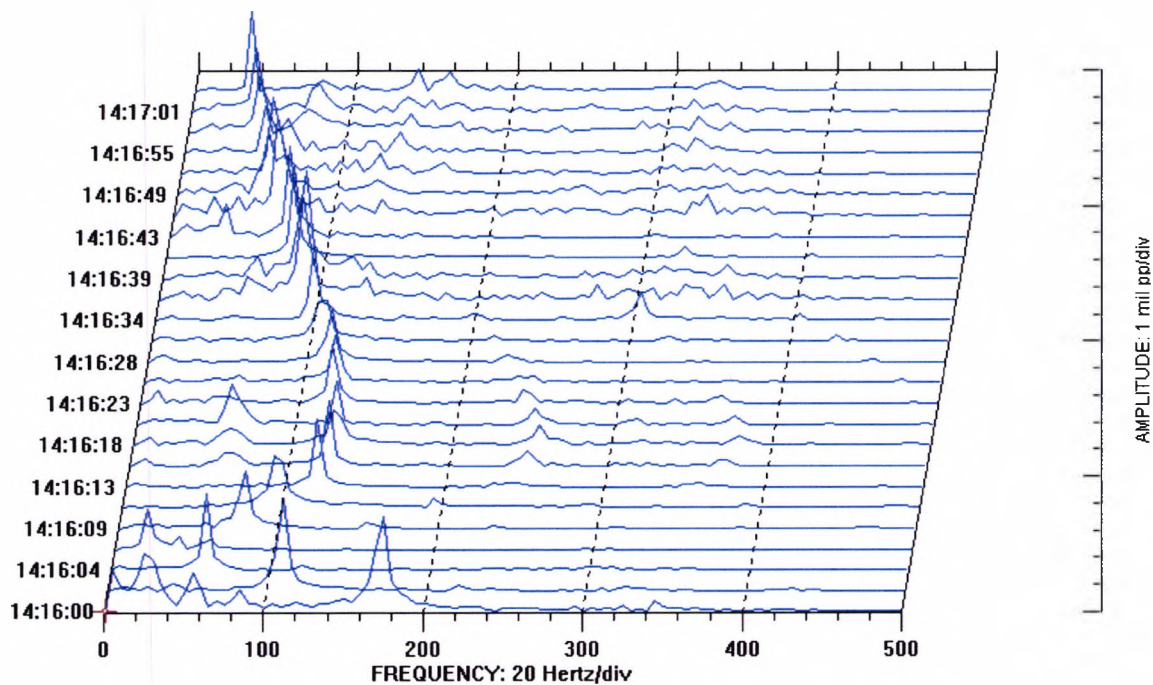


**Fig 23(B): Coast down Waterfall plot at Impeller, Y direction**

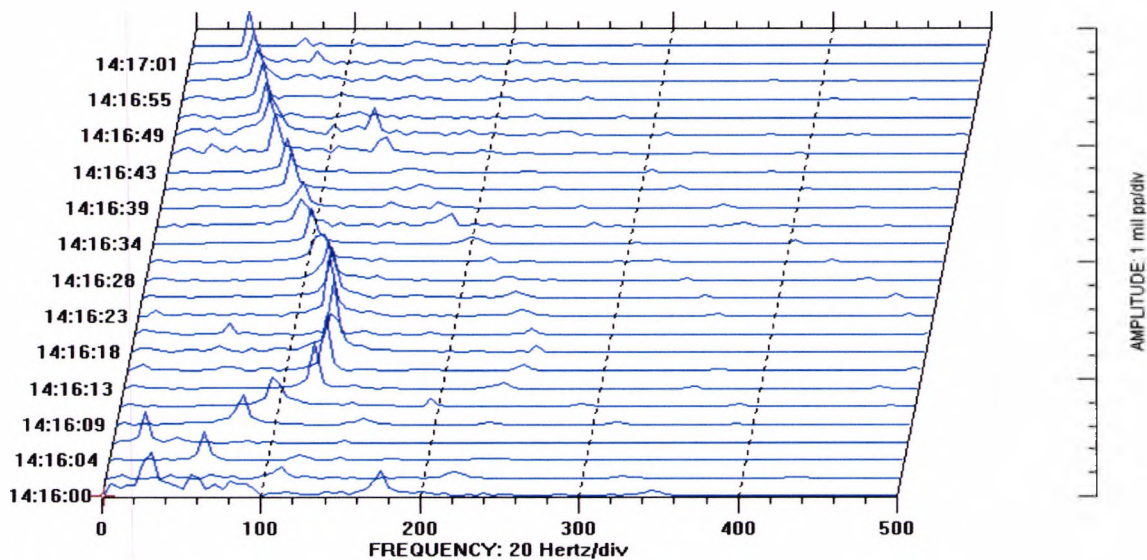


**Fig 23(C): Coast down Waterfall plot at Front Bearing, X direction**

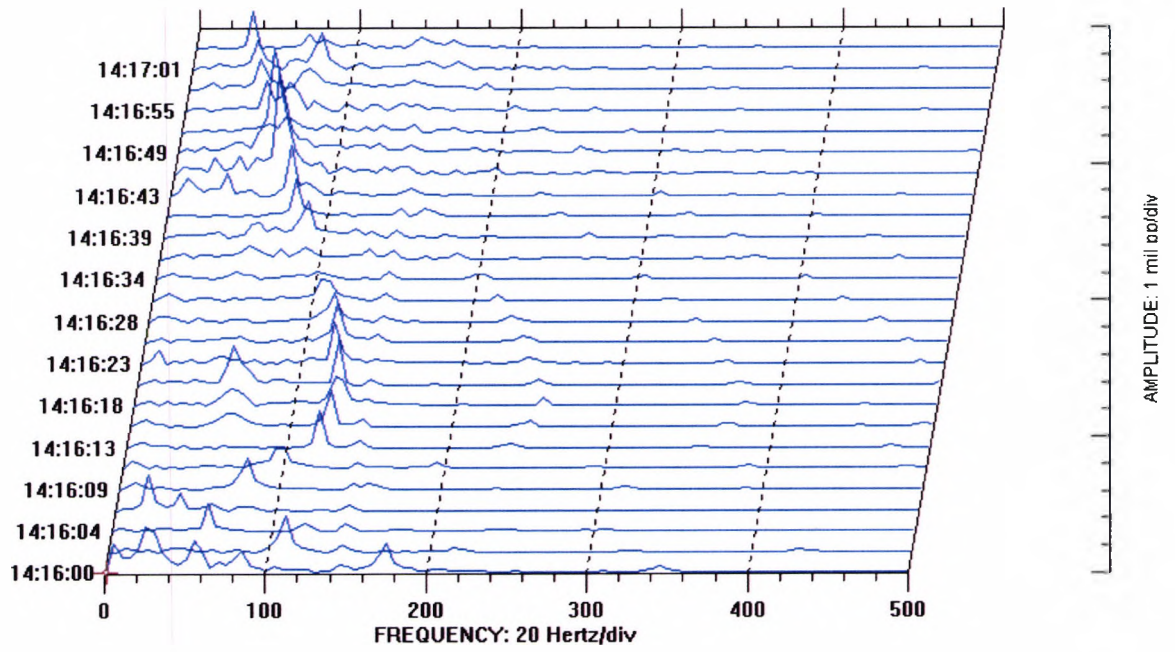


**Fig (23D): Coastdown Waterfall plot at Front Bearing, Y direction**

## APPENDIX E

### Derivation Of Laminar Lubrication Equation - Reynolds Equation

Reynolds equation is a combination of the Navier-Stokes and continuity equations.

The continuity equation for an incompressible fluid may be written as:

$$\frac{\partial u}{\partial x} + \frac{\partial v}{\partial y} + \frac{\partial w}{\partial z} = 0$$

The Navier-Stokes equation is derived by considering dynamic equilibrium of a fluid element under surface, body and inertia forces. Surface forces comprise the hydrostatic pressure and shear forces. The body force element needed to accelerate a fluid element may be an external force field, say gravity, associated with the whole body of the element. Further, the fluid behaves as a Newtonian fluid i.e. the shear rate is proportional to shear stress. The dynamic equilibrium equations for a Newtonian fluid, with constant density and viscosity are given below in Cartesian coordinates:

$$\frac{\partial u}{\partial t} + u \frac{\partial u}{\partial x} + v \frac{\partial u}{\partial y} + w \frac{\partial u}{\partial z} = \frac{1}{\rho} \frac{\partial p}{\partial x} + \nu \left( \frac{\partial^2 u}{\partial x^2} + \frac{\partial^2 u}{\partial y^2} + \frac{\partial^2 u}{\partial z^2} \right) \quad (1)$$

$$\frac{\partial v}{\partial t} + u \frac{\partial v}{\partial x} + v \frac{\partial v}{\partial y} + w \frac{\partial v}{\partial z} = \frac{1}{\rho} \frac{\partial p}{\partial y} + \nu \left( \frac{\partial^2 v}{\partial x^2} + \frac{\partial^2 v}{\partial y^2} + \frac{\partial^2 v}{\partial z^2} \right) \quad (2)$$

$$\frac{\partial w}{\partial t} + u \frac{\partial w}{\partial x} + v \frac{\partial w}{\partial y} + w \frac{\partial w}{\partial z} = \frac{1}{\rho} \frac{\partial p}{\partial z} + \nu \left( \frac{\partial^2 w}{\partial x^2} + \frac{\partial^2 w}{\partial y^2} + \frac{\partial^2 w}{\partial z^2} \right) \quad (3)$$

### Dimensional Analysis of the Navier Stokes Equation

$$\frac{\partial u}{\partial t} + u \frac{\partial u}{\partial x} + v \frac{\partial u}{\partial y} + w \frac{\partial u}{\partial z} = \frac{1}{\rho} \frac{\partial p}{\partial x} + \nu \left( \frac{\partial^2 u}{\partial x^2} + \frac{\partial^2 u}{\partial y^2} + \frac{\partial^2 u}{\partial z^2} \right)$$

Dimensions of each term, after multiplying with mass term  $\rho$ , are given as follows:

$$\rho V \frac{\partial u}{\partial t} = \frac{M}{L^3} L^3 \frac{L}{T^2} = \frac{ML}{T^2}$$

$$\begin{bmatrix} \rho V u \frac{\partial u}{\partial x} \\ \rho V v \frac{\partial u}{\partial y} \\ \rho V w \frac{\partial u}{\partial z} \end{bmatrix} = \frac{M}{L^3} L^3 \frac{L}{T} \left( \frac{L}{TL} \right) = \frac{ML}{T^2}$$

$$\frac{1}{\rho} \rho V \frac{\partial p}{\partial x} = L^3 \frac{ML}{T^2} \frac{1}{L^2} \frac{1}{L} = \frac{ML}{T^2}$$

Units of kinematic viscosity  $\nu$

$$\nu = \frac{\mu}{\rho} = \frac{M L^2}{L T M} = \frac{L^2}{T}$$

$$\begin{bmatrix} \rho V \nu \frac{\partial^2 u}{\partial x^2} \\ \rho V \nu \frac{\partial^2 u}{\partial y^2} \\ \rho V \nu \frac{\partial^2 u}{\partial z^2} \end{bmatrix} = \frac{M}{L^3} L^3 \frac{L^2}{T} \left( \frac{\partial}{\partial x} \left( \frac{\partial u}{\partial x} \right) \right) = M \frac{L}{T^2} \left( \frac{1}{L} \left( \frac{L}{TL} \right) \right) = \frac{ML}{T^2}$$

Each term represents force.

### Non-dimensional terms

#### Spatial coordinates:

$$\bar{X} = \frac{x}{R}, \bar{Y} = \frac{y}{C_r}, \bar{Z} = \frac{z}{R}$$

where  $R$  = journal radius and  $C_r$  = bearing radial clearance

Velocity:

$$\bar{U} = \frac{u}{R\omega}, \bar{W} = \frac{w}{R\omega}, \bar{V} = \frac{v}{\omega C_r}$$

where  $\omega$  = journal angular velocity in rad/sec

The following relations are useful in expressing the continuity and Navier-Stokes equations in non-dimensional form:

$$\frac{\partial u}{\partial x} = \frac{\partial u}{\partial X} \frac{d\bar{X}}{dx} = \frac{1}{R} \frac{\partial u}{\partial X} = \frac{1}{R} \frac{\partial (R\omega\bar{U})}{\partial X} = \omega \frac{\partial \bar{U}}{\partial X}$$

$$\frac{\partial v}{\partial y} = \frac{\partial v}{\partial Y} \frac{d\bar{Y}}{dy} = \frac{1}{C_r} \frac{\partial v}{\partial Y} = \omega \frac{\partial \bar{V}}{\partial Y}$$

$$\frac{\partial w}{\partial z} = \frac{\partial w}{\partial Z} \frac{d\bar{Z}}{dz} = \frac{1}{R} \frac{\partial w}{\partial Z} = \frac{1}{R} \frac{\partial (R\omega\bar{W})}{\partial Z} = \omega \frac{\partial \bar{W}}{\partial Z}$$

### The non-dimensional form of the Continuity Equation

Substituting for  $\frac{\partial u}{\partial x}$ ,  $\frac{\partial v}{\partial y}$  and  $\frac{\partial w}{\partial z}$  from the above into the continuity equation, the following non-dimensional form of the continuity equation is obtained:

$$\omega \frac{\partial \bar{U}}{\partial X} + \omega \frac{\partial \bar{V}}{\partial Y} + \omega \frac{\partial \bar{W}}{\partial Z} = 0$$

Dividing by  $\omega$ , the above equation becomes,

$$\frac{\partial \bar{U}}{\partial X} + \frac{\partial \bar{V}}{\partial Y} + \frac{\partial \bar{W}}{\partial Z} = 0$$

### The non-dimensional form of the Navier-Stokes Equation

The following **non-dimensional** pressure, time and Reynold's number will be used

$$\bar{P} = \text{Re} \left( \frac{C_r}{R} \right) \left( \frac{P}{C_r (R\omega^2)} \right)$$

$$\text{Re} = \frac{C_r (R\omega)}{\nu}, t = \omega t$$

For the sake of simplicity, each term in the Navier-Stokes equation will be derived in its non-dimensional form separately:

$$\frac{\partial u}{\partial t} = R\omega \frac{\partial \bar{U}}{\partial t} \frac{dt}{dt} = R\omega^2 \frac{\partial \bar{U}}{\partial t}$$

$$u \frac{\partial u}{\partial x} = (\bar{U} R\omega) \frac{R\omega}{R} \frac{\partial \bar{U}}{\partial X} = R\omega^2 \bar{U} \frac{\partial \bar{U}}{\partial X}$$

$$\frac{\partial u}{\partial y} = \frac{\partial u}{\partial Y} \frac{d\bar{Y}}{dy} = \left( \frac{1}{C_r} \right) \left( \frac{\partial (\bar{U} R\omega)}{\partial Y} \right) = \frac{R\omega}{C_r} \frac{\partial \bar{U}}{\partial Y}$$

$$v \frac{\partial v}{\partial y} = R\omega \frac{C_r \bar{V}}{R} \frac{R\omega \partial \bar{V}}{C_r \partial Y} = R\omega^2 \bar{V} \frac{\partial \bar{V}}{\partial Y}$$

$$w \frac{\partial u}{\partial z} = \bar{W} R\omega \frac{\partial u}{\partial Z} \frac{d\bar{Z}}{dz} = \bar{W} R\omega \left( \frac{R\omega \partial \bar{U}}{R \partial Z} \right) = R\omega^2 \bar{W} \frac{\partial \bar{U}}{\partial Z}$$

$$\frac{\partial^2 u}{\partial x^2} = \frac{\partial}{\partial x} \left( \frac{\partial u}{\partial x} \right) = \frac{\partial}{\partial x} \left( \omega \frac{\partial \bar{U}}{\partial X} \right) = \omega \frac{\partial^2 \bar{U}}{\partial X^2} \frac{dX}{dx} = \frac{\omega \partial^2 \bar{U}}{R \partial X^2}$$

$$\frac{\partial^2 u}{\partial y^2} = \frac{\partial}{\partial y} \left( \frac{\partial u}{\partial y} \right) = \frac{\partial}{\partial y} \left( \frac{R\omega \partial \bar{U}}{C_r \partial Y} \right) = \frac{R\omega \partial^2 \bar{U}}{C_r \partial Y^2} \frac{dY}{dy} = \frac{R\omega \partial^2 \bar{U}}{C_r^2 \partial Y^2}$$

$$\frac{\partial^2 u}{\partial z^2} = \frac{\partial}{\partial z} \left( \frac{\partial u}{\partial z} \right) = \frac{\partial}{\partial z} \left( \omega \frac{\partial \bar{U}}{\partial Z} \right) = \omega \frac{\partial^2 \bar{U}}{\partial Z^2} \frac{dZ}{dz} = \frac{\omega \partial^2 \bar{U}}{R \partial Z^2}$$

Using the non-dimensional pressure,

$$\frac{\partial p}{\partial x} = \frac{\partial p}{\partial X} \frac{dX}{dx} = \frac{1}{R} \left[ \rho (R\omega^2) \left( \frac{R}{C_r} \right) \frac{1}{\text{Re}} \right] \frac{\partial \bar{P}}{\partial X}$$

Substituting the above in equation (1), the **left hand side** of the equation is given as

$$R\omega^2 \frac{\partial \bar{U}}{\partial t} + R\omega^2 \bar{U} \frac{\partial \bar{U}}{\partial X} + R\omega^2 \bar{V} \frac{\partial \bar{U}}{\partial Y} + R\omega^2 \bar{W} \frac{\partial \bar{U}}{\partial Z}$$

$$R\omega^2 \left( \frac{\partial \bar{U}}{\partial t} + \bar{U} \frac{\partial \bar{U}}{\partial X} + \bar{V} \frac{\partial \bar{U}}{\partial Y} + \bar{W} \frac{\partial \bar{U}}{\partial Z} \right)$$

Dividing by  $\frac{R\omega^2 \left( \frac{R}{C_r} \right)}{\text{Re}}$ , the left hand side of equation reduces to

$$\text{Re} \left( \frac{C_r}{R} \right) \left( \frac{\partial \bar{U}}{\partial t} + \bar{U} \frac{\partial \bar{U}}{\partial X} + \bar{V} \frac{\partial \bar{U}}{\partial Y} + \bar{W} \frac{\partial \bar{U}}{\partial Z} \right)$$

Substituting the non dimensional terms into the **right hand side** of the equation, (1) can be reduced as follows:

$$-\frac{1}{\rho R} \left[ \rho (R\omega)^2 \left( \frac{R}{C_r} \right) \frac{1}{\text{Re}} \right] \frac{\partial \bar{P}}{\partial X} + \nu \left( \frac{\omega}{R} \frac{\partial^2 \bar{U}}{\partial X^2} + \frac{R\omega}{C_r} \frac{\partial^2 \bar{U}}{\partial Y^2} + \frac{\omega}{R} \frac{\partial^2 \bar{U}}{\partial Z^2} \right)$$

$$-\left[ R\omega^2 \left( \frac{R}{C_r} \right) \frac{1}{\text{Re}} \right] \frac{\partial \bar{P}}{\partial X} + \frac{\nu\omega}{R} \frac{\partial^2 \bar{U}}{\partial X^2} + \frac{\nu R\omega}{C_r} \frac{\partial^2 \bar{U}}{\partial Y^2} + \frac{\nu\omega}{R} \frac{\partial^2 \bar{U}}{\partial Z^2}$$

Dividing by  $\frac{R\omega^2}{\text{Re}} \left( \frac{R}{C_r} \right)$  or  $\frac{\nu\omega R}{C_r^2}$ , the right hand side of equation reduces to

$$\frac{\partial \bar{P}}{\partial X} + \frac{\partial^2 \bar{U}}{\partial Y^2} + \left( \frac{C_r}{R} \right)^2 \left( \frac{\partial^2 \bar{U}}{\partial X^2} + \frac{\partial^2 \bar{U}}{\partial Z^2} \right)$$

Equating the right and left hand sides, equation (1) in non-dimensional form reduces to:

$$\text{Re} \left( \frac{C_r}{R} \right) \left( \frac{\partial \bar{U}}{\partial t} + \bar{U} \frac{\partial \bar{U}}{\partial X} + \bar{V} \frac{\partial \bar{U}}{\partial Y} + \bar{W} \frac{\partial \bar{U}}{\partial Z} \right) = -\frac{\partial \bar{P}}{\partial X} + \frac{\partial^2 \bar{U}}{\partial Y^2} + \left( \frac{C_r}{R} \right)^2 \left( \frac{\partial^2 \bar{U}}{\partial X^2} + \frac{\partial^2 \bar{U}}{\partial Z^2} \right)$$

### The non-dimensional form of Equation (2) of the Navier-Stokes Equation

Equation (2) of N-S is shown below:

$$\frac{\partial v}{\partial t} + u \frac{\partial v}{\partial x} + v \frac{\partial v}{\partial y} + w \frac{\partial v}{\partial z} = \frac{1}{\rho} \frac{\partial p}{\partial y} + \nu \left( \frac{\partial^2 v}{\partial x^2} + \frac{\partial^2 v}{\partial y^2} + \frac{\partial^2 v}{\partial z^2} \right)$$

$$\frac{\partial v}{\partial t} = \frac{\partial v}{\partial t} \frac{dt}{dt} = \omega \frac{\partial v}{\partial t} = \omega \left[ (R\omega) \left( \frac{C_r}{R} \right) \frac{\partial \bar{V}}{\partial t} \right] = R\omega^2 \left( \frac{C_r}{R} \right) \frac{\partial \bar{V}}{\partial t}$$

$$u \frac{\partial v}{\partial x} = (\bar{U} R\omega) \left( \frac{\partial v}{\partial X} \frac{dX}{dx} \right) = (\bar{U} R\omega) \frac{1}{R} \left[ (R\omega) \left( \frac{C_r}{R} \right) \frac{\partial \bar{V}}{\partial X} \right] = C_r \omega^2 \bar{U} \frac{\partial \bar{V}}{\partial X}$$

$$v \frac{\partial v}{\partial y} = (R\omega) \left( \frac{C_r}{R} \right) \bar{V} \left( \frac{\partial v}{\partial Y} \frac{dY}{dy} \right) = (R\omega) \left( \frac{C_r}{R} \right) \bar{V} \left[ \left( \frac{1}{C_r} \right) (R\omega) \left( \frac{C_r}{R} \right) \frac{\partial \bar{V}}{\partial Y} \right] \\ = C_r \omega^2 \bar{V} \frac{\partial \bar{V}}{\partial Y}$$

$$w \frac{\partial v}{\partial z} = (\bar{W} R\omega) \left( \frac{\partial v}{\partial Z} \frac{dZ}{dz} \right) = (\bar{W} R\omega) \frac{1}{R} \left[ (R\omega) \left( \frac{C_r}{R} \right) \frac{\partial \bar{V}}{\partial Z} \right] = C_r \omega^2 \bar{W} \frac{\partial \bar{V}}{\partial Z}$$

Using non-dimensional pressure,

$$\frac{1}{\rho} \frac{\partial p}{\partial y} = \frac{1}{\rho} \frac{\partial p}{\partial \bar{Y}} \frac{d\bar{Y}}{dy} = \frac{1}{\rho C_r} \left[ \rho (R\omega)^2 \left( \frac{R}{C_r} \right) \frac{1}{\text{Re}} \right] \frac{\partial \bar{P}}{\partial \bar{Y}} = \left[ \frac{1}{C_r} \left( \frac{(R\omega)^2}{\text{Re}} \right) \left( \frac{R}{C_r} \right) \right] \frac{\partial \bar{P}}{\partial \bar{Y}}$$

$$\begin{aligned} \frac{\partial^2 v}{\partial x^2} &= \frac{\partial}{\partial x} \left( \frac{\partial v}{\partial x} \right) = \frac{\partial}{\partial x} \left( \frac{\partial v}{\partial \bar{X}} \frac{d\bar{X}}{dx} \right) = \frac{1}{R} \frac{\partial}{\partial x} \left[ (R\omega) \left( \frac{C_r}{R} \right) \frac{\partial \bar{V}}{\partial \bar{X}} \right] \\ &= \frac{1}{R} \frac{1}{R} \left[ (R\omega) \left( \frac{C_r}{R} \right) \frac{\partial^2 \bar{V}}{\partial \bar{X}^2} \right] = \left[ \left( \frac{\omega}{R} \right) \left( \frac{C_r}{R} \right) \frac{\partial^2 \bar{V}}{\partial \bar{X}^2} \right] \end{aligned}$$

$$\begin{aligned} \frac{\partial^2 v}{\partial y^2} &= \frac{\partial}{\partial y} \left( \frac{\partial v}{\partial y} \right) = \frac{\partial}{\partial y} \left( \frac{\partial v}{\partial \bar{Y}} \frac{d\bar{Y}}{dy} \right) = \frac{1}{C_r} \frac{\partial}{\partial y} \left[ (R\omega) \left( \frac{C_r}{R} \right) \frac{\partial \bar{V}}{\partial \bar{Y}} \right] \\ &= \frac{1}{C_r} \frac{1}{C_r} \left[ (R\omega) \left( \frac{C_r}{R} \right) \frac{\partial^2 \bar{V}}{\partial \bar{Y}^2} \right] = \left[ \left( \frac{\omega R}{C_r^2} \right) \left( \frac{C_r}{R} \right) \frac{\partial^2 \bar{V}}{\partial \bar{X}^2} \right] \end{aligned}$$

$$\begin{aligned} \frac{\partial^2 v}{\partial z^2} &= \frac{\partial}{\partial z} \left( \frac{\partial v}{\partial z} \right) = \frac{\partial}{\partial z} \left( \frac{\partial v}{\partial \bar{Z}} \frac{d\bar{Z}}{dz} \right) = \frac{1}{R} \frac{\partial}{\partial z} \left[ (R\omega) \left( \frac{C_r}{R} \right) \frac{\partial \bar{V}}{\partial \bar{Z}} \right] \\ &= \frac{1}{R} \frac{1}{R} \left[ (R\omega) \left( \frac{C_r}{R} \right) \frac{\partial^2 \bar{V}}{\partial \bar{Z}^2} \right] = \left[ \left( \frac{\omega}{R} \right) \left( \frac{C_r}{R} \right) \frac{\partial^2 \bar{V}}{\partial \bar{Z}^2} \right] \end{aligned}$$

Substituting the non-dimensional terms in equation (2) and dividing by  $C_r \omega^2$ , we obtain the equation:

$$\frac{\partial \bar{V}}{\partial t} + \bar{U} \frac{\partial \bar{V}}{\partial \bar{X}} + \bar{V} \frac{\partial \bar{V}}{\partial \bar{Y}} + \bar{W} \frac{\partial \bar{V}}{\partial \bar{Z}} = \left( \frac{R}{C_r} \right)^3 \frac{1}{\text{Re}} \frac{\partial \bar{P}}{\partial \bar{Y}} + \nu \left( \frac{\partial^2 \bar{V}}{\partial \bar{X}^2} + \frac{\partial^2 \bar{V}}{\partial \bar{Y}^2} + \frac{\partial^2 \bar{V}}{\partial \bar{Z}^2} \right)$$

Multiplying the equation by  $\left( \frac{C_r}{R} \right)^2 \frac{\text{Re} C_r}{R} \Rightarrow \left( \frac{C_r}{R} \right)^2 \frac{C_r^2 \omega}{\nu}$ :

$$\left( \frac{C_r}{R} \right)^2 \left[ \frac{C_r \omega \partial \bar{V}}{\nu \partial t} + \frac{\text{Re} C_r}{R} \left( \bar{U} \frac{\partial \bar{V}}{\partial \bar{X}} + \bar{V} \frac{\partial \bar{V}}{\partial \bar{Y}} + \bar{W} \frac{\partial \bar{V}}{\partial \bar{Z}} \right) \right] = \frac{\partial \bar{P}}{\partial \bar{Y}} + \left( \frac{C_r}{R} \right)^2 \left( \frac{\partial^2 \bar{V}}{\partial \bar{X}^2} + \frac{\partial^2 \bar{V}}{\partial \bar{Z}^2} \right) \frac{\partial^2 \bar{V}}{\partial \bar{Y}^2}$$

**the non-dimensional form of Equation (3):**

$$\frac{\partial w}{\partial t} + u \frac{\partial w}{\partial x} + v \frac{\partial w}{\partial y} + w \frac{\partial w}{\partial z} = \frac{1}{\rho} \frac{\partial p}{\partial z} + \nu \left( \frac{\partial^2 w}{\partial x^2} + \frac{\partial^2 w}{\partial y^2} + \frac{\partial^2 w}{\partial z^2} \right) \quad (3)$$

$$\frac{\partial w}{\partial t} = R\omega \frac{\partial \bar{W}}{\partial t} \frac{dt}{dt} = R\omega^2 \frac{\partial \bar{W}}{\partial t}$$

$$u \frac{\partial w}{\partial x} = (\bar{W} R\omega) \frac{R\omega \partial \bar{W}}{R \partial X} = R\omega^2 \bar{W} \frac{\partial \bar{W}}{\partial X}$$

$$\frac{\partial w}{\partial y} = \frac{\partial w d\bar{Y}}{\partial \bar{Y} dy} = \left( \frac{1}{C_r} \right) \left( \frac{\partial (\bar{W} R\omega)}{\partial \bar{Y}} \right) = \frac{R\omega \partial \bar{W}}{C_r \partial \bar{Y}}$$

$$v \frac{\partial w}{\partial y} = R\omega \frac{C_r \bar{V}}{R} \frac{R\omega \partial \bar{W}}{C_r \partial \bar{Y}} = R\omega^2 \bar{V} \frac{\partial \bar{W}}{\partial \bar{Y}}$$

$$w \frac{\partial w}{\partial z} = \bar{W} R\omega \frac{\partial w d\bar{Z}}{\partial \bar{Z} dz} = \bar{W} R\omega \left( \frac{R\omega \partial \bar{W}}{R \partial \bar{Z}} \right) = R\omega^2 \bar{W} \frac{\partial \bar{W}}{\partial \bar{Z}}$$

$$\frac{\partial^2 w}{\partial x^2} = \frac{\partial}{\partial x} \left( \frac{\partial w}{\partial x} \right) = \frac{\partial}{\partial x} \left( \omega \frac{\partial \bar{W}}{\partial X} \right) = \omega \frac{\partial^2 \bar{W} dX}{\partial X^2 dx} = \frac{\omega \partial^2 \bar{W}}{R \partial X^2}$$

$$\frac{\partial^2 w}{\partial y^2} = \frac{\partial}{\partial y} \left( \frac{\partial w}{\partial y} \right) = \frac{\partial}{\partial y} \left( \frac{R\omega \partial \bar{W}}{C_r \partial \bar{Y}} \right) = \frac{R\omega \partial^2 \bar{W} d\bar{Y}}{C_r \partial \bar{Y}^2 dy} = \frac{R\omega \partial^2 \bar{W}}{C_r^2 \partial \bar{Y}^2}$$

$$\frac{\partial^2 w}{\partial z^2} = \frac{\partial}{\partial z} \left( \frac{\partial w}{\partial z} \right) = \frac{\partial}{\partial z} \left( \omega \frac{\partial \bar{W}}{\partial \bar{Z}} \right) = \omega \frac{\partial^2 \bar{W} d\bar{Z}}{\partial \bar{Z}^2 dz} = \frac{\omega \partial^2 \bar{W}}{R \partial \bar{Z}^2}$$

Using non-dimensional pressure,

$$\frac{\partial p}{\partial z} = \frac{\partial p d\bar{Z}}{\partial \bar{Z} dz} = \frac{1}{R} \left[ \rho (R\omega^2) \left( \frac{R}{C_r} \right) \frac{1}{\text{Re}} \right] \frac{\partial \bar{P}}{\partial \bar{Z}}$$

Substituting the above in equation (3), **left hand side** of the equation is given as

$$R\omega^2 \frac{\partial \bar{W}}{\partial t} + R\omega^2 \bar{U} \frac{\partial \bar{W}}{\partial X} + R\omega^2 \bar{V} \frac{\partial \bar{W}}{\partial Y} + R\omega^2 \bar{W} \frac{\partial \bar{W}}{\partial Z}$$

$$R\omega^2 \left( \frac{\partial \bar{W}}{\partial t} + \bar{U} \frac{\partial \bar{W}}{\partial X} + \bar{V} \frac{\partial \bar{W}}{\partial Y} + \bar{W} \frac{\partial \bar{W}}{\partial Z} \right)$$

Dividing by  $\frac{R\omega^2}{\text{Re}} \left( \frac{R}{C_r} \right)$ , the left hand side of equation reduces to

$$\operatorname{Re}\left(\frac{C_r}{R}\right)\left(\frac{\partial \bar{W}}{\partial t} + \bar{U}\frac{\partial \bar{W}}{\partial X} + \bar{V}\frac{\partial \bar{W}}{\partial Y} + \bar{W}\frac{\partial \bar{W}}{\partial Z}\right)$$

Substituting the non dimensional terms into **right hand side** of the equation, (3) can be reduced as follows:

$$-\frac{1}{\rho R}\left[\rho(R\omega)^2\left(\frac{R}{C_r}\right)\frac{1}{\operatorname{Re}}\frac{\partial \bar{P}}{\partial Z} + \nu\left(\frac{\omega}{R}\frac{\partial^2 \bar{W}}{\partial X^2} + \frac{R\omega}{C_r}\frac{\partial^2 \bar{W}}{\partial Y^2} + \frac{\omega}{R}\frac{\partial^2 \bar{W}}{\partial Z^2}\right)\right]$$

$$-\left[R\omega^2\left(\frac{R}{C_r}\right)\frac{1}{\operatorname{Re}}\frac{\partial \bar{P}}{\partial Z} + \frac{\nu\omega}{R}\frac{\partial^2 \bar{W}}{\partial X^2} + \frac{\nu R\omega}{C_r}\frac{\partial^2 \bar{W}}{\partial Y^2} + \frac{\nu\omega}{R}\frac{\partial^2 \bar{W}}{\partial Z^2}\right]$$

Dividing by  $\frac{R\omega^2}{\operatorname{Re}}\left(\frac{R}{C_r}\right)$  or  $\frac{\nu\omega R}{C_r^2}$ , the right hand side of equation reduces to

$$\frac{\partial \bar{P}}{\partial Z} + \frac{\partial^2 \bar{W}}{\partial Y^2} + \left(\frac{C_r}{R}\right)^2\left(\frac{\partial^2 \bar{W}}{\partial X^2} + \frac{\partial^2 \bar{W}}{\partial Z^2}\right)$$

Equating the right and left hand sides, equation (1) in non-dimensional form reduces to:

$$\operatorname{Re}\left(\frac{C_r}{R}\right)\left(\frac{\partial \bar{W}}{\partial t} + \bar{U}\frac{\partial \bar{W}}{\partial X} + \bar{V}\frac{\partial \bar{W}}{\partial Y} + \bar{W}\frac{\partial \bar{W}}{\partial Z}\right) = \frac{\partial \bar{P}}{\partial Z} + \frac{\partial^2 \bar{W}}{\partial Y^2} + \left(\frac{C_r}{R}\right)^2\left(\frac{\partial^2 \bar{W}}{\partial X^2} + \frac{\partial^2 \bar{W}}{\partial Z^2}\right)$$

### Non-Dimensional Navier -Stokes equations

$$\operatorname{Re}\left(\frac{C_r}{R}\right)\left(\frac{\partial \bar{U}}{\partial t} + \bar{U}\frac{\partial \bar{U}}{\partial X} + \bar{V}\frac{\partial \bar{U}}{\partial Y} + \bar{W}\frac{\partial \bar{U}}{\partial Z}\right) = \frac{\partial \bar{P}}{\partial X} + \frac{\partial^2 \bar{U}}{\partial Y^2} + \left(\frac{C_r}{R}\right)^2\left(\frac{\partial^2 \bar{U}}{\partial X^2} + \frac{\partial^2 \bar{U}}{\partial Z^2}\right) \quad (4)$$

$$\left(\frac{C_r}{R}\right)^2 \left[ \frac{C_r \omega \partial \bar{V}}{\nu \partial t} + \frac{\operatorname{Re} C_r}{R} \left( \bar{U} \frac{\partial \bar{V}}{\partial X} + \bar{V} \frac{\partial \bar{V}}{\partial Y} + \bar{W} \frac{\partial \bar{V}}{\partial Z} \right) \right] = \frac{\partial \bar{P}}{\partial Y} \quad (5)$$

$$\left(\frac{C_r}{R}\right)^2 \left[ \left(\frac{C_r}{R}\right)^2 \left(\frac{\partial^2 \bar{V}}{\partial X^2} + \frac{\partial^2 \bar{V}}{\partial Z^2}\right) \frac{\partial^2 \bar{V}}{\partial Y^2} \right]$$

$$\operatorname{Re}\left(\frac{C_r}{R}\right)\left(\frac{\partial \bar{W}}{\partial t} + \bar{U}\frac{\partial \bar{W}}{\partial X} + \bar{V}\frac{\partial \bar{W}}{\partial Y} + \bar{W}\frac{\partial \bar{W}}{\partial Z}\right) = \frac{\partial \bar{P}}{\partial Z} + \frac{\partial^2 \bar{W}}{\partial Y^2} + \left(\frac{C_r}{R}\right)^2\left(\frac{\partial^2 \bar{W}}{\partial X^2} + \frac{\partial^2 \bar{W}}{\partial Z^2}\right) \quad (6)$$

In a typical bearing ( $C_r / R$ ) is typically 0.001 - 0.002. For these low values the second order terms can be neglected. Also the Reynolds number in a typical oil lubricated bearing is less than 500. Hence,  $Re (C_r / R)$  is less than 1 and as such all terms containing  $Re (C_r / R)$  can also be ignored. With these modifications, the non-dimensional Navier-Stokes equations reduce to the following:

$$\frac{\partial \bar{P}}{\partial X} = \frac{\partial^2 \bar{U}}{\partial \bar{Y}^2} \quad \text{--- (7)}$$

$$\frac{\partial \bar{P}}{\partial \bar{Y}} = 0 \quad \text{--- (8)}$$

$$\frac{\partial \bar{P}}{\partial Z} = \frac{\partial^2 \bar{W}}{\partial \bar{Y}^2} \quad \text{--- (9)}$$

Equation (8) implies that the pressure gradient across the film thickness is zero.

The object of the bearing analysis was to calculate the pressure distribution in the lubricant film from which the load carrying capacity would be calculated. In order to obtain the pressure distribution, equations (7) and (9) will be reverted back to dimensional form. The relation between the non-dimensional terms in equations (7) and (9) and their corresponding dimensional form is as follows:

$$\frac{\partial^2 \bar{U}}{\partial \bar{Y}^2} = \frac{C_r^2}{R\omega} \frac{\partial^2 u}{\partial y^2}$$

$$\frac{\partial^2 \bar{W}}{\partial \bar{Z}^2} = \frac{C_r^2}{R\omega} \frac{\partial^2 w}{\partial z^2}$$

$$\frac{\partial \bar{P}}{\partial X} = \frac{C_r^2}{\mu R\omega} \frac{\partial p}{\partial x}$$

$$\frac{\partial \bar{P}}{\partial Z} = \frac{C_r^2}{\mu R\omega} \frac{\partial p}{\partial z}$$

Substituting the above terms in equations (7) and (9), we have,

$$\frac{\partial p}{\partial x} = \mu \frac{\partial^2 u}{\partial y^2} \quad \text{--- (10)}$$

$$\frac{\partial p}{\partial z} = \mu \frac{\partial^2 w}{\partial z^2} \quad \text{---(11)}$$

Equation (10) can be rewritten as

$$\frac{\partial p}{\partial x} = \frac{\partial}{\partial y} \left( \mu \frac{\partial u}{\partial y} \right) = \frac{\partial(\text{ShearForce})}{\partial y}$$

Integrating equation (10) with respect to “y” twice, assuming constant viscosity, we obtain

$$\frac{\partial u}{\partial y} = \frac{y}{\mu} \frac{\partial p}{\partial x} + C_1$$

$$u = \frac{1}{2\mu} \frac{\partial p}{\partial x} y^2 + C_1 y + C_2$$

Similarly integrating Equation (11) twice with respect to z, assuming constant viscosity, we have

$$w = \frac{1}{2\mu} \frac{\partial p}{\partial z} y^2 + C_3 y + C_4$$

$C_1, C_2, C_3$  and  $C_4$  can be obtained from the following boundary conditions:

$$at\ y=0 \Rightarrow \begin{bmatrix} u=u_1 \\ v=v_1 \\ w=0 \end{bmatrix} \Rightarrow C_2=u_1, C_4=0$$

$$at\ y=H \Rightarrow \begin{bmatrix} u=u_2 \\ v=v_2 \\ w=0 \end{bmatrix} \Rightarrow C_1 = \frac{(u_2-u_1)}{H} \frac{H}{2\mu} \frac{\partial p}{\partial x}, C_3 = \frac{H}{2\mu} \frac{\partial p}{\partial z}$$

Substituting for  $C_1, C_2, C_3$  and  $C_4$  in equations for w and u, we have the following equations:

$$u = \frac{y(y-H)}{2\mu} \frac{\partial p}{\partial x} + \left[ \left( \frac{H-y}{H} \right) u_1 + \frac{y}{H} u_2 \right]$$

$$w = \frac{y(y-H)}{2\mu} \frac{\partial p}{\partial z}$$

Substituting  $\frac{\partial u}{\partial x}$  and  $\frac{\partial w}{\partial z}$  in the continuity equation,

$$\frac{\partial v}{\partial y} = \frac{\partial}{\partial x} \left[ \frac{y(y-H)}{2\mu} \frac{\partial p}{\partial x} \right] - \frac{\partial}{\partial x} \left[ \frac{(H-y)}{H} u_1 + \frac{y}{H} u_2 \right] - \frac{\partial}{\partial z} \left[ \frac{y(y-H)}{2\mu} \frac{\partial p}{\partial z} \right]$$

Integrating with respect to y with limits from 0 to H

$$\int_0^H \frac{\partial v}{\partial y} dy = \int_0^H \frac{\partial}{\partial x} \left[ \frac{y(y-H)}{2\mu} \frac{\partial p}{\partial x} \right] dy - \int_0^H \frac{\partial}{\partial x} \left[ \frac{(H-y)}{2H} u_1 + \frac{y}{H} u_2 \right] dy - \int_0^H \frac{\partial}{\partial z} \left[ \frac{y(y-H)}{2\mu} \frac{\partial p}{\partial z} \right] dy$$

Applying Leibnitz rule

$$\frac{d}{d\alpha} \int_0^{u(\alpha)} f(\beta, \alpha) d\beta = \int_0^{u(\alpha)} \frac{df(\beta, \alpha)}{d\alpha} d\beta + f(u, \alpha) \frac{du}{d\alpha}$$

$$\int_0^{u(\alpha)} \frac{df(\beta, \alpha)}{d\alpha} d\beta = \frac{d}{d\alpha} \int_0^{u(\alpha)} f(\beta, \alpha) d\beta + f(u, \alpha) \frac{du}{d\alpha}$$

The equivalent variables of Leibnitz's rule in term (1) are as follows:

$$\alpha = x, \beta = y, f(\beta, \alpha) = \frac{y(y-H)}{2\mu} \frac{\partial p}{\partial x}, u(\alpha) = H(x)$$

Applying Leibnitz's rule to the first term, we have:

$$f(u, \alpha) = f(H, x) = 0$$

$$\int_0^H \frac{\partial}{\partial x} \left[ \frac{y(y-H)}{2\mu} \frac{\partial p}{\partial x} \right] dy = \frac{1}{2\mu} \frac{\partial}{\partial x} \int_0^H \left[ \frac{y(y-H)}{2\mu} \frac{\partial p}{\partial x} \right] dy = \frac{1}{2\mu} \frac{\partial}{\partial x} \left[ \frac{\partial p}{\partial x} \left( \frac{y^3}{3} - \frac{Hy^2}{2} \right) \right]_0^H$$

$$\int_0^H \frac{\partial}{\partial x} \left[ \frac{y(y-H)}{2\mu} \frac{\partial p}{\partial x} \right] dy = -\frac{1}{2\mu} \frac{H^3}{6} \frac{\partial p}{\partial x}$$

The equivalent variables of Leibnitz's rule in term (2) are as follows:

$$\alpha=x, \beta=y, f(\beta, \alpha) = \left[ \left( \frac{H-y}{H} \right) U_1 + \frac{y}{H} U_2 \right], u(\alpha) = H(x)$$

Applying Leibnitz's rule to the first term, we have:

$$f(u, \alpha) = f(H, x) = U_2$$

$$\begin{aligned} \int_0^H \frac{\partial}{\partial x} \left[ \left( \frac{H-y}{H} \right) U_1 + \frac{y}{H} U_2 \right] dy &= \frac{\partial}{\partial x} \int_0^H \left[ \left( \frac{H-y}{H} \right) U_1 + \frac{y}{H} U_2 \right] dy \\ &= \frac{\partial}{\partial x} \left[ U_1 \left( y - \frac{y^2}{2H} \right) + \frac{y^2}{2H} U_2 \right]_0^H = \frac{\partial}{\partial x} \left[ \frac{HU_1}{2} + \frac{HU_2}{2} \right] \end{aligned}$$

$$\int_0^H \frac{\partial}{\partial x} \left[ \left( \frac{H-y}{H} \right) U_1 + \frac{y}{H} U_2 \right] dy = \frac{\partial}{\partial x} \left[ \frac{HU_1}{2} + \frac{HU_2}{2} \right] = \frac{\partial}{\partial x} \left( H \left( \frac{U_1 + U_2}{2} \right) \right)$$

$$f(u, \alpha) \frac{du}{d\alpha} = f(H, x) \frac{\partial H}{\partial x} = U_2 \frac{\partial H}{\partial x}$$

The equivalent variables of Leibnitz's rule in term (3) are as follows:

$$\alpha = z, \beta = y, f(\beta, \alpha) = \frac{y(y-H)}{2\mu} \frac{\partial p}{\partial z}, u(\alpha) = H(z)$$

Applying Leibnitz's rule to first term, we have:

$$f(u, \alpha) = f(H, z) = 0$$

$$\int_0^H \frac{\partial}{\partial z} \left[ \frac{y(y-H)}{2\mu} \frac{\partial p}{\partial z} \right] dy = \frac{1}{2\mu} \frac{\partial}{\partial z} \int_0^H \left[ \frac{y(y-H)}{2\mu} \frac{\partial p}{\partial z} \right] dy = \frac{1}{2\mu} \frac{\partial}{\partial z} \left[ \frac{\partial p}{\partial z} \left( \frac{y^3}{3} - \frac{Hy^2}{2} \right) \right]_0^H$$

$$\int_0^H \frac{\partial}{\partial z} \left[ \frac{y(y-H)}{2\mu} \frac{\partial p}{\partial z} \right] dy = - \frac{1}{2\mu} \frac{H^3}{6} \frac{\partial p}{\partial z}$$

$$\int_0^H \frac{\partial v}{\partial y} dy = (V_2 - V_1)$$

Using the above results, integration of equation (4) can now be written as:

$$(V_2 - V_1) = \frac{1}{2\mu} \frac{\partial}{\partial x} \left[ -\frac{H^3}{6} \frac{\partial p}{\partial x} \right] + \frac{1}{2} \frac{\partial}{\partial x} (H(U_1 + U_2)) + U_2 \frac{\partial H}{\partial x} - \frac{1}{2\mu} \frac{\partial}{\partial z} \left[ -\frac{H^3}{6} \frac{\partial p}{\partial z} \right]$$

$$\frac{\partial}{\partial x} \left[ \frac{H^3}{\mu} \frac{\partial p}{\partial x} \right] + \frac{\partial}{\partial z} \left[ \frac{H^3}{\mu} \frac{\partial p}{\partial z} \right] = 12(V_2 - V_1) + 6(U_1 - U_2) \frac{\partial H}{\partial x} + 6H \frac{\partial (U_1 + U_2)}{\partial x}$$

For a fixed bearing  $V_1$ ,  $V_2$  and  $U_1$  are equal to zero. Also note that  $\frac{\partial H}{\partial x}$  is negative

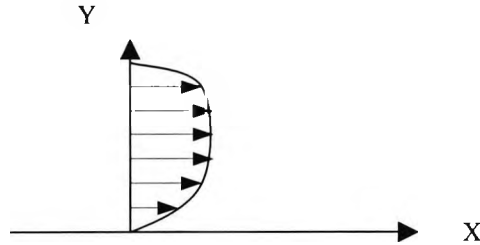
and  $\frac{\partial (U_1 + U_2)}{\partial x} = 0$ . Hence, the above equation reduces to:

$$\frac{\partial}{\partial x} \left[ \frac{H^3}{\mu} \frac{\partial p}{\partial x} \right] + \frac{\partial}{\partial z} \left[ \frac{H^3}{\mu} \frac{\partial p}{\partial z} \right] = 6U_2 \frac{\partial H}{\partial x}$$

## APPENDIX F

### Derivation Of Turbulent Reynolds equation for Journal bearings

Consider turbulent flow between two surfaces. Defining x-axis in the direction of flow , y- normal to the direction of flow and Z normal to X-Y plane, it can be noted that for lubrication problems, the length scale in y-direction is far less than x and z directions.



Shear stress in a turbulent flow can be written as:

$$\tau = \mu \left(1 + \frac{\epsilon}{\nu}\right) \frac{\partial u}{\partial y} \dots\dots(1)$$

Defining shear velocity as:

$$u_\tau = \sqrt{\frac{\tau}{\rho}}$$

Also defining following non-dimensional terms:

$$u^+ = \frac{u}{u_\tau} , y^+ = \frac{y u_\tau}{\nu}$$

According to law of wall the following relationship can be written:

$$u^+ = f(y^+)$$

Also noting that

$$\frac{\partial u}{\partial y} = \frac{\partial u}{\partial u^+} \frac{\partial u^+}{\partial y^+} \frac{\partial y^+}{\partial y} = u_\tau \frac{\partial u^+}{\partial y^+} \frac{u_\tau}{\nu}$$

$$\frac{\partial u}{\partial y} = \frac{u_\tau^2}{\nu} \frac{\partial u^+}{\partial y^+}$$

Shear stress can now be written as:

$$\tau = \mu \left(1 + \frac{\varepsilon}{\nu}\right) \frac{u_{\tau}^2}{\nu} \frac{\partial u^+}{\partial y^+} = \mu \left(1 + \frac{\varepsilon}{\nu}\right) \frac{u_{\tau}^2}{\nu} f'(y^+)$$

$$\tau = \mu \left(1 + \frac{\varepsilon}{\nu}\right) \frac{\tau}{\rho} f'(y^+)$$

$$f'(y^+) = \frac{1}{\left(1 + \frac{\varepsilon}{\nu}\right)}$$

In two-dimensional flow, neglecting inertia terms, the X-wise momentum equation is given as:

$$\frac{\partial p}{\partial x} = \frac{\partial \tau}{\partial y}$$

substituting for  $\tau$  from equation (1),

$$\frac{\partial p}{\partial x} = \frac{\partial}{\partial y} \left( \mu \left(1 + \frac{\varepsilon}{\nu}\right) \frac{\partial u}{\partial y} \right) \dots\dots\dots(2)$$

Similarly, neglecting inertia terms, momentum in z-direction is given as

$$\frac{\partial p}{\partial z} = \frac{\partial}{\partial y} \left( \mu \left(1 + \frac{\varepsilon}{\nu}\right) \frac{\partial w}{\partial y} \right) \dots\dots\dots(3)$$

Boundary conditions:  $u$  and  $w = 0$  at  $y = 0$  and  $h$ .

Equations 2 and 3 can be expressed non- dimensionally by use of the following terms:

$$p^* = \frac{p h^2}{\mu \nu}, u^* = \frac{u h}{\nu}, x^* = \frac{x}{h}, y^* = \frac{y}{h}, z^* = \frac{z}{h}, u^* = \frac{u}{h}$$

The non-dimensional derivatives can now be written as:

$$\frac{\partial p}{\partial x} = \frac{\partial p}{\partial p^*} \frac{\partial p^*}{\partial y^*} \frac{\partial y^*}{\partial y} = \frac{\mu \nu}{h^2} \frac{\partial p^*}{\partial y^*} \frac{1}{h}$$

$$\frac{\partial p}{\partial x} = \frac{\mu \nu}{h^3} \frac{\partial p^*}{\partial y^*}$$

$$\frac{\partial u}{\partial y} = \frac{\partial u}{\partial u^*} \frac{\partial u^*}{\partial y^*} \frac{\partial y^*}{\partial y} = \frac{\nu}{h} \frac{\partial u^*}{\partial y^*} \frac{1}{h}$$

$$\frac{\partial u}{\partial y} = \frac{\nu}{h^2} \frac{\partial u^*}{\partial y^*}$$

$$\frac{\partial w}{\partial y} = \frac{\partial w}{\partial w^*} \frac{\partial w^*}{\partial y^*} \frac{\partial y^*}{\partial y} = \frac{\nu}{h} \frac{\partial w^*}{\partial y^*} \frac{1}{h}$$

$$\frac{\partial w}{\partial y} = \frac{\nu}{h^2} \frac{\partial w^*}{\partial y^*}$$

$$\frac{\partial F}{\partial y} = \frac{\partial F}{\partial y^*} \frac{\partial y^*}{\partial y}$$

$$\frac{\partial w}{\partial y} = \frac{1}{h} \frac{\partial F}{\partial y^*}$$

the Equation in non-dimensional form now becomes:

$$\frac{\partial p}{\partial x} = \frac{\partial}{\partial y} \left( \mu \left( 1 + \frac{\varepsilon}{\nu} \right) \frac{\partial u}{\partial y} \right) \Rightarrow \frac{\partial p^*}{\partial x^*} \left( \frac{\mu \nu}{h^3} \right) = \frac{\mu}{h} \frac{\partial}{\partial y^*} \left( \mu \left( 1 + \frac{\varepsilon}{\nu} \right) \frac{\nu}{h^2} \frac{\partial u^*}{\partial y^*} \right)$$

$$\frac{\partial p^*}{\partial x^*} \left( \frac{\mu \nu}{h^3} \right) = \frac{\mu \nu}{h^3} \frac{\partial}{\partial y^*} \left( \mu \left( 1 + \frac{\varepsilon}{\nu} \right) \frac{\partial u^*}{\partial y^*} \right)$$

$$\frac{\partial p^*}{\partial x^*} = \frac{\partial}{\partial y^*} \left( \mu \left( 1 + \frac{\varepsilon}{\nu} \right) \frac{\partial u^*}{\partial y^*} \right) \dots \dots \dots (4)$$

Similarly equation (3) can be written as,

$$\frac{\partial p^*}{\partial z^*} = \frac{\partial}{\partial y^*} \left( \mu \left( 1 + \frac{\varepsilon}{\nu} \right) \frac{\partial w^*}{\partial y^*} \right) \dots \dots \dots (5)$$

Boundary conditions are:  $u^* = 0$  and  $w^* = 0$  at  $y^* = 0$  and  $1$ .

Integrating equation (4) once,

$$C_1 + y^* \frac{\partial p^*}{\partial x^*} = \left( 1 + \frac{\varepsilon}{\nu} \right) \frac{\partial u^*}{\partial y^*}$$

$$\frac{C_1}{\left( 1 + \frac{\varepsilon}{\nu} \right)} + \frac{y^*}{\left( 1 + \frac{\varepsilon}{\nu} \right)} \frac{\partial p^*}{\partial x^*} = \frac{\partial u^*}{\partial y^*}$$

Integrating once again with respect to  $y^*$ , we obtain

$$C_2 + \int \frac{C_1 dy^*}{\left( 1 + \frac{\varepsilon}{\nu} \right)} + \frac{\partial p^*}{\partial x^*} \int \frac{y^* dy^*}{\left( 1 + \frac{\varepsilon}{\nu} \right)} = u^*$$

Applying the boundary condition  $u^* = 0$  at  $y^* = 0$

$$C_2 + \int \left. \frac{C_1 dy^*}{(1 + \varepsilon/\nu)} \right|_{y^*=0} + \frac{\partial p^*}{\partial x^*} \int \left. \frac{y^* dy^*}{(1 + \varepsilon/\nu)} \right|_{y^*=0} = 0 \dots\dots\dots (A)$$

Applying the boundary condition  $u^* = U^*$  at  $y^* = 1$

$$C_2 + \int \left. \frac{C_1 dy^*}{(1 + \varepsilon/\nu)} \right|_{y^*=1} + \frac{\partial p^*}{\partial x^*} \int \left. \frac{y^* dy^*}{(1 + \varepsilon/\nu)} \right|_{y^*=1} = U^* \dots\dots\dots (B)$$

Subtracting equation (A) from equation (B), we have

$$C_1 \int_0^1 \frac{dy^*}{(1 + \varepsilon/\nu)} + \frac{\partial p^*}{\partial x^*} \int_0^1 \frac{y^* dy^*}{(1 + \varepsilon/\nu)} = U^* \dots\dots\dots (C)$$

Defining  $I(y^*)$  and  $J(y^*)$  as shown below:

$$I(y^*) = \int_0^1 \frac{dy^*}{(1 + \varepsilon/\nu)}, \quad J(y^*) = \int_0^1 \frac{y^* dy^*}{(1 + \varepsilon/\nu)}$$

Equation (C) now becomes,

$$C_1 I(1) + \frac{\partial p^*}{\partial x^*} J(1) = U^*$$

$$C_1 = \left( U^* - \frac{\partial p^*}{\partial x^*} J(1) \right) \frac{1}{I(1)}$$

Substituting for  $C_1$  in equation (A)

$$C_2 + \left( U^* - \frac{\partial p^*}{\partial x^*} J(1) \right) \frac{I(0)}{I(1)} + \frac{\partial p^*}{\partial x^*} J(0) = 0$$

$$C_2 = - \left( U^* - \frac{\partial p^*}{\partial x^*} J(1) \right) \frac{I(0)}{I(1)} - \frac{\partial p^*}{\partial x^*} J(0)$$

Substituting for  $C_1$  and  $C_2$ , equation can now be written as shown below:

$$u^* = \frac{\partial p^*}{\partial x^*} \int \frac{y^* dy^*}{(1 + \varepsilon/\nu)} + \left( U^* - \frac{\partial p^*}{\partial x^*} J(1) \right) \frac{1}{I(1)} \int \frac{dy^*}{(1 + \varepsilon/\nu)} - \left( U^* - \frac{\partial p^*}{\partial x^*} J(1) \right) \frac{I(0)}{I(1)} - \frac{\partial p^*}{\partial x^*} J(0)$$

The above can be further simplified as

$$u^* = \frac{\partial p^*}{\partial x^*} \left( \int \frac{y^* dy^*}{(1 + \varepsilon/\nu)} - J(0) \right) + \left( U^* - \frac{\partial p^*}{\partial x^*} J(1) \right) \frac{1}{I(1)} \left( \int \frac{dy^*}{(1 + \varepsilon/\nu)} - I(0) \right)$$

$$u^* = \frac{\partial p^*}{\partial x^*} J(y^*) + \left( U^* - \frac{\partial p^*}{\partial x^*} J(1) \right) \frac{I(y^*)}{I(1)}$$

$$u^* = \frac{\partial p^*}{\partial x^*} \left( J(y^*) - \frac{J(1)}{I(1)} I(y^*) \right) + U^* \frac{I(y^*)}{I(1)}$$

Similarly  $w^*$  can be written as:

$$w^* = \frac{\partial p^*}{\partial z^*} \left( J(y^*) - \frac{J(1)}{I(1)} I(y^*) \right) + W^* \frac{I(y^*)}{I(1)}$$

In dimensional form, the above equations can be written as:

$$\frac{uh}{\nu} = \frac{h^3}{\mu\nu} \frac{\partial p}{\partial x} \left( J(y) - \frac{J(1)}{I(1)} I(y) \right) + \frac{Uh}{\nu} \frac{I(y)}{I(1)}$$

$$\frac{wh}{\nu} = \frac{h^3}{\mu\nu} \frac{\partial p}{\partial z} \left( J(y) - \frac{J(1)}{I(1)} I(y) \right) + \frac{Wh}{\nu} \frac{I(y)}{I(1)}$$

Note that for a definite integral, the solution is not affected by changing the variable as long as the limits are also adjusted accordingly. This can be shown by considering a simple example as shown below.

$$F = \int_0^h x dx$$

$$F = \frac{h^2}{2}$$

$$\text{defining } x^* = \frac{x}{h}$$

$$F^* = h^2 \int_0^1 x^* dx^* = \frac{h^2}{2}$$

Defining average velocities,  $\bar{u}$  and  $\bar{w}$ , the equations can be written in terms of average values as:

$$\bar{u}h = \frac{h^3}{\mu\nu} \frac{\partial p}{\partial x} \left( \bar{J}(y) - \frac{J(1)}{I(1)} \bar{I}(y) \right) + \frac{Uh}{\nu} \frac{\bar{I}(y)}{I(1)}$$

$$\bar{w}h = \frac{h^3}{\mu\nu} \frac{\partial p}{\partial z} \left( \bar{J}(y) - \frac{J(1)}{I(1)} \bar{I}(y) \right) + \frac{Wh}{\nu} \frac{\bar{I}(y)}{I(1)}$$

The conservation of mass is given as :

Consider a small volume of fluid between two surfaces. Applying the conservation of mass:

$$\left( uh + \frac{\partial(uh)}{\partial x} dx \right) dz - uh dz + \left( wh + \frac{\partial(wh)}{\partial z} dz \right) dx - wh dx = 0$$

Since the gap is small, local velocities can be substituted by average velocities.

Dividing by

(dx.dz), the conservation of mass can be written as :

$$\frac{\partial \bar{u}h}{\partial x} + \frac{\partial \bar{w}h}{\partial z} = 0$$

Substituting for  $\bar{u}h$  and  $\bar{w}h$ , we have:

$$\begin{aligned} \frac{\partial}{\partial x} \left( \frac{h^3}{\mu\nu} \frac{\partial p}{\partial x} \left( \bar{J}(y) - \frac{J(1)}{I(1)} \bar{I}(y) \right) + \frac{Uh}{\nu} \frac{\bar{I}(y)}{I(1)} \right) \\ + \frac{\partial}{\partial z} \left( \frac{h^3}{\mu\nu} \frac{\partial p}{\partial z} \left( \bar{J}(y) - \frac{J(1)}{I(1)} \bar{I}(y) \right) + \frac{Wh}{\nu} \frac{\bar{I}(y)}{I(1)} \right) = 0 \end{aligned}$$

$$\begin{aligned} \frac{\partial}{\partial x} \left( -\frac{h^3}{\mu} \frac{\partial p}{\partial x} \left( \frac{J(1)}{I(1)} \bar{I}(y) - \bar{J}(y) \right) + Uh \frac{\bar{I}(y)}{I(1)} \right) \\ + \frac{\partial}{\partial z} \left( -\frac{h^3}{\mu} \frac{\partial p}{\partial z} \left( \frac{J(1)}{I(1)} \bar{I}(y) - \bar{J}(y) \right) + Wh \frac{\bar{I}(y)}{I(1)} \right) = 0 \end{aligned}$$

Noting that h is a strong function of x compared to z

$$\frac{\partial}{\partial x} \left( \frac{h^3}{\mu} \frac{\partial p}{\partial x} \left( \frac{J(1)}{I(1)} \bar{I}(y) - \bar{J}(y) \right) \right) + \frac{\partial}{\partial z} \left( \frac{h^3}{\mu} \frac{\partial p}{\partial z} \left( \frac{J(1)}{I(1)} \bar{I}(y) - \bar{J}(y) \right) \right) = \frac{\partial}{\partial x} \left( Uh \frac{\bar{I}(y)}{I(1)} \right)$$

$$\begin{aligned} \frac{\partial}{\partial x} \left( \frac{h^3}{\mu} \frac{\partial p}{\partial x} \left( \frac{J(1)}{I(1)} \bar{I}(y) - \bar{J}(y) \right) \right) + \frac{\partial}{\partial z} \left( \frac{h^3}{\mu} \frac{\partial p}{\partial z} \left( \frac{J(1)}{I(1)} \bar{I}(y) - \bar{J}(y) \right) \right) \\ = \frac{U}{2} \frac{\partial h}{\partial x} - \frac{U}{2} \frac{\partial h}{\partial x} + \frac{\partial}{\partial x} \left( Uh \frac{\bar{I}(y)}{I(1)} \right) \end{aligned}$$

$$\begin{aligned} \frac{\partial}{\partial x} \left( \frac{h^3}{\mu} \frac{\partial p}{\partial x} \left( \frac{J(\mathbf{l})}{I(\mathbf{l})} \bar{I}(\mathbf{y}) - \bar{J}(\mathbf{y}) \right) \right) + \frac{\partial}{\partial z} \left( \frac{h^3}{\mu} \frac{\partial p}{\partial z} \left( \frac{J(\mathbf{l})}{I(\mathbf{l})} \bar{I}(\mathbf{y}) - \bar{J}(\mathbf{y}) \right) \right) \\ = \frac{U}{2} \frac{\partial h}{\partial x} - \frac{\partial}{\partial x} \left( \left( \frac{1}{2} - \frac{\bar{I}(\mathbf{y})}{I(\mathbf{l})} \right) U h \right) \end{aligned}$$

$$\begin{aligned} \frac{\partial}{\partial x} \left( \frac{h^3}{\mu} \frac{\partial p}{\partial x} \left( \frac{J(\mathbf{l})}{I(\mathbf{l})} \bar{I}(\mathbf{y}) - \bar{J}(\mathbf{y}) \right) \right) + \frac{\partial}{\partial z} \left( \frac{h^3}{\mu} \frac{\partial p}{\partial z} \left( \frac{J(\mathbf{l})}{I(\mathbf{l})} \bar{I}(\mathbf{y}) - \bar{J}(\mathbf{y}) \right) \right) \\ = \frac{U}{2} \frac{\partial h}{\partial x} - \frac{\partial}{\partial x} \left( \frac{h^3}{\mu} \frac{\partial p}{\partial x} \left( \frac{1}{2} - \frac{\bar{I}(\mathbf{y})}{I(\mathbf{l})} \right) \frac{U h}{\frac{h^3}{\mu \nu} \frac{\partial p}{\partial x}} \right) \end{aligned}$$

$$\frac{\partial}{\partial x} \left( \frac{h^3}{\mu} \frac{\partial p}{\partial x} \left( \frac{J(\mathbf{l})}{I(\mathbf{l})} \bar{I}(\mathbf{y}) - \bar{J}(\mathbf{y}) + \frac{\left( \frac{1}{2} - \frac{\bar{I}(\mathbf{y})}{I(\mathbf{l})} \right) U h}{\frac{h^3}{\mu \nu} \frac{\partial p}{\partial x}} \right) \right) + \frac{\partial}{\partial z} \left( \frac{h^3}{\mu} \frac{\partial p}{\partial z} \left( \frac{J(\mathbf{l})}{I(\mathbf{l})} \bar{I}(\mathbf{y}) - \bar{J}(\mathbf{y}) \right) \right) = \frac{U}{2} \frac{\partial h}{\partial x}$$

$$\frac{\partial}{\partial x} \left( \frac{h^3}{\mu} G_x \frac{\partial p}{\partial x} \right) + \frac{\partial}{\partial z} \left( \frac{h^3}{\mu} G_z \frac{\partial p}{\partial z} \right) = \frac{U}{2} \frac{\partial h}{\partial x}$$

Where  $G_x$  and  $G_z$  are given as :

$$G_x = \left( \frac{J(\mathbf{l})}{I(\mathbf{l})} \bar{I}(\mathbf{y}) - \bar{J}(\mathbf{y}) + \frac{\left( \frac{1}{2} - \frac{\bar{I}(\mathbf{y})}{I(\mathbf{l})} \right) U h}{\frac{h^3}{\mu \nu} \frac{\partial p}{\partial x}} \right)$$

$$G_z = \left( \frac{J(\mathbf{l})}{I(\mathbf{l})} \bar{I}(\mathbf{y}) - \bar{J}(\mathbf{y}) \right)$$

The values of  $G_x$  and  $G_z$  are given as :

$$\frac{1}{G_x} = 12 + 0.0136(\text{Re})^{0.90}$$

$$\frac{1}{G_y} = 12 + 0.0043(\text{Re})^{0.96}$$

**References:**

- 1) Elrod, H.G., Ng, C.W., *A Theory Of Turbulent Fluid Films and its application to Bearings*, Trans ASME Journal Of Lubrication Technology, July 1967, pp 347 – 362.

## **APPENDIX G**

### **Computational Fluid Dynamics Analysis**

#### **G.1 Introduction:**

This appendix covers basics of computational fluid dynamics and mesh generation in CFX. Computational Fluid Dynamics is a numerical solution method. CFD analysis consists of discretizing the fluid domain into computational grid points and solving differential equations of motion at each point. The steps involved are:

- 1)
- 2) Mathematical Model
- 3) Discretization method
- 4) Numerical Grid
- 5) Finite Approximations
- 6) Solution method
- 7) Convergence Criteria

#### **G.2 Mathematical Model**

The starting point of any numerical method is the mathematical model i.e the set of partial differential or integro-differential equations and boundary conditions.

Depending upon the physics of the problem, one chooses an appropriate model such as compressible, incompressible, inviscid, turbulent, two or three-dimensional. The mathematical model may include simplifications of the exact conservation laws.

#### **Discretization method**

After selecting the mathematical model, one has to choose a suitable discretization method i.e a method of approximating the differential equations by a set of algebraic equations for the variables at some set of discrete locations in space and time. The methods most widely used are:

- 1) Finite difference
- 2) Finite volume
- 3) Finite element

### **G.2.1 Finite Difference Method (FD)**

This is the oldest method for solving numerical solution of PDE's. At each grid point, the differential equation is approximated by replacing the partial derivatives by approximations in terms of the nodal values of the functions. The result is one algebraic equation per grid node, in which the variable value at that and a certain number of neighbouring nodes appear as unknowns. A Taylor's series expansion or polynomial fitting is used to obtain approximations to the first and second derivatives of the variables with respect to the coordinates. The finite difference method is mainly applied to structured grids, though it can also be applied to unstructured grids.

### **G.2.2 Finite Volume method (FV)**

The FV method uses the integral form of the conservation equations as its starting point. The solution domain is subdivided into a finite number of contiguous control volumes (CVs), and the conservation equations are applied to each CV. At the centroid of each CV lies a computational node at which the variable values are to be calculated. Interpolation is used to express the variable values at the CV surface in terms of the nodal (CV-center) values. Surface and volume integrals are approximated using suitable formulae.

The FV method can accommodate any type of grid, so it is suitable for complex geometries. The grid defines only the control volume boundaries and need not be related to a coordinate system. The method is conservative by construction since surface integrals representing convective and diffusive fluxes are the same for CVs sharing the boundary.

### **G.2.3 Finite Element Method (FE)**

The FE method is similar to the FV; the domain is broken into a set of discrete volumes or finite elements that are generally unstructured. For two-dimensional problems the elements are either triangles or quadrilaterals while in three-

dimensional problems the elements are tetrahedral or hexahedral. The distinguishing feature of FE methods is that the equations are multiplied by a weight function before they are integrated over the entire domain. In the simplest FE methods, the solution is approximated by a linear shape function within each element in a way that guarantees continuity of the solution across the element boundaries. Such a function can be constructed from its values at the corners of the elements. The weight function is of the same form over the entire domain. This approximation is then substituted into the weighted integral of the conservation law and the equations to be solved are derived by requiring the derivative of the integral with respect to each nodal value to be zero. The result is a set of non-linear algebraic equations. FE methods are best suited for complex geometries.

### **G.3 Numerical Grid**

The discrete locations at which the variables are to be calculated are defined by the numerical grid that is essentially a discrete representation of the geometric domain on which the problem is to be solved. It divides the solution domain into a finite number of sub domains such as elements in the FE and control volumes in the FD method. The different types of grid used in CFD analysis are the following:

- A) Structured or Regular
- B) Block Structured
- C) Unstructured

#### **G.3.1 Structured grids**

Structured grids consist of families of grid lines with the property that members of a single family do not cross each other and cross each member of other families only once. This allows the lines of a given set to be numbered consecutively. The position of any grid point or control volume within the domain is uniquely identified by a set of two indices in 2D and three indices in 3D. Each point has four nearest neighbors in two dimensions and six in three dimensions.

Structured grids are further subdivided into the H-, O- or C-type based on the shapes of the grid lines. The H-grid has distinct east, west, north and south boundaries. In an O-type grid, one set of grid lines is endless, like a circle. In a C-type, one set of grid lines has the shape of a C. this type of grid is often used for bodies with sharp edges.

The neighbour connectivity simplifies programming and the matrix of the algebraic equation system has a regular structure which renders the use of efficient solvers. The disadvantage is that it can be used only for geometrically simple solution domains. Another disadvantage is that it may be difficult to control the distribution of the grid points, i.e. the concentration of points in one region, for reasons of accuracy, produces unnecessarily small spacing in other parts of the solution domain. This problem is exaggerated in 3D problems with the presence of long thin cells, adversely affecting the convergence.

### **G.3.2 Block Structured Grid**

In a block-structured grid, there is a two level subdivision of the solution domain. On the coarse level, there are blocks, which are relatively large segments of the domain, their structure may be irregular and they may or may not overlap. On the fine level, within each block, a structured grid is defined. At the interface between a coarse and a fine mesh, the nodes may or may not match.

### **G.3.3 Unstructured Grids**

For very complex geometries, the most flexible type of grid is one, which can fit an arbitrary solution domain boundary. The elements or control volumes may have any shape and there is no restriction on the number of neighbour elements or nodes. In practice, grids made of triangles or quadrilaterals in 2D, and tetrahedra or hexahedra in 3D are the most often used. The advantage of flexibility is offset by of the irregularity of the data structure. The matrix of the algebraic equation system, no longer has regular, diagonal structure and the solvers are usually slower than those for regular grids.

### **G.3.4 Finite approximations**

Following the choice of a grid type, one has to select the approximations to be used in the discretization process. In the finite difference method, approximations for the derivatives at the grid points have to be selected. In the finite volume method, one has to select the methods of approximating the surface and volume integrals. In the finite element method, one has to choose the elements and weighting functions. The choice influences the accuracy of the approximation. More accurate approximations involve more nodes and give fuller coefficient matrices

### **G.4 Solution method**

The result of discretization is a system of algebraic equations which are either linear or non-linear according to the nature of the partial differential equations from which they are derived. In the non-linear case, the discretized equations are solved by an iterative technique that involves guessing a solution, linearizing the equations about the solution and improving the solution. The process is repeated until a converged result is obtained. So, whether the equations are linear or not, efficient methods for solving linear systems of algebraic equations are needed. The matrices derived from partial differential equations are always sparse i.e. most of their elements are zero. Some of the methods used for solving system of linear algebraic equations are:

- 1) Gauss elimination
- 2) LU decomposition
- 3) Tridiagonal Matrix Algorithm
- 4) Iterative methods

For non-linear systems, the Newton-Raphson and Secant methods are widely used. The Newton-Raphson method for finding the root of  $F(x)=0$ , proceeds as follows:

- 1) Expand  $F(x)$  in Taylor series about a reference point or guessed solution
- 2) Truncate the series after second term, i.e

$$F(x_n + \Delta x) = F(x_n) + F'(x_n) \Delta x$$

- 3) Compute the value of  $\Delta x$  by setting  $F(x_n + \Delta x) = 0$
- 4) The new value is  $x_{n+1} = x_n + \Delta x$
- 5) Steps 2 and 3 are repeated until,  $x_{n+1} - x_n < \varepsilon$

Newton's method requires that  $F'(x)$  be evaluated analytically. When this is not possible, the secant generalization of the Newton's procedure is used. In the secant generalization, the derivative is replaced by a secant line approximation through two points

$$F'(x_{n-1}) \approx \frac{F(x_n) - F(x_{n-1})}{x_n - x_{n-1}}$$

After two initial guesses for  $x$ , the third approximation to the root is obtained from

$$x_{n+1} = x_n - \frac{F(x_n)}{F(x_n) - F(x_{n-1})} (x_n - x_{n-1})$$

Newton's method for a general system of non-linear equations is written as:

$$f_i(x_1, x_2, \dots, x_n) = f_i(x_1^k, x_2^k, \dots, x_n^k) + \sum_{j=1}^n (x_j^{k+1} - x_j^k) \frac{\partial f_i(x_1^k, x_2^k, \dots, x_n^k)}{\partial x_j}$$

for  $i = 1, 2, 3, \dots, n$ . When the above is set to zero, a system of linear algebraic equations is obtained, which can be solved by Gauss elimination.

### **G.6 Convergence Criteria**

When using iterative solvers, it is important to know when to quit. The most common procedure is based on the difference between two successive iterations. The procedure is stopped when this difference, measured by some norm is less than a pre-selected value.

### **G.7 Mesh Generation in CFX**

Mesh generation is the process by which spatial discretization of the CFD model is accomplished. CFX meshing is based on a triangular/tetrahedral element discretisation. CFX uses a method known as Advancing Front and Inflation (AFI) to

generate a mesh. The AFI mesher allows automatic tetrahedral mesh generation with a mechanism, called "inflation", for resolving the mesh in the near wall regions, to capture flow effects for viscous problems. AFI works by generating a "front" of triangular mesh elements on the surfaces of the fluid domain. It then generates the volume mesh from this front. The volume mesh consists of tetrahedral elements, or a tetrahedral/prismatic/pyramidal element mix when inflation is used.

The AFI mesher provides three general control mechanisms for the generation of surface and volume meshes:

- Mesh parameters

Mesh parameters control the background size of the volume and surface mesh elements. For volume mesh spacing, a maximum edge length is used to provide a background volume mesh scale. The surface mesh spacing, is controlled by specifying either an edge length or an angular resolution. A parameter, called the expansion factor, is used to control the mesh generation near curved surfaces. The expansion factor controls both the rate of growth of volume elements away from curved surfaces and the rate of growth of surface elements away from a curved into the middle of a flat surface. Another parameter, called stretching, is used to expand or contract the mesh elements in a particular direction.

- Mesh controls

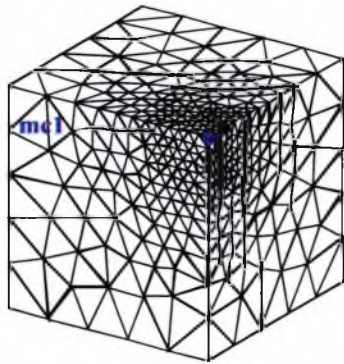
Mesh controls are used to refine the surface and volume mesh in specific regions of the model. The mesh refining effect decays with increasing distance from the control, generating progressively coarser elements. Mesh controls can be a point, a line or a triangle. Each mesh control point has attributes pertaining to the extent of the influence of the mesh refining effect. These are:

- Length scale – a length scale for the mesh size in the locality of the mesh control.
- Radius – the radial extent of the fixed length scale influence.
- Expansion factor – the mesh coarsening rate is determined by a geometric expansion factor. Large values tend to coarsen the mesh rapidly from the mesh control point.

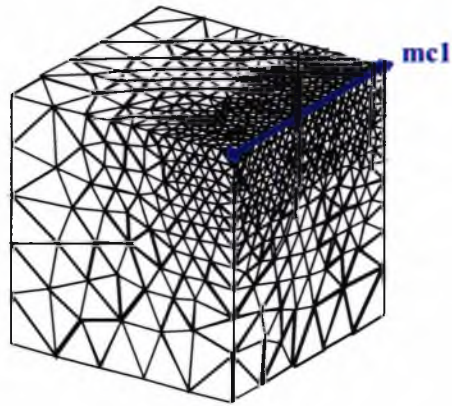
Figure (G1) below illustrates the use of mesh controls.

- Inflation

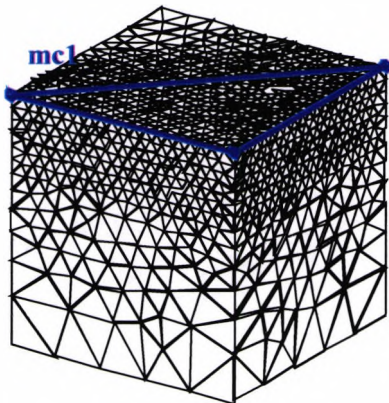
In near wall regions, boundary layer effects give rise to velocity gradients that are greatest normal to the surface. Computationally efficient meshes in these regions require that the elements have high aspect ratios. If tetrahedral elements are used, then a prohibitively fine surface mesh may be required to avoid generating highly distorted elements at the surface. The AFI mesher overcomes this problem by using prisms to create a mesh that is finely resolved normal to the wall, but coarse parallel to it. This mesh arrangement is beneficial for cost effective CFD analysis. The AFI mesher can use the local surface element normals to 'inflate' 2D triangular into 3D 'prism' elements at selected walls or boundaries. The program has input parameters to control the size and distribution of the elements in near-wall regions. The number of layers, the maximum thickness specification and the local element edge length control the thickness of the inflation layers. The mesher allows the setting of different parameters for different surfaces. When two inflated surfaces meet at a common edge and have different inflation heights set, the heights are smoothed. Figure (G2) shows an example of inflation near a boundary.



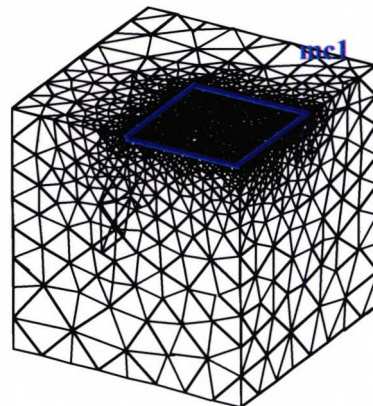
**Point**  
 Edge Length - 0.05  
 Radius - 0.2  
 Expansion Factor - 1.2



**Line**  
 Edge Length - 0.05  
 Radius - 0.2  
 Expansion Factor - 1.2



**Triangle**  
 Edge Length - 0.05  
 Radius - 0.2  
 Expansion Factor - 1.2



**Surface**  
 Edge Length - 0.02  
 Expansion Factor - 1.2

**Figure G1: Mesh Controls in CFX**

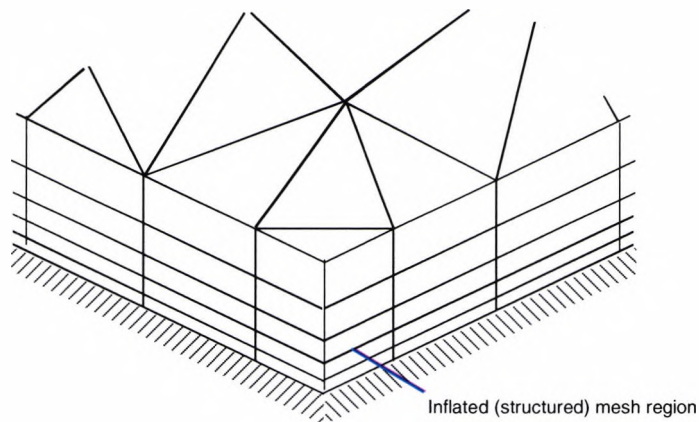


**Figure G2: Example of Inflation**